

# Asymmetrical localised synthetic jets in three-dimensional flows over bluff and streamlined bodies

**Author:**

Findanis, Nicholas

**Publication Date:**

2012

**DOI:**

<https://doi.org/10.26190/unsworks/15399>

**License:**

<https://creativecommons.org/licenses/by-nc-nd/3.0/au/>

Link to license to see what you are allowed to do with this resource.

Downloaded from <http://hdl.handle.net/1959.4/51833> in <https://unsworks.unsw.edu.au> on 2024-05-03

# UNSW



The University of New South Wales  
School of Mechanical and Manufacturing Engineering

## **Asymmetrical localised synthetic jets in three-dimensional flows over bluff and streamlined bodies**

By

Nicholas Findanis

Supervisor: A/Prof N.A. Ahmed

A thesis submitted as part fulfilment of the requirements for the degree  
of  
Doctor of Philosophy  
(Aerospace Engineering)

**May, 2012**

# Abstract

Synthetic jet, a turbulent shear flow generated from an oscillating train of coalescing vortex rings having a time-averaged zero net mass flow rate, is generally applied in a distributed manner. A distinctive method of applying synthetic jet technology, namely an asymmetrical localised synthetic jet, is developed with the aim of improving the aerodynamic performance and efficiency of three-dimensional bluff and streamlined bodies. Further, the use of an asymmetrical localised synthetic jet will contribute towards the deficiency of three-dimensional flow studies.

Two main characteristics of unsteady three-dimensional fluid-structure interaction that produce drag were investigated: flow separation of the boundary layer and the wake region. A bluff body, an 80 mm side-supported sphere, was tested at a Reynolds number of  $5 \times 10^4$  in a closed test section wind tunnel in the UNSW Aerodynamics Laboratory. Surface pressure measurements on the sphere showed a delay in flow separation and a reduction in drag due to the synthetic jet. Wake survey data obtained using a five-hole pressure probe were used to formulate a set of guiding criteria resulting in a four step process to determine wake regions with reversal of flow. Pressure and vorticity contour plots showed that the synthetic jet increased the streamwise velocity component and decreased the size of the wake. Further, the wake region was characterised using non-standard definitions of displacement thickness, momentum thickness and shape factor to show that the synthetic jet decreases the energy loss in the wake. A surprising discovery was the ability of the synthetic jet to smooth the flow at the support-sphere junction.

CFD modelling was applied to the bluff and streamlined bodies using an advanced commercial CFD package. The results agreed with the experimentally obtained data. Synthetic jet localisation produces marked differences in the flow field depending on the position of actuation. Interference drag was sensitive to the asymmetry of

the synthetic jet with the higher angles decreasing the entrainment into the sphere-support juncture.

The synthetic jet angle of incidence was optimised experimentally using a NACA0012 airfoil with a cut-off wing. The optimal synthetic jet angle of  $23^\circ$  was used on a forward swept wing based on a NACA23012 profile. The localised synthetic jet was able to reduce the drag and wing tip vorticity.

Asymmetrical localised synthetic jet can be used strategically on three-dimensional bluff and streamlined bodies to inhibit flow separation, decrease reversal of flow in the wake region and reduce interference and induced drag.

---

# List of Publications

The following is a list of publications produced throughout the duration of the thesis research.

## Journal Publications

Findanis, N., & Ahmed, N. A. (2008, October). The interaction of an asymmetrical localised synthetic jet on a side supported sphere. *Journal of Fluids and Structures*, 24(7), 1006-1020.

Findanis, N., & Ahmed, N. A. (2011, January). Three-dimensional flow reversal and wake characterisation of a sphere modified with active flow control using synthetic jet. *Advances and Applications in Fluid Mechanics*, 9(1), 17-76.

## Conference Publications

Findanis, N., & Ahmed, N. A. (2006). Wake study of flow over a sphere with synthetic jet. *AIAA 24th Applied Aerodynamics Conference*, (pp. AIAA 2006-3855). San Francisco.

Findanis, N., & Ahmed, N. A. (2007). A flow study over a sphere with localised synthetic jet. *The 12th Australian International Aerospace Congress*. (pp. 803 - 841). March, Melbourne.

Findanis, N., & Ahmed, N. A. (2009). Active Flow Control Over a Bluff Body Utilising Localised Synthetic Jet Technology. *The 13th Australian International Aerospace Congress*. March, Melbourne

---

# Acknowledgements

Embarking on such a tough challenge as this has been truly rewarding. It is a unique experience that I have enjoyed albeit with much pain along the way. As with all things in my life that have required strenuous effort and commitment I am grateful to the people around me who kept me motivated and encouraged me to continue when things look bleak and hopeless.

My PhD supervisor Dr Noor Ahmed has been the key person who has continuously encouraged me and directed me to the completion of this work. I truly appreciate his many efforts and hard work despite his immensely busy life. His persistent attitude and kindly manner have helped me along this sometimes difficult path.

The UNSW Aerodynamics Laboratory professional officer Mr Terry Flynn has often helped solve experimental problems with cost effective solutions to obtain accurate real world data. His experience and help is much appreciated.

I would like to thank my colleagues who have provided an intelligent sounding board with which to clarify and expound a physical understanding of fluid dynamics. The constant interspersed humour, that brighten-up dull days trudging through experiments and analysis.

Finally, I would like to thank my wonderful family that provides the backbone of support for me when no one else understands the hardships in my life and shares with me the joyous occasion of completing my studies.

# Table of Contents

ABSTRACT .....	I
LIST OF PUBLICATIONS.....	III
ACKNOWLEDGEMENTS .....	IV
LIST OF FIGURES .....	IX
LIST OF TABLES .....	XVIII
NOMENCLATURE .....	XX
CHAPTER 1.....	1
1. INTRODUCTION .....	2
1.1 <i>General Overview</i> .....	2
1.2 <i>Aerodynamic Performance</i> .....	3
1.3 <i>Aerodynamic Flow Control and Synthetic Jet</i> .....	5
1.4 <i>Thesis Aims</i> .....	6
1.5 <i>Thesis outline</i> .....	7
CHAPTER 2.....	10
2. LITERATURE REVIEW .....	11
2.1 <i>Flow separation</i> .....	12
2.2 <i>Flow control</i> .....	16
2.3 <i>Synthetic jets</i> .....	19
2.4 <i>Synthetic jet on bluff bodies</i> .....	25
2.5 <i>Synthetic jets on streamlined bodies</i> .....	29
2.6 <i>Interference drag</i> .....	36
2.7 <i>Computational fluid dynamics and the modelling of synthetic jets</i> .....	37
2.8 <i>Synthetic jet applications</i> .....	38

---

<b>CHAPTER 3.....</b>	<b>40</b>
3. RESEARCH METHODOLOGIES AND APPARATUS .....	41
3.1 457 mm (18") x 457 mm (18") Wind Tunnel.....	41
3.2 Experimental design of bluff body and synthetic jet .....	43
3.3 Wake surveys .....	46
3.4 Wind Tunnel testing of streamlined bodies with synthetic jet .....	52
3.5 Computational methodologies for numerical simulation of the side supported sphere .....	58
3.6 Computational methodologies for numerical simulation of the forward swept wing.....	66
3.7 Experimental Accuracy and Repeatability.....	73
<b>CHAPTER 4.....</b>	<b>75</b>
4. RESULTS AND DISCUSSION: BLUFF BODY .....	76
4.1 The theoretical coefficient of pressure on the surface of a sphere.....	77
4.2 The two- and three-dimensional effect of the localised synthetic jet .....	78
4.3 Flow visualisation study of the effect of the localised synthetic jet .....	85
4.4 Effect of sting support .....	89
4.5 Further remarks on flow separation.....	91
4.6 A comparison of the coefficient of drag on the sphere .....	93
4.7 Concluding remarks.....	95
<b>CHAPTER 5.....</b>	<b>97</b>
5. RESULTS AND DISCUSSION: BLUFF BODY WAKE ANALYSIS .....	98
5.1 Reversal of flow.....	101
5.2 Wake Characterisation: Flow visualisation.....	116
5.3 Force Balance Measurements.....	176
5.4 Summary and concluding remarks .....	177
<b>CHAPTER 6.....</b>	<b>183</b>
6. RESULTS AND DISCUSSION: CFD ON A BLUFF BODY.....	184

---

6.1	<i>Side-supported sphere with asymmetrical localised synthetic jet: Surface pressure distribution</i> .....	185
6.2	<i>Wake Analysis</i> .....	190
6.3	<i>Support-sphere junction</i> .....	195
6.4	<i>Drag Force: Side-supported sphere</i> .....	199
6.5	<i>Conclusion</i> .....	199
<b>CHAPTER 7</b>	.....	<b>202</b>
7.	<b>RESULTS AND DISCUSSION: STREAMLINED BODIES</b> .....	<b>203</b>
7.1	<i>Optimal angle of a localised synthetic jet on a NACA-0012 wing</i> .....	204
7.2	<i>Surface pressure measurements on a forward swept wing</i> .....	210
7.3	<i>CFD simulation of FSW with asymmetrical localised synthetic jet</i> .....	214
7.4	<i>Concluding remarks</i> .....	217
<b>CHAPTER 8</b>	.....	<b>219</b>
8.	<b>CONCLUSIONS AND RECOMMENDATIONS</b> .....	<b>220</b>
8.1	<i>Conclusions</i> .....	220
8.2	<i>Recommendations</i> .....	224
<b>REFERENCES</b>	.....	<b>226</b>
<b>APPENDIX A</b>	.....	<b>236</b>
APPENDIX A - MODEL DETAILS	.....	237
A.1	<i>Side-supported sphere drawings and photos</i> .....	237
A.2	<i>Forward swept wing drawings and photos</i> .....	239
A.3	<i>Synthetic jet generator</i> .....	241
<b>APPENDIX B</b>	.....	<b>243</b>
APPENDIX B – WIND TUNNEL BLOCKAGE	.....	244
B.1	<i>Wind tunnel blockage</i> .....	244
<b>APPENDIX C</b>	.....	<b>246</b>
APPENDIX C – FIVE-HOLE PROBE CALIBRATION	.....	247

---

<i>C.1 Five-hole probe calibration</i> .....	247
<b>APPENDIX D</b> .....	<b>254</b>
APPENDIX D – SURFACE PRESSURE DATA.....	255
<i>D.1 FSW Surface Pressure</i> .....	255

# List of Figures

## Chapter 2

Figure 2.1. Boundary layer on flat plate (y scale greatly enlarged) (Massey 1996). . .	13
Figure 2.2. Boundary layer flow over a curved surface (Massey 1996).....	14
Figure 2.3. Wakes (a) streamlined body, (b) common bluff bodies and (c) extreme bluff body (Massey 1996). ....	16
Figure 2.4. Flow control methods (Choi, Jeon and Kim 2008). ....	18
Figure 2.5. A pulse of fluid is ejected into a quiescent medium (Gorder 2004). .....	21
Figure 2.6. Schlieren images of jets at $Re = 2200$ . (a) continuous jet (b) synthetic jet (Smith and Swift 2003). .....	22
Figure 2.7. Schematic diagram of synthetic jet actuator (Smith & Glezer, 1998). ....	23
Figure 2.8. Smoke visualisation of a cylinder. (a) baseline and synthetic jet at (b) $60^\circ$ , (c) $180^\circ$ and (d) $180^\circ$ and $120^\circ$ out of phase (Glezer and Amitay 2002) .....	28
Figure 2.9. Flow separation from an airfoil at different AOA (Cengel and Cimbala 2006). ....	30
Figure 2.10. Spanwise flow of wing (Anderson 2001). ....	31
Figure 2.11. Wing-tip vortices produced from a rectangular wing in a cross flow. Produce in smoke tunnel (Anderson 2001). ....	32
Figure 2.12. Pressure coefficient distributions (Amitay and Glezer 2006). .....	34
Figure 2.13. Phase-averaged images at different times during the reattachment process (Amitay and Glezer 2006). ....	36

## Chapter 3

Figure 3.1. Wind tunnel: 457 mm x 457 mm, open circuit, closed test section. ....	42
Figure 3.2 Schematic diagrams of sphere: Plan view (left), Elevation view (right). ..	43
Figure 3.3. Scanivalve controller and scanivalve unit below. ....	44
Figure 3.4 Hot-wire measurement of experimental synthetic jet velocity profile. ....	45
Figure 3.5. Cobra head five-hole probe .....	47

---

Figure 3.6. Wake traverse apparatus and instrumentation. ....	48
Figure 3.7. Five-hole probe data acquisition system .....	49
Figure 3.8. five-hole probe wake survey of NACA23012 airfoil .....	51
Figure 3.9. Large Wind tunnel: 1219 mm x 914 mm.....	53
Figure 3.10. Forward swept wing (FSW) synthetic jet velocity profile. ....	54
Figure 3.11. Schematic setup of NACA-0012 wing.....	55
Figure 3.12. Forward swept wing. Measuring stations are indicated by the chord at each spanwise location. Also shown and labeled are synthetic jet orifices.....	57
Figure 3.13. Forward swept wing with NACA-23012 profile. ....	57
Figure 3.14. Fluid domain of side-supported sphere.....	59
Figure 3.15. CFD synthetic jet velocity.....	62
Figure 3.16. Side-supported sphere mesh. a) mesh 1, b) mesh 2 and c) mesh 3.....	64
Figure 3.17. Fluid domain for FSW, at 15° AOA. ....	67
Figure 3.18. CFD synthetic jet velocity.....	69
Figure 3.19. FSW mesh. a) mesh 1, b) mesh 2 and c) mesh 3.....	71

## **Chapter 4**

Figure 4.1. Analysis of surface pressure on the sphere. ....	78
Figure 4.2. Pressure-Coefficient for port 3 with respect to $\phi$ . ....	79
Figure 4.3. Pressure-Coefficient for port 3 with respect to $\theta$ . ....	80
Figure 4.4. Pressure-Coefficient for port 4 with respect to $\phi$ . ....	80
Figure 4.5. Pressure-Coefficient for port 4 with respect to $\theta$ . ....	81
Figure 4.6. Pressure-Coefficient for port 5 with respect to $\phi$ . ....	81
Figure 4.7. Pressure-Coefficient for port 5 with respect to $\theta$ . ....	82
Figure 4.8. Surface pressure contour plot of Potential flow, No synthetic jet and with synthetic jet.....	85
Figure 4.9. Sphere rotated 90° with no synthetic jet.....	87
Figure 4.10. Sphere rotated 90° with synthetic jet.....	87
Figure 4.11. Sphere rotated 110° with no synthetic jet.....	88

---

Figure 4.12. Sphere rotated $110^\circ$ with synthetic jet.....	88
Figure 4.13. Sphere plan view without rod attached. ....	89
Figure 4.14. Sphere plan view with rod attached.....	90
Figure 4.15. Top view. Diagrammatic representation of separation with and without synthetic jet.....	92

## Chapter 5

Figure 5.1. NACA 23012 wake survey. ....	115
Figure 5.2. 10 m/s without synthetic jet. Tuft screen 40 mm offset. ....	117
Figure 5.3. 10 m/s without synthetic jet. A side view of Figure 5.2 ....	117
Figure 5.4. 10 m/s with synthetic jet. Tuft screen 40 mm offset.....	118
Figure 5.5. 10 m/s with synthetic jet. Tuft screen 40 mm offset. A side view of ....	118
Figure 5.6. 20 m/s without synthetic jet. Tuft screen at 40 mm offset.....	119
Figure 5.7. 20 m/s with synthetic jet. Tuft screen at 40 mm offset. ....	119
Figure 5.8. Three-Dimensional Vector Field Plot of Sphere Wake Without Synthetic Jet – Standard Sphere .....	128
Figure 5.9. Three-Dimensional Vector Field Plot of Sphere Wake with Synthetic Jet at 6.5 Degrees .....	129
Figure 5.10. Three-Dimensional Vector Field Plot of Sphere Wake with Synthetic Jet at 76 Degrees .....	130
Figure 5.11. Three-Dimensional Vector Field Plot of Sphere Wake with Synthetic Jet at 100 Degrees .....	131
Figure 5.12. Sphere Wake Survey, Dynamic Pressure – No Synthetic Jet .....	134
Figure 5.13. Sphere Wake Survey, Dynamic Pressure – Synthetic Jet at $6.5^\circ$ .....	135
Figure 5.14. Sphere Wake Survey, Dynamic Pressure – Synthetic Jet at $76^\circ$ .....	136
Figure 5.15. Sphere Wake Survey, Dynamic Pressure – Synthetic Jet at $100^\circ$ .....	137
Figure 5.16. Sphere Wake Survey, Total Pressure - No Synthetic Jet.....	140
Figure 5.17. Sphere Wake survey, Total Pressure - Synthetic Jet at $6.5^\circ$ .....	141
Figure 5.18. Sphere Wake survey, Total Pressure - Synthetic Jet at $76^\circ$ .....	142
Figure 5.19. Sphere Wake survey, Total Pressure - Synthetic Jet at $100^\circ$ .....	143

---

Figure 5.20. Total Vorticity at different points along the x-axis. No synthetic jet...	147
Figure 5.21. Total Vorticity at different points along the x-axis. Synthetic jet @ $6.5^\circ$ . .....	148
Figure 5.22. Total Vorticity at different points along the x-axis. Synthetic jet @ $76^\circ$ . .....	149
Figure 5.23. Total Vorticity at different points along the x-axis. Synthetic jet @ $100^\circ$ . .....	150
Figure 5.24. Wake boundary – No synthetic jet .....	153
Figure 5.25. Wake boundary – Synthetic jet angle, $6.5^\circ$ .....	153
Figure 5.26. Wake boundary – Synthetic jet angle, $76^\circ$ .....	154
Figure 5.27. Wake boundary – Synthetic jet angle, $100^\circ$ .....	154
Figure 5.28. Wake displacement thickness – No synthetic jet .....	158
Figure 5.29. Wake displacement thickness – Synthetic jet angle $6.5^\circ$ .....	159
Figure 5.30. Wake displacement thickness – Synthetic jet angle $76^\circ$ .....	160
Figure 5.31. Wake displacement thickness – Synthetic jet angle $100^\circ$ .....	161
Figure 5.32. Wake momentum thickness – No synthetic jet .....	162
Figure 5.33. Wake momentum thickness – Synthetic jet angle $6.5^\circ$ .....	163
Figure 5.34. Wake momentum thickness – Synthetic jet angle $76^\circ$ .....	164
Figure 5.35. Wake momentum thickness – Synthetic jet angle $100^\circ$ .....	165
Figure 5.36. Wake – No synthetic jet (a) Displacement thickness, (b) Momentum thickness, (c) Shape factor .....	170
Figure 5.37. Wake – Synthetic jet angle $6.5^\circ$ (a) Displacement thickness, (b) Momentum thickness, (c) Shape factor .....	171
Figure 5.38. Wake – Synthetic jet angle $76^\circ$ (a) Displacement thickness, (b) Momentum thickness, (c) Shape factor .....	172
Figure 5.39. Wake – Synthetic jet angle $100^\circ$ (a) Displacement thickness, (b) Momentum thickness, (c) Shape factor .....	173

## Chapter 6

Figure 6.1. Comparison of experimental $C_p$ distribution to CFD baseline case: turbulence models. ....	186
Figure 6.2. Comparison of $C_p$ with synthetic jet at peak outflow at different angles of incidence .....	187
Figure 6.3. Synthetic jet streamlines, peak outflow. Clockwise from left synthetic jet at $6.5^\circ$ , $76^\circ$ and $100^\circ$ . ....	189
Figure 6.4. Comparison of streamwise velocity $U$ . ....	191
Figure 6.5. Comparison of crosswise velocity $V$ . ....	192
Figure 6.6. Comparison of crosswise velocity $W$ . ....	193
Figure 6.7. Velocity contour plot, synthetic jet peak outflow. Clockwise from top left baseline, $6.5^\circ$ , $76^\circ$ and $100^\circ$ . ....	194
Figure 6.8. Velocity contour plot, $V$ component, synthetic jet peak outflow. Clockwise from top left baseline, $6.5^\circ$ , $76^\circ$ and $100^\circ$ . ....	195
Figure 6.9. Contour plot baseline case, velocity component, XZ plane.....	196
Figure 6.10. Comparison of vorticity X-axis, synthetic jet peak outflow. Along streamwise centreline at support-sphere junction .....	197
Figure 6.11. Comparison of vorticity Z-axis, synthetic jet peak outflow. Along streamwise centreline at support-sphere junction .....	198

## Chapter 7

Figure 7.1. $C_p$ distribution on the NACA-0012 wing at $0^\circ$ AOA. ....	205
Figure 7.2. $C_p$ distribution on the NACA-0012 wing at $16^\circ$ AOA. ....	206
Figure 7.3. $C_p$ distribution on the NACA-0012 wing at $0^\circ$ AOA and SJ at $90^\circ$ . Upper surface with localised synthetic jet. (NJ - no synthetic jet, SJ15% - synthetic jet at 15% chord, SJ50% - synthetic jet at 50% chord) .....	207
Figure 7.4. $C_p$ distribution on the NACA-0012 wing at $20^\circ$ AOA and SJ at $45^\circ$ . Upper surface with localised synthetic jet. (NJ - no synthetic jet, SJ15% - synthetic jet at 15% chord, SJ50% - synthetic jet at 50% chord) .....	208

Figure 7.5. $C_p$ distribution on the NACA-0012 wing at $16^\circ$ AOA and SJ at $23^\circ$ . Upper surface with localised synthetic jet. (NJ - no synthetic jet, SJ15% - synthetic jet at 15% chord, SJ50% - synthetic jet at 50% chord) .....	209
Figure 7.6. $C_p$ distribution on the Upper surface of FSW at station 1, $15^\circ$ AOA and SJ at $23^\circ$ . Upper surface with localised synthetic jet. (NJ - no synthetic jet, Upper surface - synthetic jet at 19% chord of wing tip) .....	211
Figure 7.7. $C_p$ distribution on the Lower surface of FSW at station 1, $15^\circ$ AOA and SJ at $23^\circ$ . Upper surface with localised synthetic jet. (NJ - no synthetic jet, Upper surface - synthetic jet at 19% chord of wing tip) .....	211
Figure 7.8. $C_p$ distribution on the Upper surface of FSW at station 1, $15^\circ$ AOA and SJ at $23^\circ$ . Upper surface with localised synthetic jet. (NJ - no synthetic jet, Upper surface - synthetic jet at 32% chord of station 1) .....	212
Figure 7.9. $C_p$ distribution on the Lower surface of FSW at station 1, $15^\circ$ AOA and SJ at $23^\circ$ . Upper surface with localised synthetic jet. (NJ - no synthetic jet, Upper surface - synthetic jet at 32% chord of station 1) .....	212
Figure 7.10. $C_p$ distribution on the Upper surface of FSW at station 4, $15^\circ$ AOA and SJ at $23^\circ$ . Upper surface with localised synthetic jet. (NJ - no synthetic jet, Upper surface - synthetic jet at 37% chord of station 4) .....	213
Figure 7.11. $C_p$ distribution on the Lower surface of FSW at station 4, $15^\circ$ AOA and SJ at $23^\circ$ . Upper surface with localised synthetic jet. (NJ - no synthetic jet, Upper surface - synthetic jet at 37% chord of station 4) .....	213
Figure 7.12. Velocity contour comparison $15^\circ$ AOA. Clockwise from top left, NJ, WTP-F, SJ1-F, SJ4-F.....	215
Figure 7.13. Total vorticity contour comparison $15^\circ$ AOA. Clockwise from top left, NJ, WTP-F, SJ1-F, SJ4-F.....	215
Figure 7.14. Total vorticity contour comparison $15^\circ$ AOA on a plane perpendicular to streamwise direction, 150mm aft of the origin . Clockwise from top left, NJ, WTP-F, SJ1-F, SJ4-F. ....	216
Figure 7.15. Total vorticity comparison $15^\circ$ AOA at measurement station 1 cross-section through FSW wing. Clockwise from top left, NJ, WTP-F, SJ1-F, SJ4-F. ....	217

## **Appendix A**

Figure A.1. Side-supported sphere engineering drawing 1. ....	237
Figure A.2. Side-supported sphere engineering drawing 2. ....	238
Figure A.3. Side-supported sphere mounted in the 457 mm x 457 mm wind tunnel. .....	239
Figure A.4. FSW in 1219 mm x 914 mm wind tunnel.....	239
Figure A.5. FSW overall dimensions.....	240
Figure A.6. 12VDC Compressor .....	241
Figure A.7. Compressor one-way valve.....	242

## **Appendix C**

Figure C.1. Five-hole calibration, pitch plane. ....	248
Figure C.2. Five-hole calibration, yaw plane. ....	249
Figure C.3. Five-Hole probe calibration map. ....	252

## **Appendix D**

Figure D.1. FSW, $C_p$ distribution at AOA $15^\circ$ , Measuring station 1.....	259
Figure D.2. FSW, $C_p$ distribution at AOA $15^\circ$ , Measuring station 2.....	259
Figure D.3. FSW, $C_p$ distribution at AOA $15^\circ$ , Measuring station 3.....	260
Figure D.4. FSW, $C_p$ distribution at AOA $15^\circ$ , Measuring station 4.....	260
Figure D.5. FSW, $C_p$ distribution at AOA $15^\circ$ , Measuring station 5.....	261
Figure D.6. Comparison of FSW NJ and with WTP-F at $90^\circ$ , $C_p$ distribution at AOA $15^\circ$ , Measuring station 1. Upper surface. ....	261
Figure D.7. Comparison of FSW NJ and with WTP-F at $90^\circ$ , $C_p$ distribution at AOA $15^\circ$ , Measuring station 1. Lower surface. ....	262
Figure D.8. Comparison of FSW NJ and with WTP-A at $90^\circ$ , $C_p$ distribution at AOA $15^\circ$ , Measuring station 1. Upper surface. ....	262
Figure D.9. Comparison of FSW NJ and with WTP-A at $90^\circ$ , $C_p$ distribution at AOA $15^\circ$ , Measuring station 1. Lower surface. ....	263

---

Figure D.10. Comparison of FSW NJ and with SJ1-F at $90^\circ$ , $C_p$ distribution at AOA $15^\circ$ , Measuring station 1. Upper surface. ....	263
Figure D.11. Comparison of FSW NJ and with SJ1-F at $90^\circ$ , $C_p$ distribution at AOA $15^\circ$ , Measuring station 1. Lower surface.....	264
Figure D.12. Comparison of FSW NJ and with SJ1-A at $90^\circ$ , $C_p$ distribution at AOA $15^\circ$ , Measuring station 1. Upper surface. ....	264
Figure D.13. Comparison of FSW NJ and with SJ1-A at $90^\circ$ , $C_p$ distribution at AOA $15^\circ$ , Measuring station 1. Lower surface. ....	265
Figure D.14. Comparison of FSW NJ and with SJ4-F at $90^\circ$ , $C_p$ distribution at AOA $15^\circ$ , Measuring station 4. Upper surface. ....	265
Figure D.15. Comparison of FSW NJ and with SJ4-F at $90^\circ$ , $C_p$ distribution at AOA $15^\circ$ , Measuring station 4. Lower surface.....	266
Figure D.16. Comparison of FSW NJ and with SJ4-A at $90^\circ$ , $C_p$ distribution at AOA $15^\circ$ , Measuring station 4. Upper surface. ....	266
Figure D.17. Comparison of FSW NJ and with SJ4-A at $90^\circ$ , $C_p$ distribution at AOA $15^\circ$ , Measuring station 4. Lower surface. ....	267
Figure D.18. Comparison of FSW NJ and with WTP-F at $23^\circ$ , $C_p$ distribution at AOA $15^\circ$ , Measuring station 1. Upper surface. ....	267
Figure D.19. Comparison of FSW NJ and with WTP-F at $23^\circ$ , $C_p$ distribution at AOA $15^\circ$ , Measuring station 1. Lower surface. ....	268
Figure D.20. Comparison of FSW NJ and with WTP-A at $23^\circ$ , $C_p$ distribution at AOA $15^\circ$ , Measuring station 1. Upper surface. ....	268
Figure D.21. Comparison of FSW NJ and with WTP-A at $23^\circ$ , $C_p$ distribution at AOA $15^\circ$ , Measuring station 1. Lower surface. ....	269
Figure D.22. Comparison of FSW NJ and with SJ1-F at $23^\circ$ , $C_p$ distribution at AOA $15^\circ$ , Measuring station 1. Upper surface. ....	269
Figure D.23. Comparison of FSW NJ and with SJ1-F at $23^\circ$ , $C_p$ distribution at AOA $15^\circ$ , Measuring station 1. Lower surface.....	270
Figure D.24. Comparison of FSW NJ and with SJ1-A at $23^\circ$ , $C_p$ distribution at AOA $15^\circ$ , Measuring station 1. Upper surface. ....	270

---

Figure D.25. Comparison of FSW NJ and with SJ1-A at $23^\circ$ , $C_p$ distribution at AOA $15^\circ$ , Measuring station 1. Lower surface. ....	271
Figure D.26. Comparison of FSW NJ and with SJ4-F at $23^\circ$ , $C_p$ distribution at AOA $15^\circ$ , Measuring station 4. Upper surface. ....	271
Figure D.27. Comparison of FSW NJ and with SJ4-F at $23^\circ$ , $C_p$ distribution at AOA $15^\circ$ , Measuring station 4. Lower surface.....	272
Figure D.28. Comparison of FSW NJ and with SJ4-A at $23^\circ$ , $C_p$ distribution at AOA $15^\circ$ , Measuring station 4. Upper surface. ....	272
Figure D.29. Comparison of FSW NJ and with SJ4-A at $23^\circ$ , $C_p$ distribution at AOA $15^\circ$ , Measuring station 4. Lower surface. ....	273

# List of Tables

## Chapter 3

Table 3.1. Chord lengths of each measuring station .....	56
Table 3.2. Synthetic locations. ....	58
Table 3.3. Grid independence using $C_D$ . ....	65
Table 3.4. Grid independence using drag force. ....	72

## Chapter 4

Table 4.1. Potential flow deviation. ....	82
Table 4.2. Angles of flow separation. ....	92
Table 4.3. Sectional drag coefficients. ....	94

## Chapter 5

Table 5.1. Reversal of flow, Criterion 1. Streamwise location of $x = 5$ mm. ....	104
Table 5.2. Reversal of flow, Criterion 1. Streamwise location of $x = 80$ mm. ....	105
Table 5.3. Reversal of flow, Criterion 2. Streamwise location of $x = 5$ mm. ....	107
Table 5.4. Reversal of flow, Criterion 2. Streamwise location of $x = 80$ mm. ....	108
Table 5.5. Reversal of flow, Criterion 3. Streamwise location of $x = 5$ mm. ....	110
Table 5.6. Reversal of flow, Criterion 3. Streamwise location of $x = 80$ mm. ....	111
Table 5.7. Reversal of flow, Criterion 4. Streamwise location of $x = 5$ mm. ....	112
Table 5.8. Reversal of flow, Criterion 4. Streamwise location of $x = 80$ mm. ....	113
Table 5.9. Comparison of five-hole probe and hot-wire measurement data. ....	124
Table 5.10. Comparison of displacement thickness. ....	169

## Chapter 7

Table 7.1. FSW drag at $15^\circ$ AOA. ....	214
---	-----

**Appendix B**

Table B.1.....	245
----------------	-----

**Appendix D**

Table D.1. Measurement station 1. (a) 9 tappings, upper surface. (b) 8 tappings, lower surface.....	256
Table D.2. Measurement station 2. (a) 10 tappings, upper surface. (b) 10 tappings, lower surface.....	256
Table D.3. Measurement station 3. (a) 10 tappings, upper surface. (b) 10 tappings, lower surface.....	257
Table D.4. Measurement station 4. (a) 10 tappings, upper surface. (b) 10 tappings, lower surface.....	257
Table D.5. Measurement station 5. (a) 10 tappings, upper surface. (b) 10 tappings, lower surface.....	258

# Nomenclature

All measurements and calculations were performed using SI system of units.

$C_d$  - coefficient of sectional drag

$C_p$  - surface static pressure coefficient =  $(p - p_\infty) / (\frac{1}{2} \rho_\infty U_\infty^2)$

$C_{pn}$  - surface static pressure coefficient of port  $n$  =  $(p_n - p_\infty) / (\frac{1}{2} \rho_\infty U_\infty^2)$

$D$  - diameter of the sphere

$e$  - diameter of synthetic jet outlet

$f$  - frequency

FSW - forward swept wing

H - shape factor

$n$  = index (1, 2, 3, 4, 5, 6, 7)

NJ - no synthetic jet applied

NPL - National Physical Laboratory

$O_{pn}$  - centre of circle circumscribed by port  $n$

$O_s$  - centre of sphere

$p$  - static pressure at a point on the sphere

$\bar{p}$  - mean pressure

$p_\infty$  - freestream static pressure

$P_n$  - point on a circle circumscribed by port  $n$

$q_\infty$  - freestream dynamic pressure =  $\frac{1}{2} \rho_\infty U_\infty^2$

$r_n$  - radius of a slice centred at  $O_{Pn}$  of the sphere circumscribed by port  $n$

$R$  - radius of the sphere

Re - Reynolds number =  $\rho_\infty U_\infty D / \mu_\infty$

RF - reversal of flow

RANS - Reynolds-averaged Navier-Stokes equations

RMS - root mean square

St - Strouhal number =  $fD/U_\infty$

SJ - synthetic jet applied

SST - Shear Stress Transport

$u$  - local streamwise Cartesian velocity component

$\bar{u}$  - the RANS mean velocity vector

$U$  - global streamwise Cartesian velocity component

$U_{sj}$  - synthetic jet velocity

$U_{\text{sphere}}$  - velocity over the sphere

$U_\infty$  - freestream velocity

$v$  - local vertical crosswise Cartesian velocity component

$\vec{V}$  - vector  $V$

$V$  - global vertical crosswise Cartesian velocity component

$w$  - local horizontal crosswise Cartesian velocity component

$W$  - global horizontal crosswise Cartesian velocity component

$x$  - streamwise coordinate

$y$  - vertical crosswise coordinate

$z$  - horizontal crosswise coordinate

## Greek Symbols

$\alpha$  - pitch angle ( $^{\circ}$ )/angle of attack

$\beta$  - yaw angle ( $^{\circ}$ )

$\gamma$  - port location ( $^{\circ}$ )

$\delta$  - boundary-layer thickness

$\delta^*$  - displacement thickness

$\theta$  - angle in general spherical coordinates ( $^{\circ}$ )

$\theta$  - momentum thickness

$\mu$  - absolute viscosity/momentum thickness

$\mu_t$  - turbulent eddy viscosity

$\vec{\xi}$  - total vorticity

$\xi_x$  - component of vorticity about the x-axis

$\xi_y$  - component of vorticity about the y-axis

$\xi_z$  - component of vorticity about the z-axis

$\rho_{\infty}$  - freestream density

$\phi$  - angle of rotation ( $^{\circ}$ )

$\omega$  - rotational speed

---

# Chapter 1

## Introduction

---

---

## 1. Introduction

An introduction is given in this chapter of the research undertaken culminating in this dissertation.

### 1.1 General Overview

Fluid dynamics research continues to develop and improve our physical understanding of fluid flows in many diverse scientific and engineering applications (Plesniak 2010). Engineering the flow of fluids to extract as much of the available energy invested in the dynamic motion causing the fluid to flow is increasingly becoming a major concern due to environmental constraints (Camhi 2009). Even so, regardless of the external economic and environmental concerns engineers by nature strive to better the efficiency and performance of their creations.

Flow control devices have been developed and used by engineers and scientists to modify flow fields and the fluid-structure interaction to improve the performance and efficiency of the object to which they are attached (Gad-el-Hak 2000). Flow control can also be used to inhibit the occurrence of unwanted flow phenomena such as vortex shedding (Choi, Jeon and Kim 2008) such as in long cylindrical exhaust stacks used in power generation. Flow control and the ability to modify the air flow over a solid surface can improve aerodynamic performance and extended the useful operating parameters of the design. Enhancing the aerodynamic performance is particularly desirable in the design of aircraft. For example, control surfaces are used on aircraft to generate movement in different directions. This is achieved by moving the control surface which changes the overall geometry and flow over the section where the control surface is located. The resulting change in aerodynamic forces causes the aircraft to shift in attitude or orientation. Aircraft wings can also be fitted with high-lift devices such as flaps, slats and slots to name a

few. Other flow control devices fitted to aircraft include boundary layer control (BLC) devices that energise the boundary layer to prevent separation at higher angles of attack.

Developing and applying flow control devices to increase the overall efficiency of aircraft would translate to tangible savings in fuel consumption. In 2007 the world jet fuel consumption was approximately 304.7 billion litres/year (U.S. Energy Information Administration 2007). A device that could increase the overall efficiency of aircraft by 0.5% would save approximately 1523.6 million litres/year of aviation fuel. The average cost of fuel in 2010 in the U.S. was 59.28 ¢/L (U.S. Energy Information Administration 2010). A cost saving of over \$900 million U.S. for a 0.5% increase in efficiency. Small contributions to aerodynamic efficiency add up to substantial dollar savings due to the prolific use of air transportation. Moreover there are benefits of reducing aircraft exhaust pollutants such as CO<sub>2</sub> and NO<sub>x</sub> thus lowering the contribution to greenhouse gases.

## 1.2 Aerodynamic Performance

An increase in the aerodynamic performance and efficiency essentially comes from reducing the total drag on the body. A major component of drag for bluff bodies and streamlined geometries such as a wing at high angles of attack, is pressure drag. The flow over such solid bodies will initially flow smoothly after it passes the fore stagnation point. Then at a particular point downstream on the body the flow will leave the surface of the body resulting in a large vortical recirculation zone. This well-known fluid dynamic phenomenon which causes an increase in drag and eventually stall is flow separation (Anderson 2001). Flow control devices are used in as an effort to prevent separation or at least delay the onset of separated flow thus reducing the pressure drag.

Flow separation or more specifically boundary-layer separation is the result of an adverse pressure gradient. The adverse pressure gradient is formed due to the decelerated flow on the surface of a body immersed in a cross flow. The fluid particles in the boundary layer undergo an energy transformation from kinetic energy to pressure energy in moving from the front to the back of the solid body unable to overcome the losses due to friction. This results in a build-up of pressure in opposition to the oncoming flow and eventually reaching the point where the velocity gradient becomes zero. This phenomenon is the well-known separation condition (Schlichting and Gersten 2003).

Another adverse consequence of flow separation is the resulting unsteady or large wakes that can be formed. For bluff bodies the size of the wake can be large leading to high pressure drag. A frequent comparison has been made to show the effect that wake has on the drag force of body. A symmetrical airfoil with a chord length 167 times the diameter of a circular cylinder has the same drag force. The coefficient of drag of the airfoil is  $C_D \approx 0.006$  whereas of the circular cylinder its drag coefficient is  $C_D \approx 1$  (Schlichting and Gersten 2003).

When two solid bodies join to form a single composite geometry, the total drag is not simply the mathematical sum of each component member. There is an additional form of drag that is created defined as interference drag (Anderson 2000). For example, interference drag can occur on an aircraft at the junction of a wing and the fuselage. Around the region of the wing-fuselage joint the flow from each of the two bodies, the wing and the fuselage, will converge. There are two distinct flow fields before convergence, firstly the cylindrical fuselage produces a flow field which is similar to a bluff body flow and each of the wings produce a streamlined flow field. The resulting flow field is a combination of the bluff body flow and streamlined flow as well as the effects of the geometry of the wing-fuselage junction. In some cases it has been shown that the interference is favourable producing a reduction in the total drag compared to the sum of the drag

of the bodies in isolation (Tetrault 2000). As the flow converges one mixes with the other to form a disturbed flow region around the join with strong vortical structures. Understanding interference drag is tantamount to understanding the vortex dynamics around these types of regions on solid composite bodies (Kwak, et al. 1986).

Aerodynamic performance is also affected by lift-induced drag. Lifting bodies such as wings produce a pressure difference between the upper and lower surfaces dependent on the speed of the oncoming flow and the angle of attack. The pressure difference causes the air to spill onto the upper surface from the higher-pressure lower surface generating wing-tip vortices (Kroo 2001). The wing-tip vortices or induced drag can contribute up to 35% of the total drag on a typical aircraft (Thomas 1985).

### **1.3 Aerodynamic Flow Control and Synthetic Jet**

A flow control device that is becoming increasingly widespread in fluid mechanical applications and in particular aerodynamics is the synthetic jet (Mittal and Rampungoon 2002). The synthetic jet differs from the common continuous fluid jet. In both types of jet, there is a fluid that issues from an orifice of some geometrical configuration. With a continuous fluid jet there is always a positive net mass flow i.e. mass is continuously being introduced through an orifice/nozzle. By definition a synthetic jet differs due to the fact that it has a zero net mass flow. The synthetic jet flow is a “synthesised” oscillatory flow from the fluid surrounding an orifice. As such fluid is alternatively drawn in and then forced back out from the same orifice resulting in a zero net mass flow rate. The synthetic jet actuator was initially developed for jet vectoring of free shear flows (Smith and Glezer 1997) and also to modify the aerodynamic characteristics of bluff bodies (Amitay, Honohan, et al. 1997). The synthetic jet is a form of active flow control that has been shown to effect significant global changes to the baseline flow field (Smith and Glezer 1998).

Although several studies have been conducted on synthetic jet in a cross-flow such as the flow over an airfoil (Amitay, Kibens, et al. 1999), (Amitay, Smith, et al. 2001), (Lee and Goldstein 2000) there is a noticeable lack of studies on true three-dimensional bodies with synthetic jet (Jeon, et al. 2004).

Synthetic jet actuators continue to advance in actuation methods and configuration producing devices with low power requirements whilst delivering the required performance in terms of momentum coefficient and frequency. Synthetic jets have unique features that make them suitable and even preferable for fluid mechanical applications for both external and internal fluid flows (Glezer and Amitay 2002).

## 1.4 Thesis Aims

In general, flow control devices can be targeted towards different areas in the flow field that affect the vortical structures or vortex dynamics (Griffin and Hall 1991). There are two key aspects of a dynamical flow field that flow control perturbs or modifies, it is the boundary layer and/or the wake region.

The aim of this thesis is to contribute to the deficiency of understanding and development of three-dimensional flow dynamics of synthetic jets in a cross flow. Integral to forming a complete investigation of three-dimensional flow over solid objects is to begin the examination by studying bluff type geometries. They are of interest to both industry and research, for the fact bluff body shear flow has three characteristic flow phenomena of interest: the boundary layer, separated shear layer and the wake. Following on from bluff bodies is the aerodynamics of streamlined bodies in which the synthetic jet could ultimately and significantly provide beneficial flow modifications or “aeroshaping” (Mittal and Rampungoon 2002) to various forms of aircraft.

Commonly, in three-dimensional cross flows the synthetic jet has been applied in a distributed configuration (Jeon, et al. 2004). The present work provides insight on the use of a localised synthetic jet giving rise to an asymmetrical influence on the flow dynamics over bluff and streamlined geometries.

A rather natural consequence of studying asymmetrical localised synthetic jet applications has been to discover that a singular synthetic jet could provide flow correction in particular problematic flow regions. As discussed the solid body junctions such as a wing and fuselage provide regions of possible flow disturbance. Likewise the junction of a bluff body such as sphere supported by a cylindrical sting would further provide a region of possible increase in the overall drag. Thus the synthetic jet influence on these regions is also investigated in this thesis research.

Depending on the type of flow control device used this can significantly reduce vorticity (Saffman 1995) in disturbed flow regions by streamlining the flow. A region of high vorticity is the wing-tip on the wings of aircraft. The synthetic jet will be placed in a localised manner to observe the effects on the induced-drag of the wing.

## **1.5 Thesis outline**

Chapter 1 begins with an introduction into the overall theme of the research being conducted and its importance in the field of fluid dynamics. The technological development in flow control and flow separation is discussed and the aims of the current thesis work to further the progress in this area.

A literature review is presented in Chapter 2. First a description of the fundamental physics of flow separation for a body in a three-dimensional flow and the key areas of boundary-layer theory and wakes. The use of flow control in aerodynamics to modify the flow field is examined in particular to inhibit flow separation. Then the use of synthetic jet and its dynamics applied to both bluff and streamlined bodies.

This is followed by a description of problematic flow areas and interference drag for bluff bodies and streamlined bodies as a result of geometrical junctures. Importantly the applications of synthetic jets in engineering applications is briefly detailed in the final section of this chapter.

In Chapter 3 a description is given of the methodologies and equipment used to obtain the required flow information to assess the aerodynamic performance. This includes the laboratory experiments conducted on the bluff and streamlined bodies. Also the computational techniques used to supplement the experimental results which are used to build a more complete analysis of the flow field are included.

In Chapter 4 and Chapter 5, which are closely related, there is a discussion of different aspects of the results obtained from the side-supported sphere. The asymmetrical localised synthetic jet is tested at different angles of incidence and its effect on the boundary layer and wake region is investigated.

Chapter 6 is follow-on work on the side-supported sphere using CFD to obtain the complete flow field. The results are validated with previously obtained experimental data. Further details are brought out from the CFD simulation making use of the different parameters and the capability to make measurements at any desired location within the fluid volume.

Chapter 7 then completes the research work using a localised synthetic jet on streamlined bodies, namely wings. The work is a combination of experimental and computational methodologies. A study is made of flow separation at different locations on a forward swept wing with a focus on wing tip vorticity and interference effects at a geometrical juncture.

A summary of the research work and future directions is covered in Chapter 8.

Finally, a list of references follows Chapter 8. An appendix is also included giving relevant additional details for the reader.

A list of publications produced by the author during the thesis work is located immediately after the Abstract.

---

## Chapter 2

### Literature Review

---

## 2. Literature review

A literature review was undertaken to build a knowledge base of the topical area and on which this thesis is focused. Invariably, one focal area of research bleeds into another and as such the literature review expands to accumulate relevant and possible relevant information from the core and fringes of other fields of study in fluid dynamics. This thesis work is based on one key technological tool, the synthetic jet. The literature review was therefore constructed around synthetic jet technology and how it affects fluid flow. This includes the conceptual development of synthetic jets and physics of the jets themselves in isolation. More important is the use of synthetic jets in a cross flow since the purpose of this thesis is to expand on the deficiency of the synthetic jets in three-dimensional flows. As such synthetic jets in two-dimensional flows are examined. Further, part of the objective of this thesis is to study synthetic jets in an asymmetrical localised manner. The literature review shows that although synthetic jets have been applied in three-dimensional flows, they are distributed symmetrically on the body. Synthetic jets fall into the larger area of flow control which includes other measures or tools to modify aerodynamic flows. The context of placing synthetic jet in the wider topical area of flow control is described so as to enable the reader to become familiar with the objectives and applications of flow control. An appreciation for the use of synthetic jets and flow control can only be realized if the underlying flow dynamics are described which give the impetus for the necessity of modifying the flow field to obtain gains in performance and efficiency. For this reason the physics of flow separation is detailed enough to gain an understanding for the interaction between synthetic jet and the cross flow over bluff and streamlined bodies. The literature survey was conducted over a broad scope of available sources from classical physics and fluid mechanics texts to cutting edge journal publications and other reputable sources. The information was selected, based on articles that are relevant to the

topic being covered and additional material that would support and enable the author to further contribute to the use of synthetic jets and flow separation physics.

## 2.1 Flow separation

Flow separation has been described in Chapter 1 for the reason that it is the basic undesirable phenomenon that we are seeking to inhibit using flow control and a fundamental core of the underlying physics influencing the behaviour of the fluid. For completeness a more detailed and technical description is now given.

### 2.1.1 Boundary-Layer

In the flow of real fluids with viscosity, as opposed to the idealized flow model, there exists a thin layer of fluid adjacent to the surface of a body. This region of flow, defined as the boundary-layer, is retarded with respect to the velocity of the freestream flow. The velocity at the surface is necessarily zero due to the imposed no-slip condition necessitating a zero velocity at the surface wall which is itself a result of wall friction. This implies a velocity gradient from the wall to the freestream flow (Anderson 2001). Now, ordinarily the flow of fluid such as that on a flat plate will build a boundary layer that will progressively thicken as the fluid flows along the length of the flat plate. The boundary layer will initially have a laminar flow regime, but the Reynolds number which is a function of the characteristic length  $x$  measure from the leading edge to a point  $x$  downstream, will grow in thickness.

Then the flow will transition from laminar to fully turbulent whilst the boundary layer thickness continues to increase. The pressure outside the boundary layer will be constant (Massey 1996). The evolution of the flat plate boundary layer is shown in Figure 2.1.

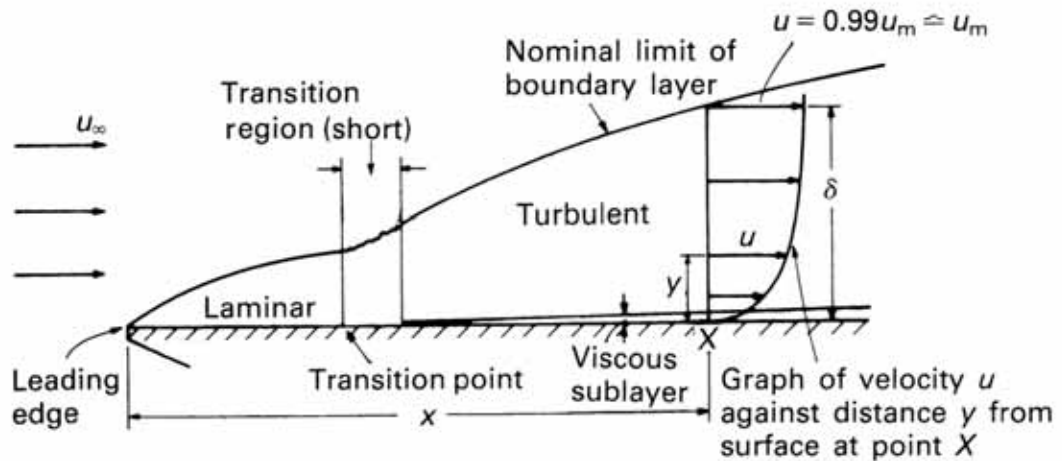


Figure 2.1. Boundary layer on flat plate ( $y$  scale greatly enlarged) (Massey 1996).

In the case of flow over a curved surface, such as a sphere or wing, the boundary layer can be very different. By observing Figure 2.2, it can be seen that as the flow begins to pass over the curve the velocity is constantly changing, accelerating the flow, similar to the physics of circular motion where the speed remains constant but the particle accelerates with a constant change in the velocity. There is a minimum in pressure at the top of the curve at point C. This means there exists a negative pressure gradient from A to C or a favourable pressure gradient pushing towards the surface onto the boundary layer. Thereafter the pressure increases after point C until the pressure gradient in the boundary layer becomes zero at point D. The increase in pressure is called an adverse pressure gradient opposing the forward flow in the boundary layer that eventually causes the boundary layer to separate from the surface before the terminal point on the body (Massey 1996). Figure 2.2 shows flow separation occurring at point E with a reversal of flow moving back and away from the surface.



in the boundary layer and so is able to withstand longer the opposing pressure thus delaying separation relative to the laminar boundary-layer.

Separation can also occur as an isolated separation bubble in which the flow separates in a laminar boundary-layer and turns turbulent reattaching itself downstream (Massey 1996). The separation is also known to form under other conditions in a cross flow (Jeon, et al. 2004).

### 2.1.2 Wakes

The wake refers to the region of flow directly aft of the body in a flow. It is the resulting flow pattern of the interaction of the body and the freestream flow. This region is frequently called the dead zone, since this region of disturbed air is effectively an energy sink that increases drag. The aerodynamic performance of a body can be indicated by the size of the wake region. Bluff bodies, also referred to as blunt bodies, usually have early and distinct separation forming large wakes and high pressure drag or form drag hence the bluntness of a bluff body (Jeon, et al. 2004). The wake is characterized by reversal of flow and increased vorticity or eddies, a highly turbulent region with low pressure resulting in high overall drag on the body. The recovery of the flow to freestream conditions would be relatively far downstream. Conversely a streamlined body such as an airfoil or wing produces a small wake region with a low pressure drag as result of its slender form. The wake region again is turbulent with increased vorticity and reversal of flow although usually less than a bluff body with a shorter length for recovery to freestream conditions. The overall drag on a body is much reduced with skin friction drag or viscous forces being a greater factor than form drag. The wakes resulting from the different geometries are visually displayed in Figure 2.3.

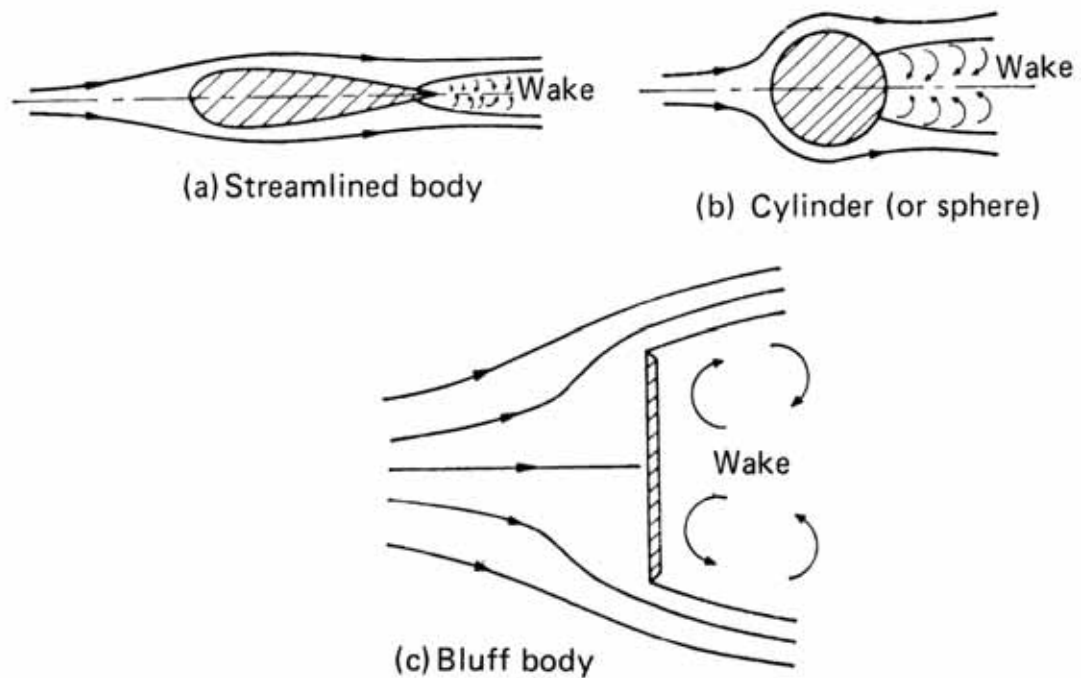


Figure 2.3. Wakes (a) streamlined body, (b) common bluff bodies and (c) extreme bluff body (Massey 1996).

### 2.1.3 Flow separation - concluding remarks

We have examined flow separation as to why this would generally be an undesirable phenomenon in aerodynamic design of machinery. The objective of using flow control in the context of this research is to inhibit this phenomenon and increase aerodynamic performance and/or efficiency although flow control can be used for a number of different purposes (Gad-el-Hak 2000).

## 2.2 Flow control

We begin by describing the relative position of the current research thesis in the greater field of fluid mechanics and more specifically fluid dynamics. At the macro level of this topic we can classify this as applied aerodynamics using flow control technology (Gad-el-Hak, 2000; Chang, 1976; Abergel & Temam, 1990).

Flow control can be used and is used in many different research and industrial applications in the flow of fluids (Haecheon Choi, Jeon, & Kim, 2008; Bearman & Harvey, 1976). Control devices are used to modify the flow of fluid in any particular system from the baseline state of the unperturbed flow system. For example, a circular cylinder placed in a cross flow will exhibit vortex shedding within a particular range of Reynolds numbers. By placing a “pin” in the near-wake region of the cylinder the vortex shedding is eliminated. This type of flow modification is termed as passive flow control (Oertel Jr 1990). Another example would be the application of suction to the surface of the same circular cylinder. As in the previous example this also suppresses vortex shedding (Oertel Jr 1990). This is typical of active flow control.

Flow control is widely researched and used in aerodynamic applications with respect to aircraft (Schwartzberg, 1959; Miranda, Telionis, & Zeiger, 2001; Hsiao, Liang, & Huang, 1998; Wu, Lu, Denny, Fan, & Wu, 371). Generally the purpose of using flow control devices on aircraft is to modify the boundary layer and if possible prevent separation. More commonly flow control delays separation to a point further downstream along the chord length of the wings to which it is applied.

Flow control can be applied to two key areas for a body in a cross flow. These two areas are common to two and three dimensional geometries whether it be a bluff body or a streamlined body. They are the boundary-layer (Lin 2002) and the wake region (Nakano and Rockwell 1993). Further, a more macro level approach may be taken to classify each of these key areas in terms of fluid control theory. Figure 2.4 shows broadly the a classification system of flow control methods, in particular bluff bodies since much research has been conducted in the last 15 years on bluff bodies although this system would also be generally applicable to streamlined bodies (Choi, Jeon and Kim 2008).

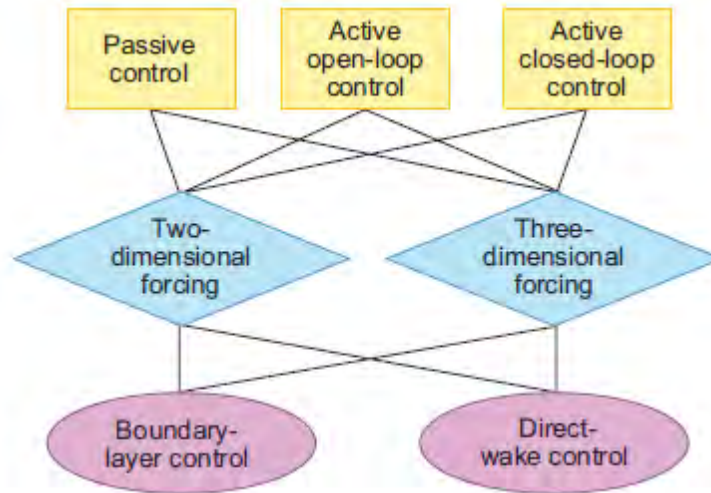


Figure 2.4. Flow control methods (Choi, Jeon and Kim 2008).

It has already been briefly described that flow control can be broken up into the two major categories of passive and active flow control. Passive control refers to control measures that do not require any external energy source to perform their designed function. Examples include altering the surface roughness (Shih, et al. 1993). Active flow control can be divided into two groups which are common in control engineering (Ogata 1997). They are: open-loop and closed systems. With an open-loop control system different inputs can be set and the device functions in a certain state based only on the input parameters. A closed-loop system will take in information based on feedback from external influences and make adjustments to remain within a set performance band (Henning, et al. 2006). Each of these control types maybe classed as two-dimensional and three-dimensional forcing. If the device produces disturbances that affect the flow significantly in only two axes then it is defined as two-dimensional forcing such as using a splitter plate at the base of a cylinder (Anderson and Szewczyk 1997). In three-dimensional forcing, the flow field changes significantly in all three dimensions. For example, by using a helical strake on a circular cylinder reduces the force fluctuations due to vortex shedding (Zdravkovich 1981). Each of these combinations of control type and forcing may

then be grouped as affecting either the boundary-layer or the wake directly. It should be noted that although a control method targeted at modifying the boundary-layer would likely also affect the wake region. On the other hand, direct wake control does not depend on what occurs in the boundary layer.

### 2.3 Synthetic jets

The interaction of solid bodies designed with synthetic jet actuators with different types of fluid flows has been of increasing interest in fluid mechanics (Gogineni et al., 2003; Gorder, 2004; Mittal and Rampunggoon, 2002). A testament to this is the ubiquitous nature of vortices and their influence in fluid dynamic theory (Saffman, 1992), synthetic jets being a case in hand that gives rise to vortical type flow. The relentless search for the perfect vortex gives promise for optimised technologies in a variety of engineering applications, in particular to an improved interaction of the flow of fluids with solid bodies. Vortex rings generated by ejecting a pulse of fluid through an orifice optimized for vortex growth gives rise to alternative propulsion systems (Gorder, 2004). Other applications of the synthetic jet include flow separation control and turbulence, control of thrust vectoring, augmentation of heat transfer and mixing. Although successful implementation of synthetic jets have been demonstrated in laboratory experimentation (Smith and Glezer, 1998) and in technological advancements (Gogineni et al., 2003), the physical mechanisms by which these modified solid bodies alter the flow field, as well as the gas/aero dynamics of the synthetic jets themselves, have not been fully developed (Mittal and Rampunggoon, 2002). This interaction of the solid body with synthetic jet and the mean flow of the system can have a significant effect on the flow behaviour of the system (Glezer and Amitay, 2002; Smith and Glezer, 1998). Thus, synthetic jets can provide substantial improvements to the performance of aerodynamic flows by decreasing drag and increasing lift through a transfer of momentum to the flow that delays flow separation and decreases the size of the wake. This is the point of

interest of the present thesis considering the interaction of a three-dimensional bluff and streamlined bodies with a synthetic jet in a cross flow.

### 2.3.1 Synthetic jet dynamics

The synthetic jet is rooted in the fluid dynamics of turbulent shear flows (Smith and Glezer 1998). A synthetic jet is generated by oscillating the flow through an orifice. The successive movement of fluid through the orifice will form vortices as the fluid separates from the edges of the orifice opening. The frequency of oscillation forming the vortices will then combine each vortex to create a train of coherent vortical structures. The turbulent shear flow of vortices issuing from an orifice of some defined geometrical shape directs the flow into a jet of fluid. The key feature making the synthetic jet unique from other jet flows is that the fluid of the synthetic jet is sourced from the existing surrounding fluid. This gives rise to the term of zero-mass jet, meaning that the net mass flow is zero. As used in the field of aerodynamics the synthetic jet can be simply described as drawing air in through the orifice into a cavity and then expelling that same air out through the same orifice to the surroundings. A normal turbulent shear flow is created by inducing a force gradient in a fluid with sufficiently high velocity between two points. The vortices shed from the fluid emanating from the orifice synthesize the same type of flow. Since the synthetic jet has zero net mass its contribution to the flow field is by way of a non-zero momentum transfer mechanism. In the way of synthetic jets, there seems to be no text that is devoted to this subject. As such one must look in journals as the main source of understanding synthetic jets. A comprehensive article is "The Formation and the Evolution of Synthetic Jets" (Smith and Glezer 1998) that describes the structure of the synthetic jet, its formation and subsequent dissolution into the mainstream fluid flow. The value of this article is shown as it describes not only the formation of conventional synthetic jets but also the synthetic jets arising from acoustic streaming as referenced to the works of the Russians Mednikov and Novitskii (1975) as well as Lebedeva (1980). Although its

experimental focus is on conventional synthetic jets, it provides a sound introduction to synthetic jets and their characteristics.

In some sense, synthetic jets may be considered a time-averaged fluid motion generated by sufficiently strong oscillatory flow at a sudden expansion. A characteristic feature of synthetic jets is that their formation takes place within the surrounding fluid flow. The net mass added is zero, but the synthetic jet energizes the flow by imparting linear momentum. The vortex pairs formed progress into turbulence and the monotonic decrease of their streamwise velocity leads to their dissolution. More simply the formation of synthetic jets is through a time-periodic alternating pressure drop across an orifice (Glezer and Amitay 2002). Generally, when a pulse of fluid is ejected from an orifice, it forms discrete vortical structures (Saffman 1995). This is shown in Figure 2.5 as a discrete fluid pulse is ejected into to quiescent medium.

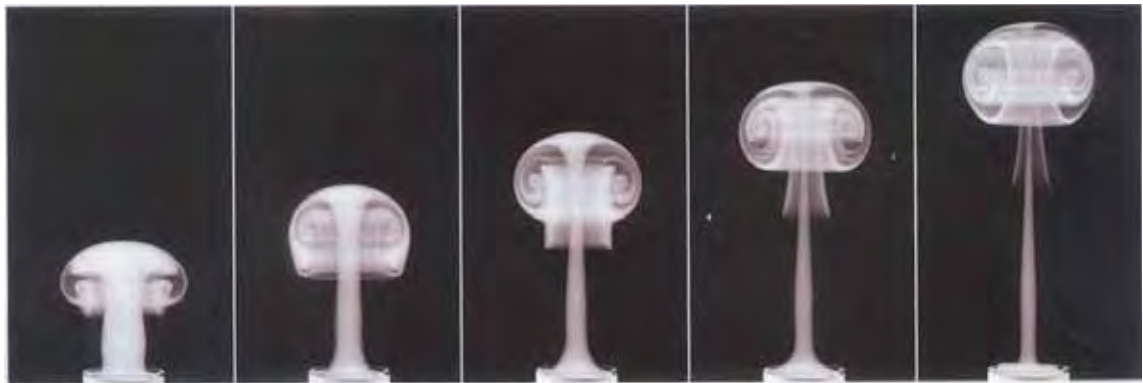


Figure 2.5. A pulse of fluid is ejected into a quiescent medium (Gorder 2004).

Synthetic jet dynamics interestingly differ from a continuous jet stream ejected from the same orifice of the same time-averaged flux of streamwise momentum. For continuous and synthetic jet at the same Reynolds number as shown in Figure 2.6 certain characteristics are clearly different. The synthetic jet is wider and

also has a lower velocity in the near field as consequence of the vorticity from counter rotating vortex pairs. Further away synthetic jets resemble the continuous jets with similar velocity profiles. Overall the synthetic jet grows more quickly than the continuous jet in width and volume flux (Smith and Swift 2003).

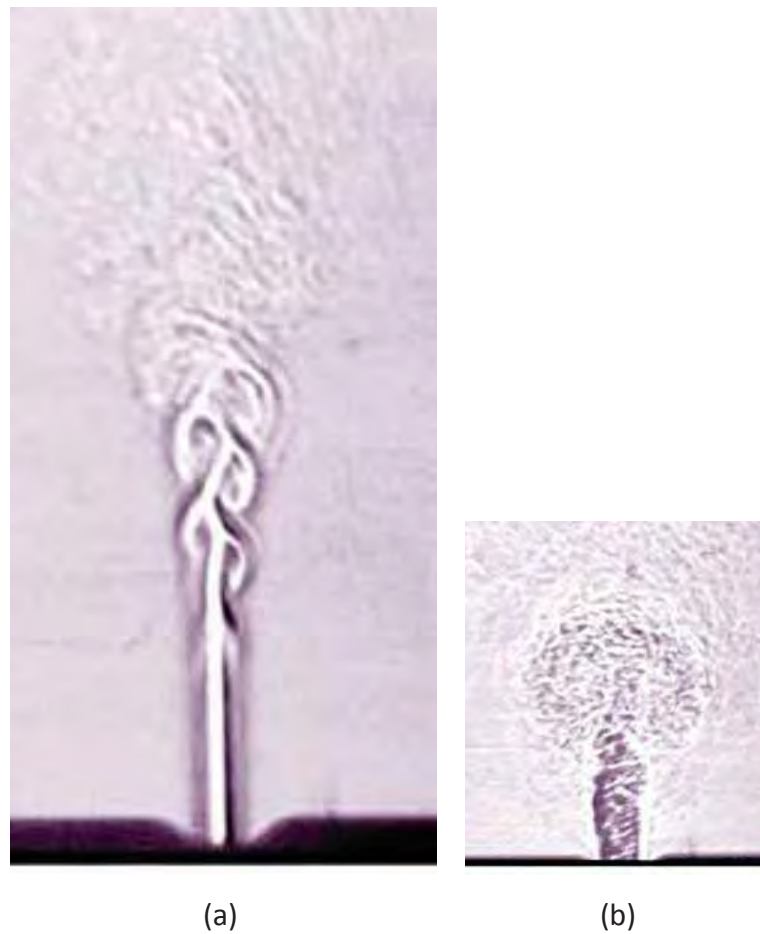


Figure 2.6. Schlieren images of jets at  $Re = 2200$ . (a) continuous jet (b) synthetic jet (Smith and Swift 2003).

### 2.3.2 Synthetic jet devices

The synthetic jet can be created using different methods. The common way of generating a synthetic jet would be to construct a piston type device with an orifice in the cavity space above the top of the piston. Thus the flow is drawn into the cavity as the piston moves downward and then ejected back out of the cavity space as the piston moves up. Alternatively a space is constructed and it can be rectangular or circular depending on the synthetic jet configuration that is required for the experimental work being undertaken. A diaphragm of some flexible material is placed at the base or it forms the base of the cavity. Then a mechanism is attached to the flexible diaphragm such as a piezoelectric actuator that causes oscillatory motion of the diaphragm. At the top of the cavity, there is an opening or orifice that allows the surrounding fluid to be drawn in and ejected as the diaphragm moves up and down. A setup of this type is shown in Figure 2.7.

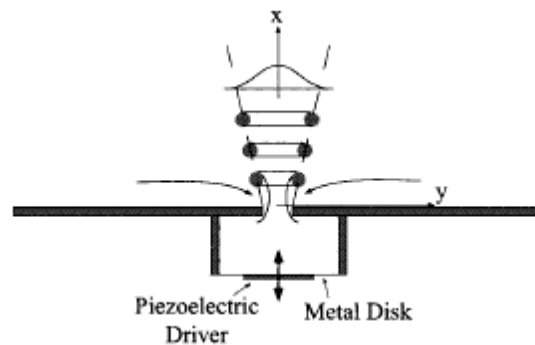


Figure 2.7. Schematic diagram of synthetic jet actuator (Smith & Glezer, 1998).

Synthetic jets may also be generated acoustically. A classical source for sound in fluids is Lighthill which produced a book titled “Waves in Fluids” in 1978 during his appointment as Lucasian Professor of Mathematics at the University of Cambridge. This text is effective in providing a strong foundation on which to build the mathematics and physics knowledge needed to be able to progress theoretical models for the aeroacoustics of synthetic jets. The first chapter provides a rigorous

treatment of the propagation of sound waves describing the mechanisms used to predict the behaviour of various types of sound generation. The second chapter deals with one-dimensional waves this chapter can provide direction in the design of a sound source for synthetic jet experiments. It also proves to be an excellent source for providing references on acoustic literature.

A key reference text that is devoted entirely to aeroacoustics is, Goldstein (1976). This text draws together the solutions to the Wave Equation and the equations of aerodynamic flow together with Lighthill's acoustic analogy to derive the fundamental aeroacoustic equation for aerodynamically generated sound in the presence of solid bodies. Then these equations are applied to jet noise which possibly could prove useful when applied to synthetic jets but this is doubtful since these flows are high Reynolds number jet flows.

The work of Howe (1998) is a highly analytical book that provides models for the interaction of unsteady fluid flow with solid bodies. This book is comprehensive in its coverage of the details of aerodynamic sound bringing together the journal articles over the years. This text should prove to be integral in formulating a mathematical structure to describe the aeroacoustics of synthetic jets.

As mentioned above, synthetic jets can be produced by acoustic streaming. Also Crocker (1978) contains a section on acoustic streaming which contains the theory, types of acoustic streaming and applications. This is a good beginning in understanding acoustic streaming and then to focus in on how it can be applied to synthetic jets. The journal "Soviet Physics-Acoustics" has published two articles (Mednikov & Novitskii, 1975; (Lebedeva 1980) that gave details of experimental setup and results of the effects acoustic streaming on air at different frequencies (Ahmed & Archer, 2001). It gives the reader the scale of velocities expected at the frequencies and amplitudes of sound generated.

## 2.4 Synthetic jet on bluff bodies

The theories developed to explain the governing dynamics of fluid motion for application to real situations are proving to be difficult (Anderson, 2001; Buresti, 2000). As such, experimental methods are still the main source of physical information for the researcher who is seeking to evaluate the aerodynamic performance of a solid or bluff body (Norberg, 2002).

The flow over the cylinder can be described with two independent variables and as such is termed axisymmetric. It is not really a two-dimensional flow and not fully three-dimensional either. It is a degenerate three-dimensional flow that exhibits certain three-dimensional effects. A common phenomenon to all three-dimensional flows is the three-dimensional relieving effect that is present in flow over a sphere but not that of a cylinder; since the flow over a cylinder has in a sense only two ways to travel to get over the body whereas in three-dimensions it has an alternative or extra path to travel past and over the body.

In such circumstances, studies on bodies such as spheres are useful in determining the aerodynamic characteristics of these true three-dimensional flows and hence form the basis of the present research (Buresti, 2000).

A striking example of the similarities of the flow over a cylinder and the flow over a sphere is the reduction in drag and the general structure of the wake following the transition from laminar to turbulent flow. There are differences in the flow over a sphere and that of a cylinder quantitatively in the values for the coefficient of drag before and after the transition from laminar to turbulent flow. The sphere shows a reduction in drag from a value of 0.4 to 0.1, whereas for a cylinder the reduction is from a value of 1 to 0.3. Similarities are also apparent in the flow-generated instabilities of the cylinder and sphere. These flow instabilities include wake instability (vortex-shedding), separated shear layer instability and boundary layer

instability. Boundary-layer instability is a term used to describe disturbances that affect the stability of the boundary layer (Reshotko, 1976). For instance, if the forced disturbance that enters the boundary layer is large enough then this will cause the boundary layer to transition from laminar to turbulent flow. If the disturbance is small, then it will tend to excite free disturbances or normal modes of the boundary layer that are generally referred to as Tollmien-Schlichting waves.

Synthetic jets may be applied either in a distributed manner or from localised sources; also as previously mentioned oscillatory streaming motions can be induced in the fluid acoustically through the transmission of sound or 'acoustic streaming' (Glezer and Amitay, 2002; Jeon et al., 2004). A case in hand is the work of Kim and Durbin (1988) in which a uniform acoustic field was applied symmetrically from a distance to the airflow interacting with the sphere in the Reynolds number range of  $500 < Re < 60000$ . The results indicated that, when the acoustic excitation was near to the natural instability of the flow, a decrease in the wake size occurred as a consequence of the separation point being delayed and pushed further downstream towards the wake region. This created a rapidly thickening but broader and shorter recirculation zone from the inwardly directed shear layer. This also produced a lower base pressure behind the sphere and possibly in the near-wake region, with a higher velocity in the recirculation zone as a result of a reduced size of the separation bubble. Since the forcing was applied away from the body, an increase in the turbulence level with a consequent increase in the base pressure over the body was produced which then resulted in higher drag.

Additionally, experimental investigations carried out by Jeon et al. (2004), on a sphere with a uniform acoustic field emanating from a slot located at an angle of  $76^\circ$  from the fore stagnation point, but equally distributed circumferentially around the sphere, showed that for forcing frequencies equal to or greater than the critical non-dimensional frequency,  $St = 2.85$  or 190 Hz, there was a reduction in drag of nearly 50%. This forcing frequency corresponded to the boundary-layer instability

frequency that delayed flow separation and consequently triggered the high shear-layer instability frequency for reattachment of the flow. The boundary-layer instability frequency falls in between the low wake instability frequency (vortex shedding) and the high shear layer instability frequency, which at this Reynolds number are, expressed in non-dimensional form by way of the Strouhal number,  $St = 0.18$  and  $St = 10$  respectively. The boundary-layer instability frequency seems to correspond to the particular frequency that is receptive of disturbances to the normal modes of the boundary-layer, or as mentioned earlier, the Tollmien-Schlichting waves, since laminar separation is maintained. The works of Kim and Durbin (1988) as described above showed that the reverse flow region became stronger and that the total drag was increased with acoustic forcing. Jeon et al. (2004) has suggested that the mechanism for reducing drag at the critical frequency could be due to the corresponding high frequency boundary-layer instability.

The work by Glezer and Amitay (2002) using a synthetic jet placed locally on one side of a cylinder showed a reduction in surface pressure both upstream and downstream of the forcing location. The actuation of the synthetic jet induced a local separation bubble beginning at the location of the synthetic jet and ending at the point of reattachment. Figure 2.8 shows the cylinder in smoke tunnel at  $Re = 4000$ . Two rectangular synthetic jet actuators are fitted to the cylinder body. The baseline of flow in Figure 2.8 (a) shows the typical bluff body wake of the cylinder. The effect of the synthetic jet at the pre-separation angle of  $60^\circ$  shows the separation bubble forming and then the flow reattaching as shown in Figure 2.8 (b). Then at the base of the sphere  $180^\circ$  in Figure 2.8 (c), the synthetic jet post-separation is able to fully correct the flow and prevent separation. Remarkably when the two rectangular synthetic jets are  $120^\circ$  out of phase at a  $180^\circ$  location the fore stagnation point is shifted in a downward direction, although the flow separates as shown in Figure 2.8 (d).

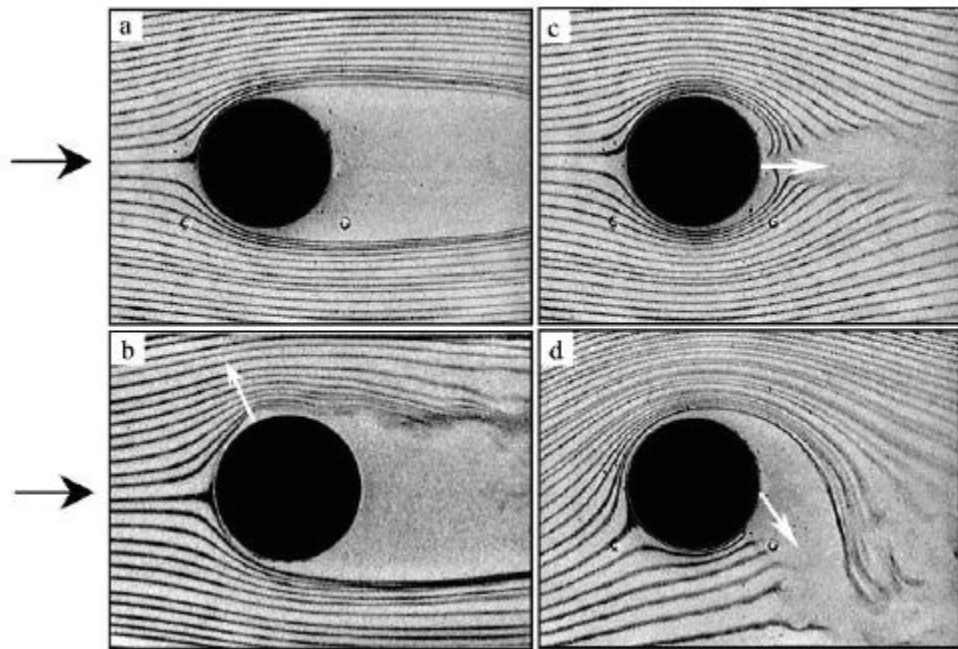


Figure 2.8. Smoke visualisation of a cylinder. (a) baseline and synthetic jet at (b)  $60^\circ$ , (c)  $180^\circ$  and (d)  $180^\circ$  and  $120^\circ$  out of phase (Glezer and Amitay 2002)

This mechanism of drag reduction was referred to as “virtual aero-shaping” (Mittal and Rampungoon, 2002) which displaces local streamlines well outside the undisturbed boundary-layer and rapidly decreases the upstream and downstream surface pressure of the forcing location. Thus, a delay in separation results from the increased velocity of the potential flow outside the surface boundary-layer which is greater than the velocity of the unforced potential flow. It is not well established as to when or under what conditions these bubbles will form, particularly in three-dimensional flows with the synthetic jet impinging on the cross-flow and forming a recirculation zone.

A rather straightforward and effective way to examine how the aerodynamic behaviour of a bluff body in terms of boundary layer growth, skin friction, separation of flow and pressure drag changes in three-dimensions under the influence of synthetic jet changes is to use a sphere, which has a symmetrical shape.

The sphere may be manufactured with a fixed synthetic jet orifice and a set of pressure tapping points around it. Designing the experiment in this fashion provides the distinct advantage of being able to describe the influence of the synthetic jet on the same set of points on the sphere as it is rotated relative to the free stream.

It is interesting to note that the maximum Reynolds numbers at which Kim and Durbin (1988) and Jeon et al. (2004) conducted their experiments form approximately the two limits of the plateau like region on the coefficient of drag curve for a sphere (Schlichting, 1968) where the drag practically remains unchanged with changes in the Reynolds number. It appears that the effect of a localised synthetic jet on the flow over a sphere at a Reynolds number that lies within those limits would be a suitable choice and part of the present thesis was, therefore, conducted at a Reynolds number of  $5 \times 10^4$ .

## 2.5 Synthetic jets on streamlined bodies

A section of the research work conducted in this thesis was the application of the synthetic jet in a localised asymmetrical manner to a bluff body. This method was developed in an attempt to delay flow separation, reduce the size of the wake, reduce vorticity and vector the flow to be more streamlined and so reduce the drag. As also mentioned previously, in an unmodified baseline bluff body, the aerodynamics are characteristic of high pressure drag whereas streamlined bodies exhibit low pressure drag at low angles of attack. As the angle of attack (AOA) is increased on a streamlined body such as an airfoil or wing, the lift force initially increases linearly with the flow being attached to the majority of the surface (Anderson 2001). When the AOA is large enough, the flow will leave the upper (suction) surface and cause flow separation, as occurs normally on a bluff body. As a result, a large wake region will form as in the case of a bluff body. When this occurs on an airfoil/wing there is a drastic drop in lift and a concomitant increase in the drag force. This is the well-established phenomenon of stall commonly referred to

in aeronautics as “the aircraft has stalled”. The way stall occurs depends on the shape of the wing cross section, the airfoil shape. When the flow separates from the leading edge of an airfoil which is characteristic for thinner airfoils it is called leading edge stall. For thicker airfoils the flow separates from the trailing edge and so this is called trailing edge stall. For a very thin airfoil, such as a flat plate, the flow separates initially from the leading edge at approximately  $9^\circ$  AOA and then reattaches. This forms a separation bubble which also occurs on bluff bodies with synthetic jet applied (Jeon, et al. 2004). As the AOA increases, the flow starts to separate again until a further increase in the AOA results in full flow separation which comes from both edges of the flat plate (Anderson 2001). An example of flow separation on an airfoil is clearly shown in Figure 2.9.

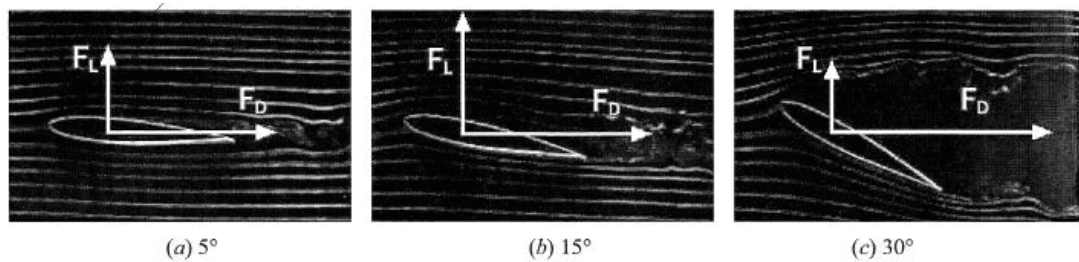


Figure 2.9. Flow separation from an airfoil at different AOA (Cengel and Cimbala 2006).

Much modern research effort has been invested in increasing the maximum lift coefficient in wing design since the maximum lift coefficient  $C_{l,max}$  occurs just before stall (Anderson 2001). Increasing the maximum lift coefficient has been possible through the use of high-lift devices such as flaps, slats and slots that are attached to the wings of an aircraft. Other devices are aimed at boundary layer control (BLC) to prevent or delay flow separation. The blown flap is an active flow control measure that energises the boundary layer by tangentially blowing air along the upper surface of the wing. The additional energy provided by the blowing allows the boundary layer to overcome any adverse pressure and remain attached to the wing

surface. These mechanical devices are deployed when it is required for the aircraft to attain maximum operating performance for high-lift such as takeoff and landing. Modern aircraft are usually designed to use a combination of high-lift devices (Anderson, 2001; Schlichting & Gersten, 2003).

With streamlined bodies, the drag due to skin friction is significant and the major contributor to the overall drag at low AOA. The surface roughness has a major effect on the skin friction. At large Reynolds numbers  $7 \times 10^6$  a moderately rougher surface could increase the drag by approximately 25% (Abbott and Von Doenhoff 1959). Flow control techniques have been applied to the surface of streamlined bodies in an effort to reduce skin friction drag (Hwang and Biesiadny 1998).

The aerodynamics of a finite wing differ from those of an airfoil. An airfoil is a two-dimensional tool used to determine the performance of an infinite wing. A real world finite wing has flow in all three-dimensions including the spanwise direction unlike an airfoil. The third component of flow is basically generated by the pressure difference between the top and bottom surface. The high pressure on the bottom tends to create a flow along the span of the wing from the root outwards towards the wing tip. The low pressure suction side on the upper surface flows along the wingspan inwards towards the wing root (Anderson 2001). Figure 2.10 shows the spanwise flow over a wing when subjected to a cross flow.

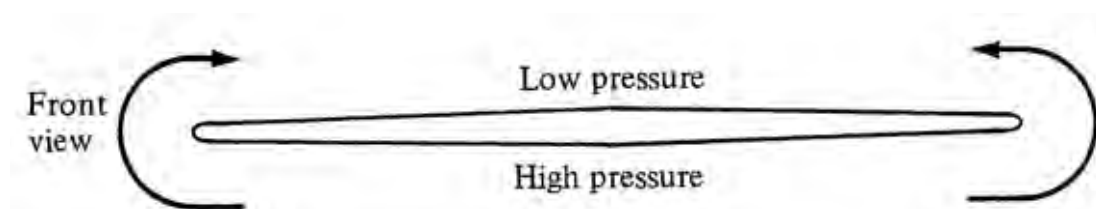


Figure 2.10. Spanwise flow of wing (Anderson 2001).

The circulation of flow from the lower to the upper surface of the wing generates flow around the wing tips and produces a vortex at each wing tip. The vortex at the wing tips trail behind leaving a disturbed wake that can affect or even cause a catastrophic accident for other aircraft if they encounter them before they have sufficiently dissipated. This is shown on a wing using smoke visualization in Figure 2.11. Further, the vortices produce a velocity component that is defined as downwash that is directed in a downward direction giving the local relative angle of attack which is lower than physical angle of attack of the wing. The downwash reduces the angle of attack and therefore reduces the lift force generated by the wing. The reduction in lift force on a lift producing wing as a result of downwash is defined as induced drag or lift-induced drag (Anderson 2001).

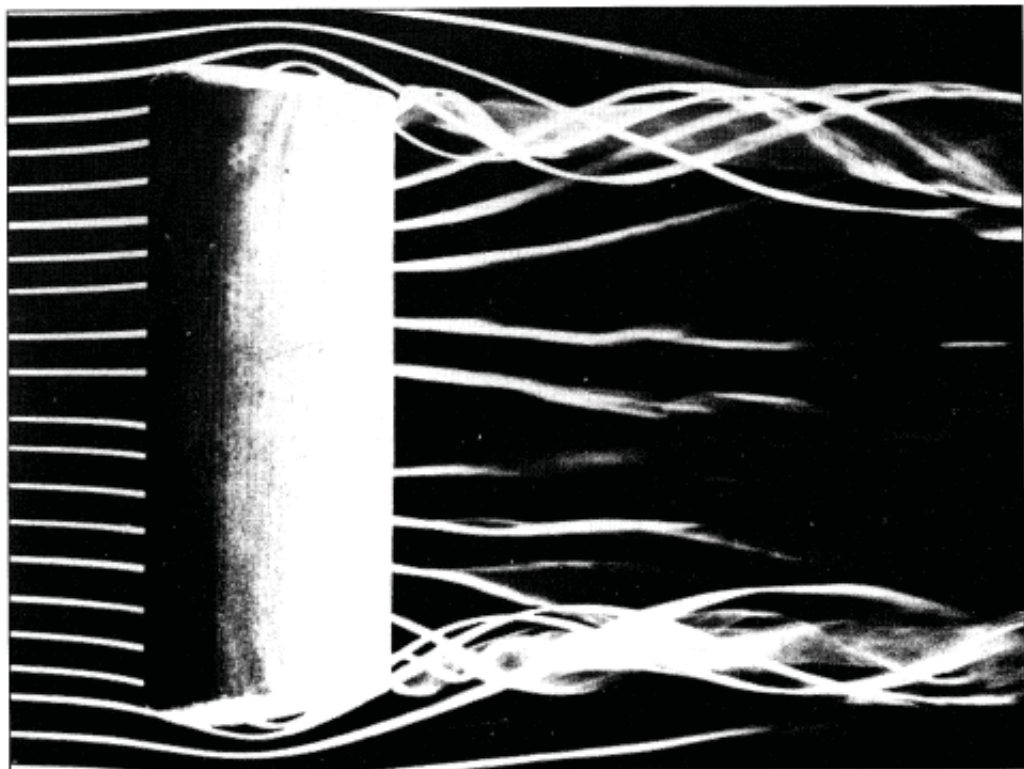


Figure 2.11. Wing-tip vortices produced from a rectangular wing in a cross flow.

Produce in smoke tunnel (Anderson 2001).

Induced drag is a significant component of the total drag of an aircraft and can account for up to 40% of the total drag (Margaris and Gursul 2006). The goal is to minimise the vortices and the strength and size of the wake (Coustols, et al. 2003). A common passive flow control device used to inhibit wing-tip vortices is to fence off the wing using winglets (Committee on assessment of aircraft winglets for large aircraft fuel efficiency and National Research Council 2007). Active flow control applied to the wing-tip has been investigated. This includes wing-tip blowing and the use of wing-tip jets (Lee, Tavella, Wood, & Roberts, 1989; Wu, Vakill, & Chen). Aside from reducing vorticity and drag, inhibiting wing tip vortex formation also has benefits in the noise attenuation (Slooff, De Wolf, Van Der Wal, & Maseland; Simpson, Ahmed, & Archer, 2002). The use of a continuous jet has proven to be beneficial.

The majority of work with synthetic jets has been conducted on two-dimensional airfoils (Duvigneau, Hay, & Visonneau, 2006; Kim & Kim, 2006). Nonetheless these works have proved the effectiveness of the synthetic jet. A uniquely designed airfoil was developed by Boeing's Phantom Work Group in St. Louis and used by Amitay and Glezer, (2006). The airfoil consisted of a circular cylinder as the leading edge and a NACA four-digit series symmetric airfoil that was uniformly stretched and attached to the circular cylinder. The two identical rectangular synthetic jet orifices were placed next to each other running along the span of the circular cylinder. The synthetic jet could be actuated at a number of high and low frequencies, the objective being to apply the synthetic jet at such a frequency that the modified flow field becomes independent of the actuation frequency.

The baseline flow was found to separate at a very low AOA of  $5^\circ$  whereas normal separation would occur at above  $15^\circ$ . The synthetic jet was proven to be effective up to the final tested angle of  $25^\circ$  completely or partially reattaching the flow even at high angles of attack. There was also an increase in the lift and the pressure drag

was lowered. The pressure distribution from the airfoil at different angles of attack is shown Figure 2.12 in (Amitay and Glezer 2006).

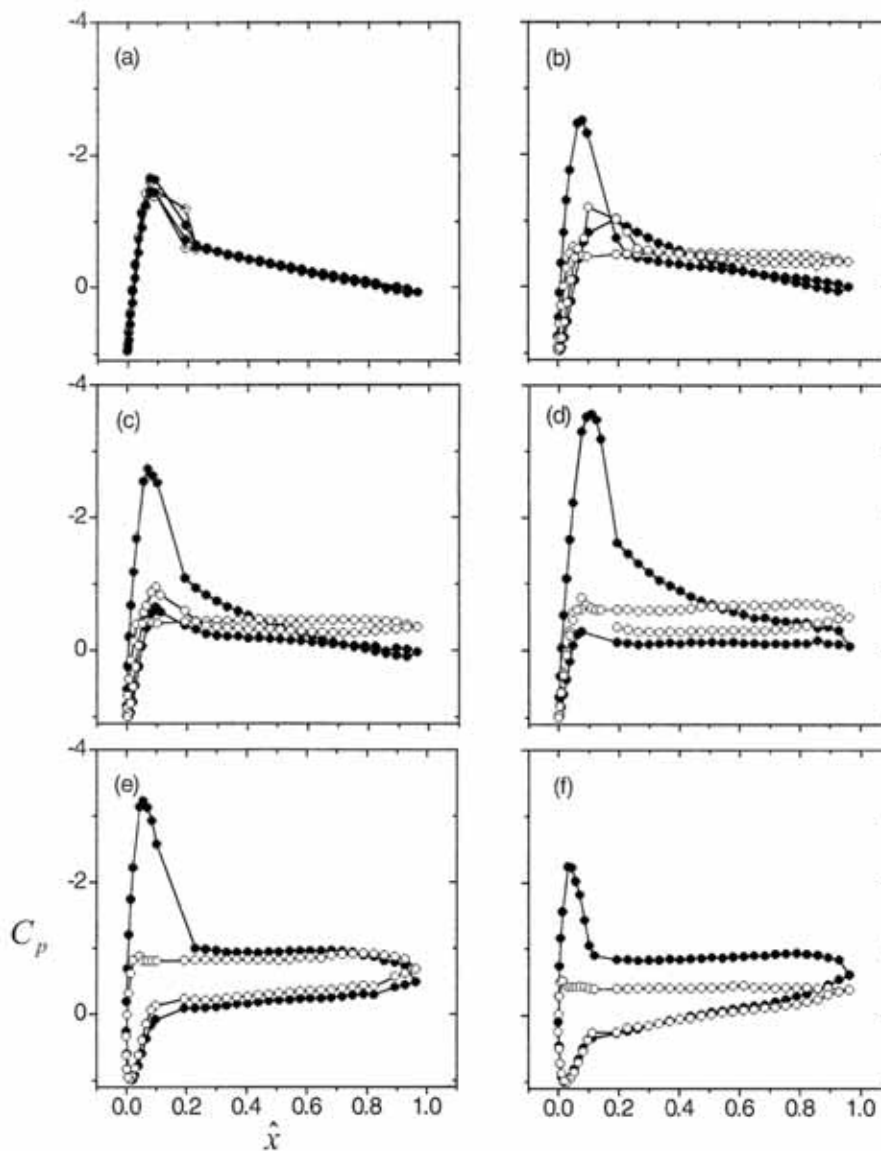


**Fig. 2.** Pressure coefficient distributions around the airfoil at different angles of attack. Forced (—●—), and unforced (—○—).  $\alpha = 0^\circ$  (a),  $\alpha = 5^\circ$  (b),  $\alpha = 10^\circ$  (c),  $\alpha = 15^\circ$  (d),  $\alpha = 20^\circ$  (e) and  $\alpha = 25^\circ$  (f)

Figure 2.12. Pressure coefficient distributions (Amitay and Glezer 2006).

The synthetic jet is placed at an angle of  $60^\circ$  to the fore stagnation point and at a Reynolds number,  $Re = 310,000$ . The flow over the airfoil remains completely attached up to an angle of  $15^\circ$ . Thereafter, at  $20^\circ$  it is partially reattached to the airfoil. The frequency used was typically higher than the vortex shedding frequency.

A time-series visualisation of the process of the flow reattaching with the synthetic jet at the high frequency was produced using smoke. The airfoil is at  $17.5^\circ$  AOA and the synthetic jets are located at  $60^\circ$  relative to the airfoil leading cylinder. The first image in Figure 2.13 (a) shows the baseline flow separated from the leading edge with a large wake indicating the stalled condition of the airfoil. In Figure 2.13 (b), the actuation of the synthetic jet has just begun in the time series and already the flow has begun to flatten on the leading edge. This indicates attachment and the vortices are being reversed as opposed to normal separation vortices along the airfoil. This opposed vorticity and flow attachment continues along the airfoil as seen in Figure 2.13 (c). The vortex is also larger with another vortex beginning to form at the leading edge. In Figure 2.13 (d) the leading edge vortex in the previous time shot has now formed and is being advected downstream along with the larger vortex. The synthetic jet is in a sense countering the adverse vorticity with its own inherent train of turbulent vortical structures. Another vortex is then formed and finally all vorticity is advected away until the flow is fully attached and the synthetic jet continues to energise the flow. Figure 2.13 (f) shows the fully attached flow contrasting the effectiveness of synthetic jet against the baseline condition.

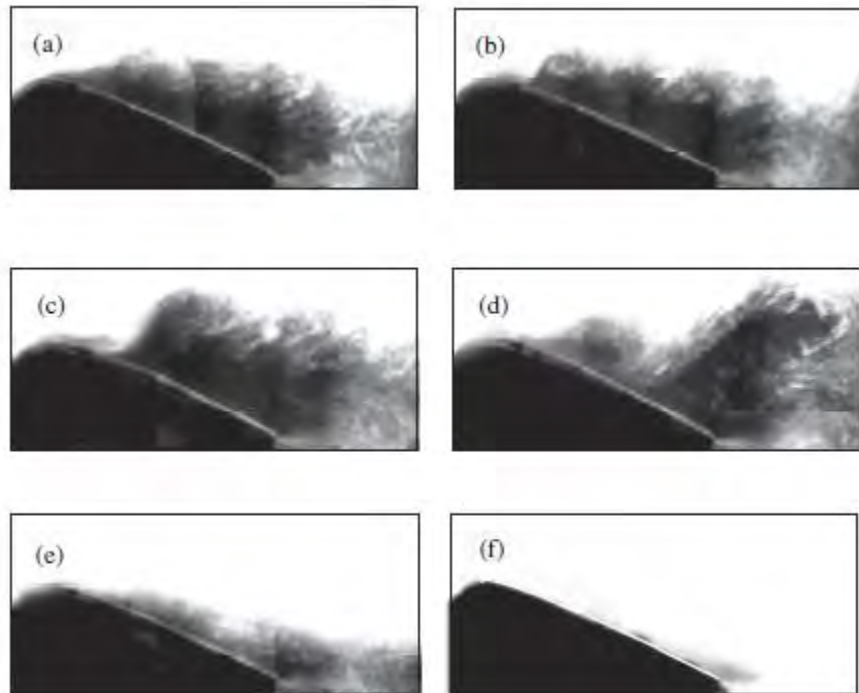


Figure 2.13. Phase-averaged images at different times during the reattachment process (Amitay and Glezer 2006).

## 2.6 Interference drag

Another aerodynamic component of drag occurs whenever we have a composite body that has changes in its geometry from one part to another. Whenever two bodies are joined together such as a wing and a fuselage or a cylinder on a flat plate the total drag of the composite joined body is not just the mathematical sum of its components. Another factor needs to be included due to the flow being affected by the transition, seam or juncture that is formed from one part of the composite body joining to another part. This drag component is referred to as interference drag (Tetrault 2000).

Interference drag has been studied in transonic and supersonic flows (Lord, 1962; Jones, 1953) where the junction between two parts can create stronger shockwaves

than the individual parts in the same high speed flow giving rise to wave drag. Interference drag has been given little attention in work based on subsonic flows since it is not the foremost contribution to the overall drag. Even so this can be an area of highly disturbed flow with eddies and flow reversal causing inefficiencies in design that can lead to unnecessary fuel costs that can be alleviated through more intelligent design address this issue. Flow control using synthetic jets technology is used in this thesis to ascertain its effect on interference drag.

## **2.7 Computational fluid dynamics and the modelling of synthetic jets**

A three-dimensional bluff body that has been researched extensively is the sphere (Achenbach, 1972; Achenbach, 1974; Taneda, 1978; Pao and Kao, 1977; Sakamoto & Haniu, 1990). The flow over a sphere has also been, in relatively more recent work, investigated numerically using various CFD codes (Nakanishi and Kamemoto, 1993; Karim, Rahman and Alim, 2009; Yun, Choi and Kim, 2003). Many of the numerical simulations on bluff bodies have been directed towards applications in industrial aerodynamics such as the flow around buildings. Buildings generally tend to have a bluff body type of geometry making fundamental bluff body flows ideal cases for the study of flow around these structures. In the present work, the sphere bluff body is used as a basis to understand the aerodynamics of the flow behaviour with active flow control. With a focus on using the gained understanding and applying this to other three-dimensional objects, in particular streamlined bodies, such as a wing. This contributes to the needs of the aeronautical sciences and associated transportation vehicles.

Computational models have been developed for synthetic jets in isolation and in a crossflow environment (Kral, Donovan, Cain and Cary, 1997; Kim and Km, 2006). A computational model is developed of synthetic jet using a high end commercially available CFD code for both bluff and streamlined bodies. An unstructured grid

approach is used and the Menter (1993) SST (Shear Stress Transport) turbulence model together with suitable boundary conditions and user defined functions to generate the oscillatory synthetic jet flow with zero net mass flow.

## 2.8 Synthetic jet applications

After examining the physics of separated fluid flow and flow control devices used to mitigate this phenomenon, in particular synthetic jets, the primary focus is to trial synthetic jets in localised three-dimensional applications where we can gain a better understanding of their benefits in applied aerodynamics. This will then lead to more advanced and intelligently designed equipment that can utilise this turbulent shear flow phenomena to better achieve their intended use or purpose. Some of these applications include:

- Micro Adaptive Flight Control (MAFC) (Gogineni, Joslin and Gaitonde 2003) - Synthetic jet actuation with the Coanda effect can provide flight control trajectory of a projectile.
- Aeroshaping Effect of Synthetic Jets (Mittal and Rampunggoon 2002) – In this article there is a description of the interaction of a synthetic jet with a flat plate and the effect of recirculation zones created by the synthetic jet in a cross flow. The article shows that indeed large recirculation zones (bubbles) are formed by the synthetic jets. Although it does state that it is only a 2D flow with no allowance for turbulence, compressibility and pressure gradients.
- Vectoring of a Primary Jet with a Synthetic Jet (Smith & Glezer, 1997) – This articles describes the physics of how a synthetic jet can be used to alter the direction of a primary jet by lowering the pressure near the exit of the

primary jet as well as the resistance posed by the synthetic jet. This would prove to be advantageous in cases of thrust vectoring.

Of particular merit is the paper by Mittal and Rampunggoon (2002) which provided references for the application of synthetic jets in separation control and turbulence, control to thrust vectoring and augmentation of heat transfer and mixing. The mention of these applications and their associated references opens up the Reader to the existing possibilities of the application of synthetic jets and thus allows the present research on synthetic jets to be used any one of these fields although the primary focus is on applied aerodynamic applications for use on aircraft.

---

## Chapter 3

### Research Methodologies and Apparatus

---

### **3. Research methodologies and apparatus**

Chapter 3 describes the experimental facility used to conduct the laboratory experiments. The solid bodies used in the experiments are detailed as well as their construction and features. The experimental method used to generate the synthetic jet flow is also described. Further, it will cover the different methods used to obtain the flow field characteristics of the three-dimensional flow over the bluff and streamlined bodies. Integral to the experimental setup and the reliability of the results was to accurately measure the added momentum generated by the synthetic jet oscillatory flow. The details of the method used to measure the synthetic jet velocity profile are given. The computational models developed for the CFD analysis are examined showing the validation process.

#### **3.1 457 mm (18") x 457 mm (18") Wind Tunnel**

The experimental results were obtained using different wind tunnels in the UNSW Aerodynamics laboratory. The first part of the experimental work was conducted in the 457 mm (18") x 457 mm (18") open circuit, closed test section, NPL (National Physical Laboratory) type wind tunnel (Barlow, Rae Jr and Pope 1999). This is shown in Figure 3.1. It has a bell-mouth inlet with a honeycomb flow straightener with an additional four flow conditioning screens that lead into a settling chamber. It has a 5.5:1 contraction after the screens to lead the flow into the first test section of 1219.2 mm length. Downstream, the flow exits into a 6° diffuser and transition to a circular section to reduce the flow velocity. The wind tunnel is driven by a 5.6kW motor coupled to an 8-blade rotor with a potentiometer controller to adjust airspeed. A survey was taken of the wind tunnel to measure the freestream turbulence level using hot wire and was found to be approximately 0.15%.



### 3.2 Experimental design of bluff body and synthetic jet

The wind tunnel was operated at an air speed of 10 m/s corresponding to a Reynolds number of  $5.1 \times 10^4$ . The reasoning for conducting the experiments at this Reynolds number has been explained in section 2.4. The bluff body used for the experiments was an aluminium sphere of 80 mm diameter and supported horizontally by a rod attached to one side of the sphere. Using the method of Barlow, Rae and Pope (1999), the blockage ratio was calculated to be 2.8%. Further information on wind tunnel blockage is given in Appendix B. Additional velocity profiles obtained using hot-wire anemometry on the centreline plane of the sphere showed little or no difference from the free stream velocity profile confirming that tunnel blockage was negligible. The sphere was designed with a synthetic jet orifice (labelled SJ in Figure 3.2) of 1 mm diameter and oriented at a  $45^\circ$  tangent to the normal of the sphere surface. It had seven pressure ports on the centreline axis of the sphere as shown Figure 3.2. An electronic scanivalve unit with controller and port indicator and an FCO510 digital manometer were used to measure the pressure. The sphere was rotated to each predetermined angular position with sufficient time allowed for the pressure to settle before a measurement was taken.

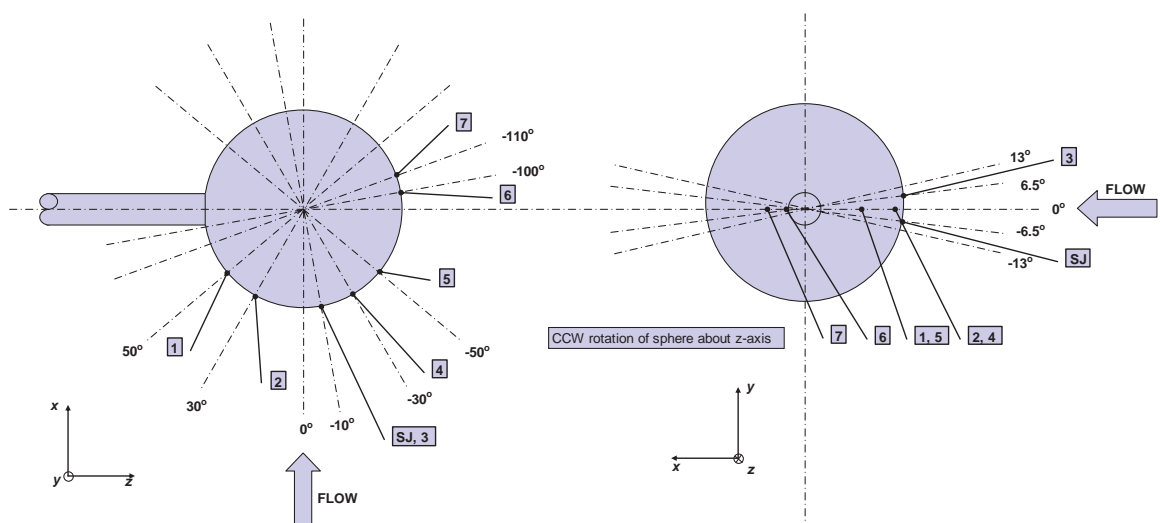


Figure 3.2 Schematic diagrams of sphere: Plan view (left), Elevation view (right).

The synthetic jet actuator was composed of a modified compressor and a 12 VDC power supply. The compressor piston was fitted with a one-way valve that was modified to cause suction and blowing as it reciprocated, instead of constant compression of the air. The compressor line was connected to the synthetic jet orifice, which was 1 mm in diameter, on the sphere using silicon tubing. The sphere support was fitted against a fixed protractor to measure the angle of rotation. The pressure measurements of the multiple tappings were conducted using a scanivalve controller with scanivalve shown in Figure 3.3.



Figure 3.3. Scanivalve controller and scanivalve unit below.

The velocity of the synthetic jet was measured using A Dantec Streamline CTA Anemometer system with a 55P14 probe. The probe was calibrated using the Dantec Flow Calibration System. The voltage supplied to the motor was through a DC power supply unit to generate the desired frequency with a range of 10 Hz up to 75 Hz. The frequency obtained from hot-wire measurement was cross-checked against the rotational speed of the motor using a laser tachometer. The velocity profile corresponding to synthetic jet is shown in Figure 3.4. Further details on the synthetic jet equipment used are found in Appendix A.

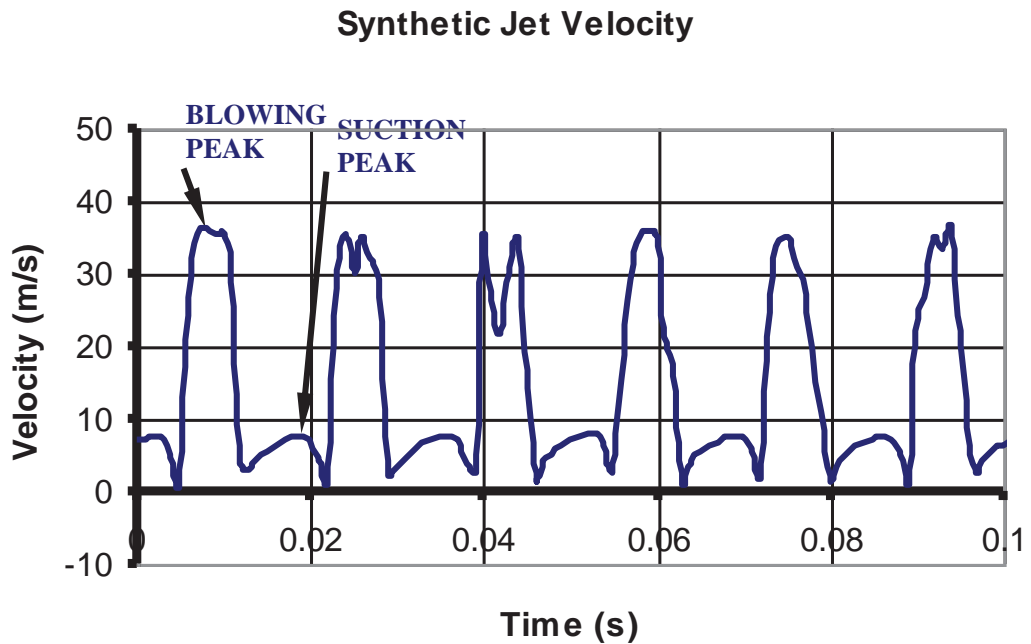


Figure 3.4 Hot-wire measurement of experimental synthetic jet velocity profile.

Since the hot-wire measurement is insensitive to flow direction and the two extremes, that is blowing and suction, are 180 degrees out of phase, the peaks are both positive for suction and blowing. The maximum velocity measured was about 35 m/s, and its RMS value was 15 m/s. The energy delivery for synthetic jets and for jets in general is measured using the momentum coefficient  $C_\mu$ . This is defined as follows in equation (3-1)

$$C_\mu = \frac{(\rho u^2 e)_{jet}}{\left(\frac{1}{2} \rho U^2 D\right)_\infty} \quad (3-1)$$

where  $e$  is the diameter of the synthetic jet orifice

For the synthetic jet to be effective it was found that a momentum coefficient greater than 0.002 should be used (Gilarranz and Rediniotis 2001). The momentum coefficient for the synthetic jet used on the sphere was 0.05625.

The actuation frequency was  $f = 60$  Hz (Figure 3.4) that corresponded to a Strouhal number of  $St = 0.53$ . This value was chosen to avoid correlation with the low wake instability frequency (vortex shedding frequency) and the high instability frequency (separating shear layer instability frequency) which are at  $St = 0.19$  and  $St = 6$  respectively at the present Reynolds number (Ahmed & Wagner, 2003). Rather than examining the effect of the synthetic jet as targeted towards flow instabilities this paper focuses on the mechanism of ‘virtual aeroshaping’ as a means to control the flow over the sphere and thereby improve aerodynamic performance through a reduction in drag. Work on a two-dimensional body (Glezer and Amitay, 2002) has shown an improvement in the delay of separation for a Strouhal number of 2.5 for a circular cylinder. Whether similar improvement of the flow over three-dimensional flow can be obtained with the application of the localised synthetic jet was, therefore, a major motivation of this project.

Flow visualization was carried out using tufts (Bradshaw, 1970) to obtain a qualitative estimate of the flow direction and location of the separation point on the sphere.

### **3.3 Wake surveys**

The instrument selected to take measurements in the wake region of the sphere was a five-hole cobra head pressure probe. The measured pressures from the five-hole probe enables the calculation of the total pressure and static pressure at the point of interest which then allows the velocity vector to be determined. The pressure probe was calibrated using a specially designed rig that rotates about the yaw and pitch planes to take pressure measurements throughout the calibration

range for the probe (Treaster & Yocum 1973). A schematic representation of the five-hole pressure probe tip is shown in Figure 3.5. The calibration process for the five-hole probe is a lengthy exercise unless it is fully automated which was not the case in this research. Further many calibrations were performed throughout the research to ensure accuracy of the results. The full procedure is given in Appendix C.

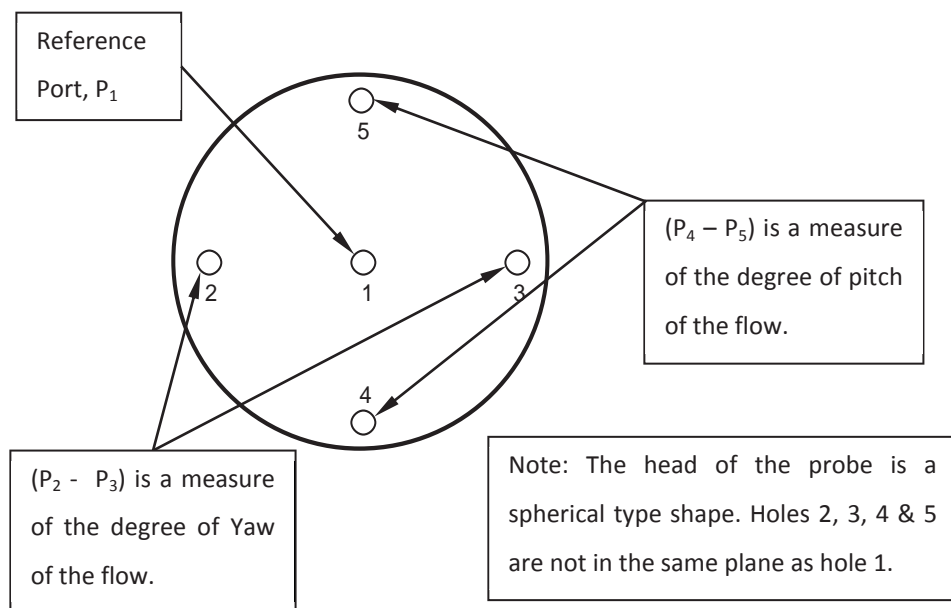


Figure 3.5. Cobra head five-hole probe

There are limitations with the five-hole probe especially when sampling pressure in a highly three-dimensional flow. Measurement difficulties are commonly encountered in highly three-dimensional flows since flow reversal is usually a part of the flow structure. Since the five-hole probe has been calibrated for a particular range, if the flow vector is beyond this range then the probe cannot provide a true measure of the local total and static pressures and therefore the flow velocity vector cannot be determined. In addition, when the probe is rotated in the pitch plane there is a noticeable effect from the stem during calibration at high pitch angles. The present work therefore, is largely concerned with formulating a set of

criteria to determine when reversal of flow is influencing the results, thereby providing a sound basis with which to analyse the results of the wake surveys and form an image of the flow structure in the wake region.

The data acquisition system for five-hole measurement, consisted of a transducer box made up of six Honeywell pressure transducers. The freestream static and total pressures were measured using a Pitot-static tube located in the test section of the wind tunnel and measured using a Furness Controls FC0510 Micromanometer. The pressure transducers were calibrated using the Micromanometer while varying the air speed of the wind tunnel. See Figure 3.6 for a typical setup. The pressure transducer box was connected to a National Instruments Type E input-output board that was then connected to a National Instruments analogue-to-digital converter card inside the computer system box. The software used to calibrate the transducers and to acquire the data was the National Instruments Labview program. Figure 3.7 shows a schematic layout of the experimental setup.



Figure 3.6. Wake traverse apparatus and instrumentation.

Research Methodologies and Apparatus

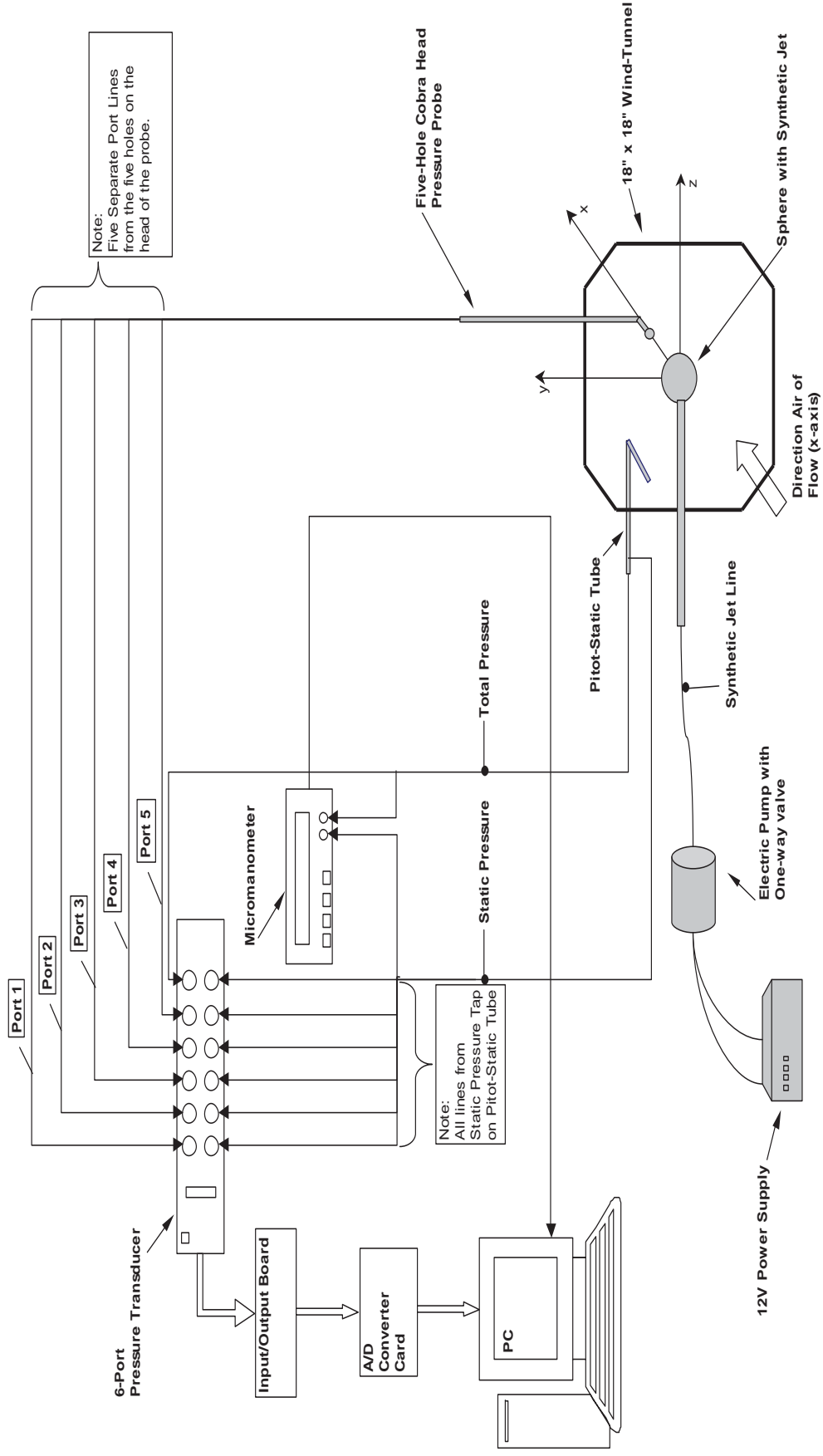


Figure 3.7. Five-hole probe data acquisition system

The five-hole probe was mounted on the topside of the wind tunnel onto a traversing mechanism that allowed the probe to be moved back and forth along the x-axis of the wind tunnel while also being able to lower and raise the probe along the y-axis of the wind tunnel. In order to facilitate measurement along the z-axis the sphere support was moved along this axis instead of moving the probe. Measurements were taken to determine if moving the sphere would give different results from those obtained by moving the pressure probe. The results showed the tunnel velocity to vary negligibly over the required measurement distance, as such moving the sphere had no significant effect.

The measurements taken were referenced to the freestream static pressure. All wake surveys were taken with and without the operation of the synthetic jet at the same set of points facilitating the comparison between cases. Furthermore, measurements were taken on the free end side of the sphere to avoid the effect of the supporting rod. The streamwise measurements were taken between  $0 < x/D \leq 3.0$ , the vertical cross-stream measurements were taken between  $-0.625 \leq y/D \leq 0.625$  and the horizontal cross-stream measurements were taken between  $0 \leq z/D \leq 0.625$ .

By rotating the sphere, the synthetic jet was located at three different locations with respect to the azimuthal angle. The initial placement was at  $6.5^\circ$  which was close to the fore stagnation point. The sphere was then rotated counter-clockwise to  $76^\circ$  which was further along the circumference of the sphere but upstream of the separation point (separation point without synthetic jet) followed by  $100^\circ$  which was well past flow separation and in the wake of the sphere.

To verify the accuracy of the measurements taken in the wake with the five-hole pressure probe as well as to aid in the formulation of the criteria for reversal of flow the velocity in the xy plane was obtained using a 1D hot-wire probe at selected sample locations in the wake region.

Further experimental wake surveys were performed on a NACA23012 airfoil, a streamlined body. The wake surveys were conducted at the same Reynolds number and at different angles of attack to ensure that separation had taken place. This then enabled us to perform wake surveys in a region with flow reversal and test the criteria for flow reversal when using a five-hole pressure probe. These results were then used to compare with the wake survey measurements taken from the sphere. Figure 3.8 below shows the setup of the NACA23012 airfoil in the wind tunnel with the five-hole probe instrumentation.



Figure 3.8. five-hole probe wake survey of NACA23012 airfoil

Physical clarification of the wake survey measurements was also sought by way of flow visualisation. This provided additional assistance in the analysis of the results to characterise the structure of the wake region and the effects of applying flow control by means of the localised synthetic jet. A grid of tufts was placed behind the sphere at different locations in the wake region corresponding to the locations of the wake survey planes.

The final phase of the experimentation was to measure the drag on the sphere using an ATI Industrial Automation Gamma SI-32-2.5 force transducer installed in the test section of the wind tunnel. The drag measurements were repeated at least ten times. This showed that the uncertainty was  $\pm 1.5\%$ .

### **3.4 Wind Tunnel testing of streamlined bodies with synthetic jet**

The localised synthetic jet was also applied to three-dimensional streamlined bodies. The experiments were carried out in the large wind tunnel at the UNSW Aerodynamics laboratory. The schematic drawing of the wind tunnel is shown in Figure 3.9. The wind tunnel has a test section size of 1219 mm (4') x 914 mm (3') in cross section and is 2970mm in length. The wind tunnel circuit has a vertical orientation with the fan drive located downstream of the test section. The 1.52 metre fan rotor is powered by a 86 kW hydraulic motor housed in the fan nacelle. The motor is driven by a 112 kW hydraulic pump with axial piston swash plate. Speed control is via servo motor fixed to the pneumatically actuated control valve that alters the swash plate angle. The servo motor is controlled by a PC with a custom designed Labview program. The test section is mechanically isolated from the tunnel circuit to prevent the transmission of any vibration. Turbulence is controlled throughout the circuit. There are four (4) flow straightening screens upstream of the test section and bellmouth contraction inlet that smoothly changes from the octagonal cross section to the chamfered rectangular test section. The side panels in the test section are constructed from Perspex to enable flow visualisation. The freestream turbulence intensity in the test section is approximately 0.3%.

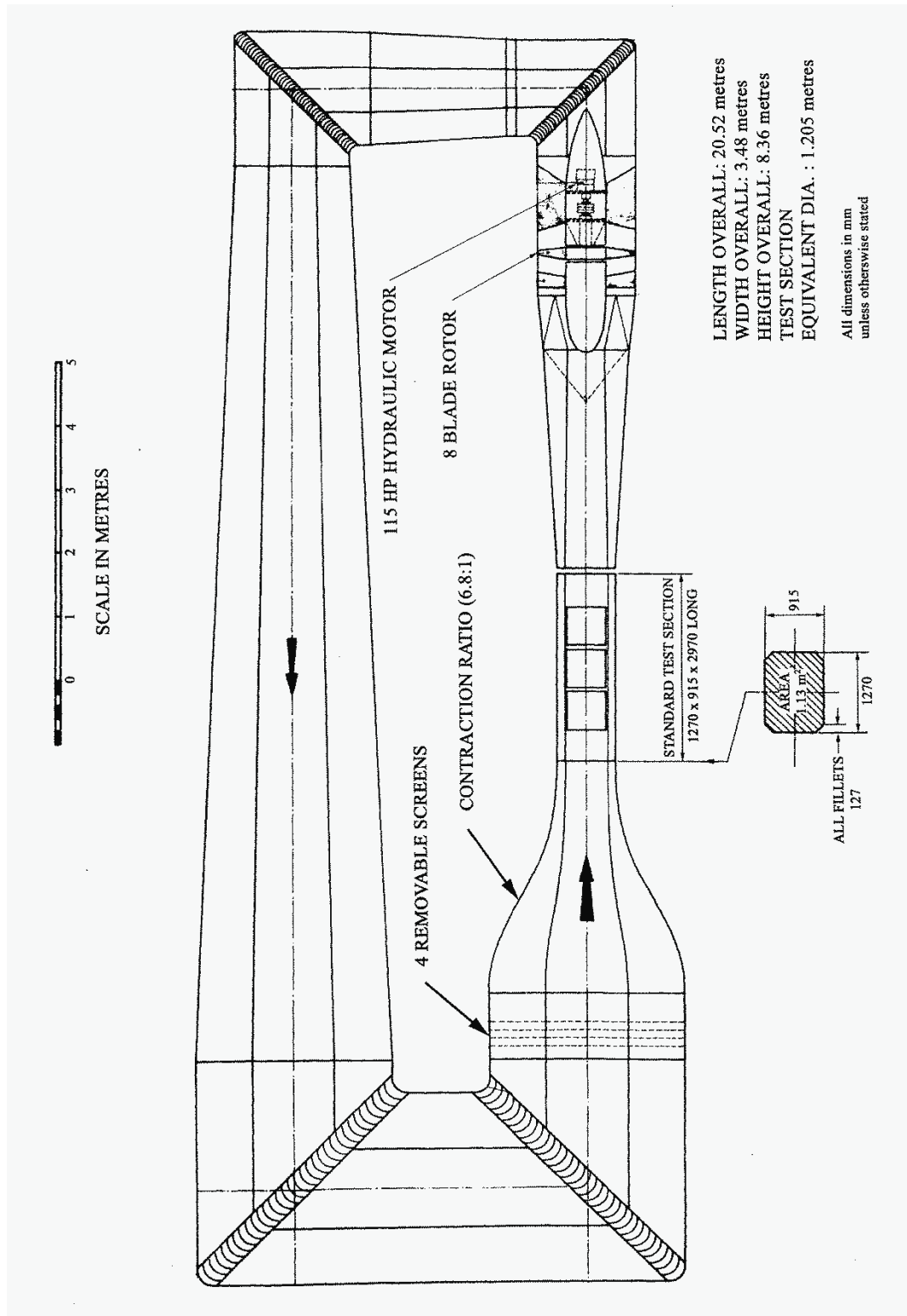


Figure 3.9. Large Wind tunnel: 1219 mm x 914 mm

The velocity of the synthetic jet was measured using A Dantec Streamline CTA Anemometer system with a 55P14 probe. The probe was calibrated using the Dantec Flow Calibration System. The velocity profile corresponding to synthetic jet is shown in Figure 3.10. The maximum velocity was 45 m/s and the frequency of actuation was 50 Hz.

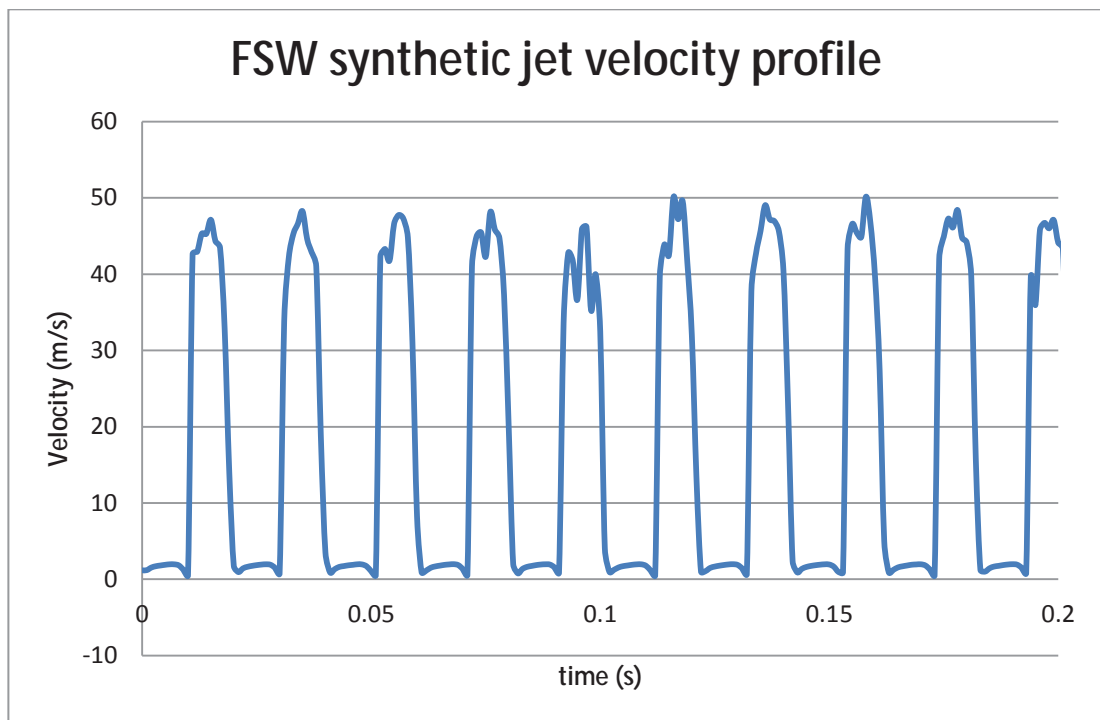


Figure 3.10. Forward swept wing (FSW) synthetic jet velocity profile.

Initial experiments were conducted on a cut-off rectangular wing based on the four digit symmetrical airfoil, NACA-0012. The wing was designed on CATIA three-dimensional modelling software and then CNC machined from Aluminium to the required profile with pressure tappings placed near the wing tip as part of a synthetic jet angle optimisation study to reduce wing tip vorticity and inhibit flow separation near or on the airfoil stall angle. The measuring station was at located at 165mm from the wing root with the total length of the wing being 185mm. The synthetic jet orifices were 1 mm in diameter and located 15% and 50% of the chord

length from the leading edge. The side of the wing (upper side) with the synthetic jet orifices had 12 pressure tapings equally spaced and the opposite side had 15 pressure tapings (lower side). A schematic of the NACA-0012 wing is shown in Figure 3.11.

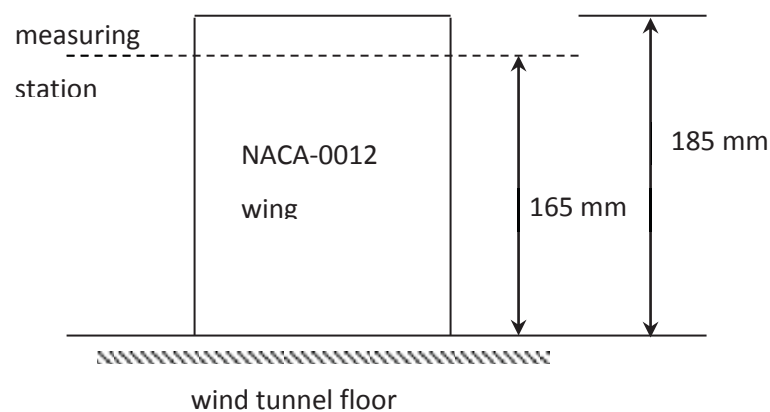


Figure 3.11. Schematic setup of NACA-0012 wing.

The experiments on the NACA-0012 airfoil allows a determination of the effectiveness of an asymmetrical localised synthetic jet on symmetrical streamlined body. Further the optimal angle from the these trials will then be used on the subsequent experiments performed on a swept wing.

The following aspect of experimental work on streamlined bodies was then advanced to a forward swept wing (FSW) based on the outline NASA's X-29 experimental aircraft (Curry 2009). The airfoil profile was not supercritical as in the case of the X-29 wing airfoil profile since it was not suitable for the subsonic experiments conducted in this thesis research. As such a more suitable profile that

has already been used in previous experimental work (Kim and Kim 2006) was used, the five digit NACA-23012 airfoil.

The forward swept wing provides advantages for the present research that conventional swept wings lack. These advantages are described in the overview of chapter 7. The wing was designed using the CATIA modeling software and manufactured from Renshape. This material is a polyurethane based plastic that with good machinable accuracy and toughness. The material is easily machined and can be sanded to the required surface finish and can be modified for unforeseeable changes. The wing tip used was rounded and streamline profiled. The wing was prepared with five stations of pressure tappings along the span of the wing. Figure 3.12 shows a schematic of the wing with each labeled line indicating a measuring station with pressure tapping and the synthetic jet nomenclature. Table 3.1 lists the chord lengths at each measuring station and Table 3.2 gives the synthetic jet locations.

Measuring Station	Chord length (mm)
0 (wing tip)	158
1	168
2	210
3	255
4	309
5	405

Table 3.1. Chord lengths of each measuring station

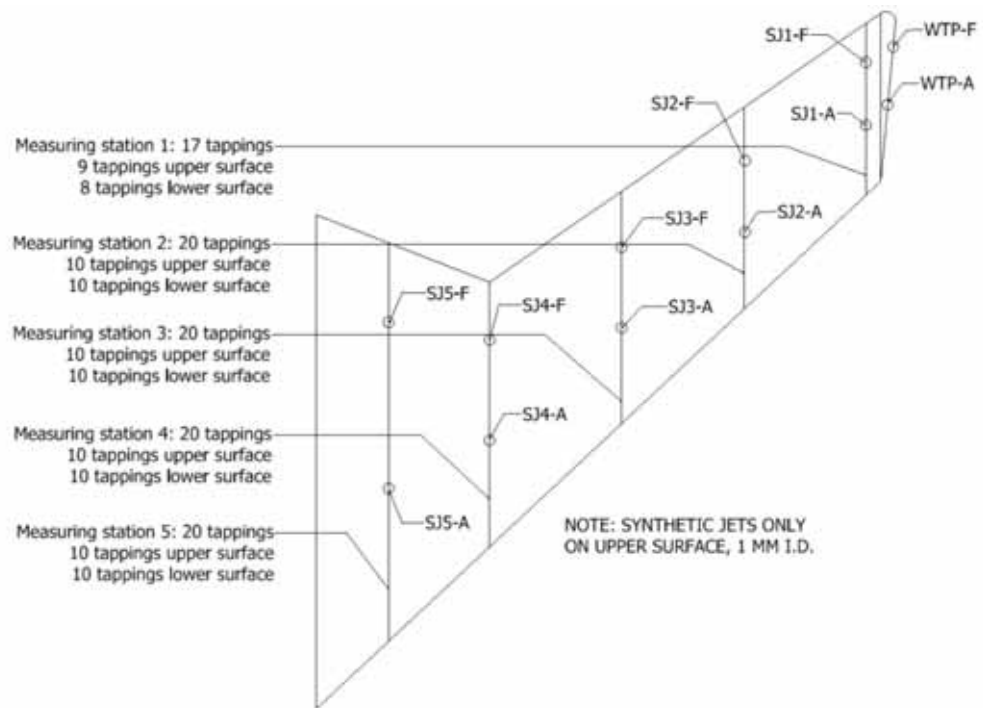


Figure 3.12. Forward swept wing. Measuring stations are indicated by the chord at each spanwise location. Also shown and labeled are synthetic jet orifices.



Figure 3.13. Forward swept wing with NACA-23012 profile.

Synthetic jet orifice	Distance from wing root mm	Distance from leading edge mm	x/c %
WTP-F	490	30	19.0
WTP-A	485	85	53.8
SJ1-F	460	53	31.5
SJ1-A	460	109	64.9
SJ2-F	350	64	30.5
SJ2-A	350	137	65.2
SJ3-F	235	75	29.4
SJ3-A	235	163	63.9
SJ4-F	125	113	36.6
SJ4-A	125	200	64.7
SJ5-F	65	136	33.6
SJ5-A	65	275	67.9

Table 3.2. Synthetic locations.

There is a small blockage effect of 5.1% (Barlow, Rae Jr and Pope 1999) at an AOA of  $20^\circ$  that does not significantly influence the measured parameters. Further details about blockage can be found in Appendix B.

### 3.5 Computational methodologies for numerical simulation of the side supported sphere

#### 3.5.1 Fluid domain setup

This computational investigation has been conducted in a three-dimensional space domain. The solid model was constructed using commercially available CAD software. This was then modified using the same software to produce the fluid volume for the side-supported as shown below in Figure 3.14.

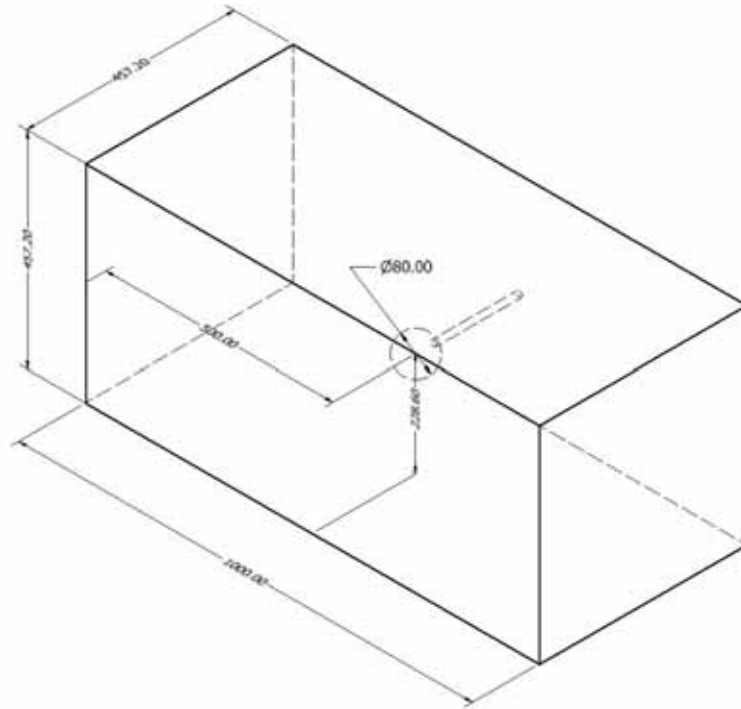


Figure 3.14. Fluid domain of side-supported sphere.

### 3.5.2 Side-supported sphere modelling and governing equations

The results of the computational simulation for the side supported sphere was compared and validated against physical experiments performed in the experimental phase of the research (Findanis & Ahmed, 2008; Findanis & Ahmed, 2011). The fluid domain was constructed based on the dimensional measurements of the side-supported sphere in the 457 mm x 457 mm wind tunnel used at the UNSW Aerodynamics Laboratory. The inlet boundary condition for the fluid domain is 10 m/s in the global streamwise direction or the Cartesian vector  $U$  which in this case was the x-axis. The other global Cartesian axes of  $V$ ,  $W$  were set to zero. The Reynolds number, equation (3-2),  $5.2 \times 10^4$  is based upon the freestream velocity  $U_\infty$  and the diameter of the sphere which is 80 mm.

$$\text{Re} = \frac{\rho_\infty U_\infty D}{\mu_\infty} \quad (3-2)$$

Flow simulations were performed with and without the no-slip condition on the test section walls. A comparison of the results showed that the choice of boundary conditions was negligible on the aerodynamic flow around the side-supported sphere. This supports the experimental results which show that the small blockage effect of 2.8% (Barlow, Rae Jr and Pope 1999) does not significantly influence the measured parameters.

A fundamental parameter used to compare the experimental with the computational results was the surface pressure distribution,  $C_p$ . The pressure coefficient is defined in the usual manner as the ratio of the difference in static pressure at a point,  $p$  and the freestream static pressure,  $p_\infty$  and the freestream dynamic pressure,  $q_\infty$ .

$$C_p = \frac{p - p_\infty}{q_\infty} = 1 - \left( \frac{V}{V_\infty} \right)^2 \quad (3-3)$$

The three-dimensional governing equations for the flow of an incompressible fluid are solved. These are, namely the unsteady Reynolds Averaged Navier-Stokes (RANS) equations. The conservation of mass and momentum equations are shown as equations (3-4) and (3-5).

$$\nabla \cdot \bar{\mathbf{u}} = 0 \quad (3-4)$$

$$\rho \frac{\partial \bar{\mathbf{u}}}{\partial t} + \rho \bar{\mathbf{u}} \cdot \nabla \bar{\mathbf{u}} = -\nabla \bar{p} + (\mu + \mu_t) \nabla^2 \bar{\mathbf{u}} \quad (3-5)$$

The simulation is conducted as a transient flow analysis for all cases with and without the synthetic jet applied. The transient scheme used is second order backward Euler for the discretisation of the transient term. A high resolution upwind advection scheme with third order spatial accuracy is used to calculate the advection terms. High resolution turbulence numerics based on the advection and

transient scheme is used in the turbulence modelling (Bardina, Huang and Coakley 1997). The turbulence model used to calculate the averaged turbulent stresses is based on Menter Shear Stress Transport (SST) two-equation model (Menter 1993) being the most suitable when flow separation occurs in the flow field.

### 3.5.3 Actuator Modelling

The synthetic jet orifice was constructed based on the physical model used in the laboratory experiments (Findanis & Ahmed, 2008). The oscillatory flow generated by the synthetic jet out of a circular orifice is modelled as a boundary condition located at the base of the synthetic jet cavity. The synthetic jet flow has been defined as an opening boundary condition that allows fluid to cross the boundary in any direction. A local coordinate system was defined such that the velocity is normal to the synthetic jet boundary, the positive direction being out of the cavity. To model the synthetic jet motion, a velocity expression was defined on the boundary based on the experimentally measured synthetic jet velocity using hot-wire instrumentation. The harmonic relationship of the synthetic jet is given by:

$$\begin{aligned}\bar{u}_n(t) &= U_{\max} \sin(\omega t) \\ \text{where } \omega &= 2\pi f \\ U_{\max} &= 35 \text{ m/s} \\ f &= 60 \text{ Hz} \\ \rightarrow \bar{u}_n(t) &= 35 \sin(120\pi t)\end{aligned}\tag{3-6}$$

Where  $\bar{u}_n$  denotes the normal velocity to the synthetic jet boundary. The synthetic jet was measured to have maximum velocity in the local streamwise direction of 35 m/s at an actuation frequency of 60 Hz. These figures were derived from the hot-wire data that are plotted in Figure 3.4. Since it is not possible to place the hot-wire

instrumentation into the synthetic jet cavity the suction peak is shown to be much less than the blowing peak.

The velocity of the synthetic jet was plotted from the CFD simulation according to relation derived in (3-6) with the influence of the 10 m/s cross flow. The velocity (m/s) versus time step is shown in Figure 3.15.

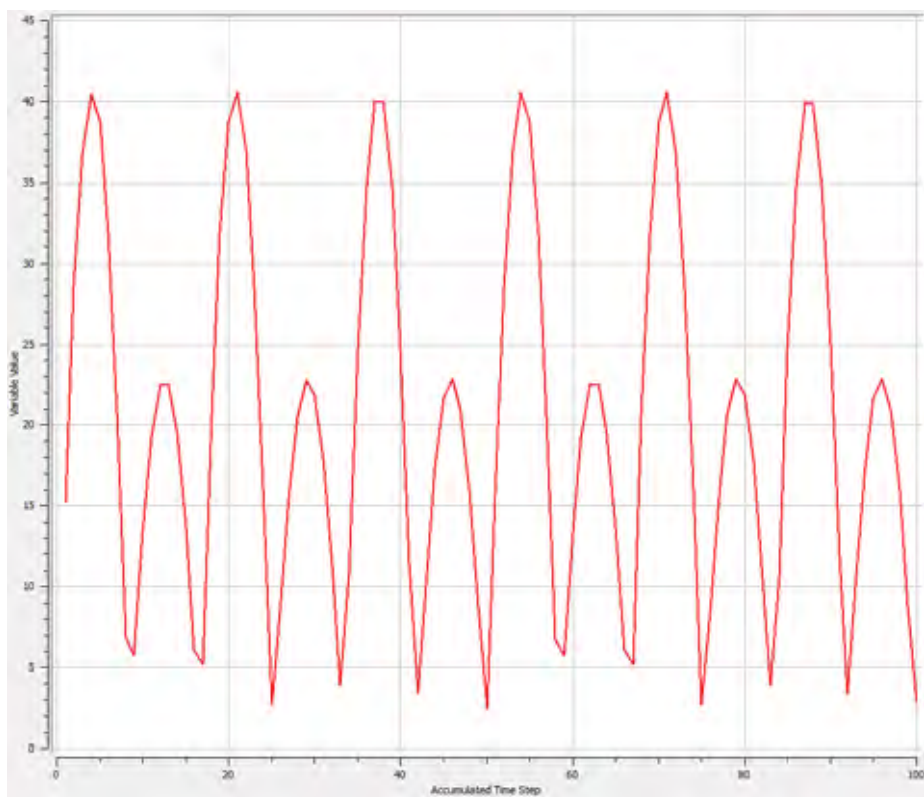
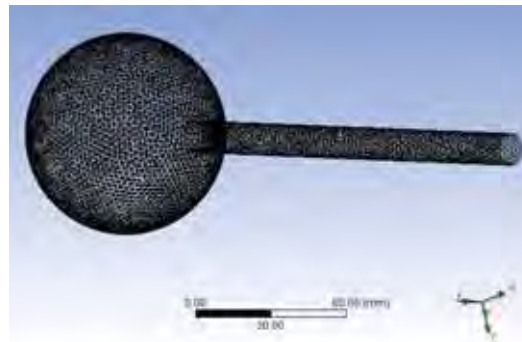


Figure 3.15. CFD synthetic jet velocity.

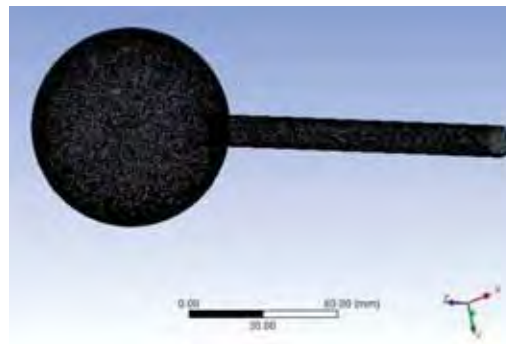
### 3.5.4 Grid-independence study and validation

The grid was generated using the ANSYS CFX mesher based on an unstructured approach. The mesh is based on a patch conforming tetrahedral method with inflation on the relevant surfaces. The mesh has been created with particular attention to sizing on the side-supported sphere, synthetic jet and wake region to capture the flow physics. Further many trials were performed with the configuration of the inflation layers to ensure the separation of flow is captured with the SST turbulence model.

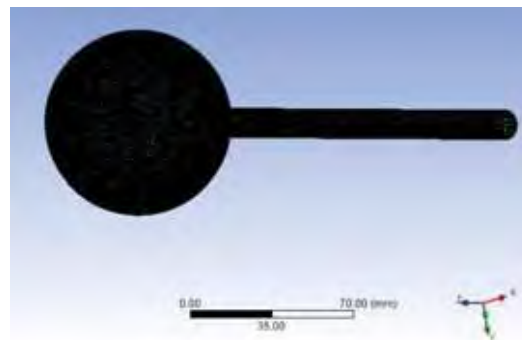
An example is shown of the mesh on the side-supported sphere at three different mesh densities as can be seen in Figure 3.16.



(a)



(b)



(c)

Figure 3.16. Side-supported sphere mesh. a) mesh 1, b) mesh 2 and c) mesh 3

The hard sizing was used on the support-sphere body to enable uniform inflation to be created around this whole part with good quality to reduce skewness. The area behind this part was also sized accordingly to capture the flow field characteristics in the transient analysis. Thus a body of influence was used to achieve mesh refinement in this region. The synthetic jet cavity was included in the inflationary method to ensure the counter rotating vortices would be realised together with a top hat velocity profile across the synthetic jet boundary. It should be noted that the fluid domain around the side-supported sphere is not shown for clarity although this region also was meshed with a good quality mesh.

A grid independence study was conducted to ensure an accurate solution to the CFD analysis. This was conducted using the three different mesh densities as partially shown in Figure 3.16. The Reynolds number was  $5 \times 10^4$  as per the previous experimental study (Findanis & Ahmed, 2008). Table 3.3 shows a comparison of the drag coefficient on the side-supported sphere with no synthetic jet applied. The results show that a maximum difference in drag coefficient of 2.1% occurs between the three grid densities. Notice that with mesh 3 the  $C_D$  actual decreased slightly indicating that there is possibly no increased benefit by using the very fine mesh. This suggested grid independence of the results obtained and thus to maintain the integrity of the solution mesh 2 would be used in the present work.

Mesh	Grid size (nodes)	$C_D$
1	220833	0.5617
2	899757	0.5739
3	2274221	0.5726

Table 3.3. Grid independence using  $C_D$ .

The CFD simulation was compared to the results obtained from the force balance as conducted by previous researchers (Findanis & Ahmed, 2008). The side-supported sphere with no synthetic jet showed a difference of 10.2% with the experimental result. Since the present work will be using the no synthetic jet case as the basis to compare results with the synthetic jet actuated, this result is within an acceptable level of error for validation.

It was required to model the oscillatory flow resulting from the actuation of the synthetic jet on the sphere at the three different angles of incidence corresponding to the laboratory experimental work conducted previously. Although the synthetic jet has been modelled by various methods computationally and the method used in the present is not unique it has not been applied in this way using the commercial CFD software package ANSYS CFX.

### **3.6 Computational methodologies for numerical simulation of the forward swept wing**

#### **3.6.1 Fluid domain setup**

The solid model was constructed using CATIA modelling software. This was then modified using the same software to produce the fluid volume for the side-supported as shown below in Figure 3.17.

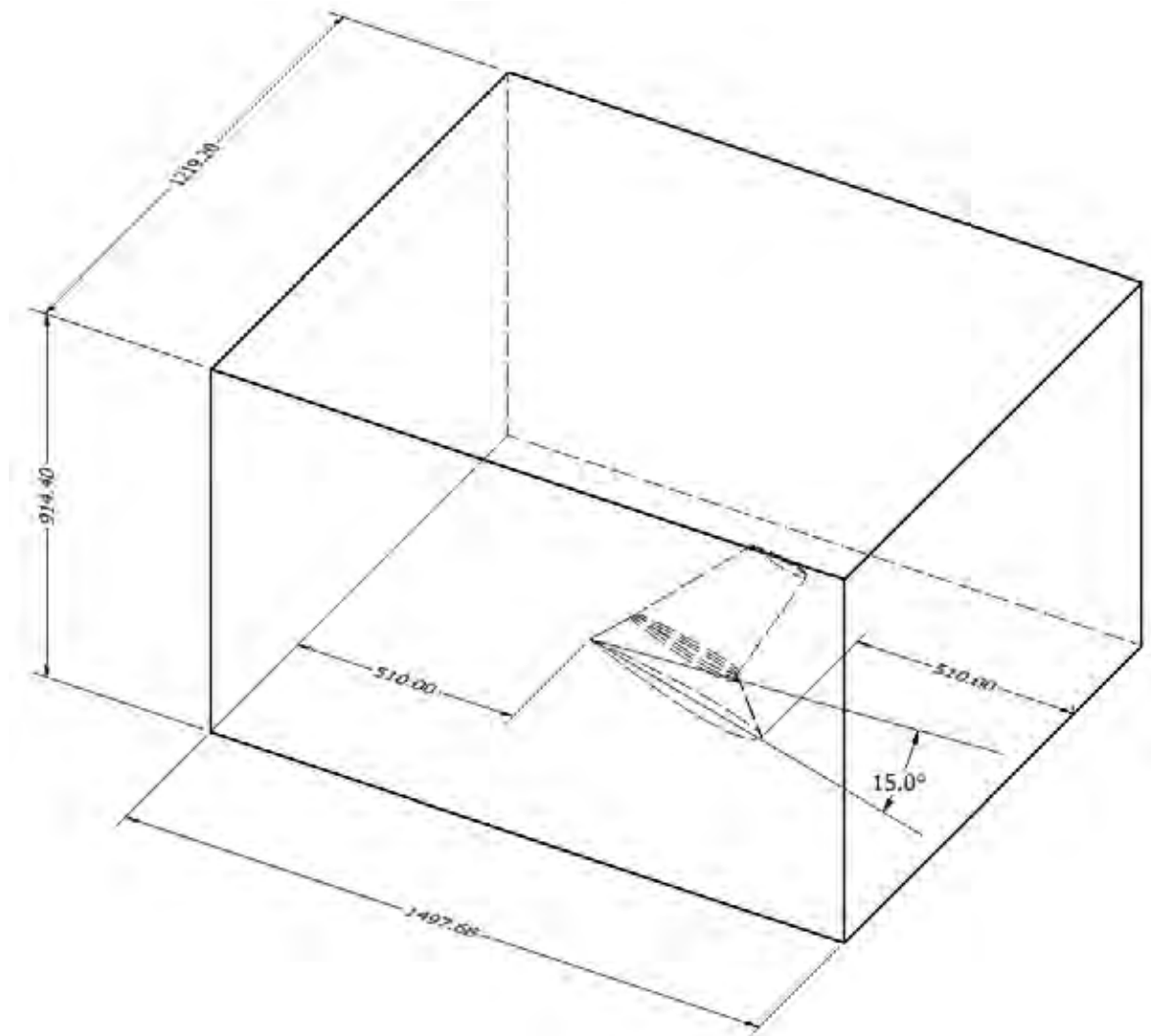


Figure 3.17. Fluid domain for FSW, at  $15^\circ$  AOA.

### 3.6.2 FSW modelling and governing equations

The results of the computational simulation for forward swept wing was compared and validated against physical experiments performed in this research work. The fluid domain was constructed based on the dimensional measurements of the FSW in the 1219 mm x 914 mm wind tunnel used at the UNSW Aerodynamics Laboratory. The inlet boundary condition for the fluid domain is 10 m/s in the global streamwise direction or the Cartesian vector  $U$  which in this case was the x-axis. The

other global Cartesian axes of  $V, W$  were set to zero. The Reynolds number  $3.3 \times 10^5$  is based upon the freestream velocity  $U_\infty$  and the reference chord length which is 500 mm.

The three-dimensional governing equations for the flow of an incompressible fluid are solved namely the unsteady Reynolds Averaged Navier-Stokes equations. The details are shown in section 3.5.2

### 3.6.3 Actuator Modelling

The physics setup of the computational modelling is identical to that of the bluff body given section 3.5.3. To model the synthetic jet motion a velocity expression was defined on the boundary based on the experimentally measured synthetic jet velocity using hot-wire instrumentation. The harmonic relationship of the synthetic jet is given by equation (3-7):

$$\bar{u}_n(t) = U_{\max} \sin(\omega t)$$

where  $\omega = 2\pi f$

$$U_{\max} = 45 \text{ m/s}$$

$$f = 50 \text{ Hz}$$

$$\rightarrow \bar{u}_n(t) = 45 \sin(100\pi t)$$
(3-7)

Where  $\bar{u}_n$  denotes the normal velocity to the synthetic jet boundary. The synthetic jet was measured have maximum velocity in the local streamwise direction of 45 m/s at an actuation frequency of 50 Hz. These figures were derived from the hot-wire data that is plotted in Figure 3.10. Since it is not possible to place the hot-wire

instrumentation into the synthetic jet cavity the suction peak is shown to be much less than the blowing peak.

The velocity of the synthetic jet was plotted from the CFD simulation according to relation derived in (3-6) with the influence of the 10 m/s cross flow. The velocity (m/s) versus time step is shown in Figure 3.18.

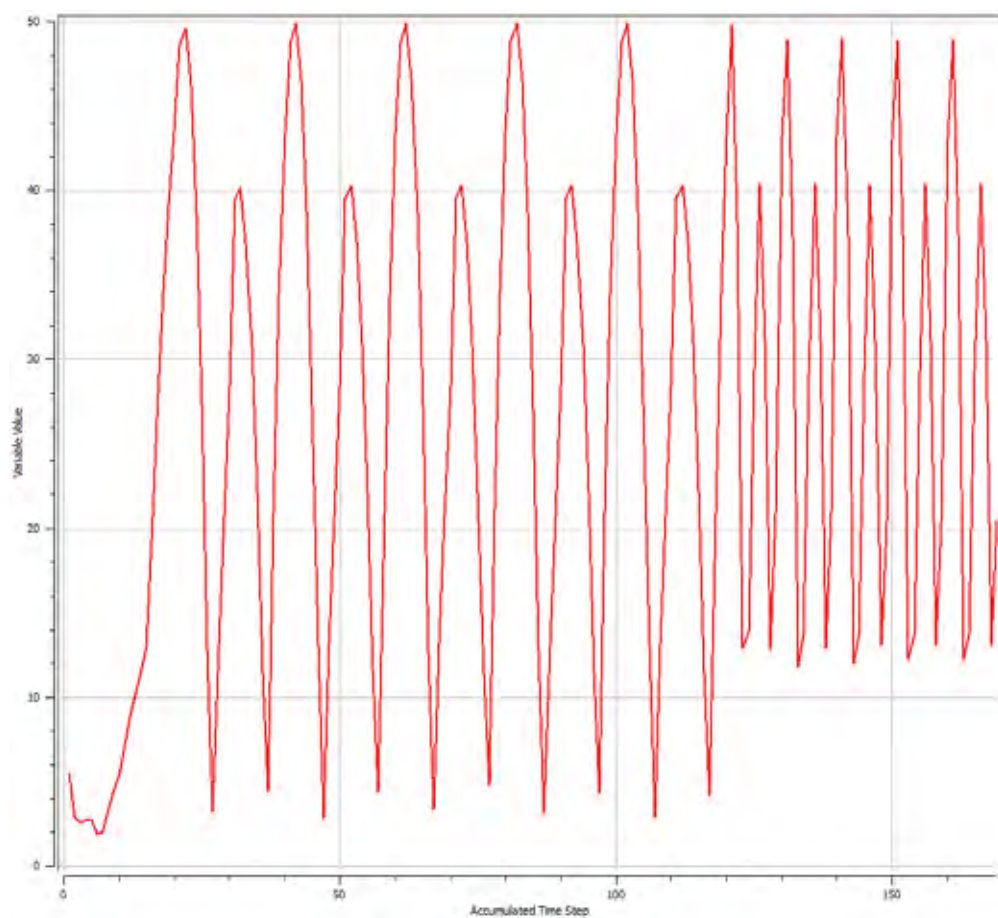
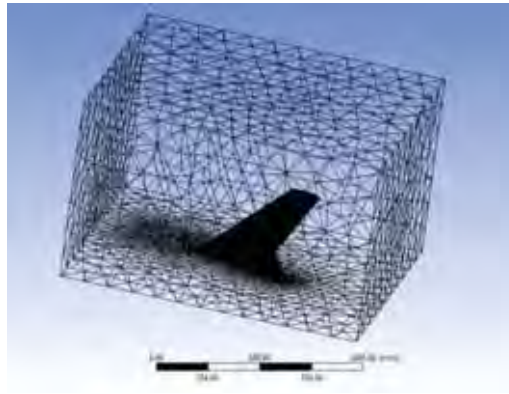


Figure 3.18. CFD synthetic jet velocity.

### 3.6.4 Grid-independence study and validation

The grid was generated using the ANSYS CFX mesher based on an unstructured approach. The mesh is based on a patch conforming tetrahedral method with inflation on the relevant surfaces. The mesh has been created with particular attention to sizing on the wing, synthetic jet and wake region to capture the flow physics. Further trials were performed with the configuration of the inflation layers to ensure the separation of flow is captured with the SST turbulence model.

An example is shown of the mesh on the side-supported sphere at three different mesh densities as can be seen in Figure 3.19.



(a)



(b)



(c)

Figure 3.19. FSW mesh. a) mesh 1, b) mesh 2 and c) mesh 3

The sizing control was used on the wing to enable sufficient inflation to be created around the whole part with good quality to reduce skewness. The area behind the wing was also sized accordingly to capture the flow field characteristics in the transient analysis. Thus a body of influence was used to achieve mesh refinement in this region. The synthetic jet cavity was included in the inflationary method to ensure the counter rotating vortices would be realised together with a top hat velocity profile across the synthetic jet boundary.

A grid independence study was conducted to ensure an accurate solution to the CFD analysis. This was conducted using the three different mesh densities as partially shown in Figure 3.19. Table 3.4 shows a comparison of the drag force on the wing at 15° AOA with no synthetic jet applied. The results show that a deviation of 0.9% occurs between grid densities 2 and 3 demonstrating grid independence.

Mesh	Grid size (nodes)	Drag force (N)
1	263657	1.521
2	450467	1.397
3	899609	1.385

Table 3.4. Grid independence using drag force.

The CFD simulation was compared to the results obtained from the force balance as conducted previously. The wing with no synthetic jet at 15° AOA showed a difference of 15.3% with the experimental result. Since the present work will be using the no synthetic jet case as the basis to compare results with the synthetic jet actuated, this result is within an acceptable level of error for validation.

### **3.7 Experimental Accuracy and Repeatability**

The reliability and accuracy of the laboratory experimental results were dependent on the experimental equipment and instrumentations used to obtain the data. The results have been statistically analysed to determine the uncertainty contained in the various experiments conducted at different stages of the research. The analysis is based on methods contained in Devore (1995).

#### **3.7.1 Pressure Measurement**

The accuracy of the pressure measurement was dependent on the combined error of the five-hole pressure probe used in the wake surveys, the Pitot-static tube for the wind tunnel speed and the instruments transducers. Low pressure Honeywell transducers were used for the measurements off the five-hole probe and the Furness Controls Micromanometer was used for the pressure taps and wind tunnel speed.

The accuracy is  $\pm 2.5\%$  with an uncertainty of  $\pm 0.01$ .

#### **3.7.2 Force Balance**

The force balance was used on both wind tunnels. The 457 mm x 457 mm wind tunnel used the ATI Force: Gamma multi-axis load cell and the 1219 mm x 914 mm wind tunnel has a custom made force balance rig.

For the ATI Gamma F/T sensor the accuracy is 0.05% with an uncertainty of  $\pm 0.01$ .

For the force balance rig (drag) on the 1219 mm x 914 mm wind tunnel the accuracy is 0.01% for an uncertainty of  $\pm 0.001$ .

### 3.7.3 Hot wire measurement system

The hot wire measurements were performed with the Dantec Streamline hardware and software. Several wake surveys were repeated to measure the uncertainty of the data acquisition system.

The accuracy is 0.001% with an uncertainty of  $\pm 0.3$ .

---

## Chapter 4

Results and Discussion:  
Bluff Body

---

## 4. Results and discussion: Bluff body

In the present Chapter it will be shown that a localised synthetic jet can achieve significant aerodynamic improvement on the flow over a three-dimensional bluff body by delaying flow separation and reattachment and reducing drag without triggering flow instability frequencies, but rather through the input of momentum to the flow. Furthermore, it will be demonstrated, that a localised synthetic jet has the ability to modify the flow over a sphere a substantial distance away from the point source in all three dimensions. The asymmetrical location of the synthetic jet on the sphere body will induce these three dimensional changes enhancing the effect of localising the synthetic jet as opposed to a distributed or symmetrically located synthetic jet. The asymmetry will also prove useful in relation to the side support of the sphere body and whether it will improve flow around this flow disturbance. This work on the asymmetrical location of a synthetic jet will prove to be most beneficial in generating lift not only on bluff bodies but more importantly on streamlined lifting bodies. Also of interest is to determine whether the localised synthetic jet will generate a separation bubble such as that observed in other recent applications of distributed synthetic jet.

## 4.1 The theoretical coefficient of pressure on the surface of a sphere

An attempt was made to compare the experimental value with the theoretical value of  $C_p$  (pressure coefficient) at each of the tappings for the no-jet condition. With reference to Figure 4.1, the static pressure at a point on a sphere (Pisasale and Ahmed, 2002; and Pisasale and Ahmed, 2004) is given by:

$$p(\theta) = p_\infty + \frac{9}{4} q_\infty \cos^2 \theta - \frac{5}{4} q_\infty \quad (4-1)$$

Re-arranging the above equation and using the geometrical relation that  $\cos \theta = \cos \alpha \cos \beta$  and dividing by the dynamic pressure  $q_\infty$ , the following expression for  $C_p$  was obtained:

$$C_{p,1,2,\dots}(\alpha, \beta) = \frac{9}{4} \cos^2 \alpha \cos^2 \beta - \frac{5}{4} \quad (4-2)$$

$$\text{where, } \cos^2 \alpha = \sin^2 \gamma + \cos^2 \gamma \cos^2 \phi \quad (4-3)$$

$$\text{and, } \cos^2 \beta = 1/(A+1) \quad (4-4)$$

$$\text{where, } A = (\sin^2 \gamma) / (\cos^2 \gamma \cos^2 \phi)$$

Here  $\alpha$  was measured from the horizontal centre plane whereas angles  $\beta$  and  $\gamma$  were measured from the vertical centreline of the sphere. Note that  $0^\circ \leq \phi \leq 180^\circ$ , which was the rotation of the sphere about its horizontal axis passing through the sting support or the z-axis. As the sphere was rotated through the range  $\phi = 0^\circ$  to  $\phi = 180^\circ$  each pressure tapping circumscribed a semicircle and the path of each tapping represented a particular slice through the sphere as it was rotated through  $\phi$ . The variation in pressure coefficient in a two-dimensional sense could thus be

examined as a function of  $\phi$ , while in a three-dimensional sense as a function of  $\theta$ , which was the angular displacement from the stagnation point and was a function of the angles  $\alpha$  and  $\beta$ .

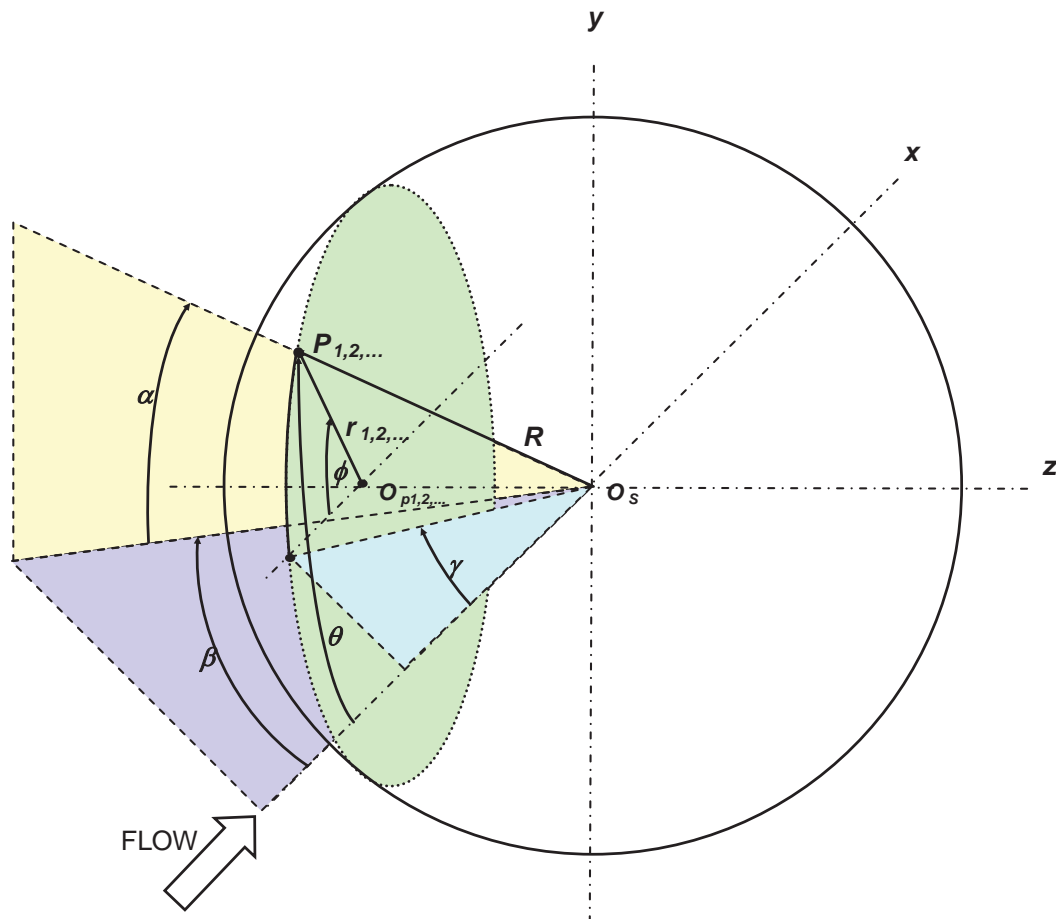


Figure 4.1. Analysis of surface pressure on the sphere.

## 4.2 The two- and three-dimensional effect of the localised synthetic jet

Figure 4.2 shows the pressure coefficients for pressure tapping or port No. 3. Port 3 is offset  $10^\circ$ , that is,  $\gamma = 10^\circ$ . The potential flow curve obtained was similar to that of

a cylinder with the experimental and theoretical curves at the front stagnation point coinciding at  $0^\circ$  to the same value. The  $C_p$  curve showed good agreement between the experimental results without and with synthetic jet and the theoretical potential flow curve at low angles. Notably in Figure 4.3, the curve began from  $\theta = 10^\circ$  since port 3 had a  $10^\circ$  offset to begin with and ended at  $\theta = 170^\circ$  for the same reason. This offset applied to all ports with their respective angular offsets. As the sphere was rotated through higher angles of  $\theta$ , the flow began to deviate from the potential flow curve at approximately  $\theta = 27^\circ$ . This is to be expected since the boundary layer is thin near the front stagnation point but gradually thickens and eventually separates (Clift et al, 1978).

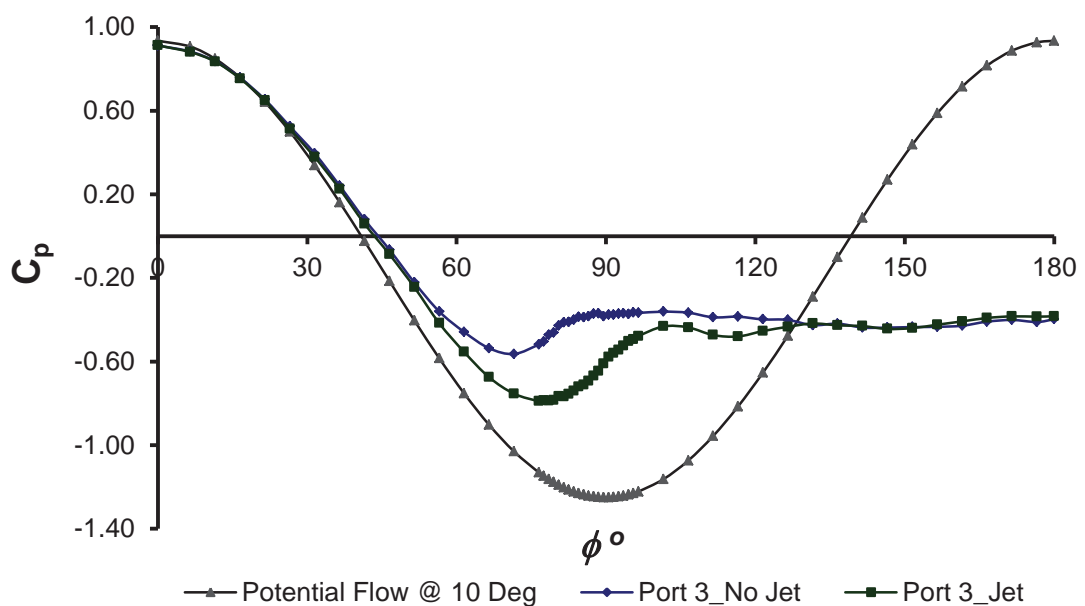
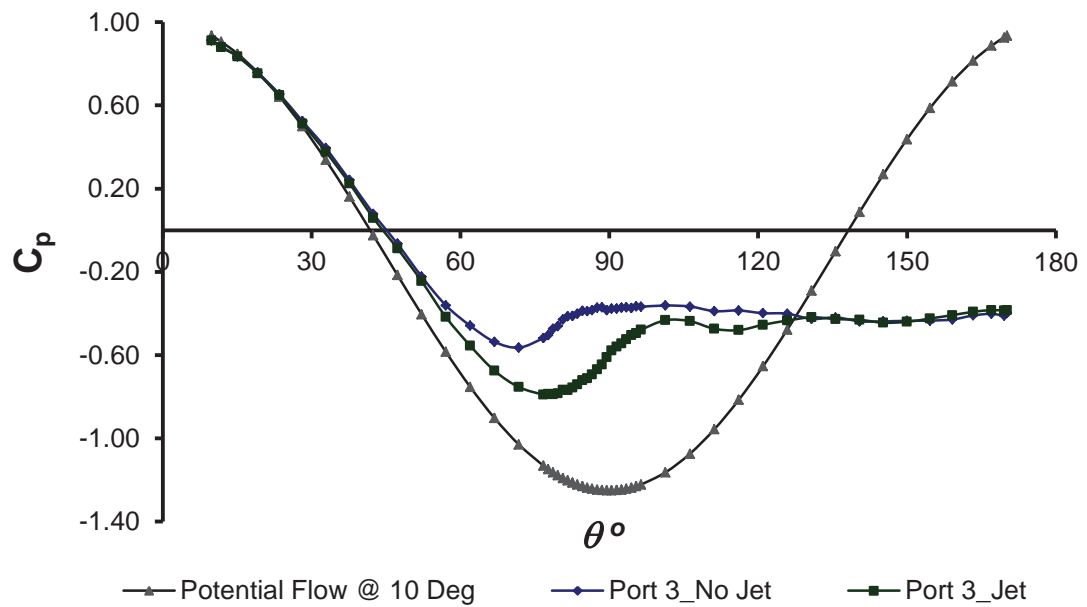
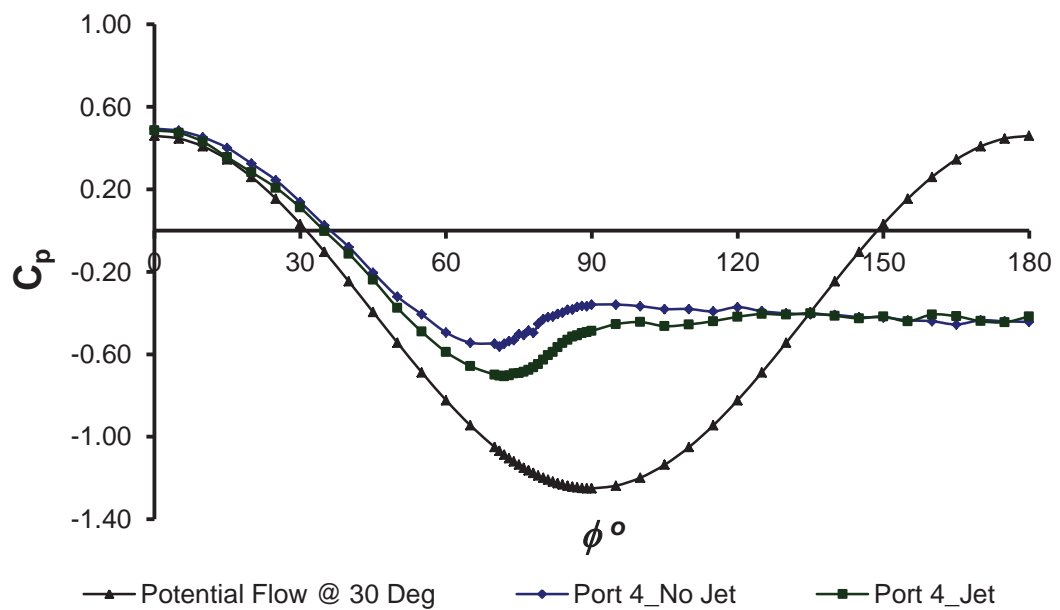
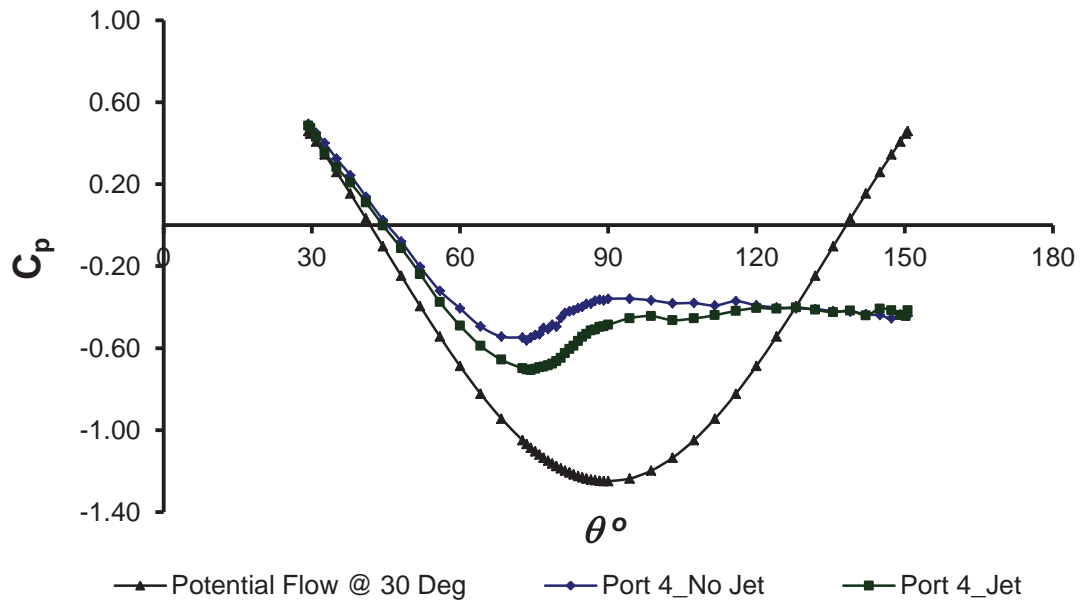
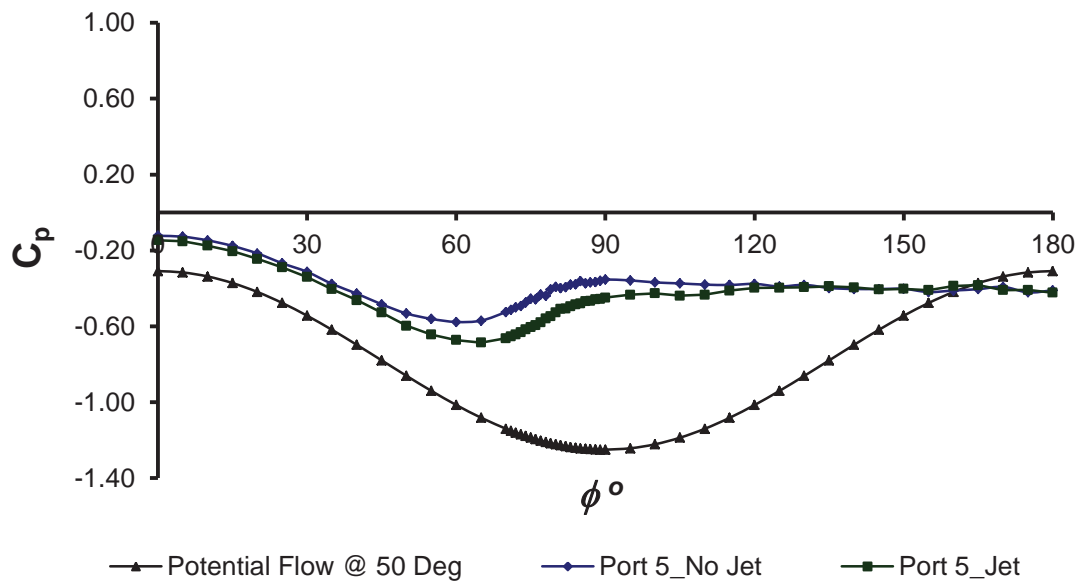


Figure 4.2. Pressure-Coefficient for port 3 with respect to  $\phi$ .

Figure 4.3. Pressure-Coefficient for port 3 with respect to  $\theta$ .Figure 4.4. Pressure-Coefficient for port 4 with respect to  $\phi$ .

Figure 4.5. Pressure-Coefficient for port 4 with respect to  $\theta$ .Figure 4.6. Pressure-Coefficient for port 5 with respect to  $\phi$ .

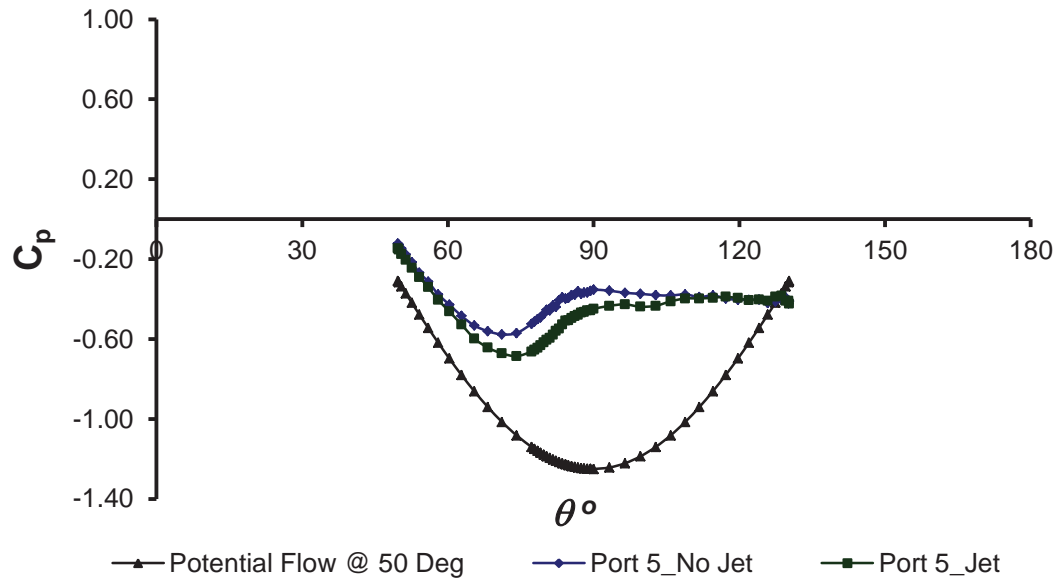


Figure 4.7. Pressure-Coefficient for port 5 with respect to  $\theta$ .

Table 4.1 shows this deviation from potential flow theory. As mentioned above port 3 is less than  $27^\circ$  offset and therefore does not show any initial deviation from potential flow theory. Port 1 and port 2 do show deviation and more so than their symmetrically opposite pair, port 5 and port 4 respectively, because of the effect of the sting support which will be discussed in more detail. Port 6 and port 7 are very close to flow separation and an escalation of the rate of deviation is observed.

Percentage Deviation from Potential Flow		
Port No.	$\gamma$	%
1	50	22.0
2	30	20.0
3	-10	0.0
4	-30	3.3
5	-50	10.0
7	-70	20.0
6	-80	32.5

Table 4.1. Potential flow deviation.

The synthetic jet begins to influence the flow characteristics over the sphere at  $\theta = 17^\circ$  but the deviation is small. The synthetic jet is most effective between  $\theta = 45^\circ$  and  $\theta = 130^\circ$ . It is within this range that the boundary layer grows considerably in size and subsequently causes the build-up of an adverse pressure gradient, which induces the reversal of flow that eventually results in flow separation. Thereafter flow separation enters the wake region of the sphere. When the synthetic jet is in this range of between  $\theta = 45^\circ$  and  $\theta = 130^\circ$  it has the capability to delay flow separation through the input of momentum to the flow and reattach flow already separated in the wake region on a three-dimensional bluff body. Figure 4.2 through to Figure 4.7 provide the evidence that the effect of the synthetic jet is to delay flow separation and reattach the flow. Every  $C_p$  distribution plot in Figure 4.2 through to Figure 4.7 shows the same trend when the synthetic jet is activated, the surface pressure is altered with a shift towards the potential flow curve. Further to this they provide even more clarity as to the extension of the separation line with the actuation of the synthetic jet. The first plot Figure 4.2 shows the surface pressure distribution of potential flow theory with the second plot showing the surface pressure distribution of the sphere with no synthetic jet. Of course potential flow theory does not show a line of separation, although the line of separation in this second plot would be indicated when the change in surface pressure coefficients becomes almost zero. This happens approximately when the  $C_p$  reaches a value of -0.39 corresponding to an angle of  $\theta = 83^\circ$ . With the activation of the synthetic jet this value changes to approximately -0.43 corresponding to a maximum angle of approximately  $\theta = 120^\circ$ . In addition, Figure 4.2 through Figure 4.7 show subtle evidence of the creation of a separation bubble after which we see reattachment of the flow. The separation bubble would seem to be located at the point on the plots where the synthetic jet curve has a very small plateau like region. For example in Figure 4.3 the separation bubble would be seem to be formed at approximately when  $\theta = 81^\circ$ . Figure 4.6 and Figure 4.7 show the formation of the separation bubble to be at approximately when  $\theta = 86^\circ$ . The work of Jeon et al. (2004) also

showed the formation of a separation bubble, although since the synthetic jet in that case was distributed around the circumference of the sphere as opposed to a localised synthetic jet in this case the plateau effect of the separation bubble in the surface pressure distribution was more pronounced. Another possibility as to the formation of the separation bubble could be due to flow transition, as indicated by the Reynolds number of the flow, and thus the synthetic jet was providing momentum to stabilize the bubble according to the published results of Jeon et al (2004). It is interesting to note that at the critical Reynolds number of about  $3.5 \times 10^5$ , laminar separation occurs at  $\theta \cong 100^\circ$  followed by reattachment at  $\theta \cong 117^\circ$ . Finally, turbulent separation occurs at  $\theta \cong 135^\circ$  (Taneda, 1978). In the present work the localised synthetic jet, at a much lower Reynolds number of  $5 \times 10^4$ , provides similar aerodynamic improvement by delaying flow separation up to an angle of  $\theta \cong 130^\circ$ .

The results indicate that a localised synthetic jet asymmetrically located on a three-dimensional bluff body has the capability to effect significant changes to the surface pressure distribution before and after flow separation has occurred not only in the local vicinity of the synthetic jet but also at significant distances from the point source. The asymmetrical synthetic jet improvement towards potential flow is shown in Figure 4.8. The train of vortices produced by the synthetic jet appear to transfer momentum in all three-dimensions to induce global flow improvements. The interaction between the synthetic jet and the cross flow over the sphere can lead to a local displacement of the cross flow and thereby induce a “virtual” modification of the flow boundary through the creation of a local separation bubble and therefore alter the local pressure and subsequent vorticity distributions. Further aerodynamic improvement could be attributed to the re-energising of the boundary-layer which would promote more mixing and possibly entrain the nearby higher energy flow into the wake region.

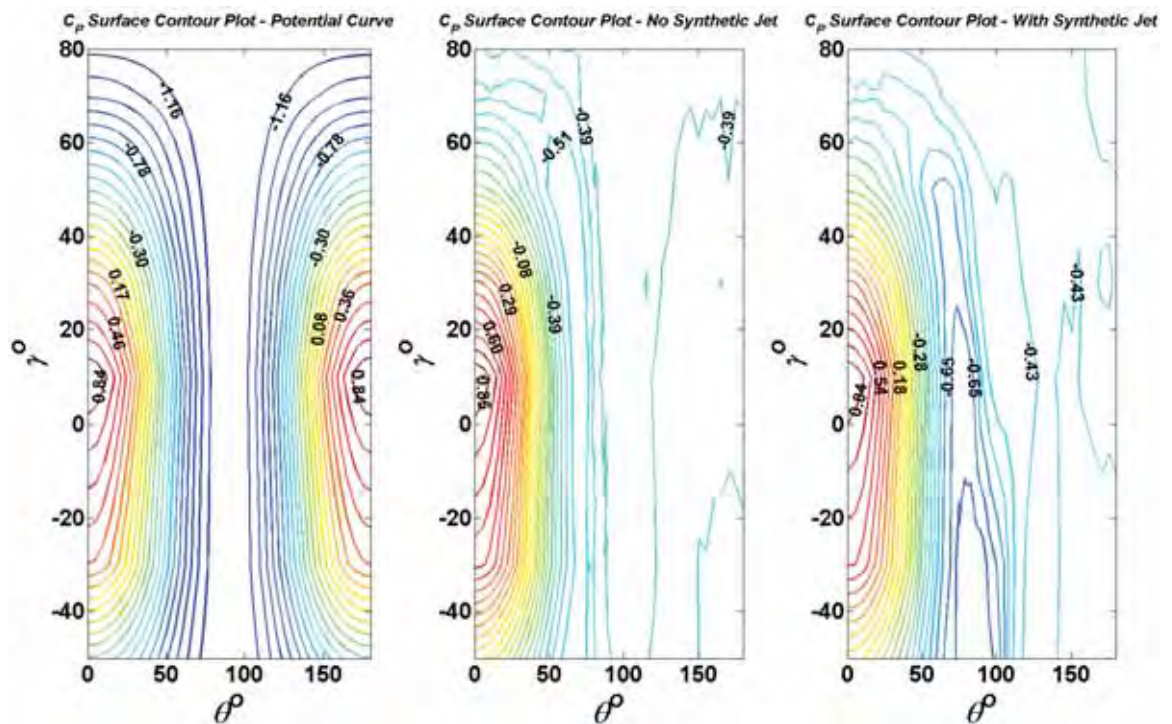


Figure 4.8. Surface pressure contour plot of Potential flow, No synthetic jet and with synthetic jet.

### 4.3 Flow visualisation study of the effect of the localised synthetic jet

The tufts themselves give evidence of flow separation. Streamlined attached flow is indicated when the tuft is attached to the surface of the sphere and is directed along the contour of the sphere surface. On the other hand, the tuft lifts off the surface of the sphere and moves erratically when flow separation occurs. This can be observed in the photographic image of the tuft indicated by a clear streamlined image for that portion of the tuft before flow separation has occurred, with the remainder of the image of the tuft being noticeably blurred due to the unsteady movement of the tuft as a result of the unsteady flow thus indicating that the flow

has separated. The surface pressure distribution of the sphere without synthetic jet (Figure 4.9) indicates that flow separation occurs at an angle of approximately  $85^\circ$  (marked by the black bold line). When the synthetic jet is activated, the separation point was seen to extend by approximately  $13^\circ$  giving a new separation angle of  $98^\circ$  [marked by the bold black line Figure 4.10]. This is comparable with the published works of a distributed synthetic jet on a cylinder which was previously examined in the surface pressure distribution results of Figure 4.6.

The sphere was then rotated further to an angle of  $110^\circ$ . The separation of the tufts occurred from the root of the tufts since the entire length of the tufts are in the separated flow region (Figure 4.11) as indicated by the separation line. When the synthetic jet was applied (Figure 4.12), the flow was streamlined and the tufts near ports 1 and 2 remained attached for a substantial length. The activation of the synthetic jet had the effect of delaying the separation until approximately  $120^\circ$  as indicated by the separation line. Not all the tufts leave the surface at the same angle from the stagnation point, that is the separation is not symmetrical around the circumference of the sphere. This visual observation can be confirmed by the  $C_p$  plots. The point of separation or the separation angle differs for ports 3, 4 and 5 (Figure 4.2 through to Figure 4.7).

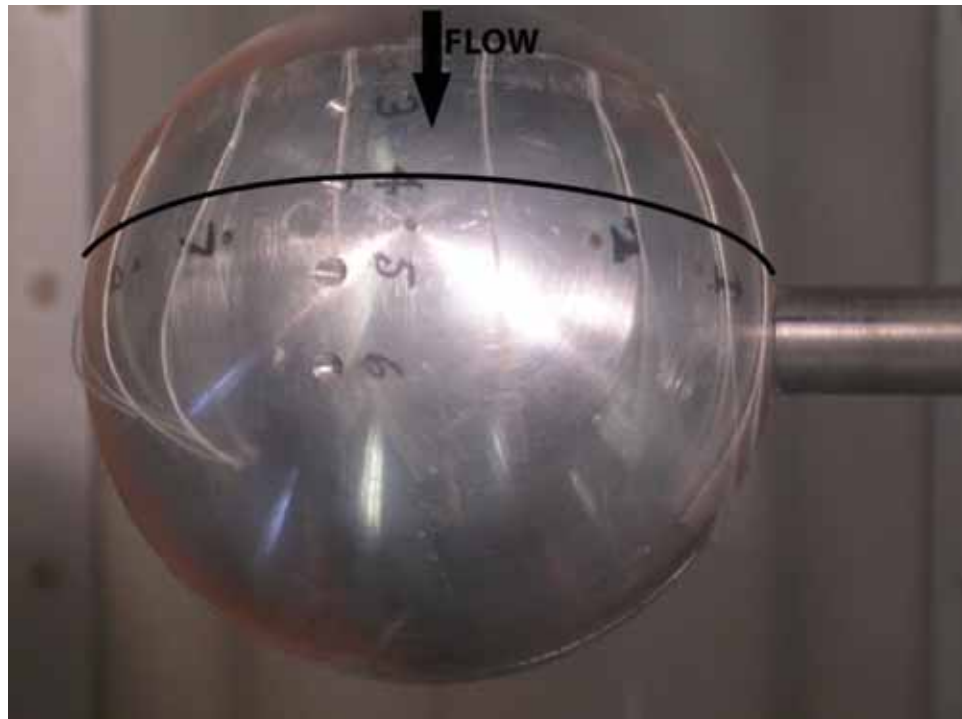


Figure 4.9. Sphere rotated  $90^\circ$  with no synthetic jet.

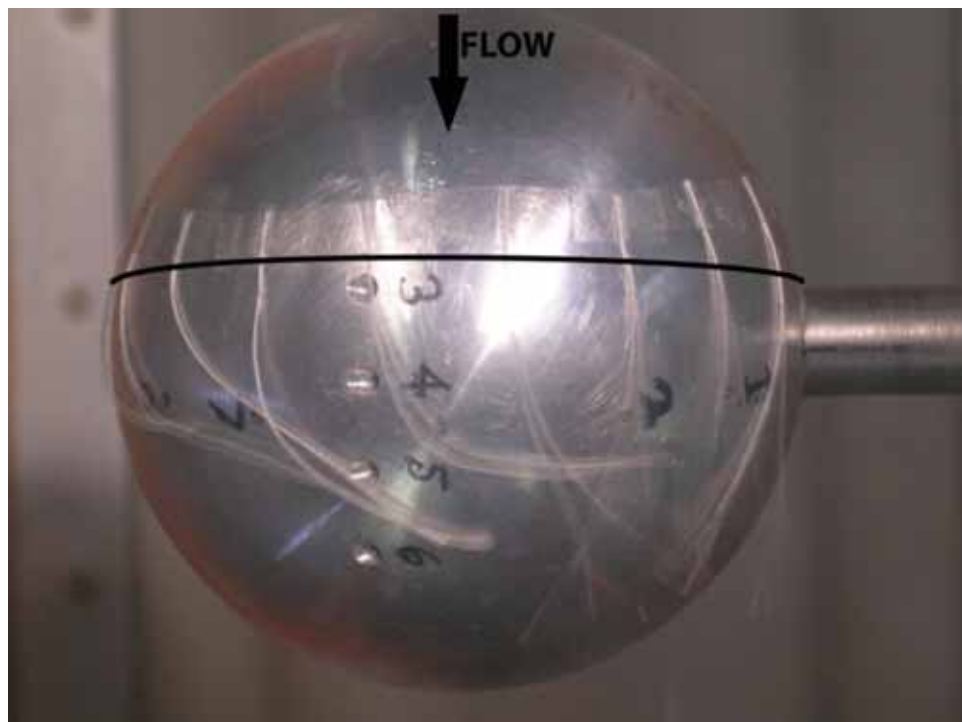


Figure 4.10. Sphere rotated  $90^\circ$  with synthetic jet.

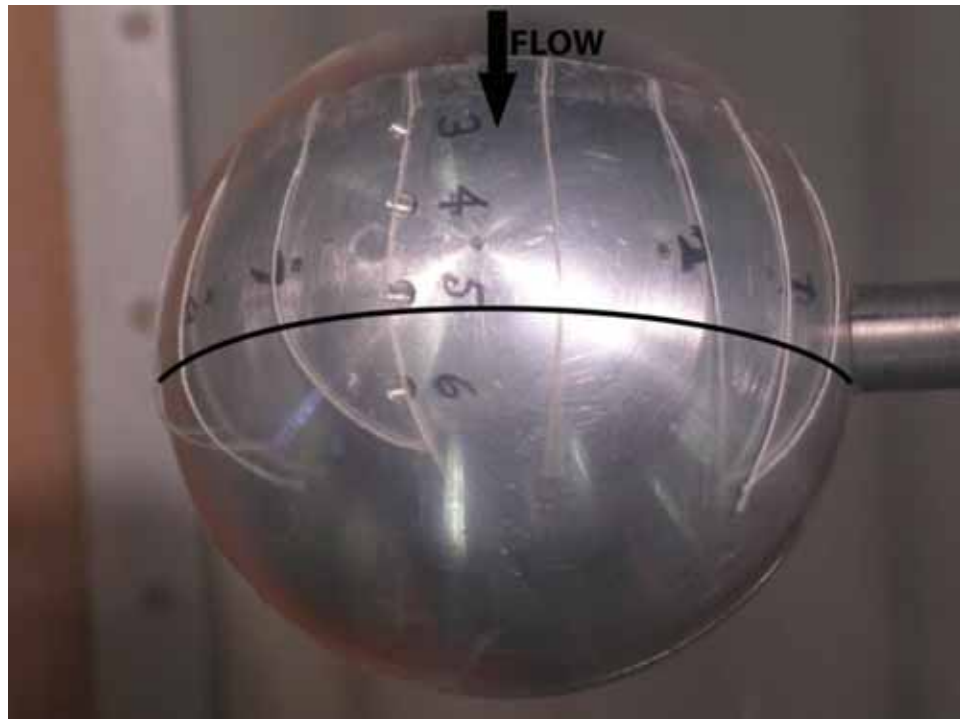


Figure 4.11. Sphere rotated  $110^\circ$  with no synthetic jet.

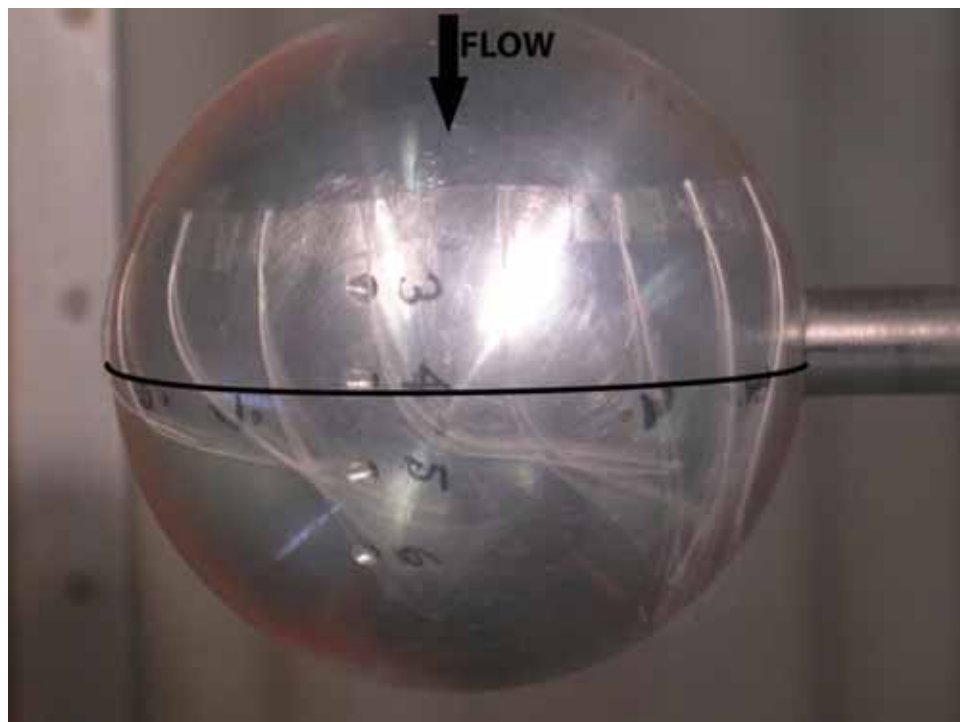


Figure 4.12. Sphere rotated  $110^\circ$  with synthetic jet.

#### 4.4 Effect of sting support

By examining closely the  $C_p$  distribution figures, an apparent asymmetry in the experimental results for the pairs of ports that are symmetrically opposite about the centre axis was observed. The results were not similar for ports 1 and 5 and for ports 2 and 4 as was expected, but markedly different for each pair of ports for the two conditions without synthetic jet and with synthetic jet. The apparent discrepancy was initially speculated to be the effect of the rod support on the nearby ports of 1 and 2. To confirm this, an experiment was conducted that consisted of placing an equivalently sized rod symmetrically opposite to the sting support of the sphere. Pressure measurements from ports 1 and 2 were compared to the results of ports 4 and 5 [Figure 4.13 and Figure 4.14]. When the rod was placed in the flow on the opposite side of the sphere, pressure measurements on both sides of the sphere strongly agreed. This confirmed that the effect of the rod altered the values of the surface pressure on the sphere.

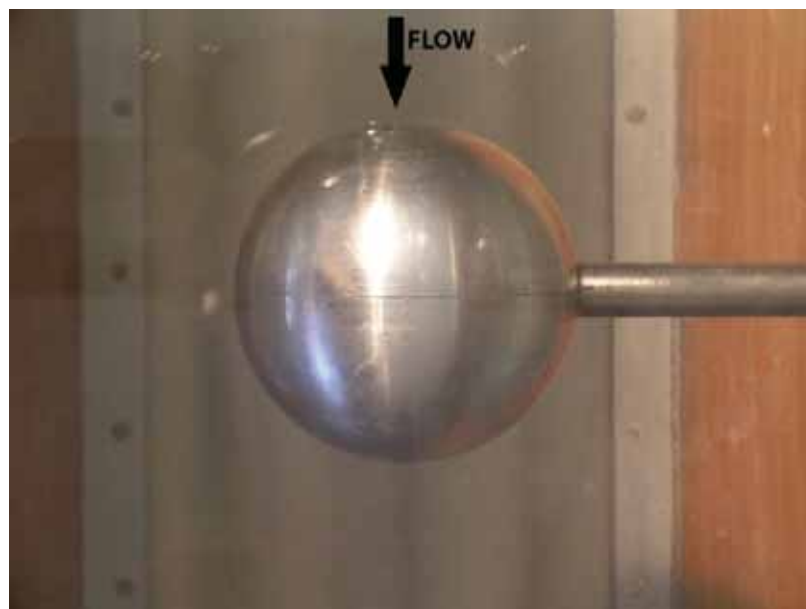


Figure 4.13. Sphere plan view without rod (sting) attached.

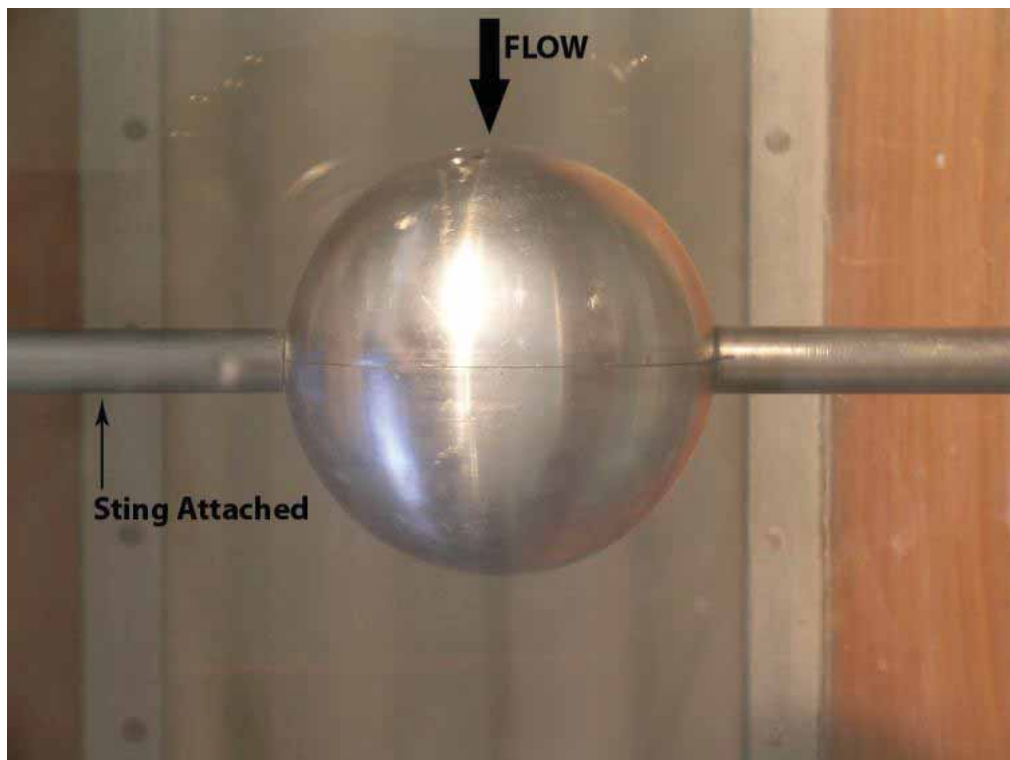


Figure 4.14. Sphere plan view with rod (sting) attached.

With the condition of synthetic jet activated, the effect of the localised synthetic jet significantly shifted the pressure distribution for port 1 toward the potential flow curve. The same can be said for port 2 which also shows a high improvement in surface pressure distribution. In fact, after approximately  $70^\circ$  the pressure distribution for port 1 corresponds to that of port 2. This shows the ability of the synthetic jet to correct flow even under the adverse flow conditions generated by the sting support. The sting support disturbs the flow pushing the pressure distribution further away from potential flow. With the activation of the synthetic jet, an asymmetrically improved flow field is generated that results in a greater improvement to the flow on the sting side of the sphere than the unsupported side of the sphere.

The correction to the flow attributed to the actuation of the synthetic jet, even with the added interference from the sting support, could have significant implications for improvements in aerodynamic applications that seek to reduce interference drag.

#### 4.5 Further remarks on flow separation

Figure 4.9 shows the sphere rotated through  $90^\circ$ . As mentioned earlier, the flow exhibited some degree of turn in towards the middle of the sphere but did not follow the contour of the sphere completely since the flow separated and formed the turbulent wake region. The slight tendency for the flow to be directed from left to right was due to the influence of the sting support on the right. With the activation of the synthetic jet [Figure 4.10], the flow showed greater stability with less erratic movement of the tufts as well as an improvement in the symmetry of the flow depicted by the tufts turning in towards the middle on both sides. It was apparent from Figure 4.11 where the rotation of the sphere was through  $110^\circ$ , that the flow turned in from the left side of the sphere and headed across the sphere towards the right side i.e. the flow was moving from port 5 to port 2. This asymmetrical tendency in the flow was due to the sting support, which at this angle had a greater influence on the flow and seemed to entrain the flow from the opposite side of the sphere. With the activation of the synthetic jet at this angle, this asymmetrical flow was stabilized as the tufts showed less flutter. It was also clear that the tuft to the left of orifice 4 was being forced to straighten due to the synthetic jet [Figure 4.9 and Figure 4.12].

Figure 4.15 shows a diagrammatic representation of the separation line as viewed top down on the sphere. There are two separation lines shown on the sphere, one without and the other with the application of the synthetic jet. It is immediately apparent that the effect of the synthetic jet was to extend the line of separation. It is also striking that with the application of the synthetic jet, the flow around the

sting support was significantly improved or streamlined, a finding that has promising implications in reducing or eliminating interference drag. The results are summarised in Table 4.2.

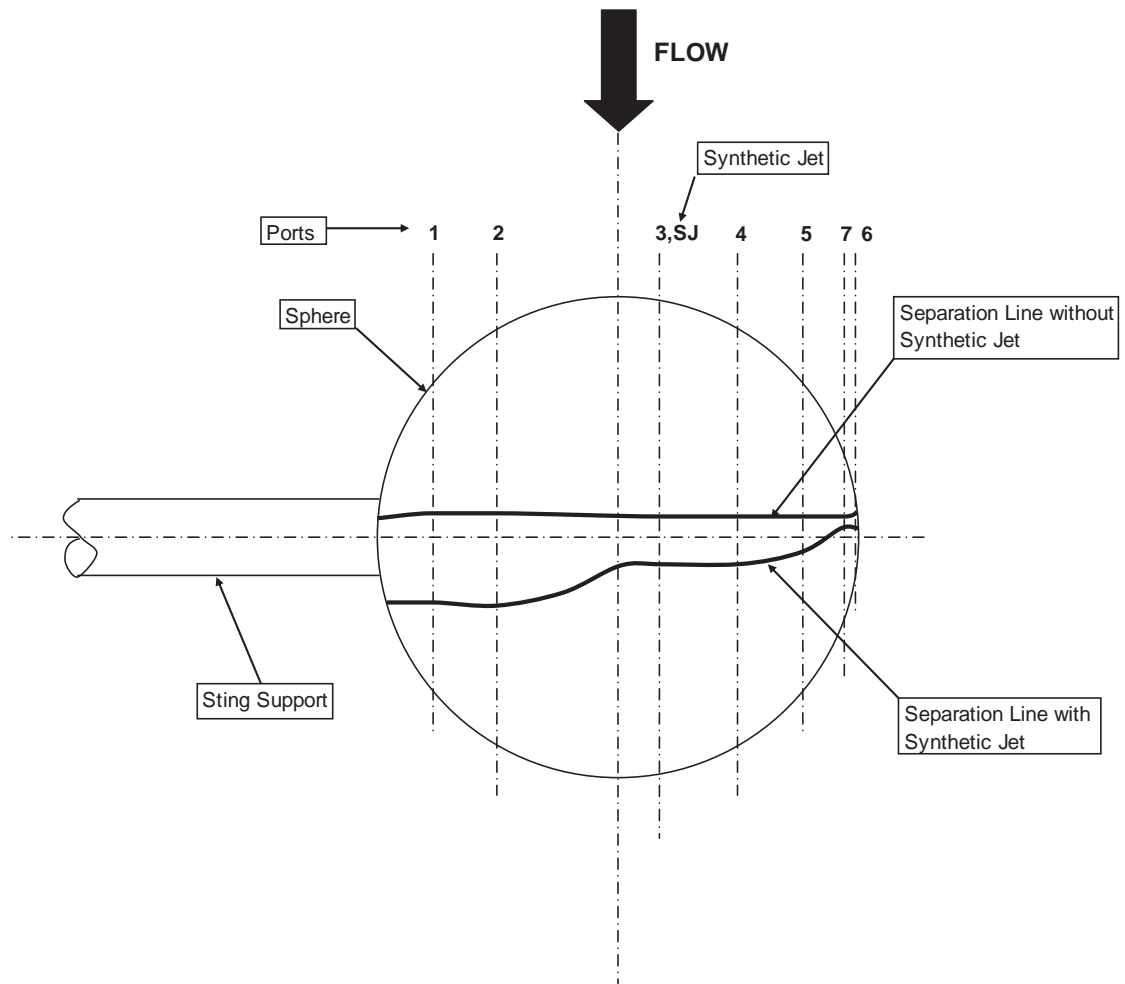


Figure 4.15. Top view. Diagrammatic representation of separation with and without synthetic jet.

Port No.	Port Location $\gamma$	Angle of Separation No Synthetic Jet	Angle of Separation Synthetic Jet	Improvement
1	50	85	115	35.3%
2	30	84	117	39.3%
3	-10	82	101	23.2%
4	-30	82	99	20.7%
5	-50	83	93	12.0%
7	-70	83	82	-1.2%
6	-80	82	83	1.2%

Table 4.2. Angles of flow separation.

With no synthetic jet applied, the flow separation line was reasonably constant over the sphere surface. With the actuation of the synthetic jet, however, an asymmetrical flow field was generated which improved the flow by delaying separation three-dimensionally over the sphere. Interestingly, as previously mentioned, the synthetic jet was able to delay the separation of flow in the region of interference from the sting support more so than the free end. With the section around port 2 the improvement was twice as that of port 4, approximately by 40% as opposed to nearly 20% [Table 4.2].

The flow over the sphere, even with the actuation of the synthetic jet and a side mounted sting support, remained in the laminar flow regime as evidenced by the pressure distribution. Thus, the present synthetic jet strength and frequency of actuation did not trip the flow regime into turbulent flow.

#### 4.6 A comparison of the coefficient of drag on the sphere

The sectional drag, defined in the usual sense as the drag acting on a section or on a particular plane of the body, was examined as circumscribed by each of the pressure ports on the sphere using the relationship given by equation (4-5). Although it does not account for the skin friction drag it provides a reasonable estimate of the drag on the sphere since form drag is the major contributor to the total drag at this Reynolds number.

$$C_D = \int_0^{\pi} C_p \sin(2\phi) d\phi \quad (4-5)$$

The values of the coefficient of sectional drag are listed in Table 4.3 as well as the improvement for each section.

The three-dimensional drag coefficient of the sphere was calculated by integrating each of the sectional drag coefficients using the software called Matlab. The drag on the sphere without the application of the synthetic jet was 0.491. This compares

favourably with the coefficient of drag,  $C_D = 0.485$  given by Schlichting (1968). The total drag with the application of the synthetic jet was 0.431. This gives a total reduction in drag due to the actuation of the localised asymmetric synthetic jet of slightly over 12%. Table 4.3 shows the effect of the sting support, which is generating more drag on the side of the sphere it is attached to than the free side as would be expected. Also of interest is port 5 which at this section of the sphere the asymmetric flow field seems to have created such a great reduction in drag, especially with the synthetic jet applied, that it produces a lift force on the sphere. This was also pointed out in the flow visualization study that showed the tufts were strongly influenced across the sphere surface towards the sting support. Although there is a lift force opposing the drag on this section of the sphere and there is an immense improvement of nearly 220%, it contributes slightly less than 5% to the overall reduction in drag.

Drag Analysis				
Port No.	Port Location $\gamma$	$C_{d_s}$ (No Synthetic Jet)	$C_{d_s}$ (Synthetic Jet)	Reduction in $C_d$ ( $\Delta C_d$ )
1	50	0.0487	0.0314	35.4%
2	30	0.2708	0.2378	12.2%
3	-10	0.4380	0.4029	8.0%
4	-30	0.1991	0.1607	19.3%
5	-50	-0.0101	-0.0322	219.5%
7	-70	0.0134	0.0102	23.8%
6	-80	0.0018	0.0001	95.3%

Table 4.3. Sectional drag coefficients.

## 4.7 Concluding remarks

In Chapter 4 it has been shown that there are some notable effects of a synthetic jet and its impact on the flow over a true three-dimensional bluff body.

The investigation suggest a critical angle of  $27^\circ$  below which the effects of synthetic jet on the flow over a sphere become ineffective. The limitations of the potential flow theory beyond this critical angle where the growth of the boundary layer becomes more pronounced, were also demonstrated. The deviation from potential flow theory increased as the angle offset increased as was expected.

The aerodynamic improvement owing to the asymmetric localisation of the synthetic jet was manifest in the delay of separation of flow that was found to range the angles of  $83^\circ$  to  $120^\circ$  at a Reynolds number of  $5 \times 10^4$ . Additionally, the synthetic jet generated significant reductions to the total drag on the sphere with an overall reduction of over 12%.

The sting support had the effect of disturbing the flow upstream and downstream in its near vicinity. The downstream effects were observed from the flow visualization study, which showed the flow from the sphere wake combining with the wake from the sting support forming an asymmetrical interference type of flow. Fluid from the opposite side of the sting support was tending towards the sting at angles beyond  $90^\circ$ . The actuation of the synthetic jet lessened the asymmetric effect of the sting and improved the flow. This indicated that synthetic jets were capable of not only improving the flow on two-dimensional bodies but also streamlining the flow on three-dimensional bluff bodies with the added complexity of flow disturbances from interference effects. The pressure distribution plots provided further qualitative and quantitative evidence.

Significant drag reductions were also observed at certain points away from the synthetic jet but with generally less contribution to the overall drag of the sphere. Thus, activation of the asymmetric localised synthetic jet provided a technique to substantially improve the aerodynamic drag of the sphere.

The above findings will have significance beyond those envisioned in this study. Apart from localised synthetic jet used as an effective tool for aero-shaping true three-dimensional bluff and lifting bodies, the use of localised synthetic jet will also have significance of practical importance in various fluid mechanical devices and in industries where control of three-dimensional flow separation and re-attachment and streamlining of flows is required.

---

## Chapter 5

### Results and Discussion: Bluff Body Wake Analysis

---

## 5. Results and discussion: Bluff body wake analysis

Substantial experimental work with synthetic jets in various flow regimes and in different types of flow i.e. laminar and turbulent flows, has been performed over recent years. Moreover, there has been an increased effort by many researchers in this field of fluid mechanics. Some of the applications, as already mentioned in Chapter 1, of the use of synthetic jet include flow separation control and turbulence, control of thrust vectoring, augmentation of heat transfer and mixing, and microfluidics. Specifically, synthetic jets are proving to be a beneficial device in terms of active flow control in applied aerodynamics. This has been demonstrated with the use of synthetic jet in subsonic crossflows in which typically the synthetic jet emanates from the surface of a bluff or streamlined body reducing the wake region and overall drag as evidenced in the works of Amitay, Kibens, et al. (1999). Interestingly, synthetic jets improve the flow by imparting a net momentum transfer to the flow without a net mass addition, a defining property of synthetic jets. This added momentum has the effect of modifying the crossflow over the body producing a delay in flow separation and reattachment with a separation bubble forming above the surface of the body. The flow structure of the synthetic jets themselves consists of a time-periodic formation of vortex pairs that eventually progress into transition to turbulence and the monotonic decrease in their stream wise velocity that ultimately leads to their dissolution.

There have been several articles published on synthetic jet in a crossflow such as the flow over a circular cylinder (Amitay et al. 1999; Amitay et al. 2001; Lee & Goldstein 2000). Nonetheless there is a noticeable lack of published research on true three-dimensional bodies with a synthetic jet (Jeong et al. 2004). The flow over a cylinder can be described with two independent variables and so is defined as axis symmetric flow. This is a degenerate three-dimensional flow that exhibits certain three-dimensional effects and therefore is not really a two-dimensional flow and

not fully three-dimensional either. A common feature to all three-dimensional flows is the three-dimensional relieving effect that is present. A good example is the flow over a sphere but not that of a cylinder. A greater understanding of the synthetic jet in three-dimensional flows is essential to enable successful inception in various engineering applications, especially in the aerospace industry.

Chapter 5 is a continuation of the author's research in Chapter 4 conducted on the sphere bluff body and to therefore contribute to the need for further three-dimensional experimental work. This part of the work will provide a clearer understanding of the three-dimensional effects encountered when applying a synthetic jet to a three-dimensional body in a crossflow. A parallel purpose of this present study is to investigate the validity of using a five-hole pressure probe to measure the total and static pressures at a point and then indirectly calculate the velocities in a highly three-dimensional wake. Since the flow over the sphere is a true three-dimensional flow, and it is also a simple and symmetrical three-dimensional bluff body, this became a suitable choice with which to perform our experiments. The wake survey for the standard sphere was used as a basis to form the criteria for flow reversal using the five-hole pressure probe. These criteria were tested using wake survey measurements obtained from the flow over a NACA23012 airfoil with flow reversal in the wake region. Using the standard sphere flow as a benchmark, we were then able to observe the effects of synthetic jet flow control applied to the sphere at three angles of incidence. The experiment was designed to show the effects of applying this method of flow control near the fore stagnation point where the boundary layer is in the early stages of growth and therefore relatively thin. Then we observe the effects of applying the synthetic jet in the near vicinity and prior to flow separation where the boundary thickness has almost reached its maximum before the adverse pressure gradient causes it to separate (Jeong et al. 2004). A wake survey was then taken with the synthetic jet located in the separated flow region i.e. within the wake region. These three locations in which the synthetic jet was applied shows the effects of flow control in different

local flow fields and the effect on the overall flow structure in the wake. Use was made of the wake survey measurements to generate total and static pressure fields and the velocity field. Further, the vorticity field is also used to gain understanding of the highly reversing flow and the improvements made with the use of synthetic jet. The present study leads to a rather straightforward and effective way to examine the three-dimensional behaviour of the bluff body in terms of boundary layer growth, skin friction, separation of flow and pressure drag changes in three-dimensions under the influence of a localised asymmetrical synthetic jet.

An alternative approach has been developed and used in this work to examine the three-dimensional wake structure behind the sphere. The boundary-layer concepts of displacement thickness and momentum thickness (Anderson 2001) have been used to measure in some sense the entropy of the wake, by that we mean the amount of disorder in the wake. The influence of boundary-layers and wakes on external fluid flow has been and continues to be thoroughly investigated. Displacement thickness and the law of the wake and momentum thickness or similarly momentum defect have been used to measure properties in the wake (Coles 1956; Lighthill 1958; White 2006; Moore 1952). In the present work they are used in a more direct manner to characterise the wake region and provide useful measures of the effect of the wake on the flow over solid bodies.

The synthetic jet is then used as a control method to bring streamlining or order into the flow. It was also found that the shape factor used in airfoil theory proved to be useful in this regard as a means of characterising the wake with and without a synthetic jet.

## 5.1 Reversal of flow

In highly three-dimensional flows, such as that encountered in the present work with the flow behind that of a sphere, it is crucial to ascertain when we have reversal of flow in analysing and interpreting the results of the wake region. This is especially the case when using instrumentation such as the five-hole pressure probe to acquire the physical parameter of pressure at a point. The instrument will typically be calibrated to measure the pressure from each of the five orifices within a limited range of yaw and pitch angles. In a highly reversing flow it is possible that the direction of the flow vector is outside this calibrated range and thus will give inaccurate data of the true, local total and static pressure and velocity vector at that point. Thus, the intention was to establish a set of rules or criteria that can be used to determine if the incumbent flow on the five-hole pressure probe is within a reverse flow region and/or beyond the probe's calibrated region. To generate a generic set of rules or a methodology that establishes whether the acquired pressure data is indicative of reversal of flow, we have used as a basis the work of Pisasale & Ahmed (2003) which resulted in a methodology for use with the seven-hole pressure probe.

As mentioned previously, the use of the five-hole probe is limited to the range of calibration conducted prior to carrying out the experiment. The results obtained from the five-hole probe must be analysed according to this range. The first criterion is now formed in the process that will enable the determination of when the probe is in a region of flow reversal or separated flow, thus nullifying the results obtained from the probe in that data region. According to the work on five-hole probes by Treaster and Yocum (1973), they use Bernoulli's equation as a method for calculating the flow velocity vector. The velocity is obtained using the following equation:

$$\bar{V} = \sqrt{\frac{2}{\rho_{\infty}}(\Delta P_T - \Delta P_S)} \quad (5-1)$$

The above equation (5-1) requires the local total and static pressure be obtained from the calibration curves that are formed when the five-hole probe is calibrated. It is clearly seen that if the term  $\Delta P_T < \Delta P_S$  then we cannot calculate a velocity since the term underneath the square root operation is negative. This is the first criterion that indicates that we definitely have reversal of flow.

$$\Delta P_T < \Delta P_S \quad (5-2)$$

In addition, this simple criterion applies generally to all cases whether the synthetic jet is active or not in use. In addition to this and in line with the work of Treaster and Yocum (1973) we can proceed to consider the validity of this criterion based on Bernoulli's equation which states the following:

$$P_T = P_S + P_{dyn}$$

$$\text{where, } P_{dyn} = \frac{1}{2} \rho_{\infty} \bar{V}^2 \quad (5-3)$$

This conservation of energy equation (better known as Bernoulli's equation) is applied under the following well-known assumptions. The flow of fluid is ideal i.e. incompressible, inviscid and steady. It follows from equation (5-1) that if we have the condition as stated in equation (5-2), in differential pressure measurement form, then  $P_{dyn} < 0$  and  $\bar{V} < 0$ . Again, we note that it is impossible for the total velocity vector to be less than zero, it being zero when we have stagnation of the fluid flow. However this is not the case in the free flow region of the wake or when we encounter separated flow. Therefore, when we obtain the local total and static

pressures from the five-hole pressure probe and these are found to give a negative total velocity we can conclusively say that we have reversal of flow.

Table 5.1 and Table 5.2 are indicative samples of the analysis of the data for the standard sphere with no synthetic jet (NJ) and then followed by the three cases of synthetic jet application at  $6.5^\circ$  (SJ6.5),  $76^\circ$  (SJ76) and  $100^\circ$  (SJ100). The measured points shown are, near wake, at 5 mm downstream of the rear of the sphere in the centre and traversed in the y-axis. Thus, the Cartesian coordinates for the location are:  $x = 5$  mm,  $z = 0$  mm and  $-50 \leq y \leq 50$ . The second set of results, are taken further downstream at:  $x = 80$  mm,  $z = 0$  mm and  $-50 \leq y \leq 50$ . In the first case, with the standard sphere, we have taken the wake measurement close to the rear of the sphere in a region where we expect to have highly reversing flow (RF). Contrast this to the situation downstream at a location 80 mm away from the rear of the sphere at a point we expect the flow to have recovered or corrected to some extent. The percentage of recirculation has indeed decreased from 73% to 27%. Now we compare the cases with the application of the synthetic jet. The same trend occurs between  $x = 5$  mm and  $x = 80$  mm, except for the case of the synthetic jet applied at  $100^\circ$ . Since, in this case, the synthetic jet is applied in a region that has already separated flow, well into the wake region, the energy imparted to the flow in the wake could directly influence the flow by streamlining the flow. The increase in flow energy introduced in the near wake corrects the flow at that early stage. The effects are lesser downstream. The synthetic jet applied at  $76^\circ$  is seen to have a small effect on the near wake region although the flow recovers more so than the other cases producing only 9% recirculation at  $x = 80$  mm. The synthetic jet at  $6.5^\circ$  has a significant impact on the near wake reducing the recirculation to 36% with a further reduction to 18% downstream.

Criterion 1 ( $\Delta P_T < \Delta P_S$ )												
At x = 5 mm												
	NJ			SJ6.5			SJ76			SJ100		
y (mm)	$\Delta P_T$ (Pa)	$\Delta P_S$ (Pa)	Test									
50	57	-9	OK	61	-12	OK	59	-10	OK	60	-11	OK
40	-17	-24	OK	36	-22	OK	56	-16	OK	58	-16	OK
30	-34	-31	RF	-41	-34	RF	18	-31	OK	13	-34	OK
20	-35	-32	RF	-41	-36	RF	-37	-35	RF	-39	-34	RF
10	-34	-31	RF	-39	-35	RF	-39	-34	RF	-36	-33	RF
0	-31	-28	RF	-38	-34	RF	-33	-32	RF	-32	-32	RF
-10	-31	-28	RF	-31	-33	OK	-31	-30	RF	-29	-29	OK
-20	-32	-29	RF	-31	-33	OK	-30	-29	RF	-28	-29	OK
-30	-32	-28	RF	-31	-33	OK	-29	-28	RF	-27	-28	OK
-40	-29	-26	RF	-26	-30	OK	-30	-26	RF	-27	-27	OK
-50	50	-14	OK	55	-23	OK	58	-17	OK	57	-18	OK
% RF			73				36				64	27

Table 5.1. Reversal of flow, Criterion 1. Streamwise location of x = 5 mm.

Criterion 1 ( $\Delta P_T < \Delta P_S$ )												
At $x = 80$ mm												
	NJ			SJ6.5			SJ76			SJ100		
y (mm)	$\Delta P_T$ (Pa)	$\Delta P_S$ (Pa)	Test									
50	57	0	OK	57	-1	OK	60	2	OK	57	1	OK
40	48	-1	OK	53	0	OK	59	4	OK	51	1	OK
30	30	-1	OK	51	1	OK	58	5	OK	41	2	OK
20	13	-2	OK	38	1	OK	51	5	OK	27	-1	OK
10	0	-3	OK	31	-4	OK	40	0	OK	-1	-2	OK
0	-9	-6	RF	25	-5	OK	24	-4	OK	-17	-5	RF
-10	-11	-7	RF	-16	-5	RF	-2	-7	OK	-12	-6	RF
-20	-8	-5	RF	-12	-9	RF	-14	-7	RF	-8	-5	RF
-30	2	-3	OK	3	-6	OK	1	-4	OK	0	-2	OK
-40	18	0	OK	15	-5	OK	11	-2	OK	24	0	OK
-50	39	2	OK	32	-4	OK	30	0	OK	42	1	OK
% RF			27				18				9	27

Table 5.2. Reversal of flow, Criterion 1. Streamwise location of  $x = 80$  mm.

The instrument used in the work by Pisasale and Ahmed (2003), a seven-hole cobra head pressure probe, was geometrically similar to that used in the present work, a five-hole cobra head pressure probe. It follows that all pressure ports would have approximately the same value in the region when  $\beta > 125^\circ$  or  $\beta < -125^\circ$ , yaw angle. Thus, when the flow vector was at these extreme angles then it would imply that the probe tip was either immersed in stalled flow/separated flow or equivalently reversing flow such as that encountered in the wake region in the flow past a body. In formulating the second criterion, different relations that are used to gauge the differences in pressure of each hole on the probe head were investigated. A simple relation we could form would be the norm of the difference between the mean

pressure and each pressure port. This is shown in the following equation which also may be denoted as the Square Root Sum of Squares (SRSS):

$$M_{TE} = \sqrt{m_1^2 + m_2^2 + \dots + m_n^2} \quad (5-4)$$

where  $m_n^2 = (\hat{P}_{12345} - P_n)^2$  and  $n = 1, \dots, 5$  refer to the pressure ports on the probe head.

The normal mean pressure is defined as  $\hat{P}_{12345} = (P_1 + P_2 + P_3 + P_4 + P_5)/5$ . This was seen to be the most stringent of all criteria since its inherent simplicity also allows for transparency in its application. The calculation of  $M_{TE}$  at each data point produces relatively low values in the wake region. Thus in order to set a criterion for reversal of flow a prescribed value must be set below which we define to have flow reversal. Thus in a sense we could calibrate the flow field between highly reversed flow and freestream flow and thereby set a gradient between these two regions. Careful consideration though must be taken to ensure that this criterion does not exclude valid data points or, conversely, include values that should be marked as flow reversal. An insightful limit means that it is possible to fully capture reversing flow with the ability to extend this to partially reversing flow or separated flow as seen by the probe instrument. It was found that when we set the criterion to  $M_{TE} \leq 15$  Pa this would be a reasonable limit to classify the flow as fully reversed flow. It was found that this condition alone for this criterion was not sufficient. To test this criterion against the measured data it was not used in conjunction with Criterion 1. In this way it was possible to assess the effectiveness of this criterion to filter out the reversed flow data points. Application of this criterion showed that data points that would be marked as reverse flow according to Criterion 1 would pass through as valid measurements according to this second criterion. Further to this data points further downstream in the wake surveys that should pass were being marked as reverse flow. In the first instance this would not cause a problem as long as the first

criterion was applied then points that would pass according to the second criterion would be picked up before we progress to this second stage. In the second instance a deeper analysis of the data revealed that it was possible to have an  $M_{TE} \leq 15$  Pa and still have a sufficiently high velocity. Therefore the SRSS can have a sufficiently low value since the majority of the ports will be close to the calculated average for that data point. There will exist, though, at least one port that will be pointed in the flow direction to the extent that it places the probe within the calibrated flow region. As a secondary condition to this criterion we can use the total velocity vector to ensure valid data points are not marked as reverse flow. It was found that when the total velocity was set at  $V_T \leq 2$  m/s then this condition applied together with the first condition  $M_{TE} \leq 15$  Pa which would allow valid data points to pass through unmarked. The tables below, Table 5.3 and Table 5.4 show the second criterion only applied to the same set of data as shown for Criterion 1.

Criterion 2 ( $M_{TE} \leq 15$ Pa, $V_T \leq 2$ m/s)				
At $x = 5$ mm				
y	$M_{Te}$	$M_{Te}$	$M_{Te}$	$M_{Te}$
(mm)	(NJ)	(SJ6.5)	(SJ76)	(SJ100)
50	61	66	67	68
40	16	64	75	77
30	3	10	53	48
20	3	5	23	14
10	3	5	6	3
0	3	5	2	1
-10	4	2	1	1
-20	4	2	1	1
-30	4	2	1	2
-40	4	4	2	2
-50	64	70	67	66
% RF	73	64	64	64

Table 5.3. Reversal of flow, Criterion 2. Streamwise location of  $x = 5$  mm.

Criterion 2 ( $M_{TE} \leq 15$ Pa, $V_T \leq 2$ m/s)				
At $x = 80$ mm				
y	$M_{TE}$	$M_{TE}$	$M_{TE}$	$M_{TE}$
(mm)	(NJ)	(SJ6.5)	(SJ76)	(SJ100)
50	58	55	55	57
40	55	53	54	53
30	43	53	54	44
20	32	45	51	30
10	19	38	44	20
0	12	29	36	14
-10	7	18	29	8
-20	8	8	19	6
-30	15	12	10	10
-40	29	24	13	24
-50	43	37	28	39
% RF	27	18	9	36

Table 5.4. Reversal of flow, Criterion 2. Streamwise location of  $x = 80$  mm.

It is interesting to note that we could have used  $\bar{P}$  instead of  $\hat{P}_{12345}$  as the mean pressure. Further, as will be seen in the proceeding formulation,  $\bar{P}$  could be used as a normalisation parameter where  $\bar{P}$  is defined as the probe mean pressure,  $\bar{P} = (P_2 + P_3 + P_4 + P_5)/4$ . In the region where flow reversal occurs there is little difference between the two calculation methods for the mean pressure values, since all pressure ports are in a separated flow or highly reversing flow region. This non-dimensionalising parameter is indicative of the local dynamic pressure. It has already been established (Treaster and Yocum, 1973) that this parameter reduces the scatter in the calibration data which could also be inferred to a reduction in scatter of the acquired results. Besides, attempting to use the true dynamic pressure would introduce an unknown quantity into the criterion, therefore making it uncertain. Thus, it seems to be of no substantial significance which definition of

mean pressure is used to calculate the value for the normalising parameter when determining reversal of flow. Since  $\hat{P}_{12345}$  gives slightly lower values, this will be the preferred choice for calculating  $M_{TE}$ . This is also the preferred normalisation parameter, because  $\hat{P}_{12345}$  is slightly larger than  $\bar{P}$  and it is used in the proceeding equation since the overall value of the function will be lower.

This next method used to investigate flow reversal involved the use of percentage error as used by Pisasale and Ahmed (2003). This is defined as  $e_i = |(\hat{P}_{12345} - P_i)/\hat{P}_{12345} \times 100|$  for each port with the total percentage error becoming  $e_T = \sqrt{e_1^2 + e_2^2 + \dots + e_n^2}$  where n is the number of ports, five in this case. This can also be written as:

$$Y = (100/\hat{P}_{12345}) \left[ \sum_{i=1}^5 (\hat{P}_{12345} - P_i)^2 \right]^{\frac{1}{2}} \quad (5-5)$$

Equation (5-5) has been used in determining reversal of flow in the seven hole probe for very high angles in the wake region. In the wake region we expect the numerator to be of low values, almost equal and therefore we could theoretically encounter the scenario that we have an undefined function. Experimentally, as has been noted by Pisasale and Ahmed (2003), this is unlikely. This has been evidenced in large amount of data points taken from the wake surveys of the sphere with reversing flow and the NACA23012 stalled airfoil that also experiences highly reversing flow.

For the present work concerning the use of the five-hole probe, this criterion would also be applicable for highly separated flow regions such as the near wake where the angles of the flow incident on the probe head would be large. It was found that by setting this parameter to a value of  $Y \leq 25\%$  we could conclude that we have flow reversal. The results of the third criterion were applied to all cases of the flow over

the sphere, as shown in Table 5.5 and Table 5.6 for the near wake at  $x = 5$  mm and the downstream location at  $x = 80$  mm respectively.

Criterion 3 ( $Y \leq 25$ )				
At $x = 5$ mm				
y	Y	Y	Y	Y
(mm)	(NJ)	(SJ6.5)	(SJ76)	(SJ100)
50	1917	1864	2398	2506
40	71	525	2541	2496
30	10	29	221	175
20	10	13	66	39
10	10	14	19	9
0	12	15	5	3
-10	13	6	4	4
-20	12	6	5	5
-30	12	6	5	6
-40	16	15	9	8
-50	2842	1917	3696	2550
% RF	73	64	55	55

Table 5.5. Reversal of flow, Criterion 3. Streamwise location of  $x = 5$  mm.

Criterion 3 ( $Y \leq 25$ )				
At $x = 80$ mm				
y	Y	Y	Y	Y
(mm)	(NJ)	(SJ6.5)	(SJ76)	(SJ100)
50	565	456	423	509
40	657	472	386	547
30	977	475	385	574
20	3150	675	437	1221
10	738	1993	674	1120
0	190	1489	3556	274
-10	96	294	488	109
-20	136	85	290	119
-30	751	273	318	451
-40	956	2356	1634	716
-50	501	823	485	453
% RF	0	0	0	0

Table 5.6. Reversal of flow, Criterion 3. Streamwise location of  $x = 80$  mm.

It is clear that the criterion works well in the near wake with high wake angles, however downstream where there could still be some reversal of flow, the criterion is not sensitive enough to identify the possible erroneous readings.

Another means or criterion to determine complete flow reversal or separated flow is to use a basic relation which is the difference between the central pressure port and the normal mean value,  $P_1 - \hat{P}_{12345}$ . This fourth criterion can be stated as:

$$P_1 - \hat{P}_{12345} < 0 \quad (5-6)$$

This was seen to be as effective as using the first criterion, equation (5-2). When the probe is immersed in a fully reversed flow or a partially separated flow on the probe

head but angled enough so as to cause Port 1 to be affected, then the normal average will be greater than the pressure on Port 1. This can be used effectively to decide whether the reading is affected by flow reversal.

Table 5.7 and Table 5.8 show this criterion applied at the same locations as with the preceding criteria.

Criterion 4				
At x = 5 mm				
y	Y	Y	Y	Y
(mm)	(NJ)	(SJ6.5)	(SJ76)	(SJ100)
50	53	55	56	57
40	5	40	56	57
30	-3	-3	20	14
20	-2	-4	0	-1
10	-2	-3	-2	-1
0	-2	-4	-1	0
-10	-3	2	0	0
-20	-3	1	0	0
-30	-3	1	0	0
-40	-2	2	0	0
-50	52	59	56	56
% RF	73	36	27	27

Table 5.7. Reversal of flow, Criterion 4. Streamwise location of x = 5 mm.

Criterion 4				
At x = 80 mm				
y	Y	Y	Y	Y
(mm)	(NJ)	(SJ6.5)	(SJ76)	(SJ100)
50	47	46	46	45
40	40	42	45	38
30	25	38	42	26
20	12	25	34	10
10	2	13	22	0
0	-3	4	9	-4
-10	-3	-2	1	-4
-20	-2	-2	-1	-3
-30	4	4	1	1
-40	15	12	9	13
-50	30	25	23	28
% RF	27	18	9	27

Table 5.8. Reversal of flow, Criterion 4. Streamwise location of x = 80 mm.

As further evidence of the robustness of the criteria, it was tested on the wake of a NACA23012 airfoil without the application of a synthetic jet. The results were taken for the airfoil at zero degrees AOA with the five-hole probe in the normal orientation and thereafter placed at  $180^\circ$  to the flow direction or in the opposing direction. With the application of the above criteria, based on the data obtained from the sphere, we were able to find the true velocity at different points in the wake. By placing the probe in the wake of the airfoil in the two opposing orientations in the steady state flow, we are able to obtain the two sets of data, the combination of which will contain the true velocity in the wake. The criteria enable one to sort the data set, identifying the points of data that would be in error due to flow reversal, and those points of data that are valid, generating a new set of experimental data that contains only the true velocities of the surveyed wake

region. Figure 5.1 shows the two sets of data and resulting curve after applying the flow reversal criteria. Also noteworthy is that these criteria seem to be valid at different Reynolds numbers since the airfoil was tested at an air speed of 15m/s or Reynolds number of the order of  $1.5 \times 10^5$ .

## Results and Discussion: Bluff Body Wake Analysis

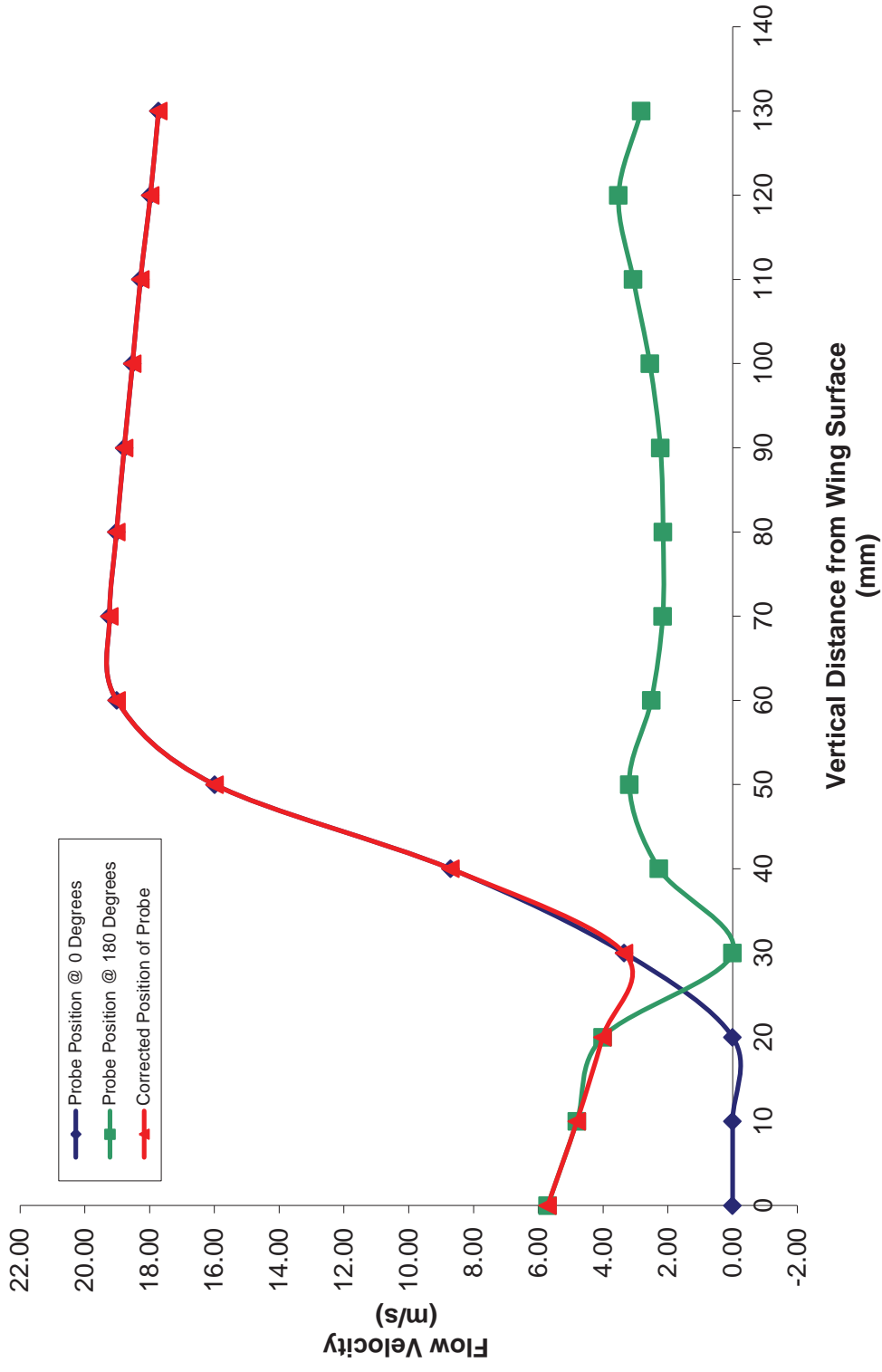


Figure 5.1. NACA 23012 wake survey.

Further analysis on the performance of the synthetic jet will be explained in the following sections where the analysis of the wake surveys is shown in various plots of pressure and velocity, which also relate to reverse flow.

## 5.2 Wake Characterisation: Flow visualisation

The flow visualisation using the tufts was intended to provide some qualitative clarity and provide an additional aid in understanding and establishing the standard flow over the sphere and any improvement in flow due to the activation of the synthetic jet. This adds to the visual exposition seen in the proceeding section resulting from the analysis conducted on the wake surveys. The synthetic jet was orientated at an angle of  $80^{\circ}$  which is approximately the location of separation for a standard sphere Schlichting (1968). Figure 5.2 through to Figure 5.7 show the flow visualisation results observed at the designed experimental wind speed of 10 m/s. The light thin string tufts are fixed to a thin wire screen to minimise the interference to the flow whilst giving an indication of the flow direction and steadiness. Figure 5.2 and Figure 5.3 show the standard sphere flow with the screen placed at 40 mm to the rear of the sphere in the wake region. It is clearly seen in these images that the flow is reversing as evidenced by the tufts tending to curl back onto the screen and flutter back towards the sphere. In Figure 5.4 and Figure 5.5, the airspeed is also at 10 m/s with the screen at the same location, although now the flow has been modified using the synthetic jet at the above mentioned location. A different picture is seen to emerge in this case, with the tufts pointing in the streamwise flow direction. This is evidence of significant straightening of the flow field in the wake region of the sphere.

Figure 5.6 and Figure 5.7 show the flow pattern of the tufts at 20 m/s without and with the synthetic jet activated at 40 mm from the sphere. These figures suggest that the wake region of the sphere with the synthetic jet activated has been shortened at the two different Reynolds numbers.

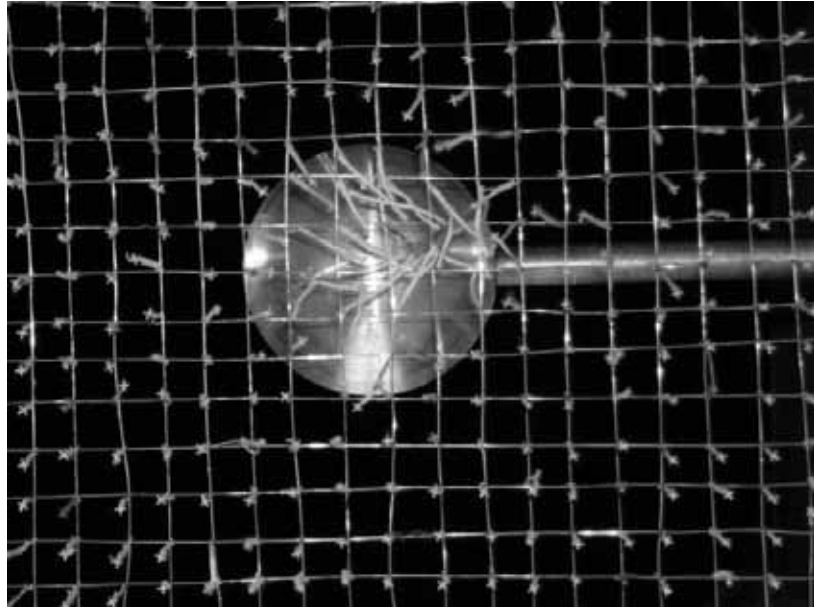


Figure 5.2. Tuft mesh. Flow speed of 10 m/s without synthetic jet. Tuft screen 40 mm offset.



Figure 5.3. Tuft mesh. Flow speed of 10 m/s without synthetic jet. A side view of Figure 5.2

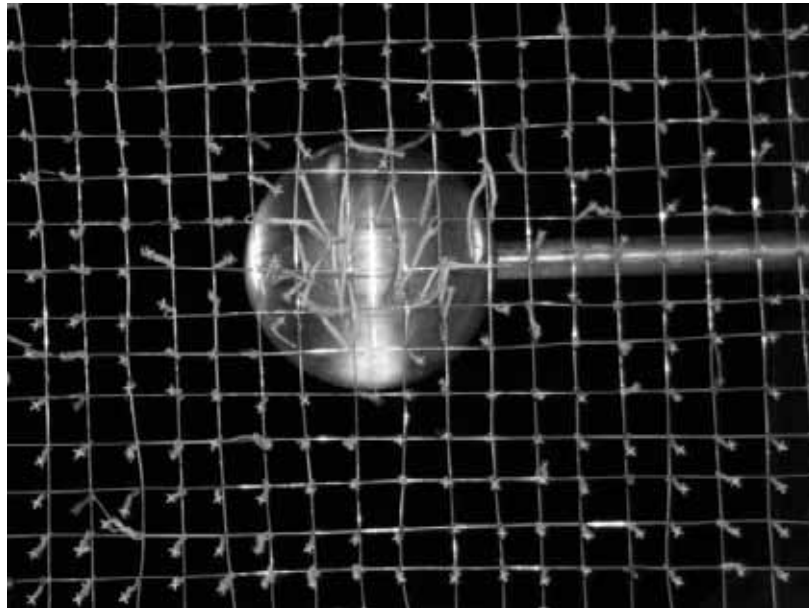


Figure 5.4. Tuft mesh. Flow speed of 10 m/s with synthetic jet. Tuft screen 40 mm offset.



Figure 5.5. Tuft mesh. Flow speed of 10 m/s with synthetic jet. Tuft screen 40 mm offset. A side view of Figure 5.4.

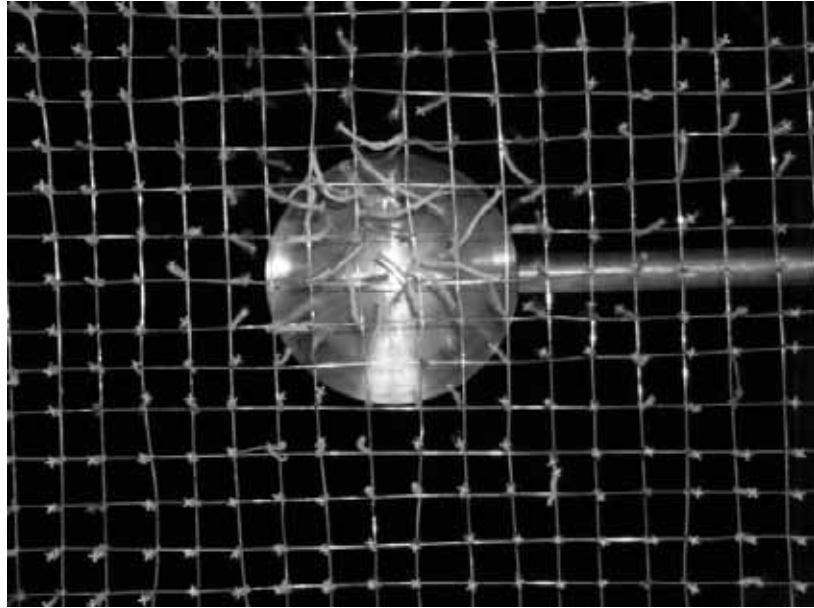


Figure 5.6. Tuft mesh. Flow speed of 20 m/s without synthetic jet. Tuft screen at 40 mm offset.

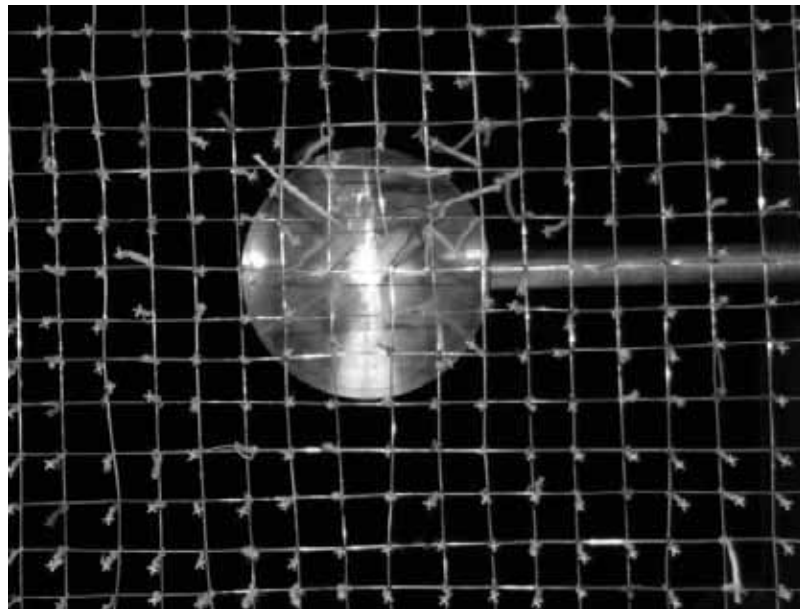


Figure 5.7. Tuft mesh. Flow speed of 20 m/s with synthetic jet. Tuft screen at 40 mm offset.

### 5.2.1 Wake Characterisation: An introduction to wake surveys and data validation

The criteria developed in the present work made possible the reliable analysis of the wake survey data obtained from the five-hole pressure probe. The criteria proved extremely useful, serving as a validation tool with which to assess the wake survey measurements to determine regions of reversal of flow and to assist in characterising the wake region.

The pressure measurements obtained from the five-hole probe directly provide the total and static pressure at the measurement point in the flow field. As a consequence of acquiring these two different pressures we can then use Bernoulli's equation to obtain the unknown dynamic pressure component which, together with the static pressure, makes up the measured total pressure at each survey point. The dynamic pressure component is due to the kinetic energy of the flow, and we are thus able to calculate the magnitude of the velocity of the flow at each survey point. The calibration of the probe not only allows for the determination of the total and static pressure but also the flow vector or directionality of the flow at the measurement point. This enables the calculation of the total velocity vector,  $\vec{V}$  which is then used to construct the three-dimensional velocity field. The magnitude of total velocity vector together with the known flow angle allows us to determine the three-dimensional velocity components ( $u, v, w$ ). The three-dimensional velocity components can then in turn be used to calculate other useful wake characterisation parameters such as the total vorticity,  $\vec{\xi}$  and its components ( $\xi_x, \xi_y, \xi_z$ ).

We begin by characterising the flow for the standard sphere and then use this as a benchmark with which we can then compare the effects of applying the synthetic jet at three different angles.

We sought to validate the measurements taken from the five-hole probe and ascertain the accuracy with a more sophisticated measurement method. For this reason we employed the use of hot-wire anemometry. We used a one-dimensional Dantec sensing probe as outlined in Chapter 3 to measure the velocity in a sample region within the wake. The results of the two methods have been tabulated for the sampled wake region and a comparison is made using two difference parameters as follows. As shown in Table 5.9, we have firstly calculated the percentage difference between the two methods based on the hot-wire velocity and secondly based on the maximum velocity attained in that sampled traverse of the probe. The purpose of making these two different comparisons is to show the direct difference in velocity measurements and then weigh this up relative to the maximum velocity which is approximately equal to the freestream velocity.

The two measurement methods were tested on the standard sphere and also with the synthetic jet applied at an angle of incidence of  $6.5^\circ$ . The first column shows the measurements of velocity as calculated from the five-hole probe. It should be noted that since the measurements of the five-hole probe were in the separated flow region the velocity was calculated on the absolute difference between the total and static pressures. When taking measurements with the five-hole probe in a region with reversing flow, the fluid velocity in the direction of the x-axis along the wind tunnel will be small. The static pressure in the near wake region, where this highly reversing flow is occurring can be considered constant. Further, the total pressure in this region will be significantly closer to the static pressure. Thus it is a reasonable measure to take the absolute value which will give us a rough indication of the very much reduced velocity in this region with respect to the freestream velocity along the x - axis.

Consider the percentage difference between the five-hole probe and hot-wire velocity relative to the hot-wire velocity as denoted by  $\Delta U_{\% \text{ hot-wire}}$  in Table 5.9. In the no synthetic jet case, very close to the sphere the velocity difference is

substantial and then decreases at a distance between 10 and 30 mm from the surface and then rises rapidly around the 40 mm point and finally decreases as freestream is approached. At this closeness, the probe could be influenced by the effects of the sphere surface so we see a higher percentage difference. At the 40mm point, the flow begins to recover slightly which brings the probe within the calibrated range producing more accurate values than the hot-wire since the velocity will not be one-dimensional as per the hot-wire probe. Nonetheless when we compare the column of  $\Delta U_{\% \text{ of } U_{\max}}$  we see that the error compared with the maximum velocity is small in the region of flow reversal and only becomes significant when we approach regions where the probe velocity is within its calibrated range.

Now consider the case were we apply the synthetic jet. It shows an even greater difference between the two instruments although it follows a similar pattern to the no synthetic jet case with the highest difference occurring around the transition to freestream at  $x = 40$  mm. With the application of the synthetic jet the reverse flow is reduced producing more accurate results than previously in this high reversal of flow region within the wake. Thus there is a greater difference between the two instruments.

The same understanding can be gained from examining the column of  $\Delta U(\% \text{ of } U_{\max})$ . The percentage difference in the region very close to the sphere becomes negligible relative to the maximum velocity since we are in a high reverse flow region and the velocity is small. Moving further away from the sphere the velocity starts to be corrected back towards freestream in fact earlier with the application of synthetic jet, thus again bringing the flow within the probe's calibrated data set.

The use of hot-wire to validate the five-hole probe proved successful in allowing the full use of the survey measurements. In addition, it has shown that the application of the synthetic jet has the effects of improving the flow within the wake. As

mentioned already this was only a sample region to validate the entire set of five-hole probe survey measurements and we only examined the synthetic jet applied at  $6.5^\circ$ . This formed a positive basis for the effects of synthetic on the sphere flow as well as characterising the flow with the measured data set.

## Results and Discussion: Bluff Body Wake Analysis

			No Synthetic Jet				Synthetic Jet at 6.5°			
x	y	z	$U_{\text{five-hole probe}}$ (m/s)	$U_{\text{hot-wire mean}}$ (m/s)	$\Delta U_{\% \text{ hot-wire}}$ (m/s)	$\Delta U_{\% \text{ of } U_{\text{max}}}$ (m/s)	$U_{\text{five-hole probe}}$ (m/s)	$U_{\text{hot-wire mean}}$ (m/s)	$\Delta U_{\% \text{ hot-wire}}$ (m/s)	$\Delta U_{\% \text{ of } U_{\text{max}}}$ (m/s)
1	0	5	2.66	1.57	69	10	3.15	1.52	107	15
1	10	5	2.25	2.48	-9	-2	2.84	2.07	37	7
1	20	5	1.84	2.43	-24	-6	2.71	2.26	20	4
1	30	5	1.92	2.20	-13	-3	2.75	2.67	3	1
1	40	5	3.50	1.96	79	15	7.96	2.11	277	54
1	50	5	10.63	9.65	10	9	10.81	10.20	6	6
5	0	5	1.91	1.80	6.06	1	2.73	1.68	63	10
5	10	5	1.94	2.12	-8.31	-2	2.71	1.78	53	9
5	20	5	1.82	2.59	-30.02	-7	3.36	1.62	108	16
5	30	5	2.05	2.19	-6.49	-1	2.69	2.41	12	3
5	40	5	4.05	2.18	86.23	18	9.41	5.52	71	36
5	50	5	10.66	9.51	12.08	11	10.77	9.49	14	12
10	0	5	1.87	2.26	-17.10	-4	2.82	2.11	34	7
10	10	5	1.78	2.76	-35.66	-9	3.12	2.09	50	10
10	20	5	1.79	2.66	-32.58	-8	4.72	1.88	151	26
10	30	5	2.01	2.28	-11.92	-3	1.21	2.42	-50	-11
10	40	5	4.41	2.59	70.26	17	9.82	4.52	117	49
10	50	5	10.74	10.02	7.26	7	10.74	9.87	9	8
20	0	5	1.81	2.98	-39.40	-11	2.75	3.35	-18	-6
20	10	5	1.92	2.78	-30.76	-8	3.11	3.01	3	1
20	20	5	2.03	2.47	-17.79	-4	4.78	2.55	87	21
20	30	5	2.14	1.99	7.63	1	1.21	3.10	-61	-18
20	40	5	6.55	4.96	32.23	15	9.58	3.75	156	55
20	50	5	10.96	9.52	15.16	13	10.68	9.25	15	13
40	0	5	2.00	3.88	-48.39	-18	4.19	4.22	-1	0
40	10	5	2.41	3.71	-35.04	-12	7.33	3.81	92	34
40	20	5	3.18	3.36	-5.34	-2	3.56	3.65	-3	-1
40	30	5	3.99	3.43	16.29	5	6.23	3.69	69	25
40	40	5	8.67	5.99	44.76	25	10.18	6.04	68	40
40	50	5	10.58	9.35	13.16	12	10.27	8.92	15	13

Table 5.9. Comparison of five-hole probe and hot-wire measurement data.

### 5.2.2 Wake Characterisation: Wake surveys – velocity field

The velocity field was obtained using pressure measurements from the five-hole probe and then plotted using the Matlab software program. The plots of the results analysis is shown in Figure 5.8 through to Figure 5.11. Figure 5.8 shows the standard sphere case without the application of synthetic jet with the magnitude of the vector represented by its length in the plot. In the case of the standard sphere, the vectors form a reasonably symmetrical near wake region behind the unsupported portion of the side supported sphere which we should expect at this Reynolds number. We can see that there exists a reversal of flow in areas of the velocity field where the vectors follow a curvilinear path and then the vector magnitude decreases to a small value as indicated by the length of the vector being reduced to almost a point. This is especially the case in the region  $0 \leq x/D \leq 1$ , whereas beyond  $x/D \geq 1.5$ , the flow tends back towards freestream conditions. Also the wake stretches to the boundaries of the sphere in the vertical axis going from  $-0.625 \leq y/D \leq 0.625$  with the flow fully recovering within a very small region at the limit of the wake survey in this direction. The same is also observed along the z-axis with the flow being highly reversed around the origin at  $z/D = 0$  and then changing to freestream velocity close to the limit of the wake survey at  $z/D = 0.625$ . Further detailed plots were compiled by taking sections of the surveyed wake region showing the velocity profile in the xy plane along the z-axis, yz plane along the x-axis and xz plane along y-axis. The velocity profiles gave the same trends already observed in the overall vector field, although the flow direction could be more clearly distinguished throughout the region.

The difference in the velocity field when the synthetic jet is activated can be seen in all of the following cases. In Figure 5.9, the synthetic jet is applied at an angle of incidence of  $6.5^\circ$  giving an increase in vector magnitude and a corresponding straightening of the vectors. With the synthetic jet being applied only at  $6.5^\circ$ , this

produces an asymmetry to the improved flow field with greater increase in velocity evident in the top part of the near wake. The synthetic jet at such an acute angle and close to the fore stagnation point does provide some improvement to the flow across the vertical axis.

In the next case, Figure 5.10, the synthetic jet was applied very close to the standard sphere separation point which occurs at  $83^\circ$  and was established by the previous work (Findanis. & Ahmed. 2007). The synthetic jet was now located at  $76^\circ$  from the fore stagnation point. This seems to have had the advantage of delaying separation substantially on the upper side of the sphere as evidenced from the higher velocity and the reduced wake much more so in the top region of the near wake. It can also be observed that there is a stream of vectors in the top half that seems to indicate a trajectory of increased velocity caused by the application of the synthetic jet. At  $76^\circ$ , the localised synthetic jet is advanced further along and closer to the wake and thus a more direct asymmetrical affect may be seen.

Finally we placed the synthetic jet post-separation within the wake region at  $100^\circ$  angle of incidence, as shown in Figure 5.11. It might seem improbable that the synthetic jet would be able to have any effect in a region without any boundary-layer and in a highly turbulent shear flow but it can be seen that, here too, we are able to see an improvement in the aerodynamics of bluff body wake. The greatest asymmetry is shown in this case with momentum imparted from the synthetic jet contributing directly to the disturbed flow in the top part of the sphere wake increasing the velocity. This increase of velocity in this region must also transmit to other parts of the wake since it is seen that the wake reduced in size. Increases in streamwise velocity can be seen further downstream and in the bottom region of the wake, an improvement which was also shown in the vector field.

The three-dimensional vector plots correspond to the results of the flow visualisation where we saw in the results a shortening of the wake region with an increase in streamwise velocity and less reversal of flow as was indicated by the tufts.

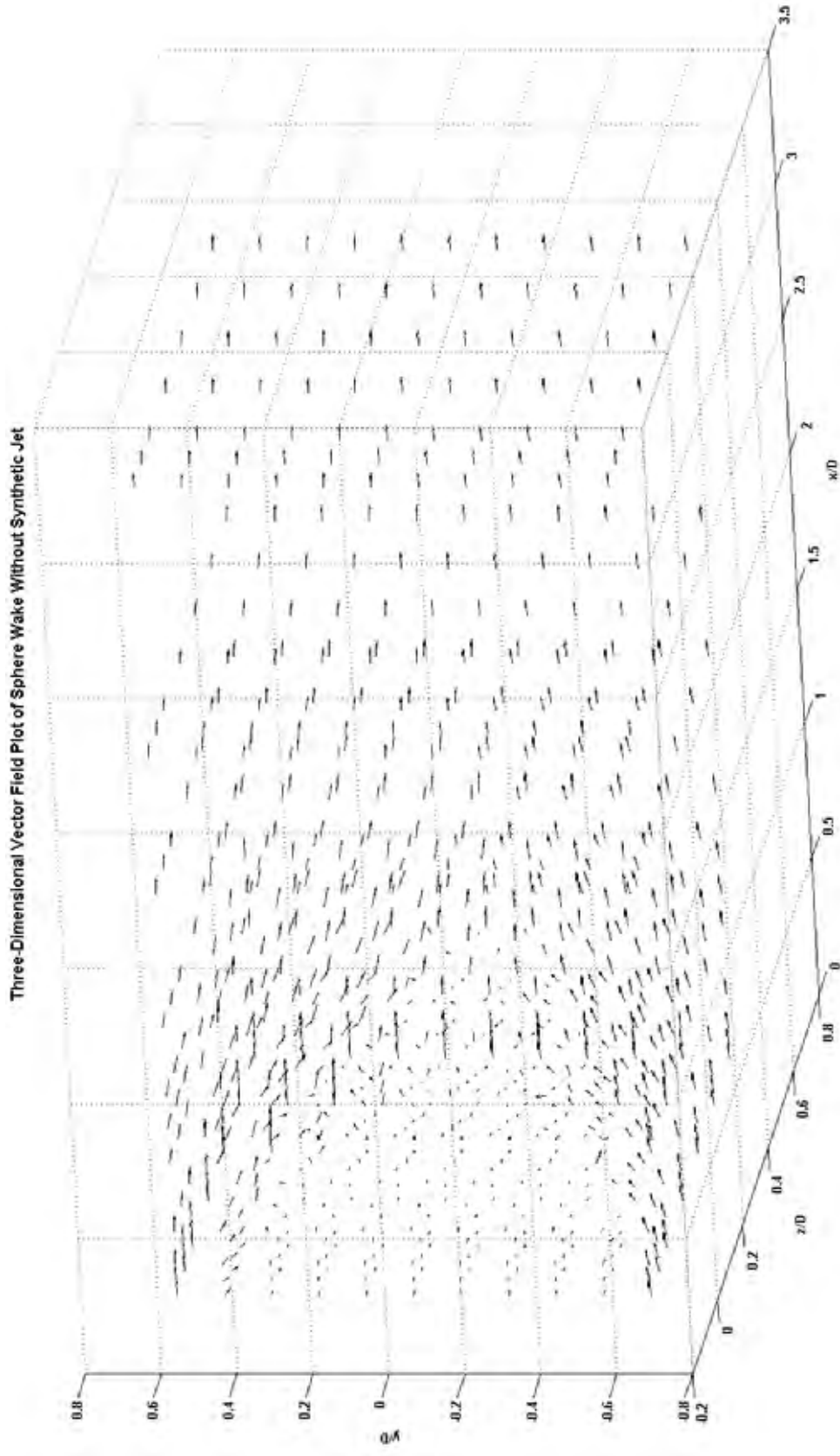


Figure 5.8. Three-Dimensional Vector Field Plot of Sphere Wake Without Synthetic Jet – Standard Sphere

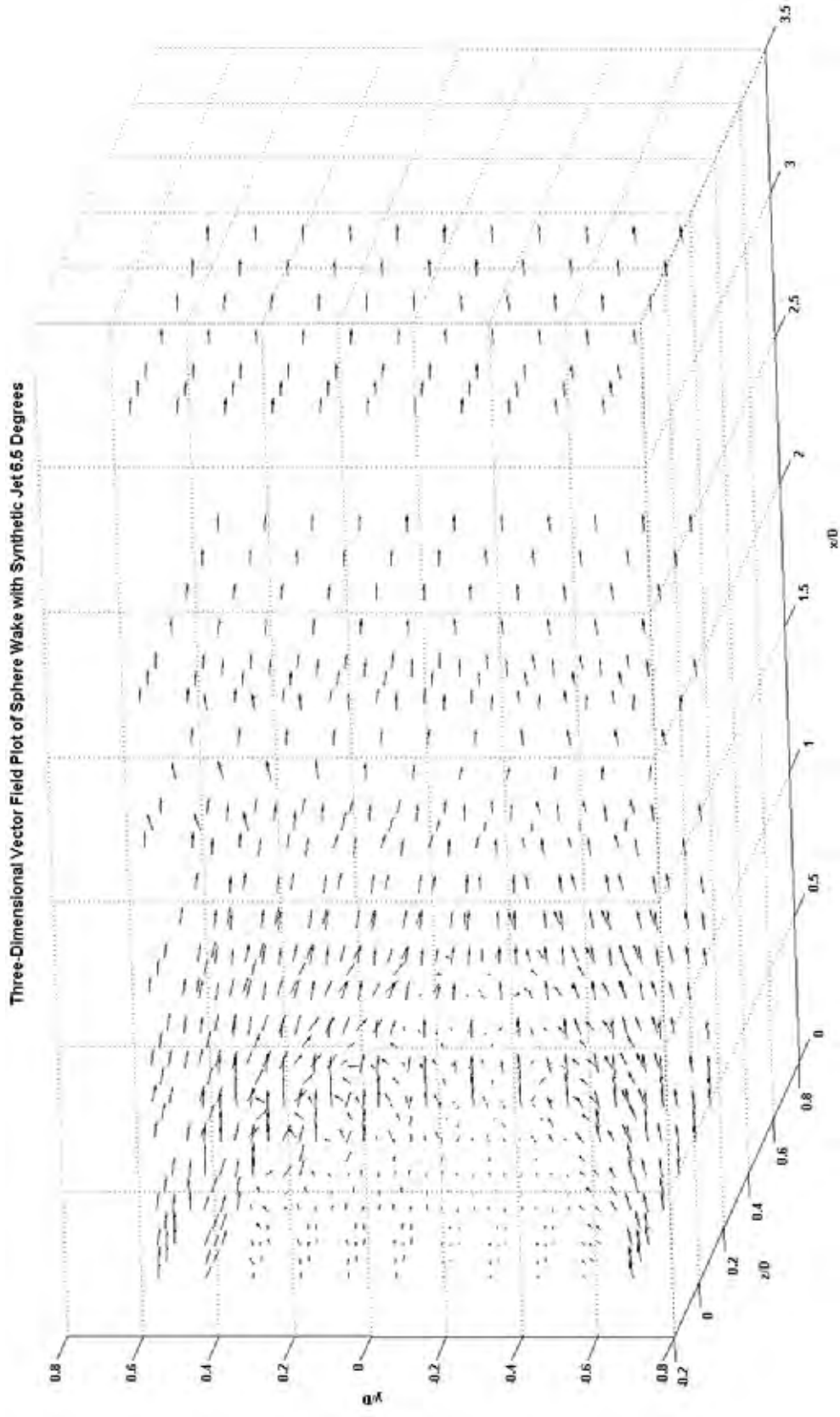


Figure 5.9. Three-Dimensional Vector Field Plot of Sphere Wake with Synthetic Jet at 6.5 Degrees

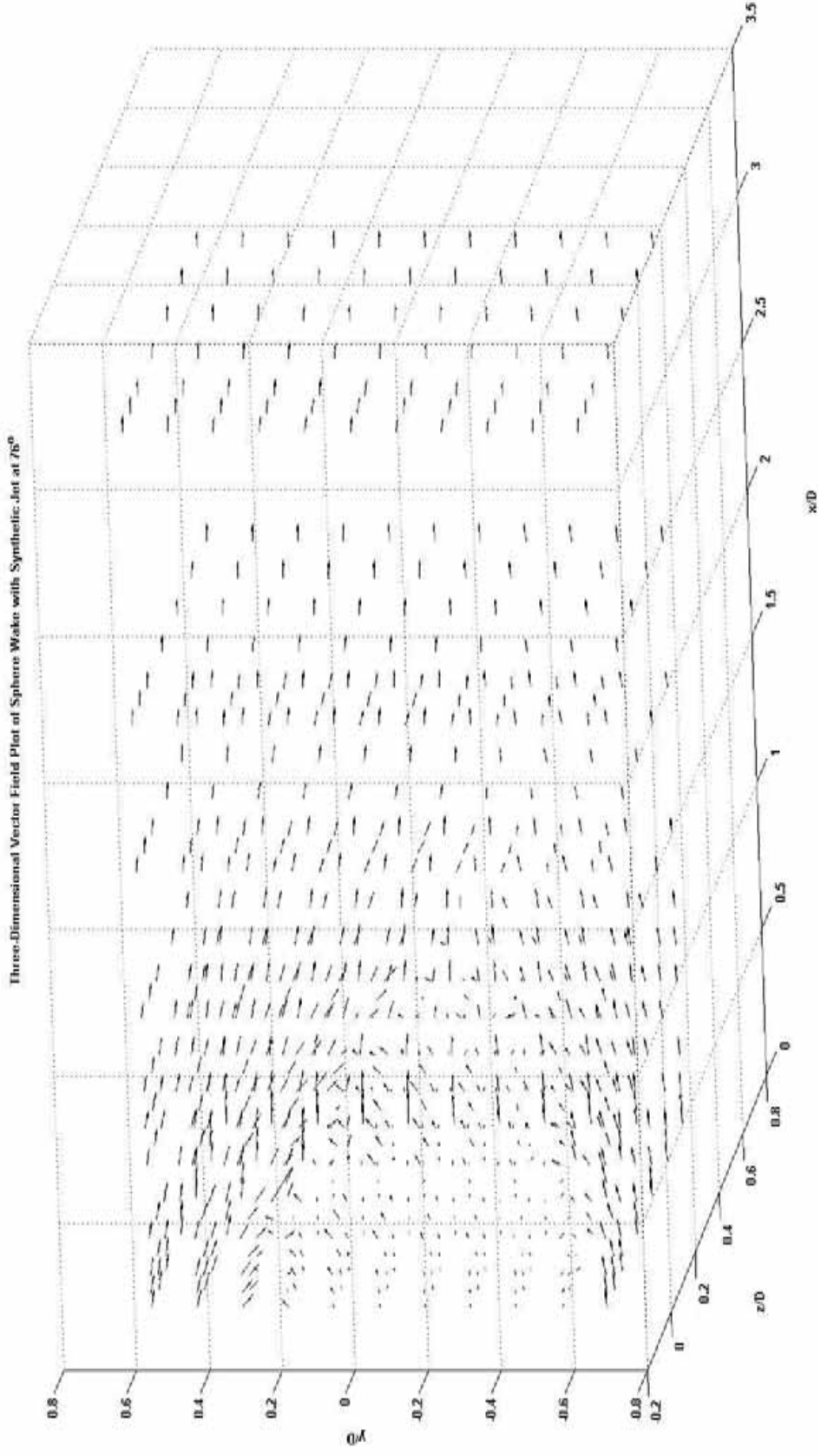


Figure 5.10. Three-Dimensional Vector Field Plot of Sphere Wake with Synthetic Jet at 76 Degrees

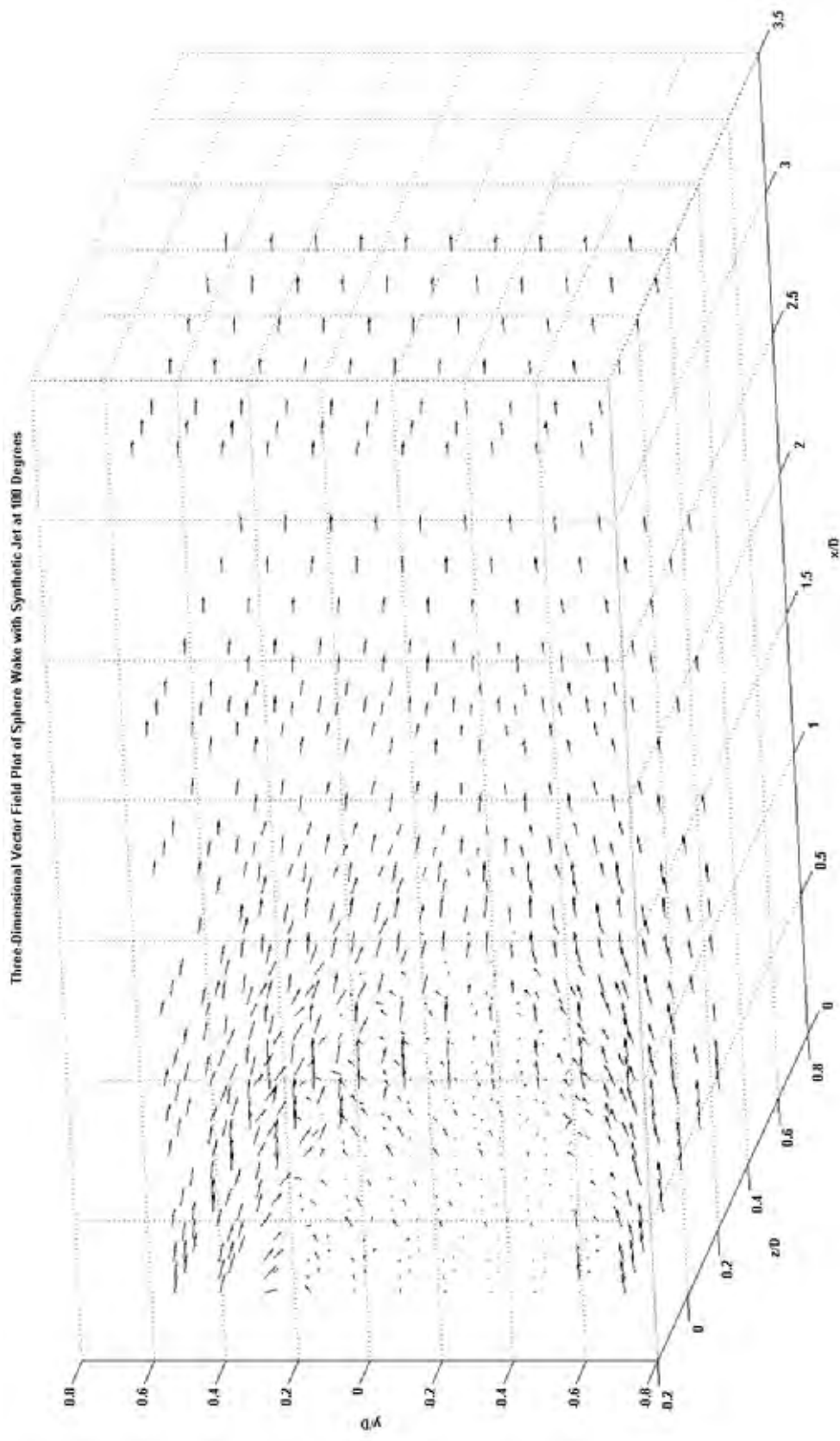


Figure 5.11. Three-Dimensional Vector Field Plot of Sphere Wake with Synthetic Jet at 100 Degrees

### 5.2.3 Wake Characterisation: Wake Surveys – pressure and vorticity contours

#### 5.2.3.1 Pressure Contours

##### a. Dynamic Pressure

The dynamic pressure field can be used to give an indication of the movement of fluid through the wake region or in a sense the kinetic energy in the wake. The dynamic pressures are given in the following contour maps shown in Figure 5.12 through to Figure 5.15. The dynamic pressure contours are plotted as sections of the xy plane along the z-axis with all axes normalised against the characteristic length of the sphere diameter. The negative values in the plots represent regions of flow reversal, although highly negative values tend to indicate that the flow has been accelerated due to the difference between the total and static pressures measured on the five-hole probe. The no synthetic jet case or the standard sphere case shows a uniform retardation of dynamic pressure in the wake of the sphere as indicated by the dark region with a value of zero in Figure 5.12. This near wake region possess highly three-dimensional reversing flow as indicated by the criteria developed in the present work. This slow moving region decreases in size, as would be expected, in the outwards direction along the z-axis towards the freestream. When we reach the limit at  $z/D = 0.625$  we can see the flow splits into different regions as indicated by the various contour islands which could indicate vortices forming as the flow separates from the solid sphere surface.

As seen in Figure 5.13, with the synthetic jet at  $6.5^\circ$ , there is a decrease in the area of retardation of the fluid velocity as indicated by a smaller region of zero value. Further, the application of the synthetic jet indicates the asymmetry induced in the

flow and the resulting influence on the wake. Upon closer examination, we notice that the contour lines gather closely on the top half portion of the wake near the sphere body showing the effect of the synthetic jet to reduce wake size. The plot of  $z/D = 0.625$  shows smoother flow overall than the corresponding plot for the standard sphere case, indicating less reversal of flow and reduced vortex strength as the flow separates from the sphere especially in the upper half of the wake. Further, the asymmetry of the wake due to the influence of synthetic jet can be seen even at this extreme location along the  $z$  - axis. These trends of the synthetic influence on the wake region are also observed in Figure 5.14 and Figure 5.15, which show the synthetic jet at  $76^\circ$  and  $100^\circ$  respectively.

Figure 5.14 with the synthetic jet at  $76^\circ$  accentuates the localised synthetic jet applied only in the upper portion of the sphere, clearly showing the asymmetry of the wake region. The dark bubble like region is likely the accelerated flow due to the synthetic jet. There is a greater decrease in the upper half of the wake region with the contour lines pushed closer together than in the case of the synthetic jet at  $6.5^\circ$ .

Figure 5.15 shows the synthetic jet at  $100^\circ$ . At this extreme location, the synthetic jet still has an influence on the wake region showing improvements in the upper portion of the wake, where the synthetic jet is applied with a reduction in the wake and reversal of flow. As such the effects are much more localised, because the momentum imparted from the synthetic jet can only attempt to correct the already separated flow in the wake region. A large effect can be seen around the region  $z/D = 0.25$  where the synthetic jet is applied.

Results and Discussion: Bluff Body Wake Analysis

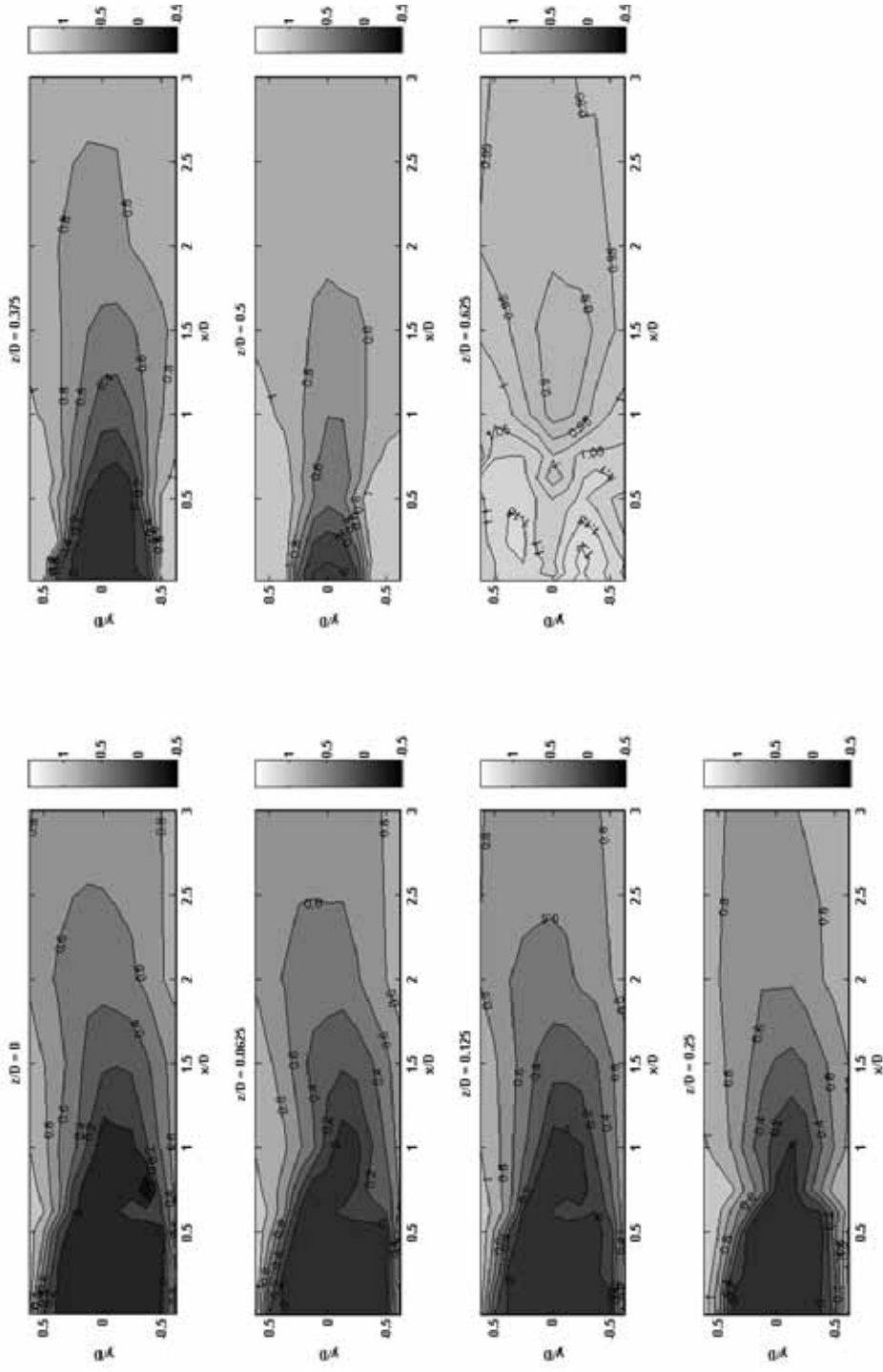
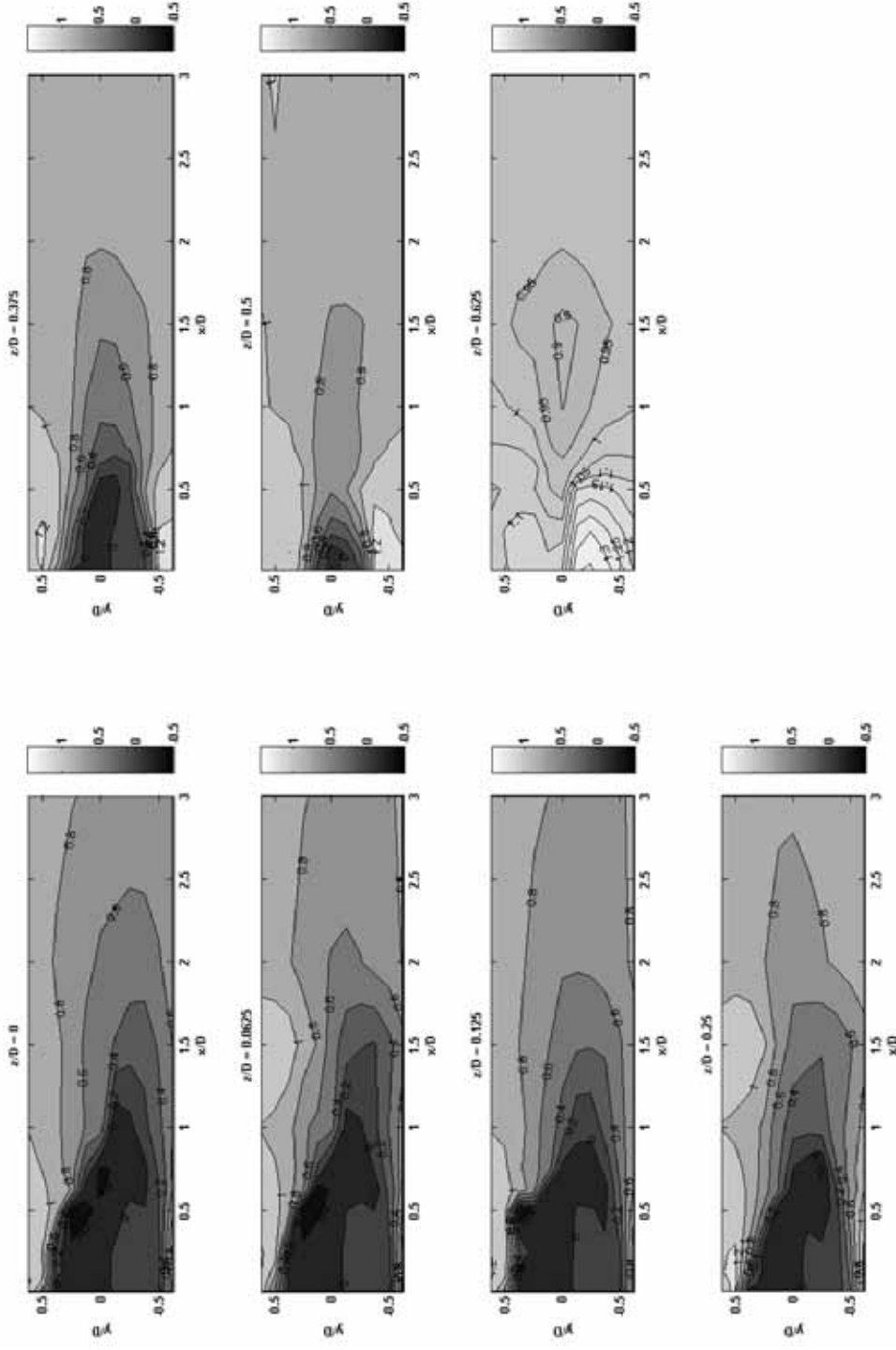


Figure 5.12. Sphere Wake Survey, Dynamic Pressure – No Synthetic Jet

## Results and Discussion: Bluff Body Wake Analysis

Figure 5.13. Sphere Wake Survey, Dynamic Pressure – Synthetic Jet at  $6.5^\circ$

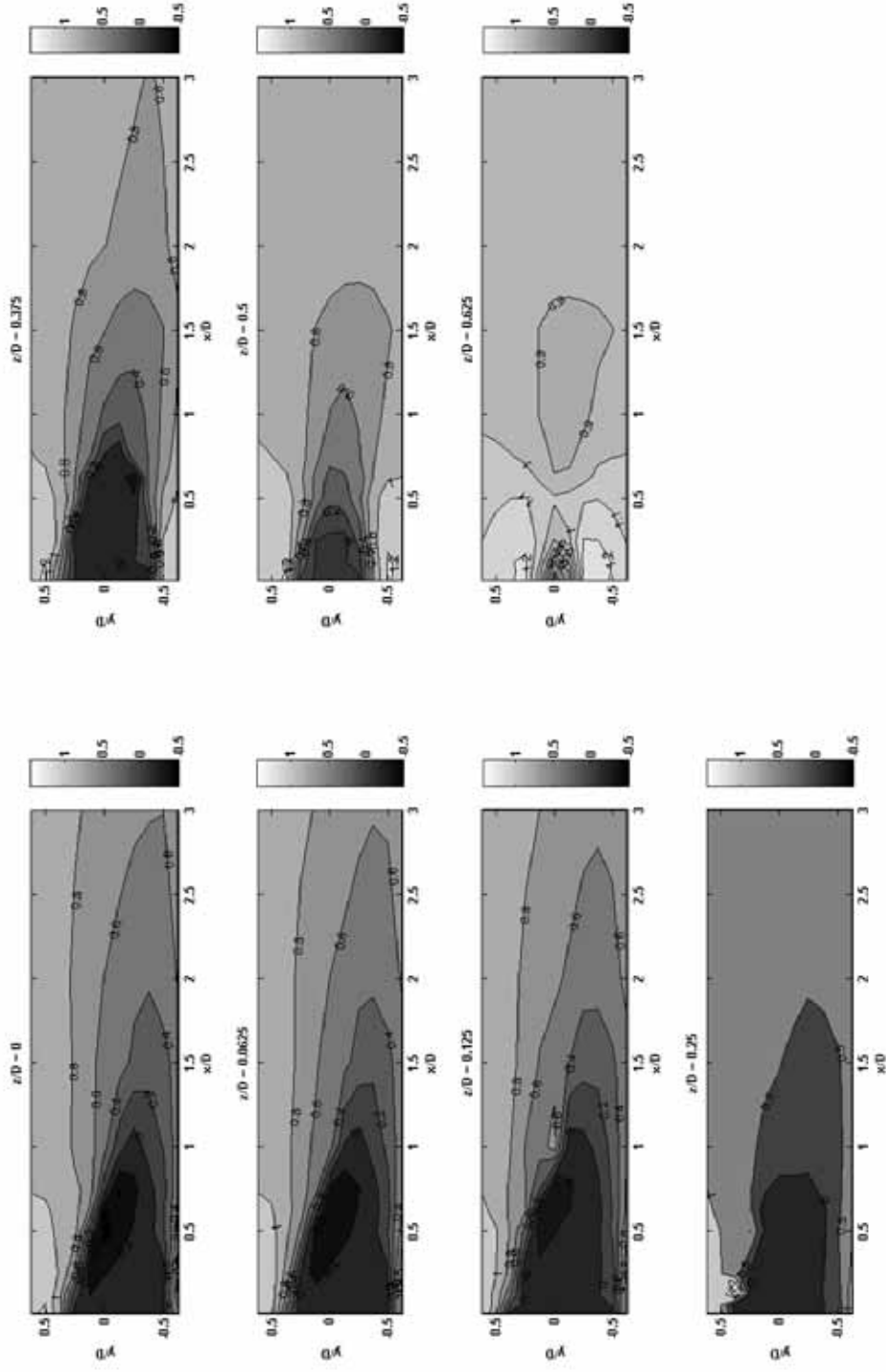
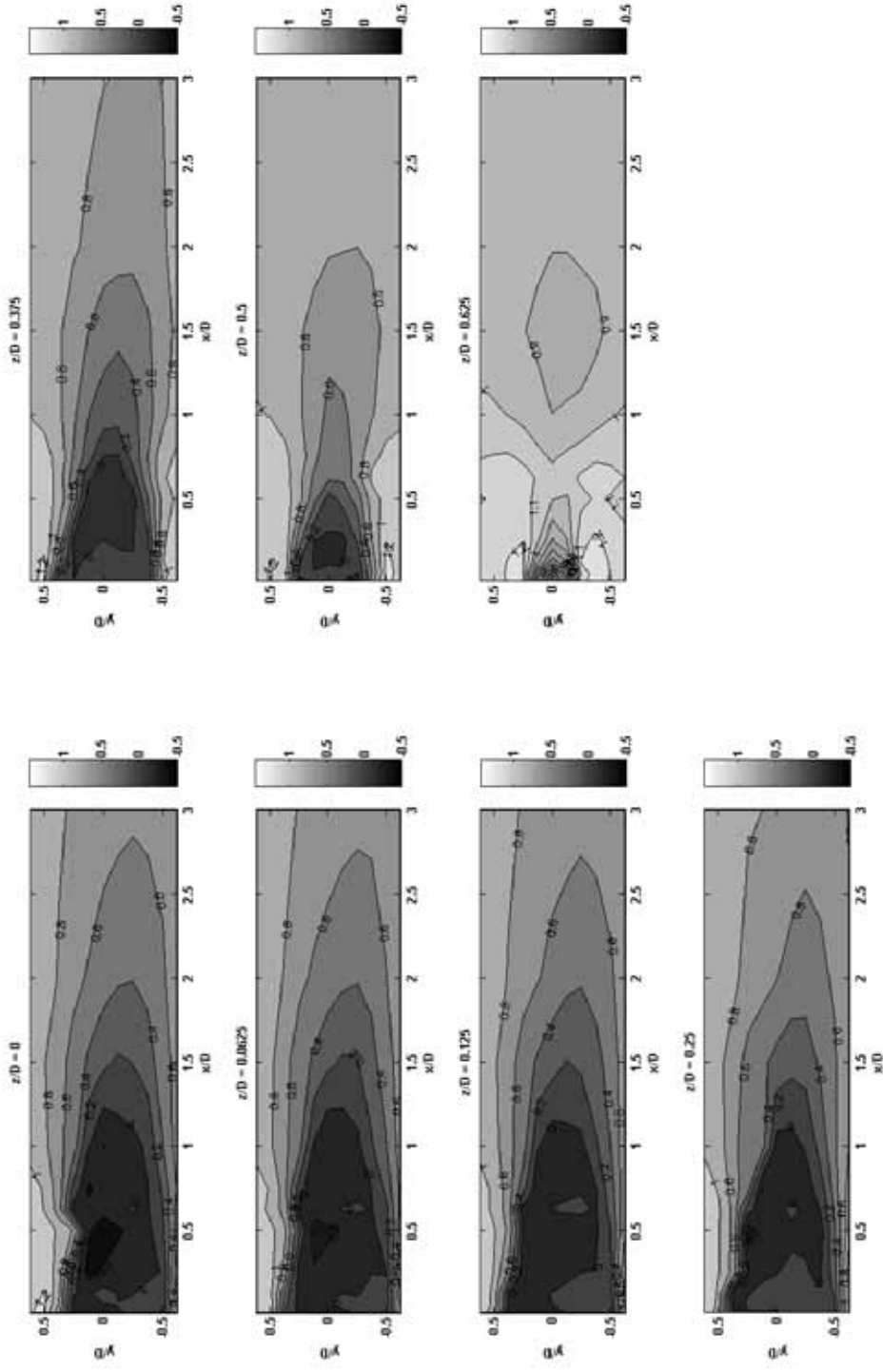


Figure 5.14. Sphere Wake Survey, Dynamic Pressure – Synthetic Jet at 76°

## Results and Discussion: Bluff Body Wake Analysis

Figure 5.15. Sphere Wake Survey, Dynamic Pressure – Synthetic Jet at  $100^\circ$

**b. Total Pressure**

The total pressure field reflects the amount of available energy that can bring about changes in its dynamic composition. A comparison of Figure 5.16, of the standard sphere, with Figure 5.17 through to Figure 5.19, indicates the momentum supplied by the synthetic jet generally increases the total pressure field so that it returns to its free stream value earlier downstream than without the activation of the synthetic jet. Thus, the total velocity vector is increased in the streamwise direction. This is in agreement with the streamwise component calculated for the velocity field.

The wake survey data from the five-hole pressure probe was arranged to represent each of the terms of the Bernoulli Equation. Bernoulli's equation, essentially representing the total energy of the incompressible fluid, can be stated as follows.

$$p_T = p_s + p_{dyn} + p_L \quad (5-7)$$

Now if point 1 is upstream of the sphere and point 2 is in the wake of the sphere then,

$$p_{T,1} = p_\infty + q_\infty + p_{L,1} \quad (5-8)$$

but  $p_{L,1} = 0$  since there are assumed no losses in the freestream flow and

$$p_{T,2} = p_{s,2} + p_{dyn,2} + p_{L,2} \quad (5-9)$$

Accordingly the five-hole probe measures the total and static pressure in the wake from which we then calculate the dynamic pressure. The total pressure in the wake is then expressed as,

$$p_{T,w} = p_{s,w} + p_{dyn,w} \quad (5-10)$$

and

$$p_{T2} = p_{T,w} + p_{L,w} \quad (5-11)$$

where  $p_{L,w} = p_{L,2}$ ,  $p_{s,w} = p_{s,2}$

For a general irrotational flow along a streamline  $p_{T,1} = p_{T,2}$  and so we can then calculate the losses in the wake.

$$p_{L,w} = p_{T,1} - p_{T,w}. \quad (5-12)$$

In addition to the dynamic pressure and total pressure contours, the static pressure and pressure losses contours were also constructed and plotted. These graphs provided evidence to substantiate the findings mentioned above, illustrating similar trends of the synthetic jet to improve the flow of the standard sphere at all three angles of incidence. The wake region was reduced along with the reversal of flow thus the losses in the wake decreased. In particular the static pressure plots indicated the changes to the pressure field when applying the localised synthetic jet at the different angles of incidence. Thus we could select different angles of localised synthetic jet to produce the desired changes in the flow field.

## Results and Discussion: Bluff Body Wake Analysis

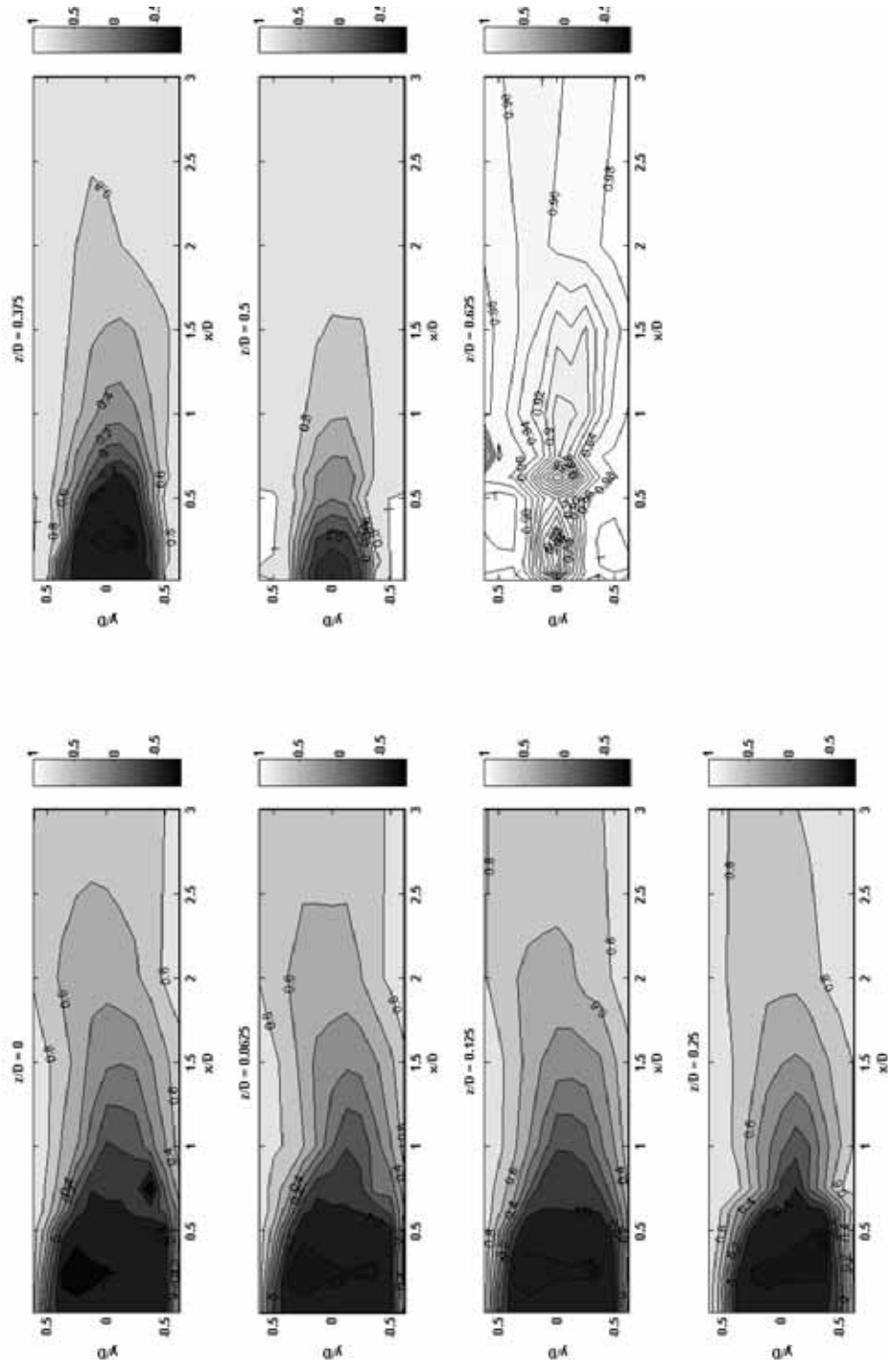
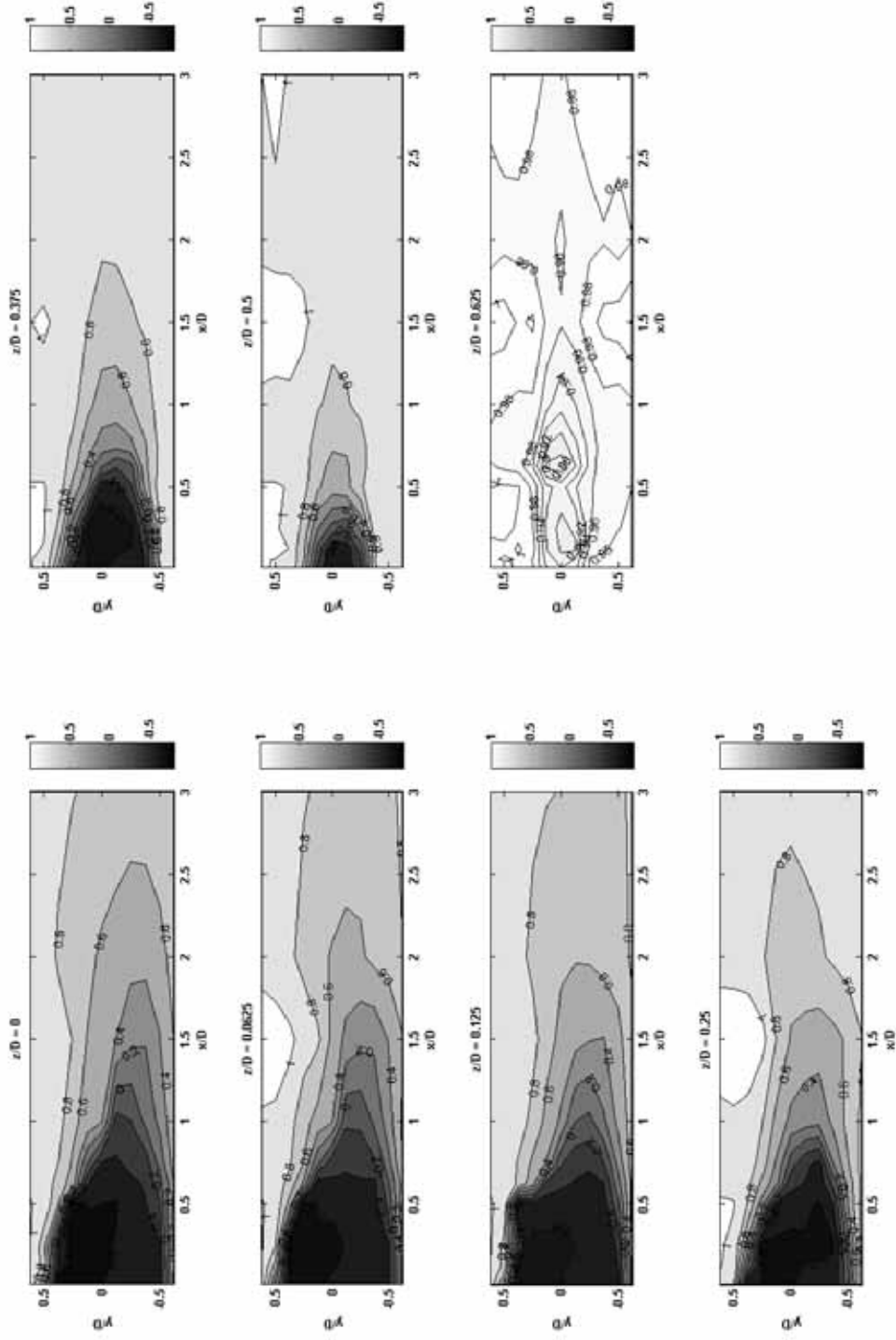
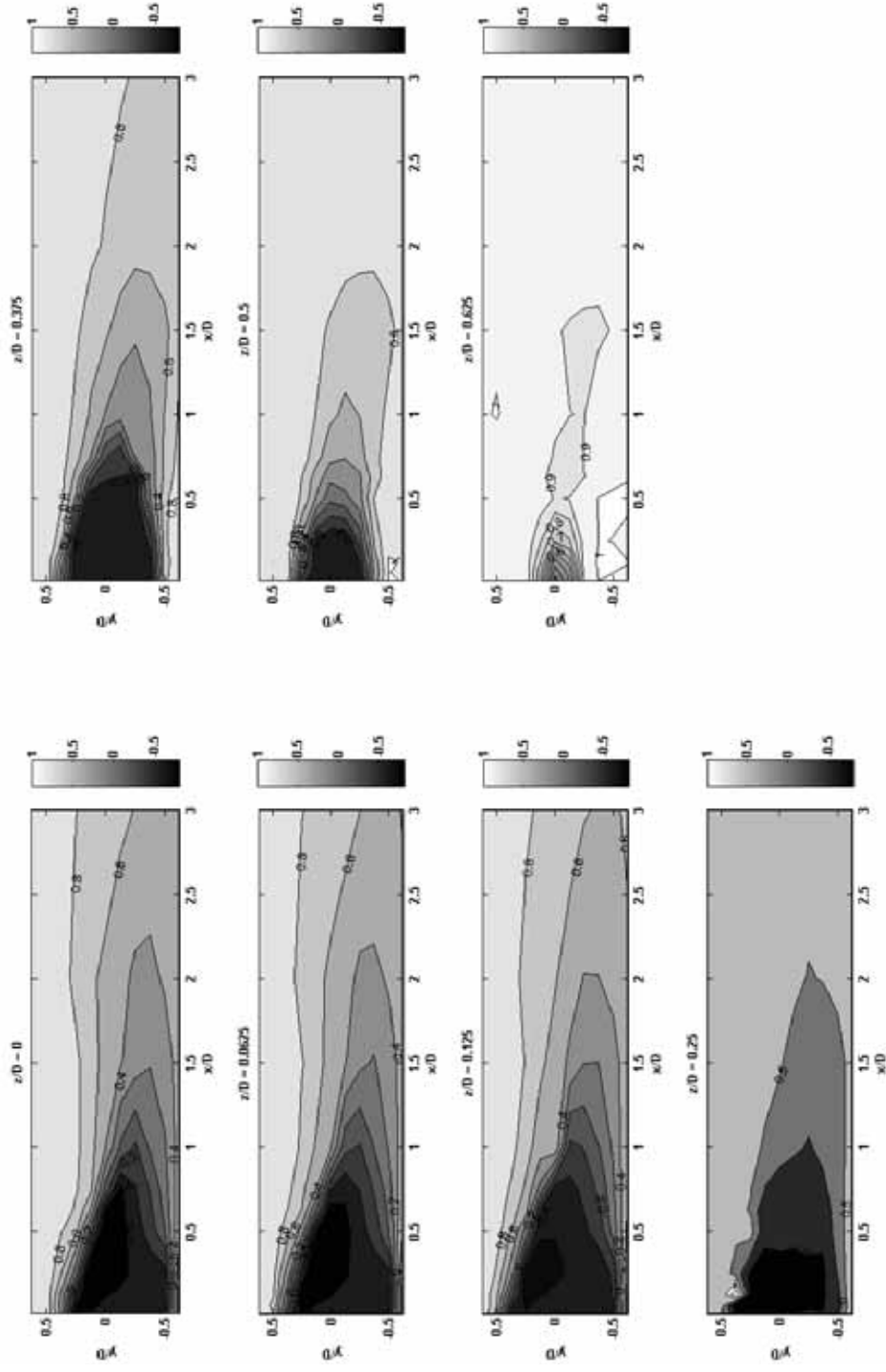


Figure 5.16. Sphere Wake Survey, Total Pressure - No Synthetic Jet

## Results and Discussion: Bluff Body Wake Analysis

Figure 5.17. Sphere Wake survey, Total Pressure - Synthetic Jet at  $6.5^\circ$

## Results and Discussion: Bluff Body Wake Analysis

Figure 5.18. Sphere Wake survey, Total Pressure - Synthetic Jet at  $76^\circ$

## Results and Discussion: Bluff Body Wake Analysis

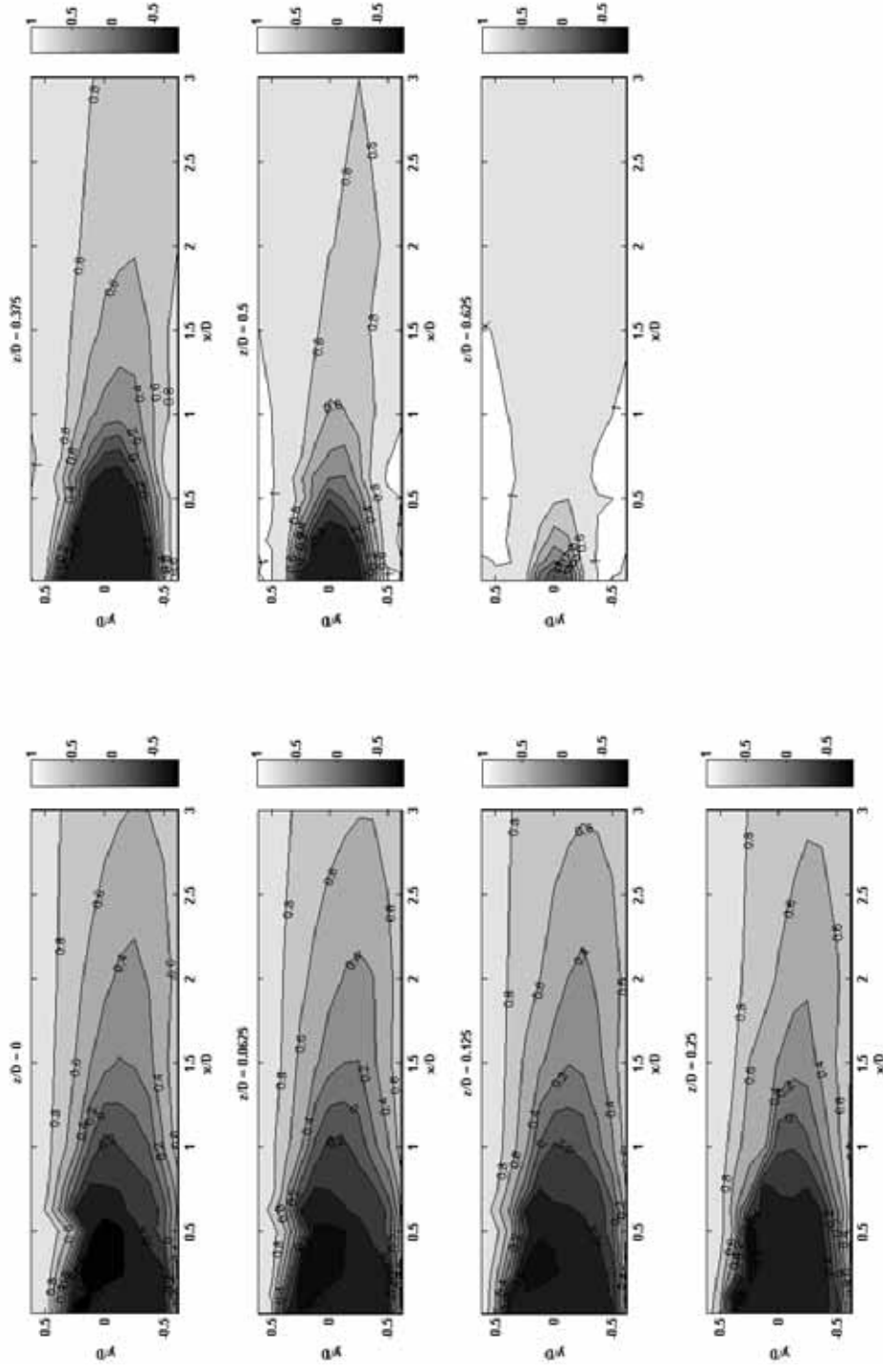


Figure 5.19. Sphere Wake survey, Total Pressure - Synthetic Jet at 100°

### 5.2.3.2 Vorticity Contours

The vorticity, a kinematic property of a fluid element, is defined as the curl of the velocity vector. The vorticity is twice the angular velocity vector and thus is a measure of the rotation of a fluid particle. The rotation of fluid elements is associated with flow over solid bodies and surfaces where the fluid interacts with a surface and viscosity affects the orientation of the fluid particle or causes rotation (Cengel and Cimbala 2006).

In Cartesian coordinates,  $(\vec{i}, \vec{j}, \vec{k})$ ,  $(x, y, z)$  and  $(u, v, w)$  the vorticity vector or the total vorticity in three-dimensional space is given by (Cengel and Cimbala 2006):

$$\vec{\zeta} = \left( \frac{\partial w}{\partial y} - \frac{\partial v}{\partial z} \right) \vec{i} + \left( \frac{\partial u}{\partial z} - \frac{\partial w}{\partial x} \right) \vec{j} + \left( \frac{\partial v}{\partial x} - \frac{\partial u}{\partial y} \right) \vec{k} \quad (5-13)$$

The total vorticity calculation was performed using non-dimensionalised physical variables of the velocity components  $(u, v, w)$  and of the distance along the coordinate axes  $(x, y, z)$ . Each velocity component was non-dimensionalised using the freestream velocity,  $U_\infty$ . The distance at each data point along the respective  $(x, y, z)$  coordinate axis was non-dimensionalised using the characteristic length of the solid body, which in this case is the sphere diameter,  $D$ .

The following plots in Figure 5.20 through to Figure 5.23 show the manner in which the total vorticity vector varies at different  $yz$  planes along the  $x$ -axis. When we observe Figure 5.20, we can immediately verify the validity of our experimental results, as mentioned earlier, using the standard sphere which produces relatively

symmetrical contours for all components of the total vorticity vector. Thus it can be used as a basis for comparison of the experimental results with the synthetic jet applied. We should note that, for all figures, only half of the sphere is shown, as was the case with the three-dimensional velocity vector and contour plots.

Firstly, comparing Figure 5.20 and Figure 5.21, we observe the effects of the synthetic jet at  $6.5^\circ$  with respect to the total vorticity vector along the x-axis. The size of the vortex, which is centred at approximately  $z/D = 0.5$  and is apparent in the graphs from  $x/D = 0.0125$  to  $x/D = 0.25$  with no synthetic jet, dissipates in strength. It is also broken into two separate vortices at  $x/D = 0.125$  with the synthetic jet applied. Also, the vortex has decreased in size when the synthetic jet is applied on all planes shown. For all plots for  $x/D > 0.0125$ , the total vorticity in the yz plane has been substantially dispersed with a breaking up of the key coherent flow structure at the outer edge of the sphere, although surprisingly at  $x/D = 1.5$ , there appears to be some vorticity formed. Previously it did not appear in the no synthetic jet case. This could be due to vortex oscillations being formed, due to the application of the synthetic jet which would contribute to the vorticity at this particular synthetic jet frequency.

Comparing Figure 5.20 and Figure 5.22, the effects of the synthetic jet are even more prominent. The vorticity at  $z/D = 0.5$  is broken up from the very first measurement plane, that is from  $x/D = 0.0125$ . However, it is interesting that there exists vorticity on one of the planes that does not seem to have been affected by the synthetic jet, that plane being at  $x/D = 0.125$ . Thereafter, when  $x/D > 0.125$ , the vorticity has been dispersed but even more so than when the synthetic jet was applied at  $6.5^\circ$ .

Finally, looking at Figure 5.20 and Figure 5.23, we see the significant effect a relatively weak synthetic jet can have, even in the separated flow region of the sphere. This figure shows the vorticity being dispersed and inhibited from forming

strong recirculation zones. Thus vorticity strength of the flow has been reduced as well as the flow being significantly pushed towards an irrotational flow or streamlined flow.

## Results and Discussion: Bluff Body Wake Analysis

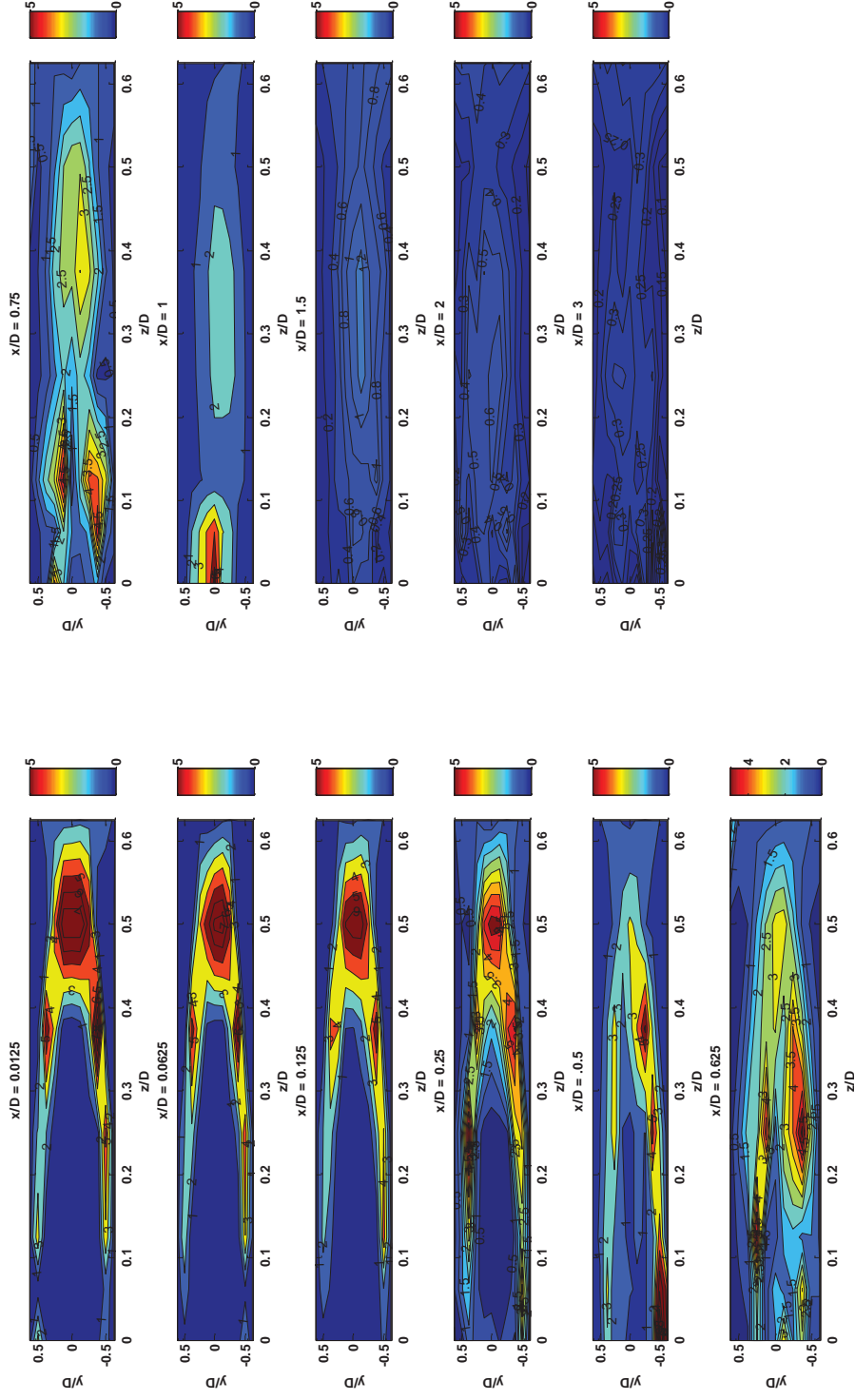
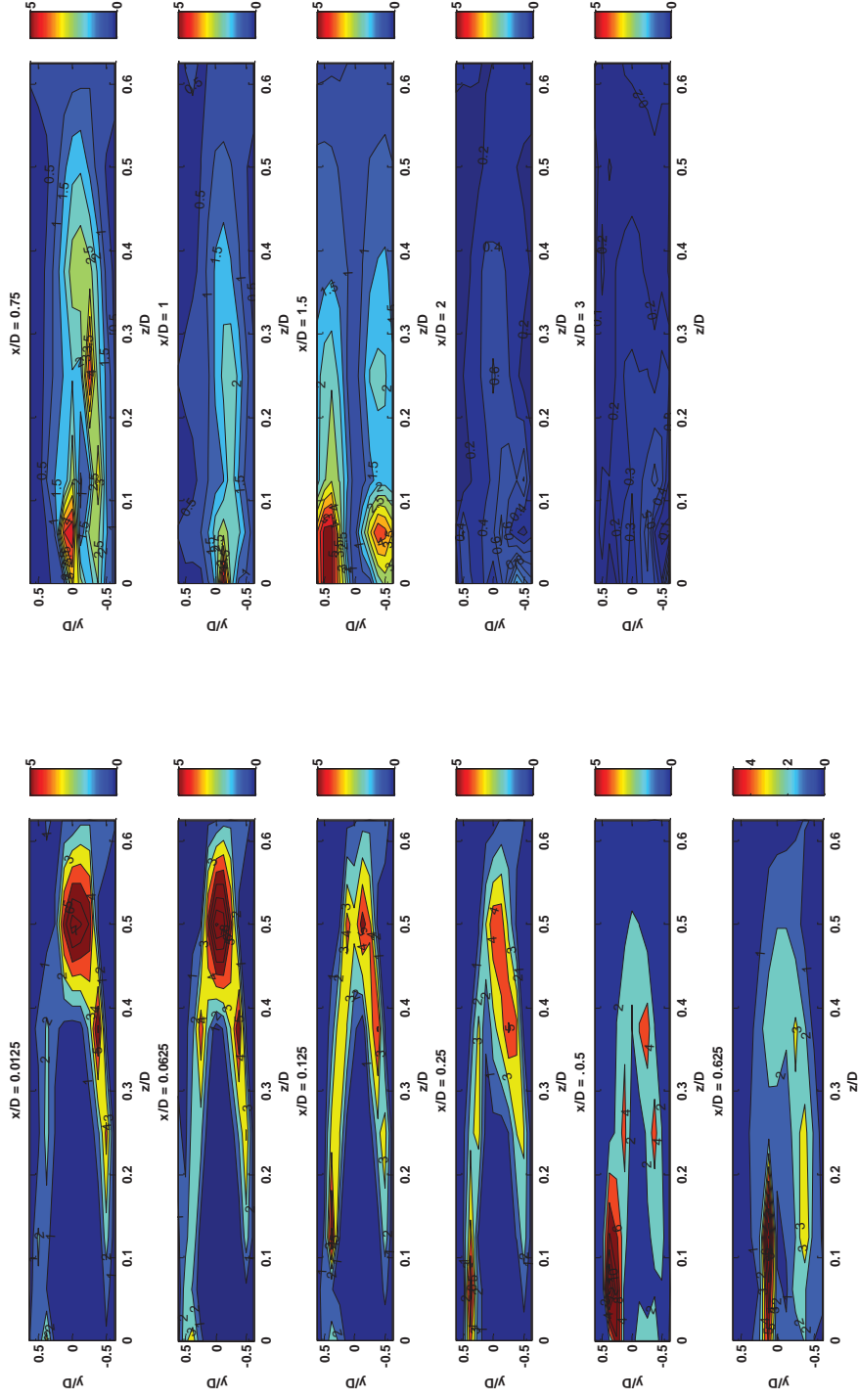
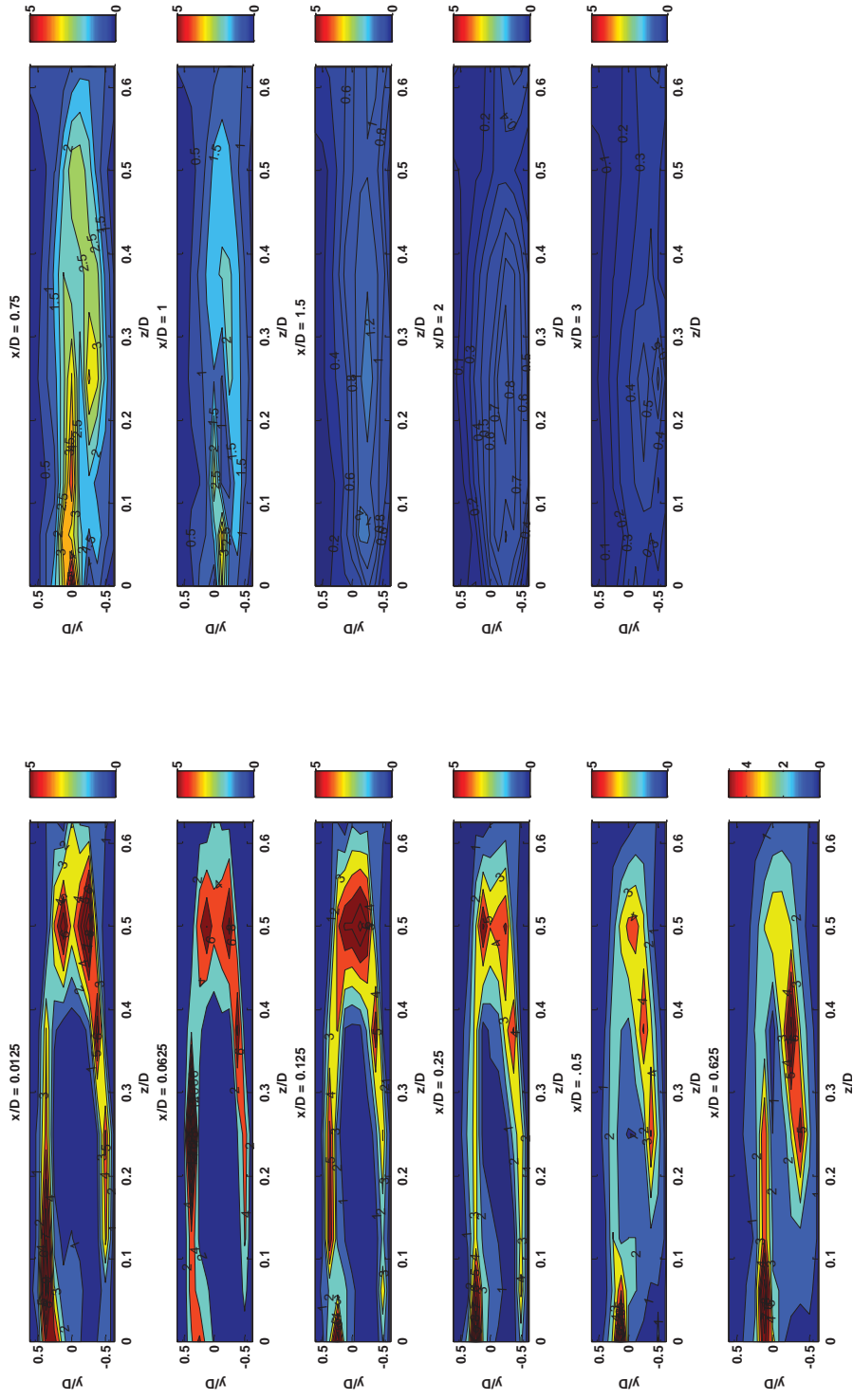


Figure 5.20. Total Vorticity at different points along the x-axis. No synthetic jet.

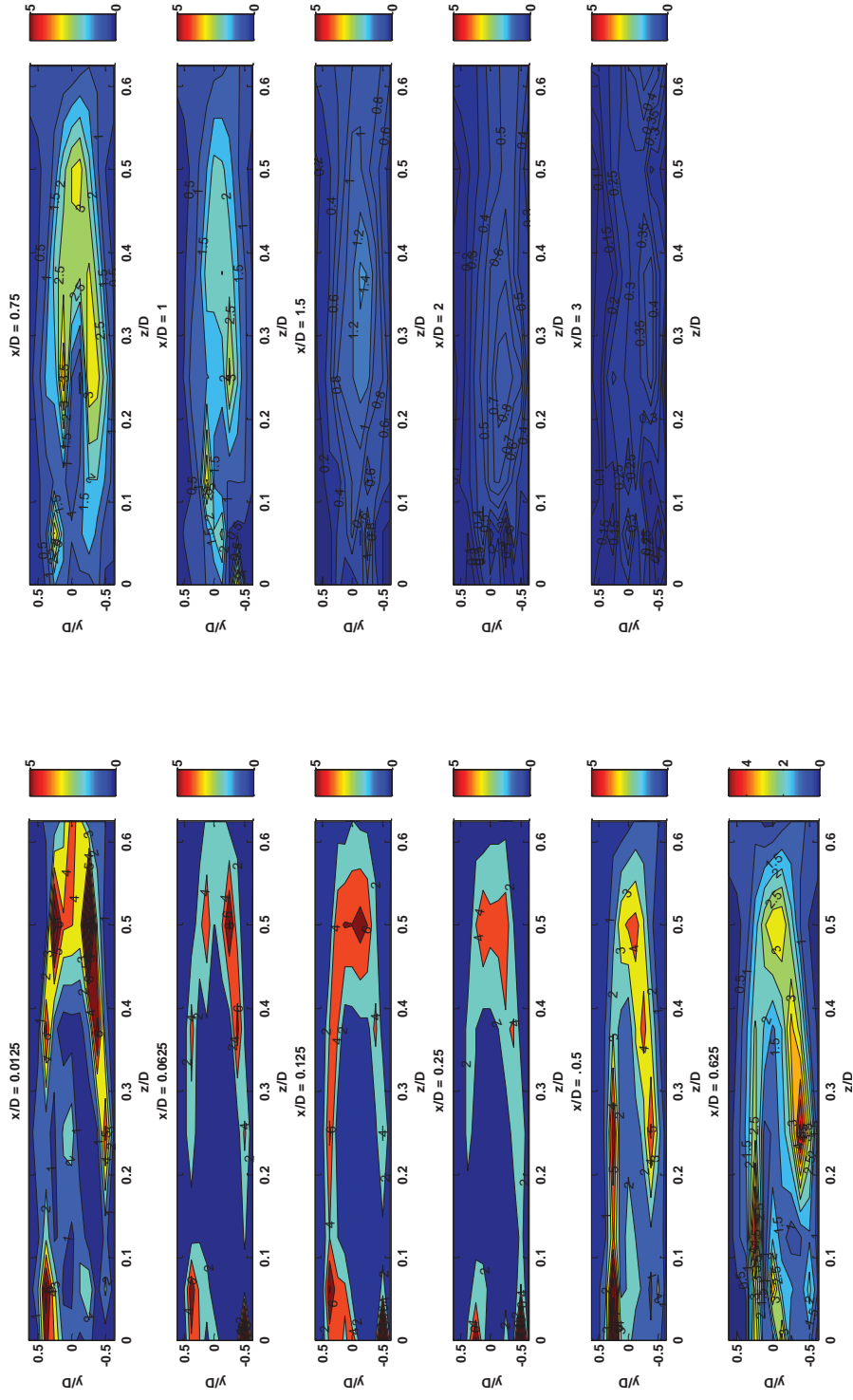
## Results and Discussion: Bluff Body Wake Analysis

Figure 5.2.1. Total Vorticity at different points along the x-axis. Synthetic jet @  $6.5^\circ$ .

## Results and Discussion: Bluff Body Wake Analysis

Figure 5.22. Total Vorticity at different points along the x-axis. Synthetic jet @  $76^\circ$ .

## Results and Discussion: Bluff Body Wake Analysis

Figure 5.23. Total Vorticity at different points along the x-axis. Synthetic jet @  $100^\circ$ .

#### 5.2.4 Wake Characterisation: Wake Boundary

Another way we can gauge the performance of the synthetic jet and characterise the wake region is to compare the actual wake boundary of all synthetic jet cases with that of the standard sphere. Figure 5.24 shows the wake boundary of the standard sphere. The wake boundary for each case has been formed from the wake survey data, in particular the velocity field data. We take the boundary as the point where the velocity has almost returned to the freestream velocity. In the standard sphere case, we see what all the other plots and contours have shown-that we have a symmetrical wake region indicating the integrity of the wake surveys using the five-hole probe with the reversal of flow criteria.

Figure 5.25 shows the wake boundary of the synthetic jet at an angle of incidence of  $6.5^\circ$ . We observe, that it is immediately apparent the asymmetrical effect of the synthetic jet on the wake region. This is especially evident in the upper portion of the wake where we observe a flattening and shortening of the boundary lines. The synthetic jet at  $6.5^\circ$  also affects the lower portion of the wake, as can be seen in Figure 5.26, with some of the boundary lines mostly being drawn in thereby reducing wake size.

The next plot, Figure 5.26, is the boundary with the synthetic jet applied at  $76^\circ$ . This shows a similar trend to that observed with the synthetic jet at  $6.5^\circ$ , decreasing the wake size especially in the upper portion of the wake region. Interestingly, the asymmetry of the localised synthetic jet seems to disturb the lower wake region and at times tends to push out the wake. This was also observed in the vorticity contour plots for this angle of incidence.

The synthetic jet was also applied at  $100^\circ$ . This is shown in Figure 5.27. The effect of applying the synthetic jet in the highly separated region within the wake has a

dramatically different result on the wake boundary. From the previous results, it seems that the synthetic jet at this angle does energise the flow and straighten the velocity field producing less reversal of flow. However, the wake region seems to remain for a greater distance downstream, before the flow is completely recovered back to freestream conditions, as was observed in the dynamic and total pressure contour maps.

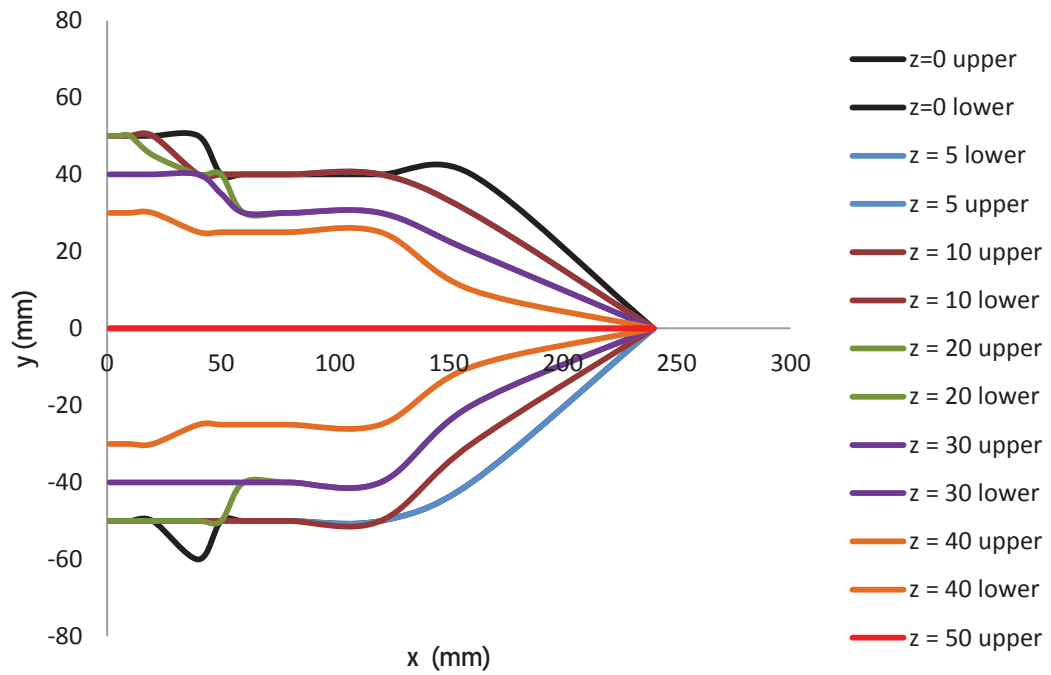


Figure 5.24. Wake boundary – No synthetic jet

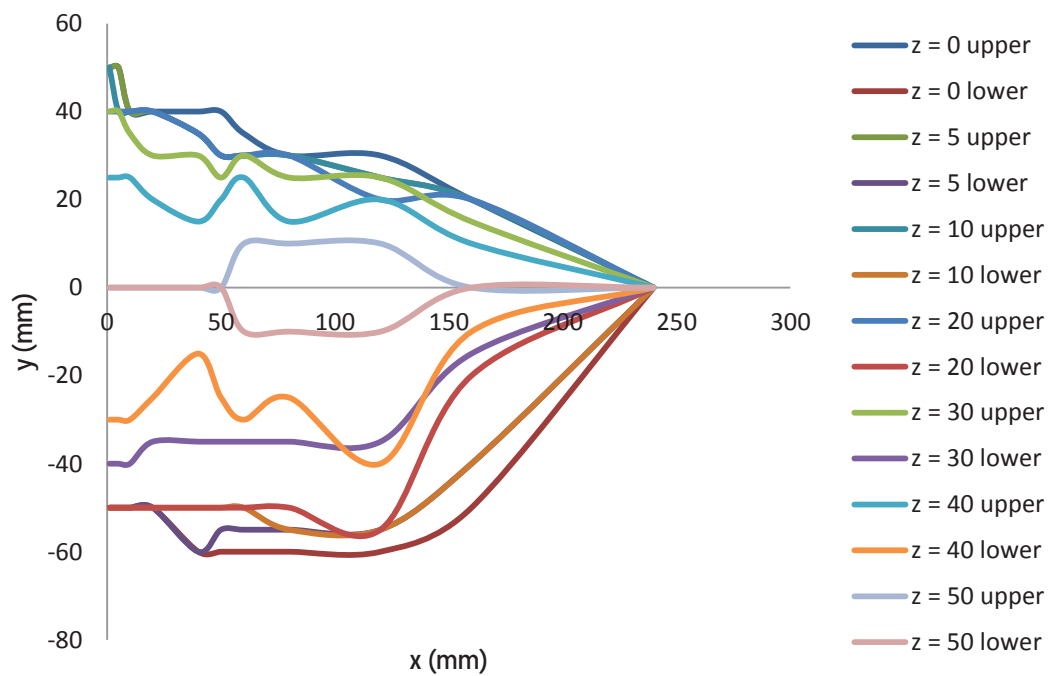
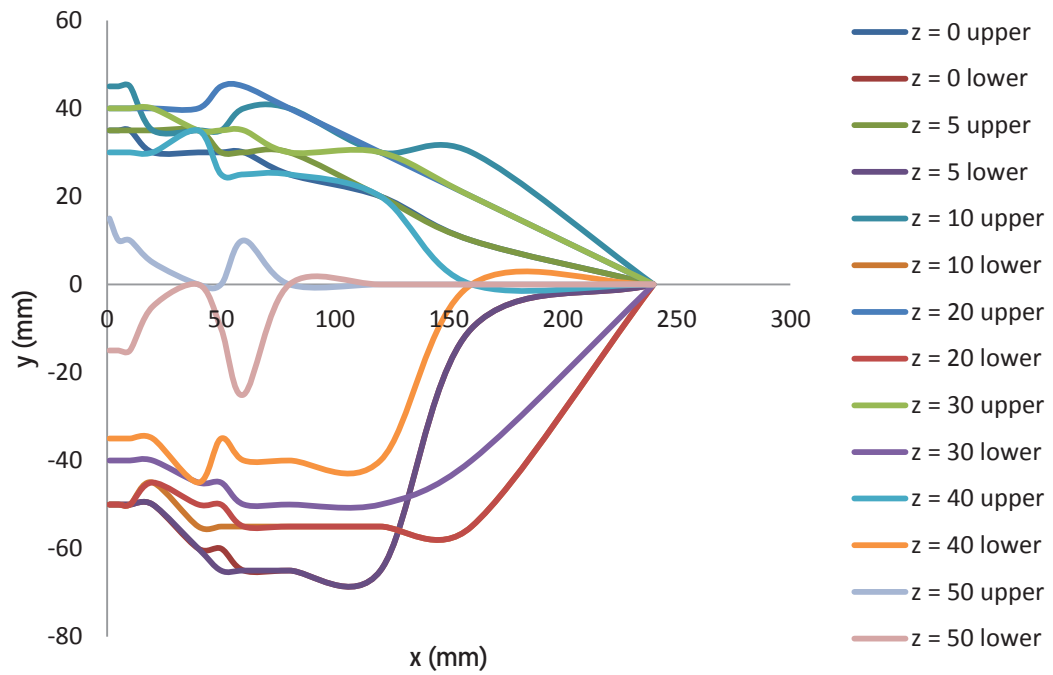
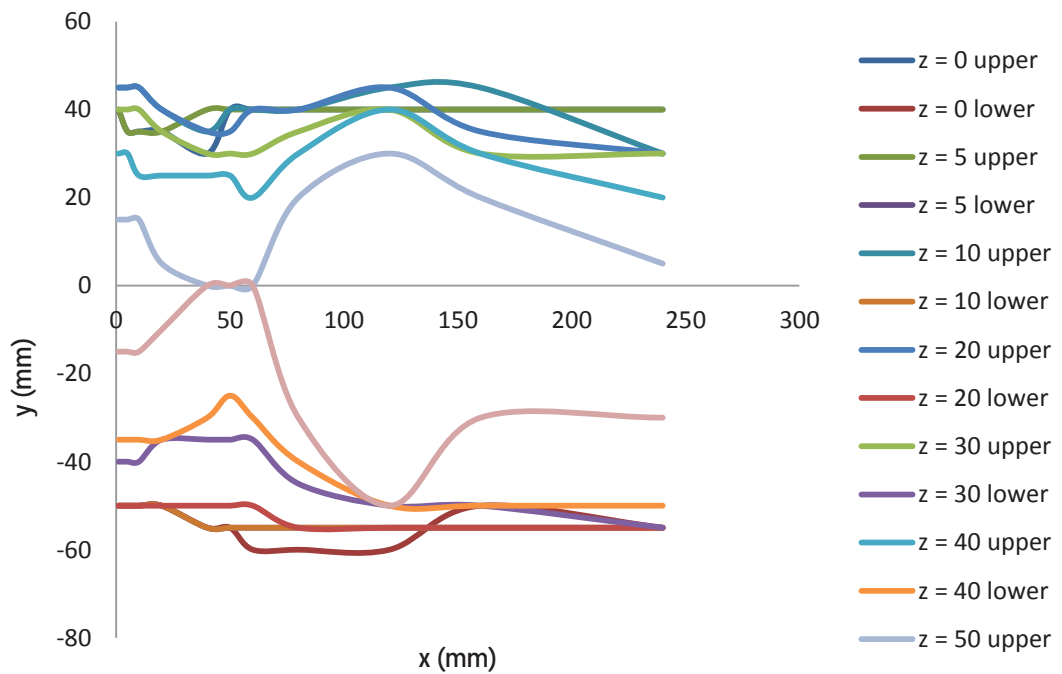


Figure 5.25. Wake boundary – Synthetic jet angle, 6.5°

Figure 5.26. Wake boundary – Synthetic jet angle,  $76^\circ$ Figure 5.27. Wake boundary – Synthetic jet angle,  $100^\circ$

## 5.2.5 Wake Characterisation: Wake Properties

### 5.2.5.1 Boundary Layer Displacement Thickness

The displacement thickness is seen as a measure of the amount that a streamline outside the boundary layer is deflected away from the no slip boundary as a consequence of the formation of the boundary layer on the surface. It is the virtual increase in wall thickness due to the presence of the boundary-layer as seen by the outer, effectively, inviscid flow. It is given by:

$$\delta^* = \int_0^{y_1} \left( 1 - \frac{\rho u}{\rho_\infty u_\infty} \right) dy \quad \delta \leq y_1 \rightarrow \infty$$

(5-14)

where  $\delta$  is the boundary layer thickness

### 5.2.5.2 Boundary Layer Momentum Thickness

In the boundary layer we also define the momentum thickness,  $\theta$ . The meaning of this parameter can be seen as accounting for the decrement in momentum due to the viscous effects of the fluid solid interaction as a result of the presence of the boundary layer. The momentum thickness is the height of a virtual streamtube consisting of the missing momentum or momentum decrement. The formulation is stated as:

$$\theta = \int_0^{y_1} \frac{\rho u}{\rho_\infty u_\infty} \left( 1 - \frac{u}{u_\infty} \right) dy \quad \delta \leq y_1 \rightarrow \infty$$

(5-15)

We may assume that since we are dealing with incompressible flow, the density is constant throughout the flow field.

This concept has proven very useful in fluid dynamics to analyse the growth of the boundary layer and account for viscous effects in the flow field due to the fluid-solid interface. These concepts of displacement and momentum thickness (momentum defect) have been used by Lighthill (1958), Coles (1956) and Moore (1953) to analyse the properties of the wake based on the measured velocity. Thus the present work characterises the wake using these parameters as measures.

### 5.2.5.3 Wake Displacement Thickness

The wake displacement thickness has been integrated over the vertical distance the probe traverses at the data measurement points along the x-axis for the different z-planes. Figure 5.28 shows the wake displacement thickness for the standard sphere case. The trend is for the displacement thickness to tend to zero as we move to regions in the flow field that are further away from the sphere and the flow has substantially recovered. The displacement thickness has the highest values where the flow is highly three-dimensional and reversing.

Figure 5.29 shows a reduction in the displacement thickness uniformly over all z-planes with the synthetic jet at  $6.5^\circ$ . The displacement thickness curves are smoother and more closely packed together indicating a streamlining of the flow.

Figure 5.30 with the synthetic jet at  $76^\circ$  shows a sudden drop in the displacement thickness in the near wake region even more so than that at  $6.5^\circ$ . This indicates that there is a greater effect in this region by placing the synthetic jet close to the flow separation point. There continues to be not only an improvement in this region of the wake but further downstream the displacement lines are pulled back in towards zero.

The synthetic jet at  $100^\circ$  shown in Figure 5.31 has the most impact around the region it is applied although this is not as effective as at the other two angles of incidence. In addition further downstream the wake region is substantially reduced since the displacement thickness is not reduced.

#### **5.2.5.4 Wake Momentum Thickness**

The wake momentum thickness has been calculated over the same limit points as the wake displacement thickness. We expect the momentum thickness to be at a minimum where the velocity of the flow either tends to zero or the freestream velocity.

Figure 5.32 of the standard sphere has a low momentum thickness very close to the sphere where the velocity is low and further downstream when the velocity has almost recovered. In between these, we see a peak in the momentum thickness for all z-planes.

With the application of the synthetic jet at  $6.5^\circ$  as shown in Figure 5.33, the momentum thickness is slightly reduced at the central peak value with a higher gradient in the near wake. Thus, momentum is added in the low region near the sphere body. This is emphasised even more so in Figure 5.34 with the application of the synthetic jet at  $76^\circ$  showing the added momentum and the step rise of the near wake to the peak value. This is further shown in Figure 5.35 with the synthetic jet at  $100^\circ$  although as previously the direct injection of momentum in the wake region is not as effective although an aerodynamic improvement is experienced.

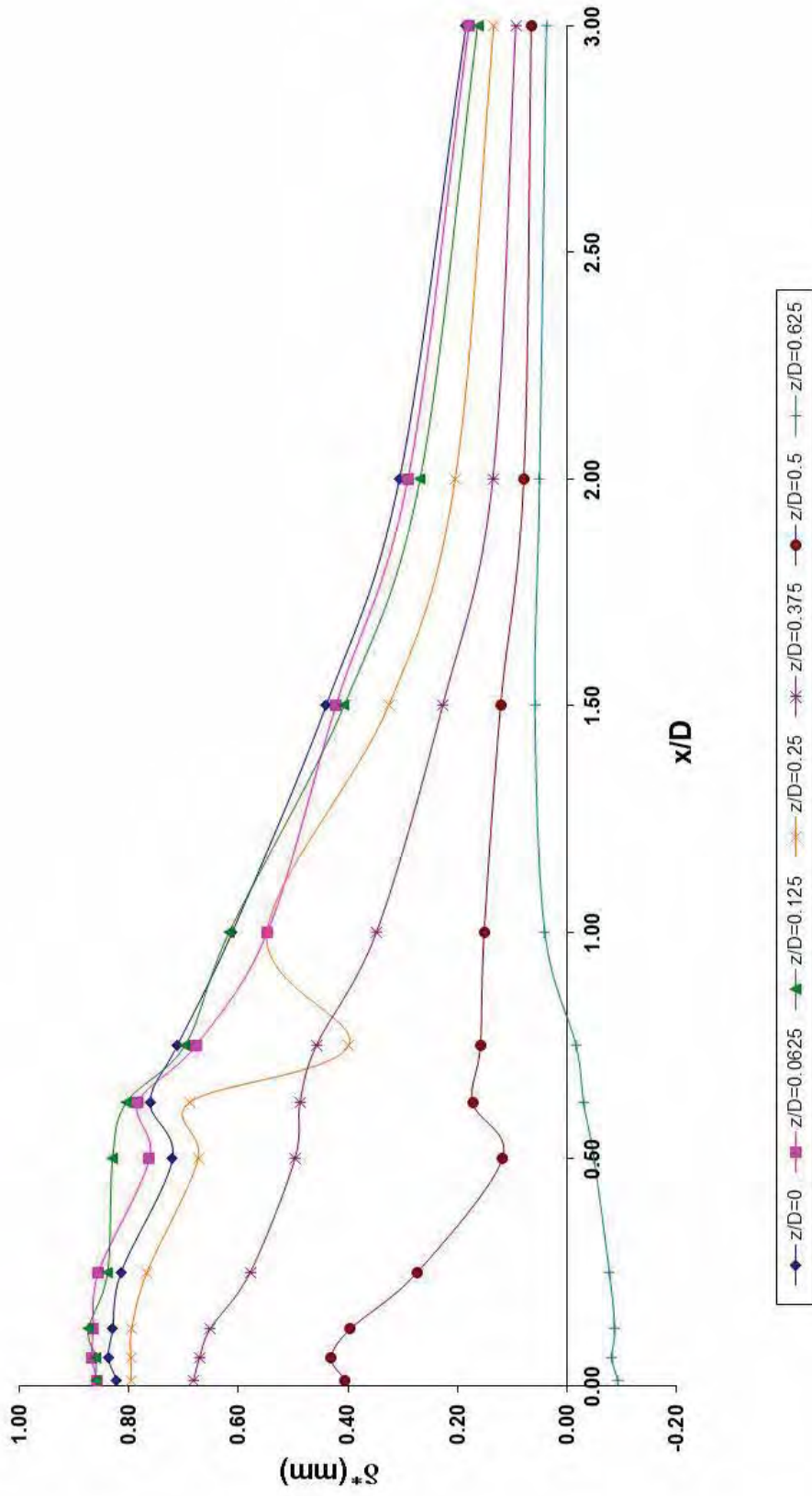
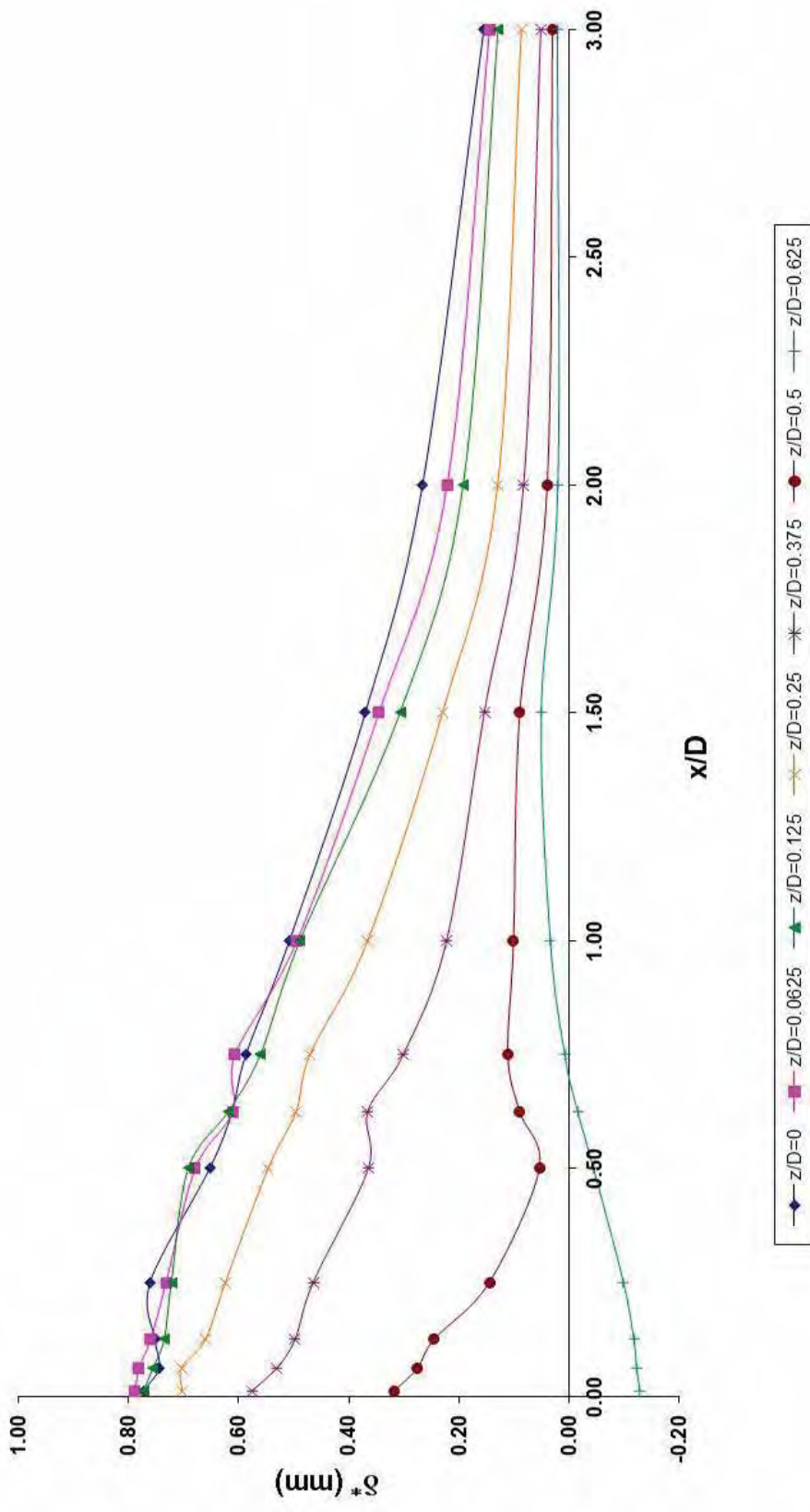


Figure 5.28. Wake displacement thickness – No synthetic jet

Figure 5.29. Wake displacement thickness – Synthetic jet angle  $6.5^\circ$

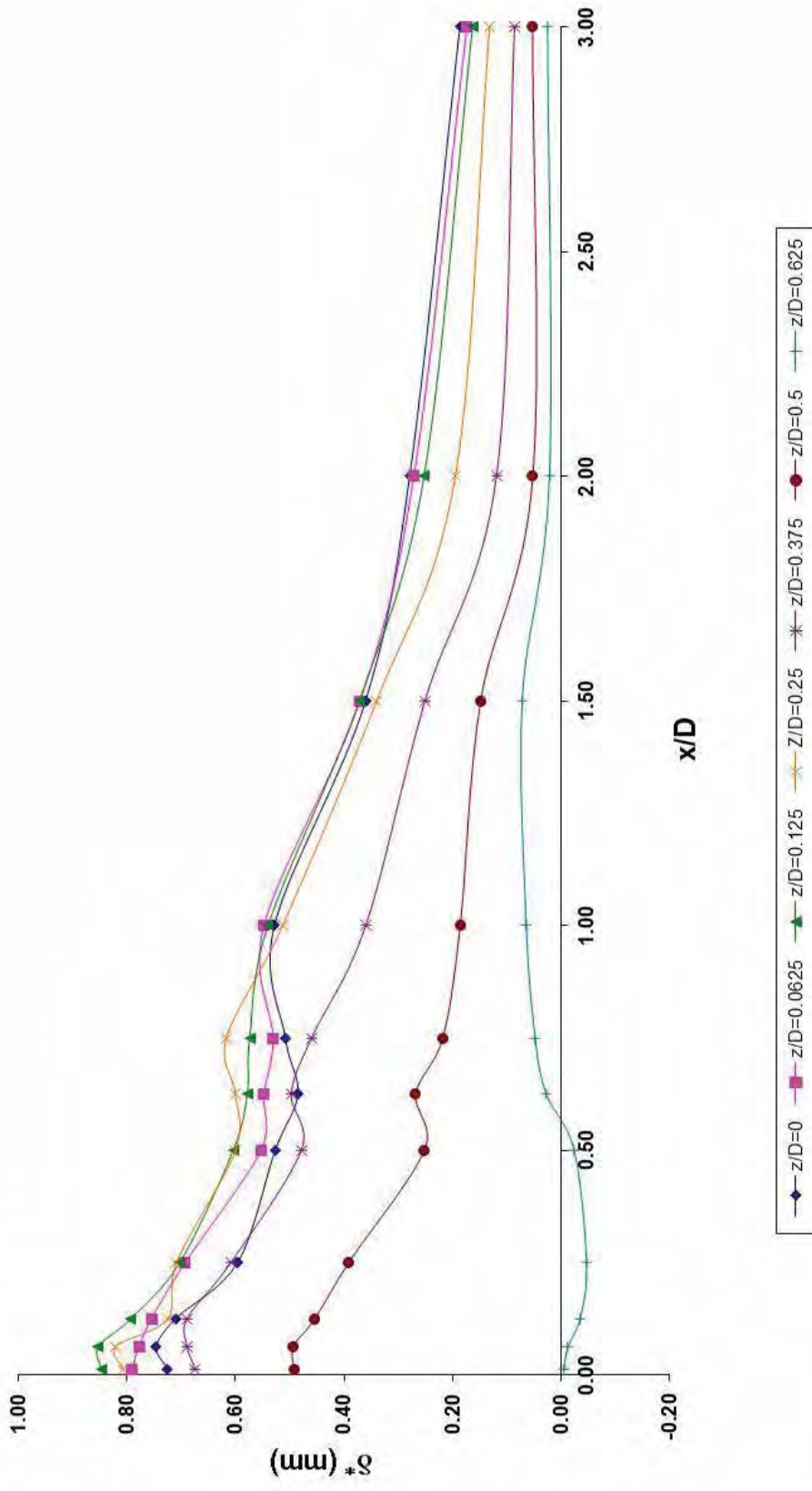
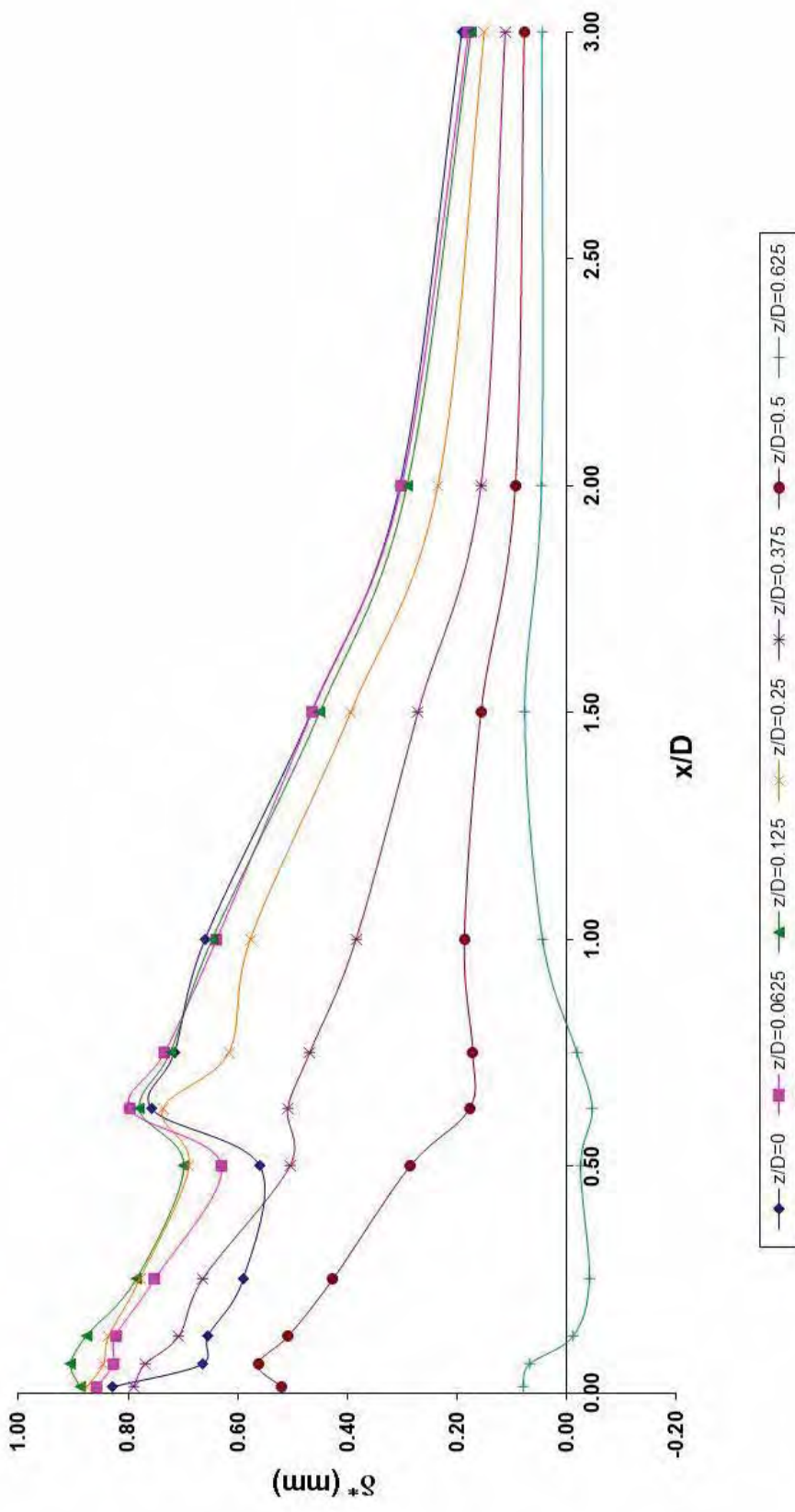


Figure 5.30. Wake displacement thickness – Synthetic jet angle  $76^\circ$

Figure 5.31. Wake displacement thickness – Synthetic jet angle  $100^\circ$

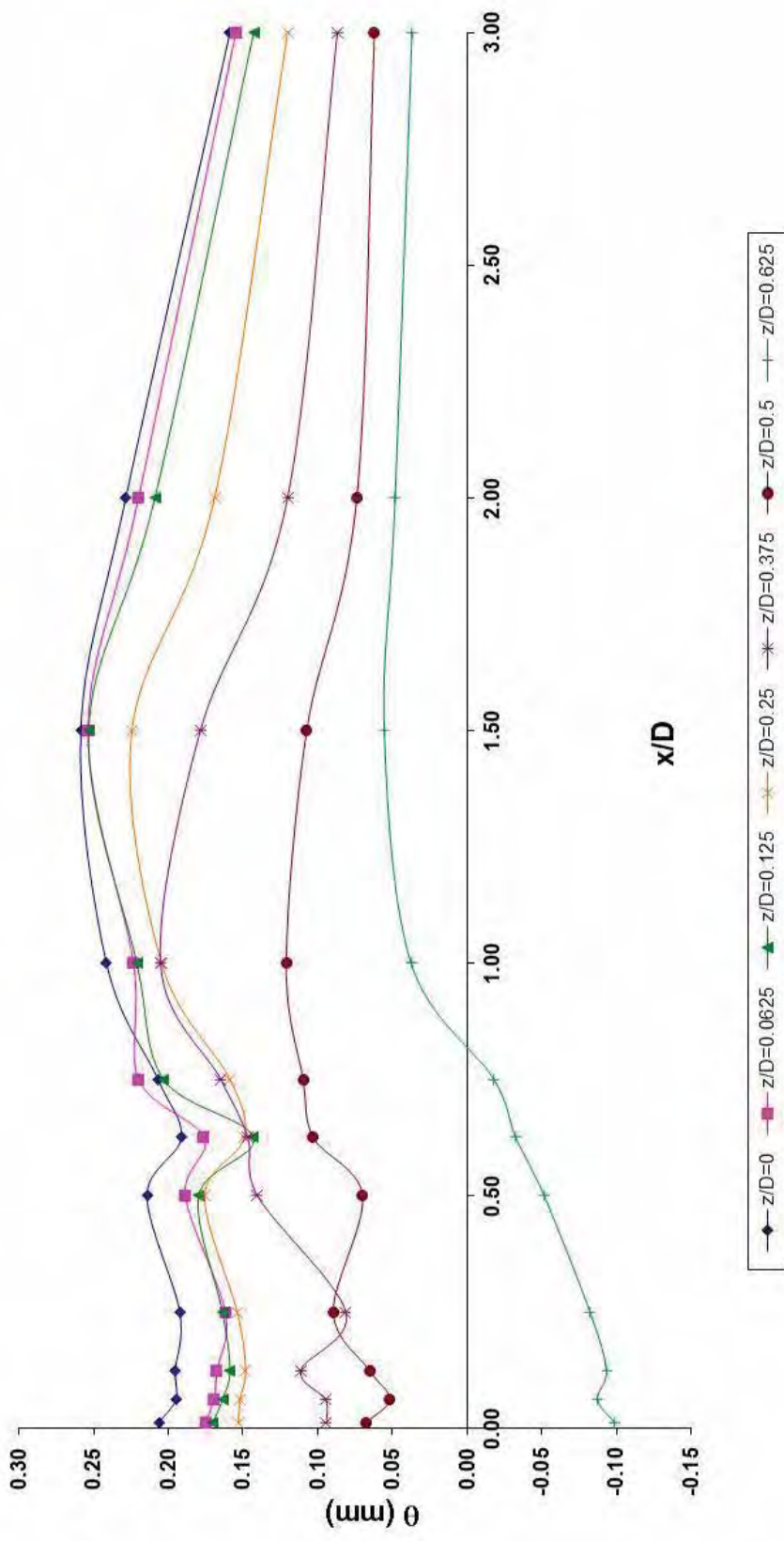
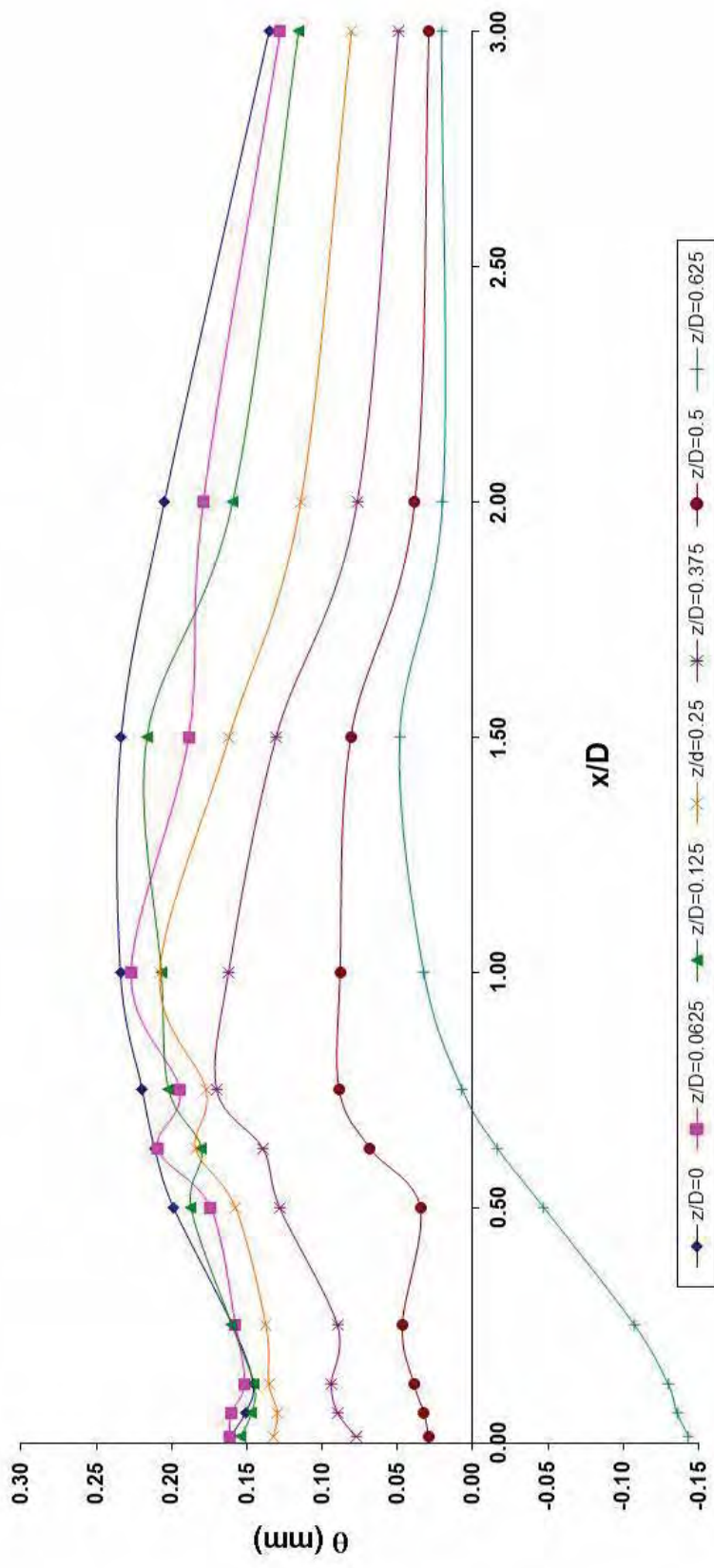
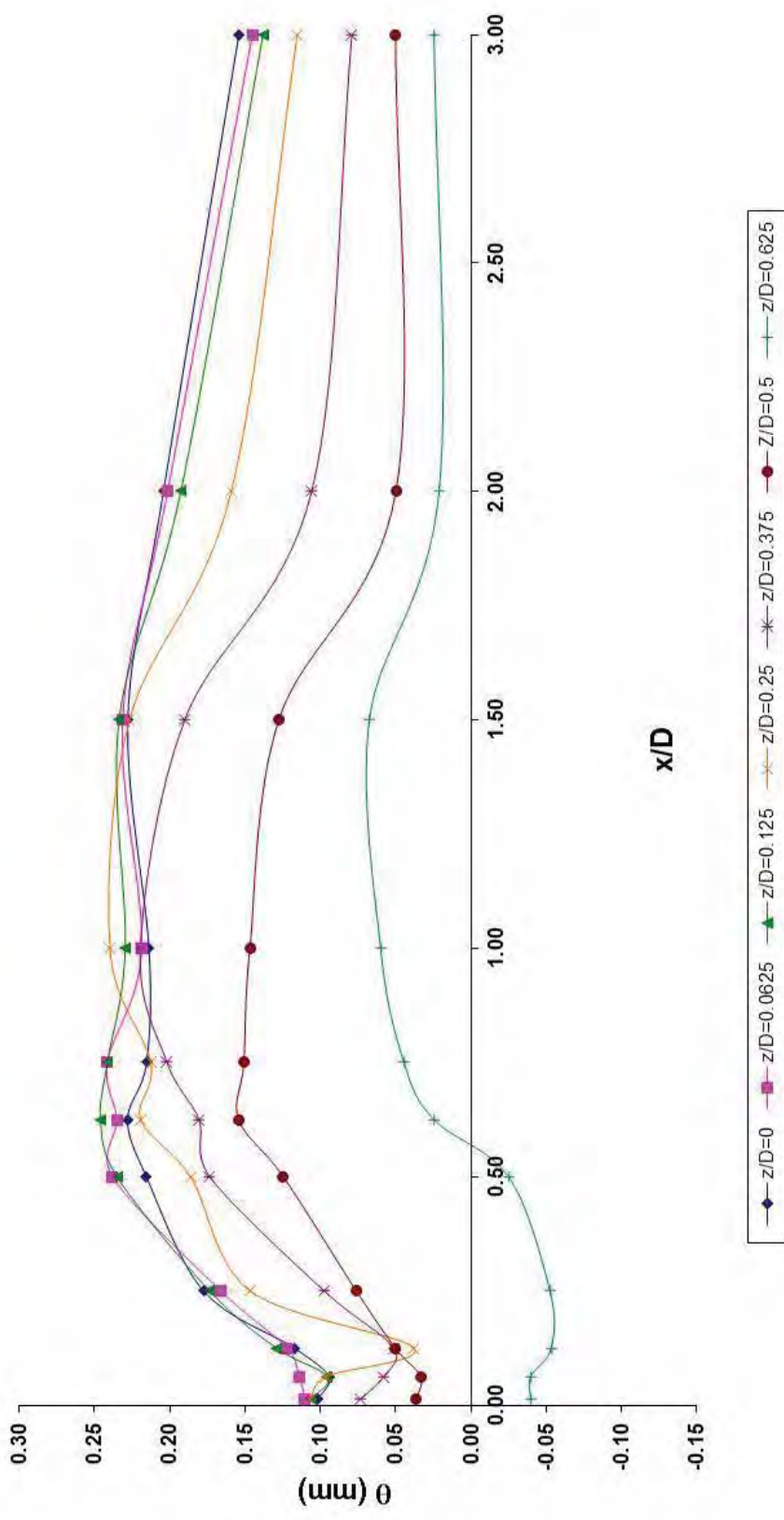
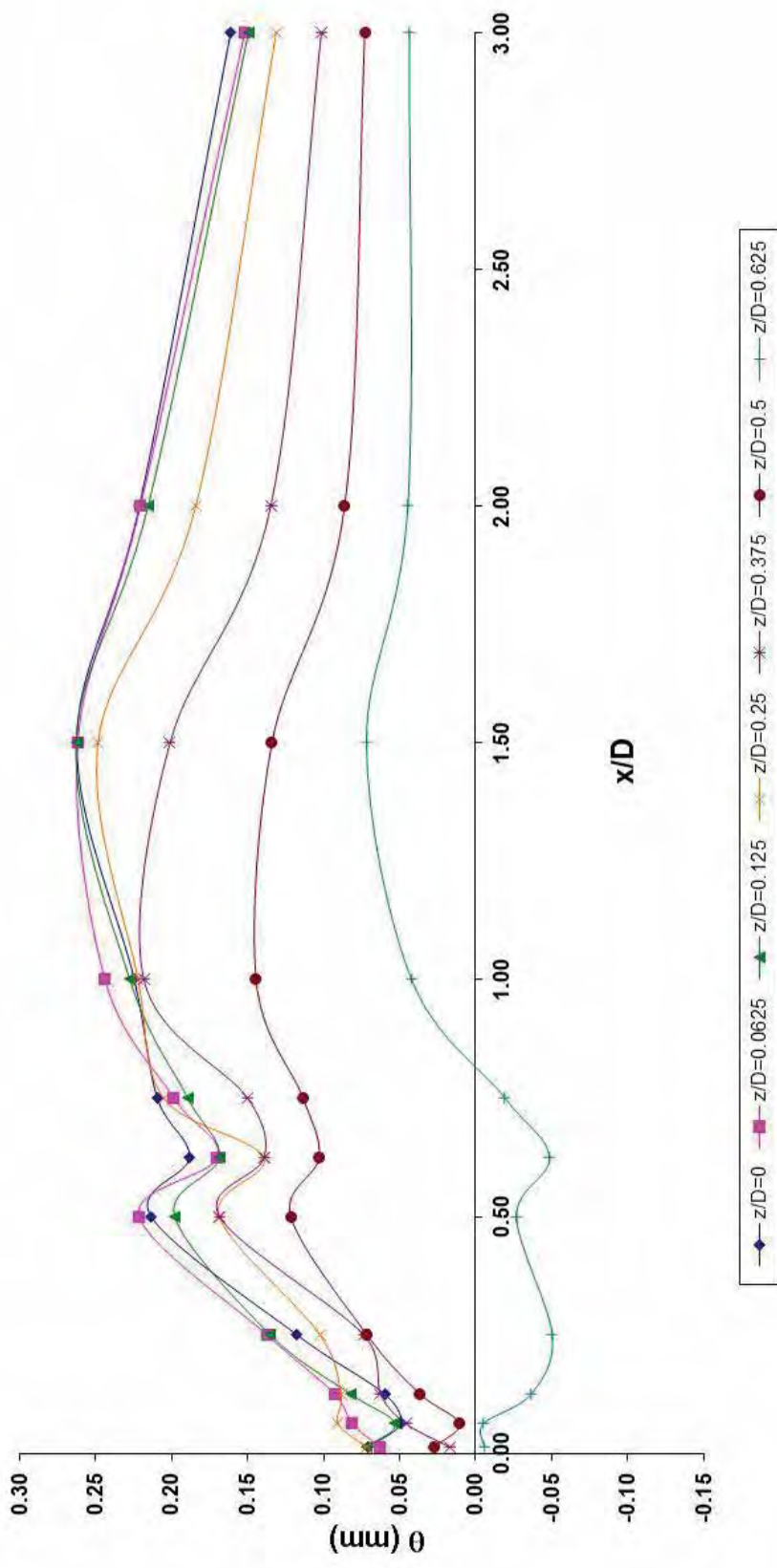


Figure 5.32. Wake momentum thickness – No synthetic jet

Figure 5.33. Wake momentum thickness – Synthetic jet angle  $6.5^\circ$

Figure 5.34. Wake momentum thickness – Synthetic jet angle  $76^\circ$

Figure 5.35. Wake momentum thickness – Synthetic jet angle  $100^\circ$

### 5.2.6 Bernoulli's Principle in the Wake

From Bernoulli's equation which is a statement about the total energy within the flow field we can calculate the total energy per unit volume upstream of the sphere.

$$p_t = p_\infty + \frac{1}{2} \rho U_\infty^2 \quad (5-16)$$

At two points along the streamline, firstly upstream of the sphere the total pressure is denoted as  $p_t$ . Downstream within the wake, total pressure is denoted as  $p_{tw}$ . The wake region is characterised as a viscous dominated flow region with highly turbulent rotational flow. Due to losses as a result of viscous effects giving rise to frictional forces in this flow separated region we see  $p_t < p_{tw}$ . We can assume that the average total pressure within the wake remains constant.

Next we take a measurement point, denoted by  $m$ , at a known location downstream within the wake of the sphere such that the static pressure within the wake has not recovered to the free stream static pressure.

$$p_{tw} = p_m + \frac{1}{2} \rho U_m^2 \quad (5-17)$$

Now we take a point at an unknown location, denoted by  $a$ , further downstream of the measurement point within the wake of the sphere such that the static pressure has recovered to the free stream static pressure.

$$p_{tw} = p_\infty + \frac{1}{2} \rho U_a^2 \quad (5-18)$$

We know the measured value  $m$  and we can calculate the actual value, using equation (5-17).

$$u_a = \sqrt{\frac{2(\rho_{tw} - \rho_\infty)}{\rho}} \quad (5-19)$$

The wake displacement thickness at the measurement point  $m$  is defined as:

$$\delta_m^* = \int_0^{y_{m1}} \left(1 - \frac{u_m}{u_\infty}\right) dy_m \quad \delta \leq y_m \rightarrow \infty \quad (5-20)$$

Also we can define the displacement thickness at a point downstream where the static pressure has recovered to freestream static pressure:

$$\delta_a^* = \int_0^{y_a} \left(1 - \frac{u_a}{u_\infty}\right) dy_a \quad \delta \leq y_a \rightarrow \infty \quad (5-21)$$

Using the continuity principle and applying it between the measurement point  $m$  and the recovered point  $a$  we have:

$$u_m dy_m = u_a dy_a \quad (5-22)$$

Thus we may calculate the displacement thickness at this point using the following relation:

$$\delta_a^* = \int_0^{y_m} \left(1 - \frac{u_a}{u_\infty}\right) \frac{u_m}{u_a} dy_m \quad \delta \leq y_m \rightarrow \infty$$

Which then becomes

$$\delta_a^* = \int_0^{y_m} \left(\frac{u_m}{u_a} - \frac{u_m}{u_\infty}\right) dy_m \quad \delta \leq y_m \rightarrow \infty \quad (5-23)$$

Similarly with the displacement thickness.

At the measured location we have

$$\theta_m = \int_0^{y_m} \frac{u_m}{u_\infty} \left(1 - \frac{u_m}{u_\infty}\right) dy_m \quad \delta \leq y_m \rightarrow \infty \quad (5-24)$$

At the covered location or actual required measurement point

$$\theta_a = \int_0^{y_a} \frac{u_a}{u_\infty} \left(1 - \frac{u_a}{u_\infty}\right) dy_a \quad \delta \leq y_a \rightarrow \infty \quad (5-25)$$

Applying the continuity principle and reducing the equation we have

$$\theta_a = \int_0^{y_m} \frac{u_m}{u_\infty} \left(1 - \frac{u_a}{u_\infty}\right) dy_m \quad \delta \leq y_m \rightarrow \infty \quad (5-26)$$

This is then applied to produce the shape factor

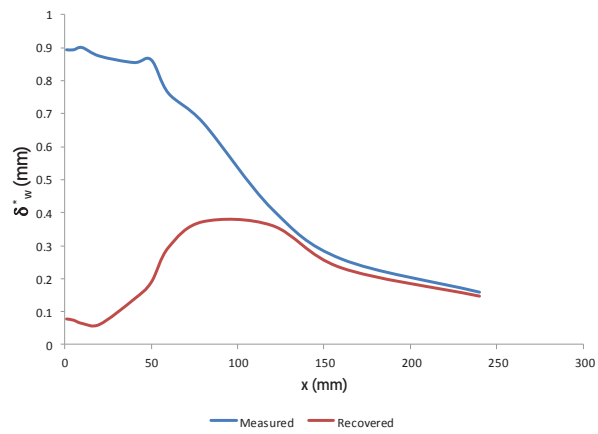
$$H_w = \frac{\delta_w}{\theta_w} \quad (5-27)$$

Now the results of the wake surveys and the calculated velocities show that wake displacement thickness has decreased over the no synthetic jet case. Likewise the momentum thickness or momentum defect has decreased with synthetic jet applied. The results of which are shown in Table 5.10.

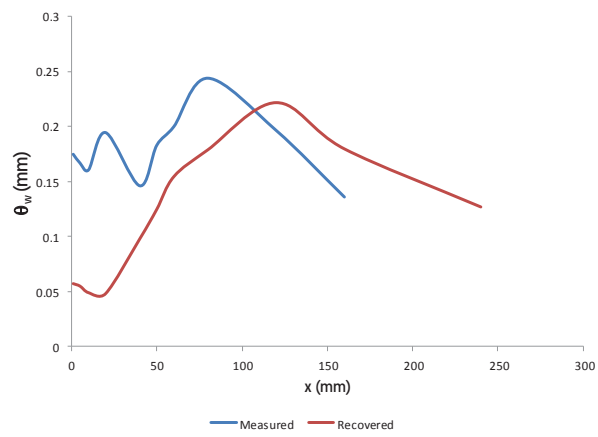
Case	Displacement Thickness (mm)	
	Measured	Actual
No synthetic jet	0.85	0.13
Synthetic jet @ 6.5°	0.79	0.15
Synthetic jet @ 76°	0.71	0.14
Synthetic jet @ 100°	0.76	0.23

Table 5.10. Comparisons of displacement thickness.

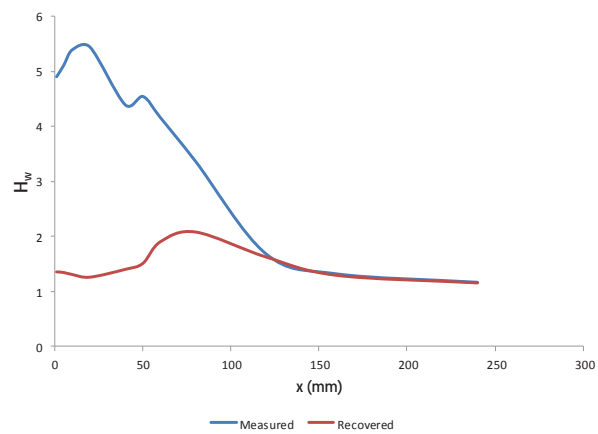
Figure 5.36 to Figure 5.39 show the application of using the above calculated wake properties. Using the wake characterisation properties it is possible to estimate a downstream distance such that the wake is known to have recovered so that flow measurements can be conducted without the wake defect. Having the three different parameters of displacement thickness, momentum thickness and shape factor increases the confidence level for the point of recovery as well as allowing different characteristics of the flow to be revealed.



(a)



(b)



(c)

Figure 5.36. Wake – No synthetic jet (a) Displacement thickness, (b) Momentum thickness, (c) Shape factor

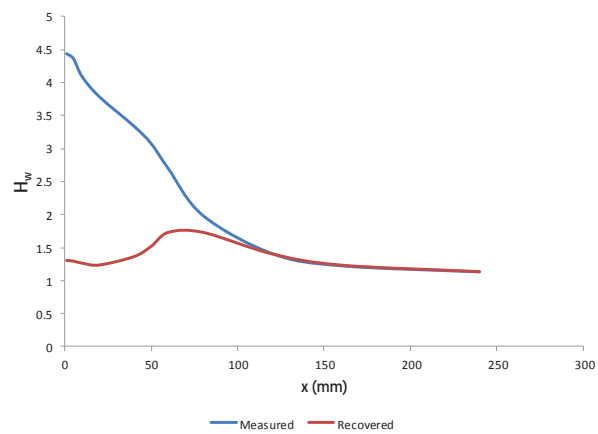
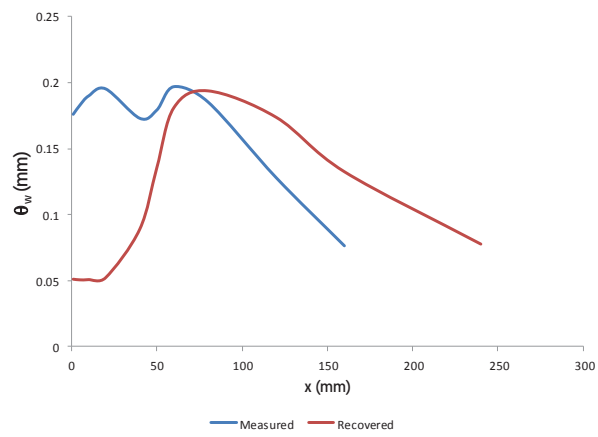
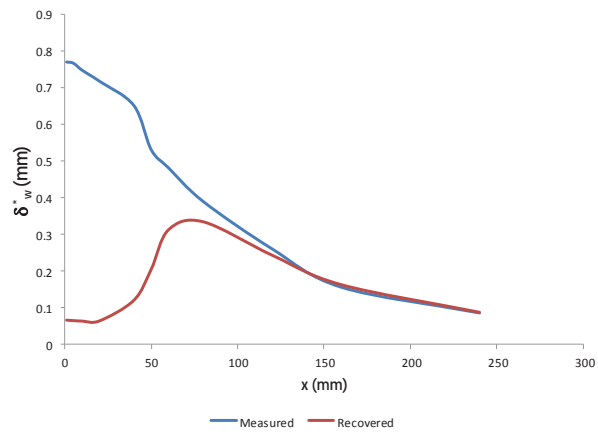
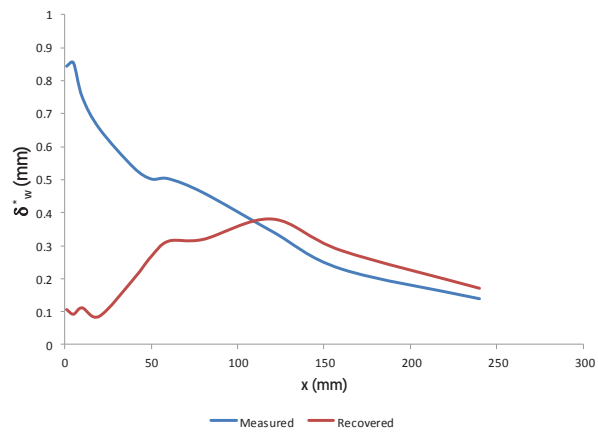
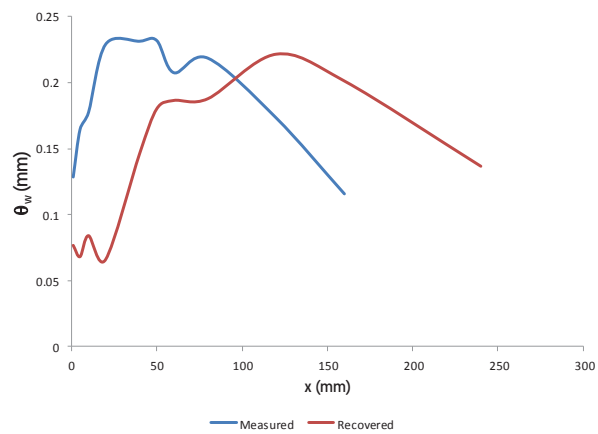


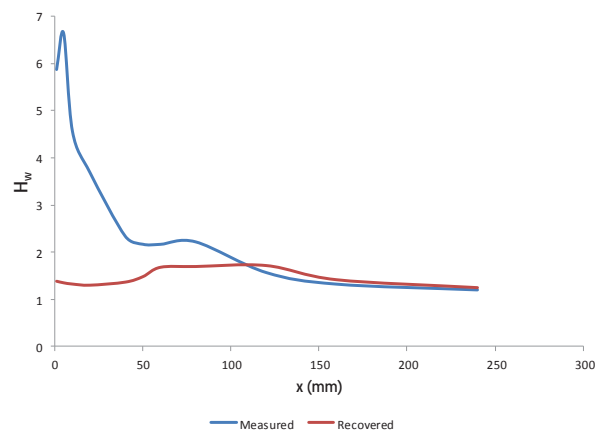
Figure 5.37. Wake – Synthetic jet angle  $6.5^\circ$  (a) Displacement thickness, (b) Momentum thickness, (c) Shape factor



(a)

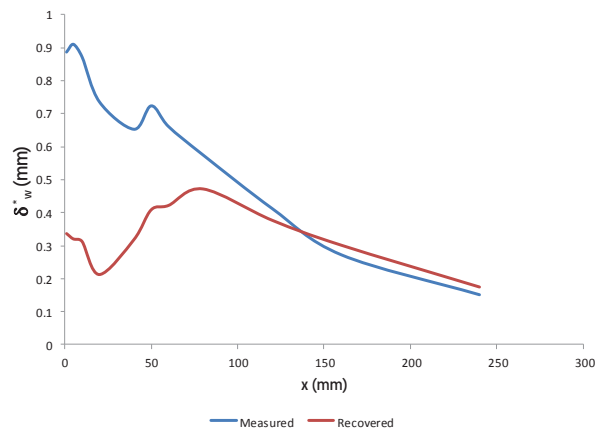


(b)

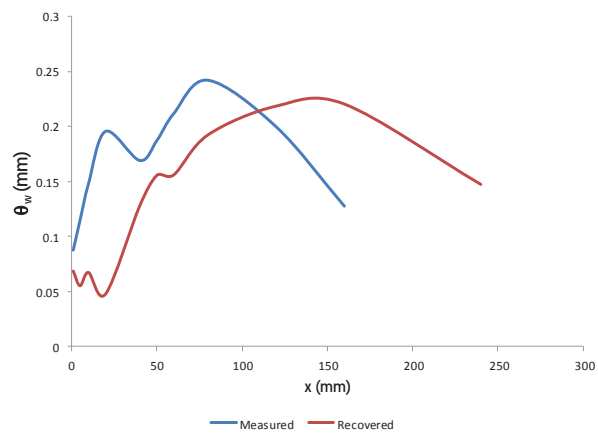


(c)

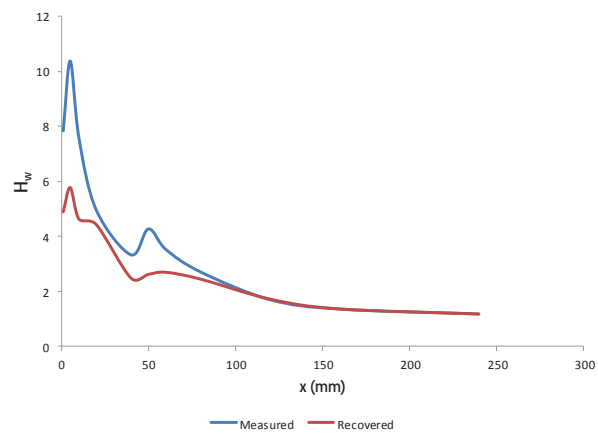
Figure 5.38. Wake – Synthetic jet angle  $76^\circ$  (a) Displacement thickness, (b) Momentum thickness, (c) Shape factor



(a)



(b)



(c)

Figure 5.39. Wake – Synthetic jet angle  $100^\circ$  (a) Displacement thickness, (b) Momentum thickness, (c) Shape factor

### 5.2.7 Wake Characterisation Comments

In the present work we show that global changes to the wake of a sphere can occur at a low angle of incidence of a localised synthetic jet at a location of  $6.5^\circ$  above the stagnation point and a relatively high momentum coefficient of  $2.8 \times 10^{-3}$ . Firstly, we compared the dynamic pressure contours and clearly see the differences between all three different angles of incidence of the localised synthetic jet. At  $6.5^\circ$  angle of incidence the synthetic jet produces an asymmetry of the dynamic pressure field and as a consequence also the static pressure distribution indicating that the flow is accelerating in the upper half of the sphere due to a static pressure reduction which is the result of the increase of the velocity imparted by the synthetic jet. A corresponding slight increase in the dynamic pressure field occurs on the underside of the sphere. Thus, the synthetic jet has the effect of restoring the flow. There are increases in the total pressure for values of  $z/D = 0$  to  $z/D = 0.375$  on the top part of the sphere as we would expect from the momentum injection of the synthetic jet. Looking at the contour plots for  $z/D = 0.5$  and  $z/D = 0.625$ , the total pressure is symmetrical about  $y/D = 0$  whereas there was an asymmetry in the dynamic pressure plots. This would indicate that for the total pressure remaining the same for the upper and lower half of the sphere there must be another different source increasing the total pressure to the freestream value and concomitantly decreasing the static pressure and giving rise to the asymmetry of the dynamic pressure field. I would suggest that this would be the vorticity experienced near the extremes of the sphere. This vorticity gives rise to the total pressure but concomitantly decreases the static pressure in the upper side of the sphere.

Now we compare the dynamic pressure of the synthetic jet at an angle of incidence of  $76^\circ$ . For this angular position the synthetic jet has the effect of localising the added momentum imparted to the cross flow more so than at an angle of  $6.5^\circ$ , as is seen by the concentrated effect on the dynamic pressure field. By observing the

measurement planes further away from the synthetic jet source in the direction of the positive  $z$  axis, the effect of the synthetic jet suddenly disappears and the static pressure is uniform at approximately  $z/D = 0.375$  and onwards. The synthetic jet has the greatest impact at the plane  $z/D=0.25$  which is seen to increase the dynamic pressure and lower the static pressure on the upper side of the sphere and increase or push the static pressure to the underside of the sphere. This would be expected at an angle of incidence of  $76^\circ$ , because placing the localised synthetic jet further along the curvature of the sphere surface means there is less time for the synthetic jet to interact and diffuse its influence on the flow field and thus have more of a global effect. A substantial three-dimensional global effect might be induced in the flow over the sphere at this angle if the localised synthetic jet were able to trip the flow from a laminar to turbulent flow regime. The total pressure contour plots emphasize that the greatest effect is happening in the plane  $z/D = 0.25$ . This would be reasonable since the synthetic jet is located in the plane  $z/D = 0.0625$  although it is angled away from the centreline of the sphere at an angle of  $45^\circ$ . Thus, the combination of the momentum of the jet and the oncoming free stream flow pushes its effect mainly onto this plane. The total pressure contour plots show a higher pressure on the upper side of the sphere for the planes in the near vicinity of the plane containing the synthetic jet. Although, for the planes that are further away towards to the extremities of the sphere, we can also see an increase in the uniformity of the total pressure field, as well as an increase in the magnitude of the total pressure contours. This indicates that the localised effects of the synthetic jet are also being dissipated throughout the flow at a  $76^\circ$  angle of incidence.

At an angle of incidence of  $100^\circ$ , the total pressure is increased in the wake region with the added momentum of the synthetic jet. The momentum imparted from the synthetic jet in the wake region is even more so localised than at the previous two angles of incidence. At this late stage of the development of the flow over the sphere, it is difficult to influence the flow separation with the current amount of momentum imparted by the synthetic jet. The improvements to the flow field are a

direct modification of the highly three-dimensional flow in the dead region or wake. An increase in the total pressure is observed on all planes which decreases the amount of reversal of flow. Although it seems that it takes longer for the flow field to return to the freestream conditions. This shows that the synthetic jet improves the flow but not through the same mechanisms as for the other angles of incidence. This is particularly evident in the dynamic pressure plot which shows activity in the wake region due the synthetic jet. The contour lines continue to flow to the end of the measurement plane rather than closing in as with the other cases.

### 5.3 Force Balance Measurements

Finally, the force balance measurements were taken with the supported sphere mounted on the multi-axis load cell. It was observed that the load cell was sensitive to external influences making it difficult to obtain accurate measurements thus the measurements were repeated until the error was reduced. The magnitude of the force measured using the load was small at this velocity of the order of 0.30 N. This fits well with the theoretical predictions for the force on a sphere with a support rod. The estimated force on an 80 mm sphere with a subsonic airflow at 10 m/s would be 0.15 N. For a support of 12.7 mm diameter (cylinder drag) the force would be 0.22 N. The addition of these two parts brings the total drag to 0.36 N not accounting for the interference between the two bodies. The results of the load cell found the synthetic jet to have the effect of reducing the drag on the sphere at all angles of incidence in the range of 2.5 to 5.5%. The result is close to the value predicted by the surface pressure measurements (Findanis and Ahmed, 2007) which indicated it would be at a maximum of approximately 8.0%.

Furthermore, the works of Glezer and Amitay (2002) show that, for an angle of incidence of  $60^\circ$ , the velocity profile is reduced. That is, the velocity defect is reduced, and this shows that the drag has been reduced. This also occurs at the lower angle of  $6.5^\circ$  for the sphere, although at this angle the effects of the synthetic

jet are reduced, since the vortices emanating from the synthetic jet orifice have a greater distance to travel inside the boundary-layer and thus the effects of skin friction would also dissipate the added energy. When we place the synthetic jet at an angle of  $76^\circ$ , the added energy of the synthetic jet will be transferred more directly to affect the shear layers of the flow and thus have a straightening effect on the flow over the sphere. Hence, the velocity defect in the wake region is reduced and the drag which is due to pressure drag is also reduced. Since the majority of the drag for the sphere is due to the pressure drag, the synthetic jet at  $76^\circ$  produces a greater reduction on drag than when the synthetic jet is at  $6.5^\circ$ , which produces a reduction in skin friction drag as well some reduction although a lot less in form or pressure drag than when the synthetic jet is angled at  $76^\circ$ . The influence on the drag at  $100^\circ$  is almost entirely due to the effect of the momentum from the synthetic jet on the shear layers of the cross flow.

#### 5.4 Summary and concluding remarks

The underlying motivation for the present work was to gain a greater understanding of the three-dimensional flow in the wake region of the sphere. In particular, the plan was to characterise the flow field within this region and the modified behaviour of the fluid flow resulting from the influence of the localised synthetic jet. Experimental fluid dynamics was used as the method to investigate the physics of the flow, mainly using a five-hole pressure probe.

The highly three-dimensional flow in the wake region produces flow reversal. The five-hole probe instrumentation used to survey the wake region has a defined calibration range of yaw and pitch angles. Thus, in order to determine when the flow vector was outside the calibrated region of the instrument, a number of reversal of flow criteria were developed to be used for this purpose. The reversal-of-flow-criteria can be used effectively throughout the flow field which enable the data set to be sorted into mainly three categories. The criteria will filter those data

points that are certain to be in the reversal of flow category and outside the calibration range of the probe. Other criteria were formulated to sift out those points that are likely to be on the fringes of the calibrated range that could produce misleading values. The remainder of data set would be within the calibrated region of the probe and could be used for the analysis. The reversal of flow criteria was effectively tested using a NACA23012 airfoil profile which confirmed the criteria to be applicable to other separated flows.

Flow visualisation provided the means to qualitatively analyse the flow field behind the standard sphere and then compare the results with the application of the synthetic jet. It was shown using a grid of tufts that the reversal of flow was reduced markedly with the application of synthetic jet at angle of incidence of  $80^\circ$ .

The wake surveys conducted with the five-hole pressure probe were validated not only with the reversal of flow criteria. Rather, further confirmation of the validity was obtained by using hot-wire anemometry. The results of the hot-wire probe enabled us to measure the accuracy of the five-hole probe measurements which were within an acceptable percentage of each other. It was only in regions of flow reversal or the fringes of the reversal of flow regions that there exists a large error between the two methods. It was shown however that this error was small relative to the freestream flow, since the flow velocity is small where there is flow reversal and so the error is reduced. Using the hot-wire results further enabled us to make use of the entire data set obtained from the five-hole probe to construct the complete velocity field.

The three-dimensional velocity field was constructed for all cases with synthetic jet ( $6.5^\circ$ ,  $76^\circ$ ,  $100^\circ$ ) and the standard sphere which was used as the basis to compare the effects of the application of synthetic jet. The synthetic jet produced a streamlining of the flow and a reduction of the wake region at all three angles of incidence indicating an increase in the streamwise velocity component with a

decrease in reversal of flow and vorticity. With these beneficial effects to the flow field the localised synthetic jet has a similar effect as that of tripping the flow.

Since the measurements were taken using the five-hole pressure probe it was possible to visualise the variation of the pressure distribution in the wake region of the sphere and analyse the changes in the static, dynamic, and total pressure and the losses in the pressure field using contour plots constructed with Matlab.

The localised synthetic jet with a cross flow Reynolds number of  $5.1 \times 10^4$  produces a different effect on the flow field according to its location on the sphere body. When the synthetic jet is located at an angle of  $6.5^\circ$  from the fore stagnation point we find similarities with those experiments conducted on a cylinder with synthetic jet. The flow field was improved with a reduction in the size of the wake of the sphere and a corresponding reduction in the drag. Changes in the flow occur upstream and downstream of the actuation point giving rise to global effects in the flow field.

When the synthetic jet is placed at an angle of incidence of  $76^\circ$ , the local effects of the synthetic jet are amplified since the flow has almost reached the separation point. The asymmetry of the wake region is affected more so than with the case when the synthetic jet is angled at  $6.5^\circ$ . This would suggest that less aero-shaping is occurring on the sphere surface and more energy is placed into wake modification. Although even in the wake there is more of a localised effect in the plane of the synthetic jet actuation.

At the tested location of  $100^\circ$  from the fore stagnation point, the localised synthetic jet improves the wake region in a direct manner since it is completely immersed in the separated flow of the wake. A streamlining of the flow was produced reducing reversal of flow, although the effects were even more so localised than at the tested location of  $76^\circ$ . A large reduction in the vorticity was seen in all measured

planes with an increase in the total pressure that was carried through further downstream than the other localised synthetic jet test points.

The wake region was further characterised by constructing the plots of the wake boundary and using the concepts of displacement thickness, momentum thickness and shape factor. The wake boundary plots proved useful in clearly showing that the asymmetrical localised synthetic jet was able to reduce the size of the wake at all synthetic jet locations. The boundary plots also show that applying the synthetic jet prior to separation produces a greater reduction than when directly applied within the wake region.

The displacement thickness and momentum thickness in the wake region were used effectively in measuring the performance of the synthetic jet at the different locations. With the synthetic jet placed at  $6.5^\circ$ , the displacement thickness is reduced smoothly over the surveyed region. Whereas placing the synthetic jet close to the separation point, again reduces the displacement thickness. However, the reduction was apparently more local to the point of application. This is emphasised at  $100^\circ$  as shown in the momentum thickness plot. Interestingly, the synthetic jet showed a greater increase in the near wake region at  $76^\circ$  than at  $100^\circ$  which shows particular advantages to applying the localised synthetic jet close to the point of separation.

Applying Bernoulli's principle in the wake and incorporating the concepts of wake displacement and momentum thickness we were able to successfully show that it is possible to predict the actual values that are obtained when the wake has sufficiently recovered to freestream conditions. The shape factor was also used to clearly characterise the difference between the measured and actual values showing that the synthetic jet improves these characteristics of the wake region.

The asymmetrical localised synthetic jet is capable of improving the aerodynamic performance of three-dimensional bluff bodies through the aero-shaping mechanism. The location of the jet closer to the stagnation point of the sphere affects the flow field globally more so than when it was located closer to the separation point or within the wake region. The synthetic jet in the wake of the sphere also improves the aerodynamic performance, since the momentum of the synthetic jet is mostly transferred to the wake of sphere and does not interact with the attached boundary layer.

The wake region was effectively analysed by taking surveys using the five-hole pressure probe. The reversal-of-flow regions, resulting from the highly three-dimensional flow over the sphere bluff body, were successfully identified using the various criteria developed to filter the measured data.

The wake of the standard sphere was compared to the cases of applied synthetic jet. The wake region was characterised extensively with conventional methods derived from the measured data. The velocity field and contour maps of the pressure fields and vorticity were developed and used along with flow visualisation. Following this, an analysis using displacement and momentum thickness and the shape factor provided additional tools to conduct an in depth analysis of the three-dimensional flow field and the modifications of synthetic jet at different angles of incidence.

Force balance measurements were used to bolster the results already obtained showing that the synthetic jet has the effect of reducing the drag on sphere in highly reversing three-dimensional flow.

The asymmetrical localised synthetic jet can be used as a localised point source to effect changes to the wake region. It can be strategically placed at different areas on both a bluff and a streamlined body to produce significant changes in the

characteristics of the wake by reducing reversal of flow through delaying separation or directly injecting momentum in the separated flow region thereby reducing the vorticity and streamlining the flow.

---

## Chapter 6

### Results and Discussion: CFD on a Bluff Body

---

## 6. Results and discussion: CFD on a bluff body

Chapter 6 is concerned with making progress with applications related to the field of aeronautics using computational fluid dynamics. The synthetic jet is applied to three-dimensional flow fields. The natural progression has been to study the behaviour of the synthetic jet in isolation operating in an environment of stationary ambient atmospheric air (Glezer and Amitay 2002). More advanced research is then conducted in increasingly complex arrangements, such as in a crossflow generated in a wind tunnel with the synthetic jet located on a stationary solid body (Jeon, et al. 2004; Glezer and Amitay 2002; Findanis and Ahmed 2008). To study the synthetic jet on a basic bluff body that has a well-established body work and therefore a well-defined flow field at a specific Reynolds number or range of Reynolds number allows for the accurate determination of the effects of the synthetic jet. Whether that be a quantitative approach concerned with, for example the coefficient of drag obtained from a load cell transducer, or qualitative which could be more concerned with providing insight into the reduction of vortices formed in the wake region of a solid body using tufts and photography (Bradshaw 1970).

Chapter 6 builds on the physical experimental investigations conducted on a side-supported sphere with synthetic jet that was performed earlier at UNSW (Findanis and Ahmed 2008; Findanis & Ahmed 2011). The drag on a side supported sphere considerably increases when supported in this manner as opposed to locating the support directly behind the sphere in the wake region (Krause 2005). The advantage of the side-supported sphere used in the previous experimental work is that it allows for the continuous rotation of the synthetic jet through  $360^\circ$ . Also, any angle can be fixed by rotating the support relative to a protractor fixed to the wind tunnel side wall. This proved useful for fixing the synthetic jet at various predetermined angles of incidence and then conducting wake surveys. The local

synthetic jet orifice was located on the sphere at a  $45^\circ$  angle to the surface normal towards the unsupported end. Another interesting flow feature that the side-supported sphere exhibits in the crossflow is the disturbed flow region at the support-sphere junction. The side support affords us the opportunity to examine more closely the flow features or flow characteristics of solid body junctions in a crossflow

A computational model is developed in the present work to simulate the flow past the side-supported sphere firstly as a baseline case without active control. The computational model is then further developed to include the momentum imparted by synthetic jet motion. The resulting flow field which includes the effect of synthetic jet is compared to the baseline flow field or reference flow field. The synthetic jet is actuated at different angles of incidence to the incumbent flow. The results of the computational study will be seen to compare well with the experimental results taken in a wind tunnel. The surface pressure on the side supported sphere and the wake region are the areas investigated to provide evidence of aerodynamic flow modifications due to the asymmetrical localised synthetic jet.

## **6.1 Side-supported sphere with asymmetrical localised synthetic jet: Surface pressure distribution**

The baseline model of the side-supported sphere was simulated as a transient analysis until the flow had fully developed from the initial conditions to the resultant flow field. The baseline surface pressure distribution,  $C_p$  was compared to that calculated from the physical experimental result obtained at the UNSW Aerodynamics Laboratory. Figure 6.1 shows this comparative plot of the  $C_p$  distribution between the two different turbulence models used to compare the accuracy of the analysis. The widely used standard  $k-\varepsilon$  turbulence model, is known to be robust using a scalable wall-function for the near-wall fine mesh. The Shear

Stress Transport (SST) turbulence model is designed to be used for flows with adverse pressure gradients with flow separation. As can be observed from the plot, the SST turbulence model predicts rather late separation at approximately  $104^\circ$  compared to the experimental result of approximately  $83^\circ$ , producing a 25.3% difference. In comparison, the SST model is significantly better than k- $\epsilon$  model, which predicts flow separation at approximately  $142^\circ$ , a difference of 71% with the experimental result.

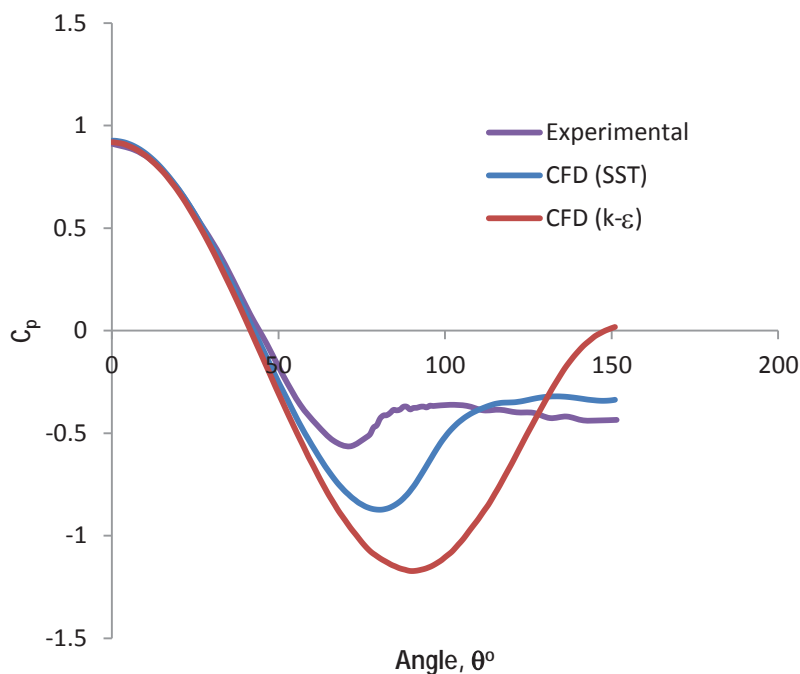


Figure 6.1. Comparison of experimental  $C_p$  distribution with CFD baseline case: turbulence models.

The synthetic jet was applied at the three angles of incidence of  $6.5^\circ$ ,  $76^\circ$  and  $100^\circ$  relative to the fore stagnation point. A representative time frame with the synthetic jet at a peak of the oscillatory pulsating motion was taken for all cases and the pressure coefficient along the sphere centreline was plotted in Figure 6.2.

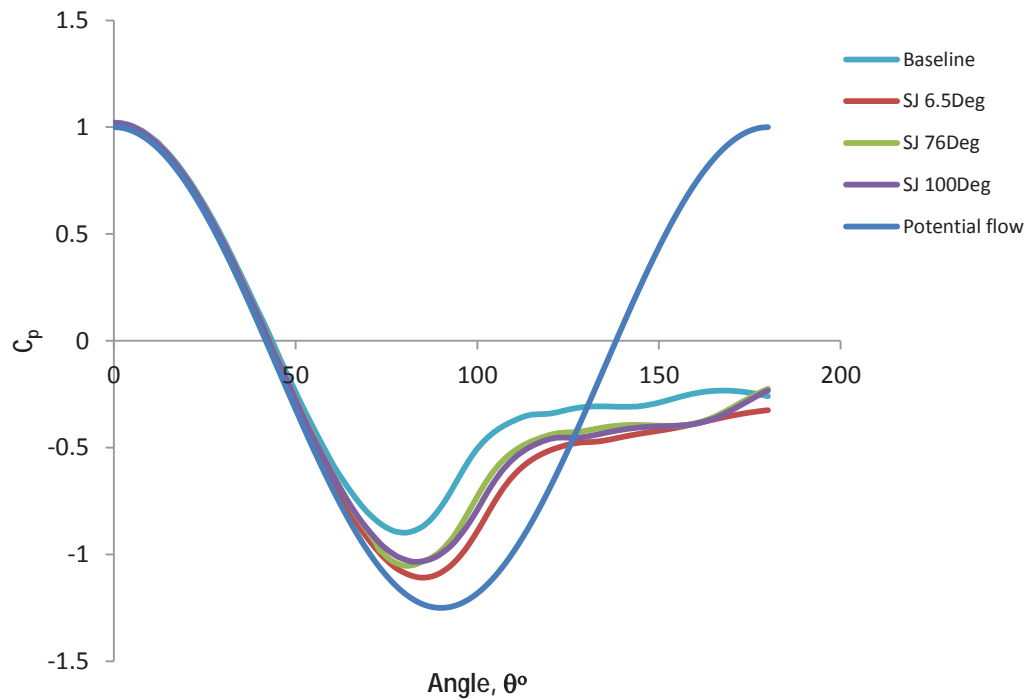


Figure 6.2. Comparison of  $C_p$  with synthetic jet at peak outflow at different angles of incidence

It is apparent from Figure 6.2 that the application of the synthetic jet modifies the surface pressure over the side-supported sphere. The synthetic jet alters the surface pressure at all angles of incidence, even at the small angle of  $6.5^\circ$  being close to the fore stagnation point. The angle of incidence has a large impact on the development of the flow field and the aerodynamic performance of the supported sphere. It would seem from Figure 6.2 that, with the synthetic jet at  $6.5^\circ$ , the surface pressure drops ahead of the separation point, thus accelerating the fluid flow relative to the baseline case. The separation point is only slightly delayed and the  $C_p$  post-separation is lower than the base line case, indicating negligible or a small effect on the drag. With the synthetic jet at  $76^\circ$  just prior to separation and  $100^\circ$  well after separation the move to towards potential flow pre-separation is not

as substantial as at  $6.5^\circ$ , as can be observed from Figure 6.2. At  $76^\circ$  there is less distance for the momentum of the synthetic to have an impact on the development of the boundary-layer and contribute positive momentum to the flow field globally from the localised synthetic jet. At  $100^\circ$  the momentum is injected directly into the separated wake region and, thus, any beneficial effects to the flow would be by accelerating the fluid out of a recirculation zone which could then feedback to the surface pressure, as indicated in Figure 6.2. The common trend with all angles of incidence of the synthetic is the move towards potential flow before separation occurs. This is especially counter-intuitive at the synthetic jet angle of incidence of  $100^\circ$ . This suggests that, by placing a localised synthetic jet in a separated flow region, the momentum imparted by the synthetic jet is capable of producing changes in the flow field that can feedback to modify the upstream flow conditions. This would then change the flow field that the synthetic jet interacts with and, thus, the momentum imparted to the separated flow region could further modify the flow downstream which could again feedback to change the upstream flow conditions. An iterative process is then generated until a steady state flow field has been reached due to the perturbation of the synthetic jet on the cross flow. Alternatively if the flow is highly unsteady and/or asymmetric stemming from wake instability, vortex shedding, geometry etc, then it is possible that a steady state condition is not attained in the flow field. Rather, a constantly changing state is present, in which case the results would be transient in nature requiring a time series snapshot that is sufficient in length to capture the changing conditions. The synthetic jet actuation frequency could also affect the unsteady flow field by increasing the degree of unsteadiness, causing an increase in turbulence or conversely dampen the unsteady changing flow field to incline the flow and bring about a steady state condition. Each outcome would then be beneficial depending upon the application that is being considered. For example a flow field that requires the mixing of different inflows would benefit from an increase in turbulence, whereas aerodynamic applications such as the flow over a wing would benefit by decreasing the size of the wake or vortex shedding.

The synthetic jet angle with incidence of  $6.5^\circ$  would be expected to generate a different wake flow than that for the synthetic at  $76^\circ$  and  $100^\circ$  angle of incidence. This would also go towards clarifying the differences in surface pressure distribution. A method of analysing the flow due to the synthetic jet on the cross flow is by observing the direction of the streamlines emanating from the synthetic jet cavity.

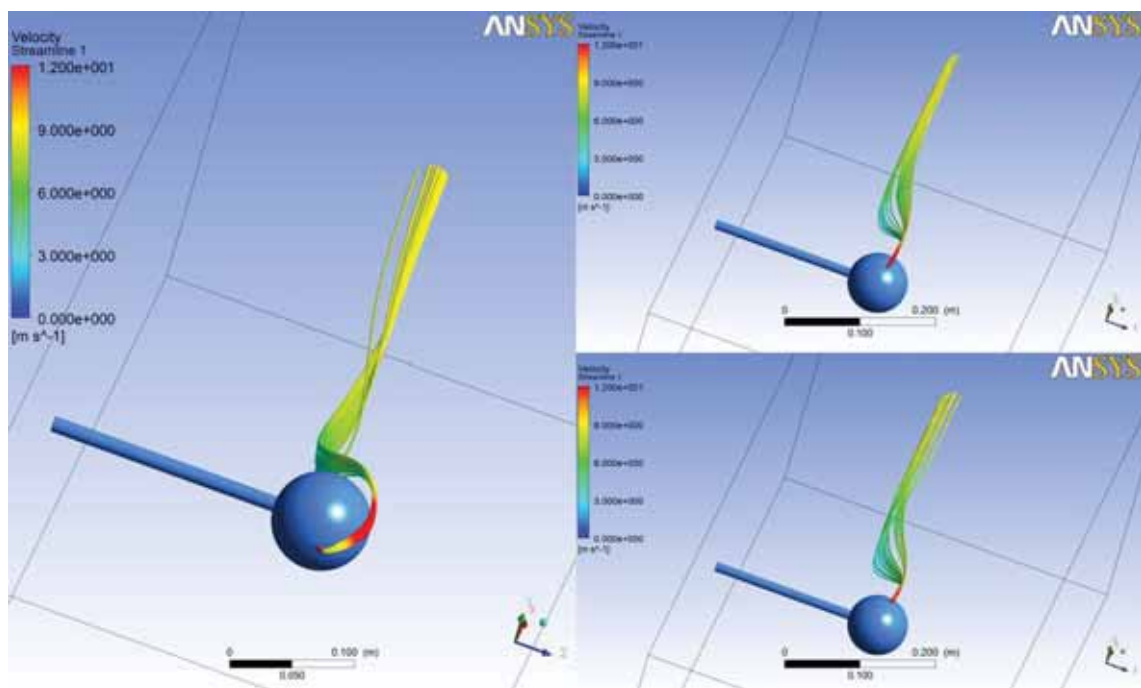


Figure 6.3. Synthetic jet streamlines, peak outflow. Clockwise from left synthetic jet at  $6.5^\circ$ ,  $76^\circ$  and  $100^\circ$ .

With the synthetic jet at  $6.5^\circ$ , the flow is absorbed into the cross flow over the sphere following the surface contour of the sphere wrapping around the solid body in almost a Coanda fashion. At the other two angular locations of the synthetic jet, the streamlines indicate a similar result which follows from the  $C_p$  distribution. With the localised synthetic jet at  $6.5^\circ$ , the momentum does not substantially seem to

benefit flow separation. The flow is entrained into the vortical structures formed in the wake region. The streamlines of the synthetic jet at  $76^\circ$  and  $100^\circ$  are directed into the wake region with the sphere body itself not affecting the flow in the same manner as in the case with the synthetic jet at  $6.5^\circ$ . The momentum imparted to the cross flow produces a straightening of the flow breaking up the flow reversal which would increase the  $C_p$  in the base region on the sphere as observed in Figure 6.2.

## 6.2 Wake Analysis

The wake region is a key region to target and improve the bluff body aerodynamics of the side-supported sphere. The experimental work conducted previously (Findanis and Ahmed 2008, Findanis and Ahmed 2011) showed that the localised synthetic jet was able to decrease the size of the wake region and increase the streamwise velocity component. The experimental results indicate that the wake region has almost completely recovered to the freestream conditions at a downstream distance of  $3D$  (280 mm from the sphere centre). For the CFD simulation plots, they have been prepared showing the velocity in the wake region along the centreline axis from the base of the sphere to a point three diameters downstream or 240 mm from the base of the sphere for all three global velocity components  $U$ ,  $V$  and  $W$ .

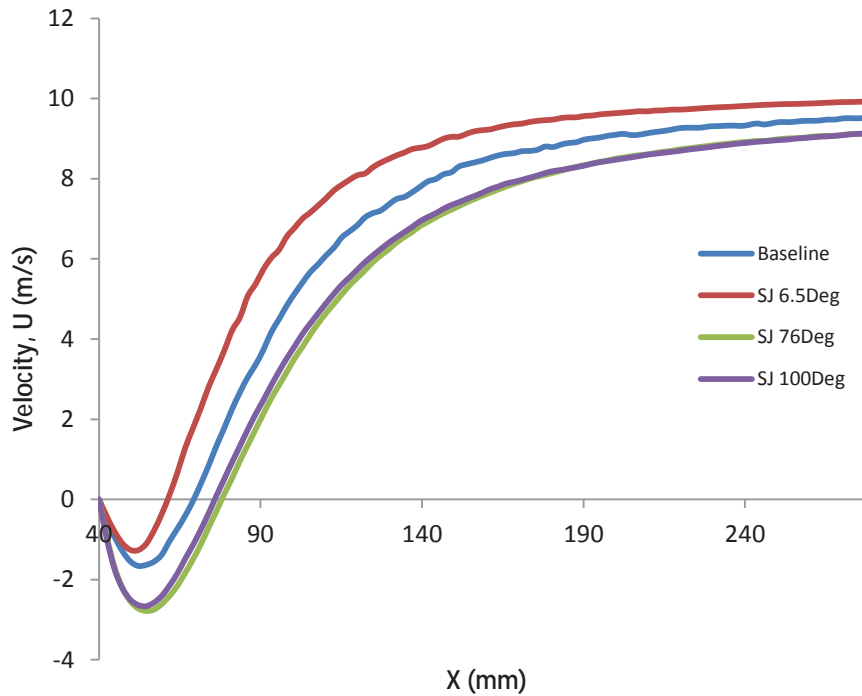


Figure 6.4. Comparison of streamwise velocity  $U$ .

Figure 6.4 shows an increase in the streamwise velocity component over the baseline case for the synthetic jet at  $6.5^\circ$ . However, there is a decrease in the streamwise velocity component of approximately the same amount for the other angular locations of  $76^\circ$  and  $100^\circ$ . The increase coming from the synthetic jet at  $6.5^\circ$  would be the added momentum entrained into the flow combining to increase the velocity. It could be that at  $76^\circ$  and  $100^\circ$  the cross flow is perturbed in a manner that could cause a decrease in the velocity  $U$  due to the vector combination of the synthetic jet velocity  $U_{sj}$  and the cross flow velocity over the sphere  $U_{sphere}$ . This would be suggested since according to Figure 6.2 the synthetic jet provides corrective flow modification towards potential flow in the separated flow region on the sphere surface more so than at  $6.5^\circ$ .

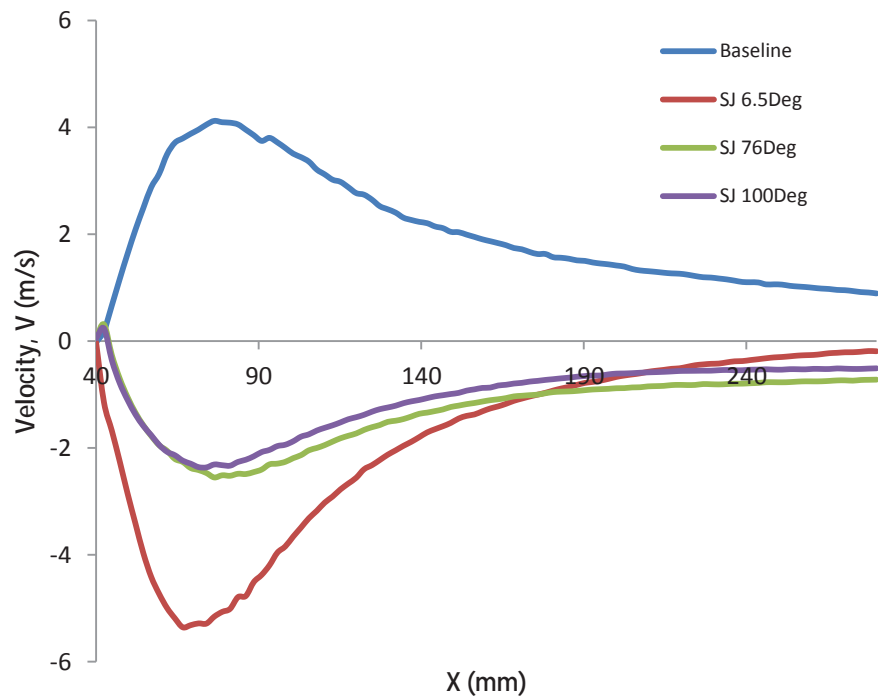


Figure 6.5. Comparison of crosswise velocity  $V$ .

Further insight is gained from the crosswise velocity  $V$  as shown in Figure 6.5. A drastic change of direction of  $V$  occurs with all three angular locations of the synthetic jet. Instead of the  $V$  pointing upwards the velocity component is now pointing downwards along the centreline opposite of the baseline case. The synthetic jet at  $76^\circ$  and  $100^\circ$  not only alter the direction of the vector but also manage to decrease this component. At  $6.5^\circ$  it actually increases  $V$  but more quickly reduces this to almost zero as we move downstream in the wake. This would be a reason why the synthetic jet  $6.5^\circ$  does not increase the base pressure on the sphere as much as at  $76^\circ$  and  $100^\circ$ .

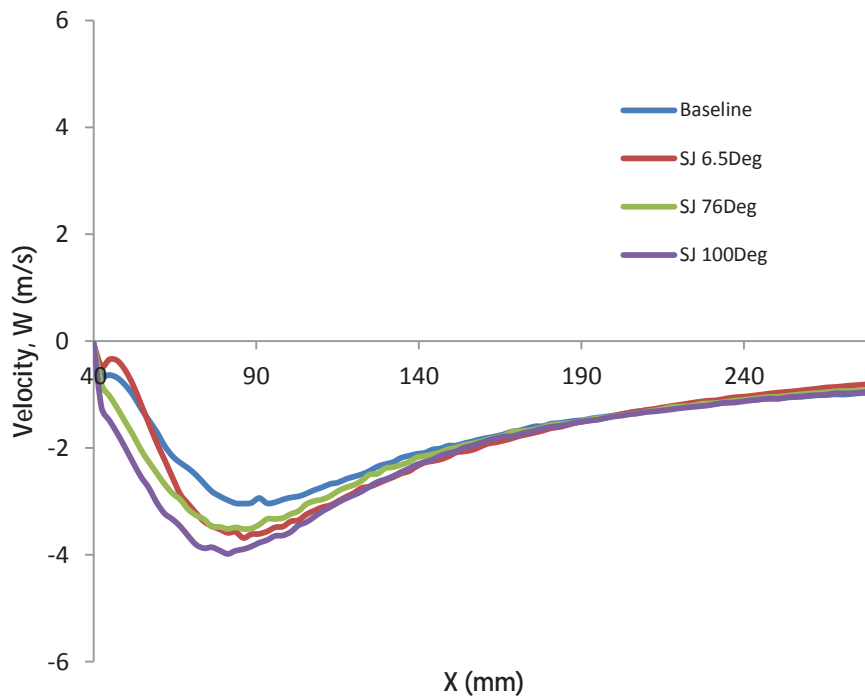


Figure 6.6. Comparison of crosswise velocity  $W$ .

In Figure 6.6 the crosswise velocity  $W$  does not alter greatly although the synthetic jet as would be expected does modify this component as well. The synthetic jet at  $100^\circ$  imparts the greatest increase to the  $W$  vector component. Interestingly, close to the sphere base at  $X = 40$  mm, the synthetic jet at  $6.5^\circ$  follows the same trend as that of the baseline case with a slight hump in the velocity. It then drops although further than the baseline case. In other two cases of synthetic jet at  $76^\circ$  and  $100^\circ$  the component  $W$  immediately starts to increase in the negative  $W$  direction indicating that at these locations the flow over sphere does not influence the synthetic jet with same behaviour as that at  $6.5^\circ$ .

A velocity contour plot shows the influence of the synthetic jet on the wake region in Figure 6.7. The baseline case shows slither of low velocity in the upper part

coming off the sphere and around the bottom but accumulated to the base of the sphere. With the synthetic jet applied in all cases the velocity in the upper half of the sphere increases significantly. This is countered by an increase of low velocity flow in the lower half of the sphere when the synthetic jet is applied over the baseline case. The advantage of the synthetic jet is seen in the decrease of the crosswise velocity component  $V$  as in Figure 6.8. A large decrease is observed in the upper half of the sphere without a concomitant increase in the lower half.

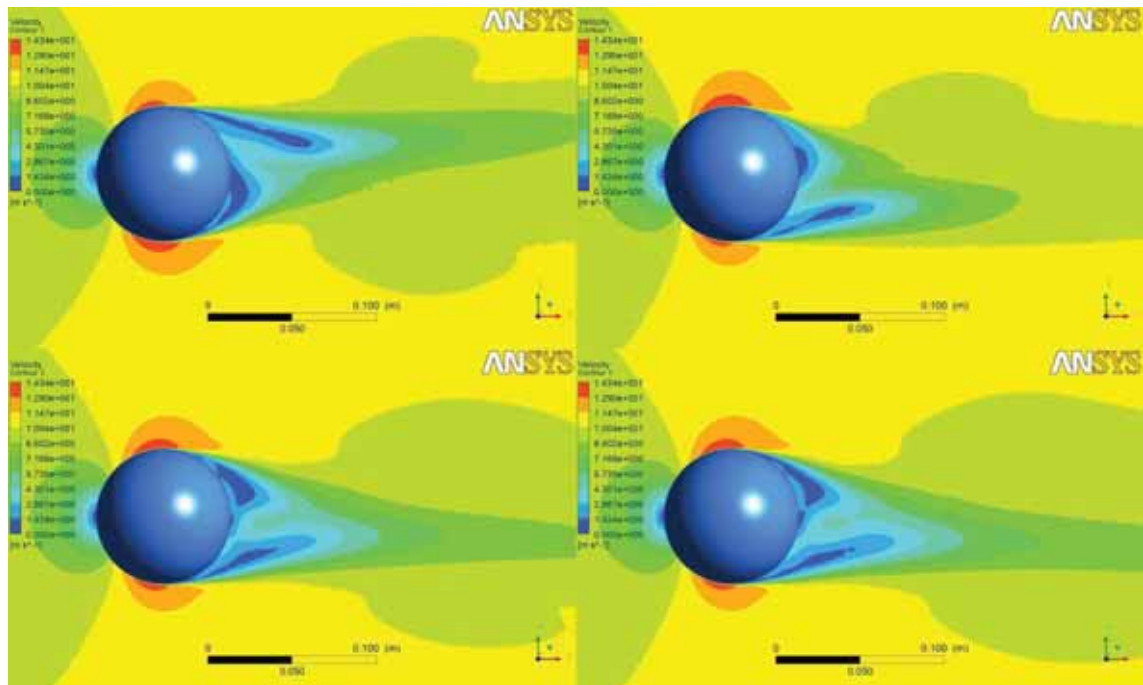


Figure 6.7. Velocity contour plot, synthetic jet peak outflow. Clockwise from top left baseline,  $6.5^\circ$ ,  $76^\circ$  and  $100^\circ$ .

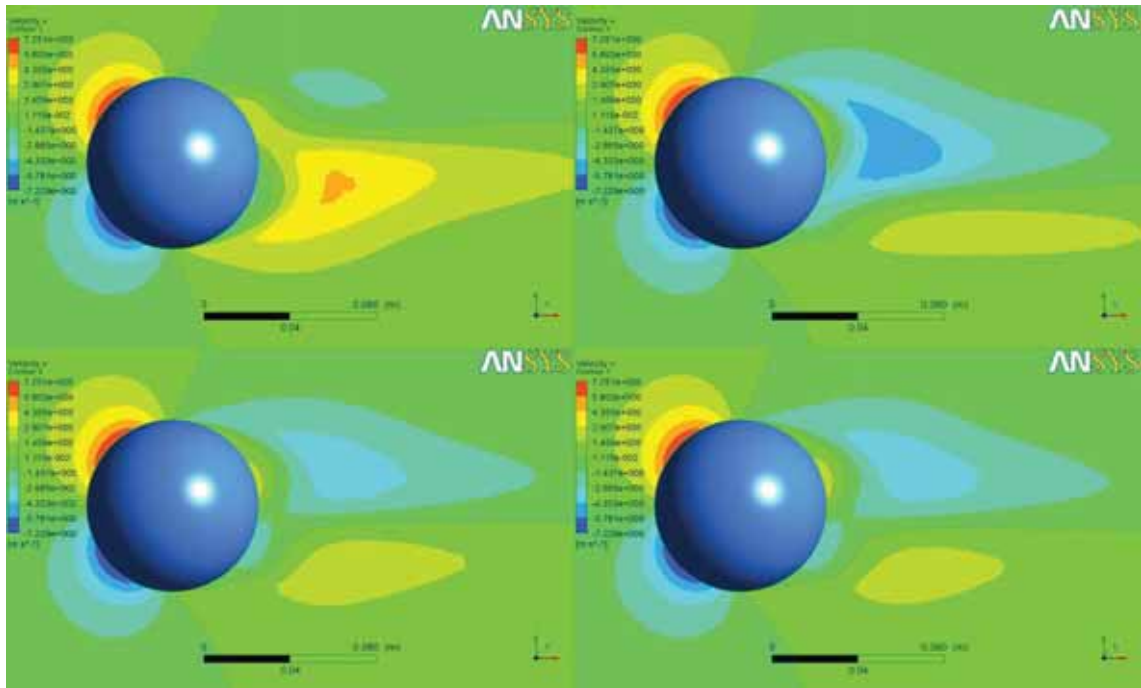


Figure 6.8. Velocity contour plot, V component, synthetic jet peak outflow. Clockwise from top left baseline,  $6.5^\circ$ ,  $76^\circ$  and  $100^\circ$ .

### 6.3 Support-sphere junction

The junction between the sphere and side-support is a geometrical feature that adversely influences the aerodynamic performance of the fluid structure interaction. This is a source of interference drag that we would seek to reduce through the introduction of the synthetic jet. Firstly, considering the baseline case, this highlights the problematic regions of flow reversal in the wake. The results are taken at a transient time with the flow fully developed in its unsteady condition. Figure 6.9 is a contour plot of the streamwise velocity vector  $U$  on the centre plane through the side-supported sphere in the XZ plane. A strong recirculation zone is formed in that region of the sphere connected to the cylindrical support. The reversal of flow region influences the surrounding flow through entrainment of fluid into this dead zone of the flow field.

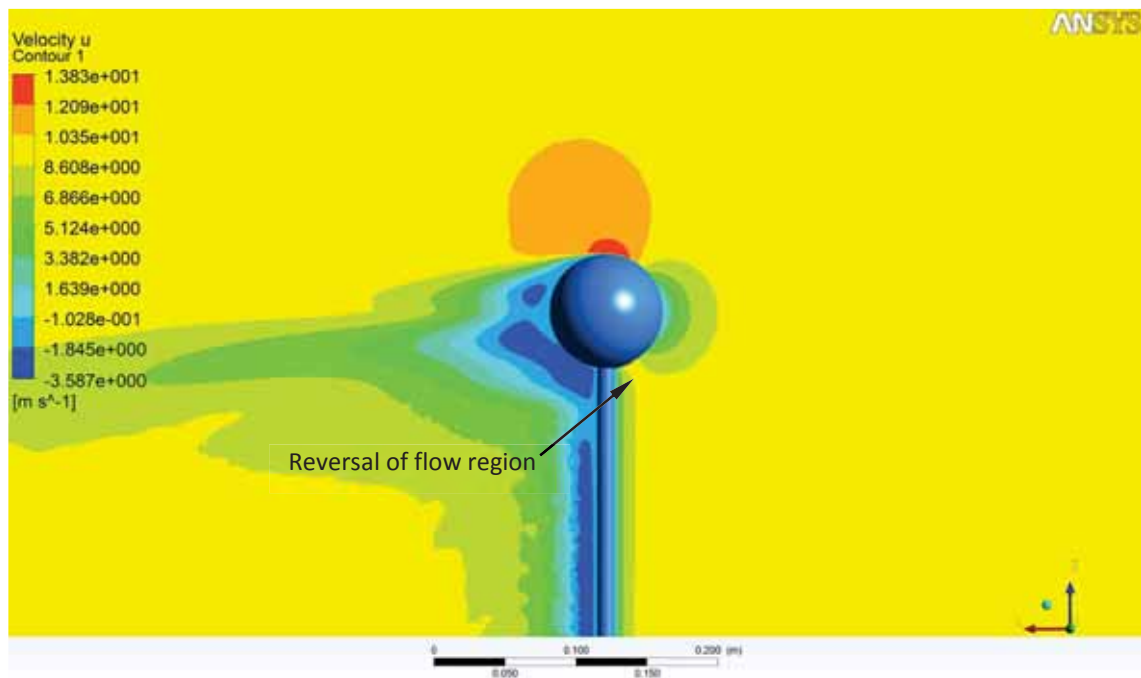


Figure 6.9. Contour plot baseline case, velocity component, XZ plane

The vorticity has been reduced in the interference region, most notably about the X and the Z axes. Figure 6.10 shows the vorticity about the X axis along  $Y = 0$  and at the Z point corresponding to the junction of the support-sphere. The vorticity direction is reversed due to synthetic jet at all angles of incidence relative to the baseline case indicating a significant effect on the flow field at the junction. The synthetic jet at  $6.5^\circ$  initially lowers the vorticity almost to zero at about  $X = 55$  mm almost directly opposite the baseline case which also drops at about this streamwise location with reverse sign of vorticity. The drop is only local followed by a steep rise and peak at about  $X = 130$  mm after which it begins to subside in the streamwise direction. With the synthetic jet located at  $76^\circ$  and at  $100^\circ$  we observe a similar trend happening in both cases with an initial decrease over the baseline case and then kept relatively constant in the streamwise direction.

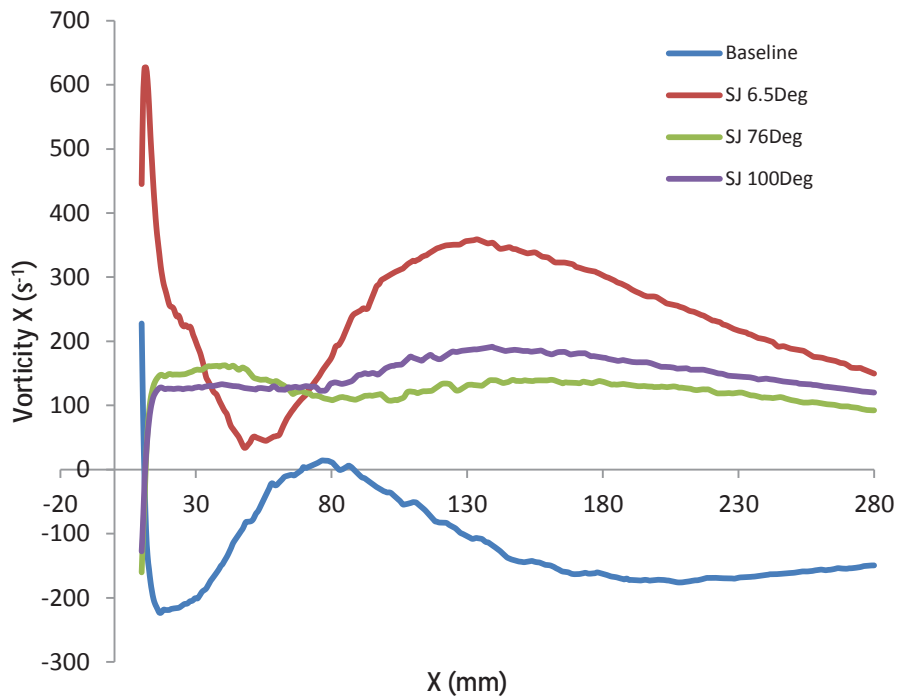


Figure 6.10. Comparison of vorticity X-axis, synthetic jet peak outflow. Along streamwise centreline at support-sphere junction

In Figure 6.11 we see the vorticity about the Z axis at the same location along the streamwise centreline at  $Y = 0$ . A similar trend occurs for vorticity Z with the synthetic jet at  $6.5^\circ$  acting to reverse the vorticity direction and producing a peak almost directly opposite relative to the baseline case. Downstream at approximately  $X = 115$  mm the plot then follows the baseline case. The synthetic jet at the two other locations seems to lower the vorticity Z over the baseline case and decreases down to zero at about  $X = 130$  mm. This proves that the synthetic jet is much more effective at  $76^\circ$  and  $100^\circ$  at reducing this component of vorticity in this problematic region.

There was no significant effect in the vorticity about the Y axis when the synthetic jet was actuated over the baseline case at this same location therefore this component of vorticity has not been plotted in this analysis. Thus, any change in the total vorticity would be mainly due to vorticity X and vorticity Z.

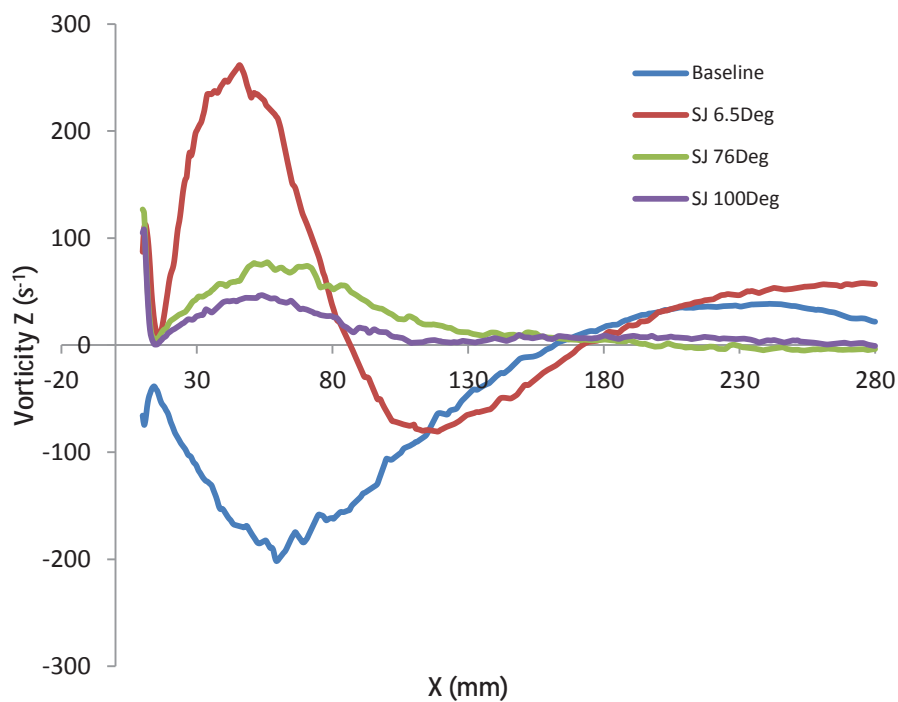


Figure 6.11. Comparison of vorticity Z-axis, synthetic jet peak outflow. Along streamwise centreline at support-sphere junction

## 6.4 Drag Force: Side-supported sphere

The drag was calculated at the time-step that was used for the wake analysis although it was also determined at other time-steps and found to vary significantly dependent on the unsteady nature of the flow field for the side-supported sphere. At this particular time-step, it was found that with the synthetic jet at  $6.5^\circ$  the drag on the side-supported sphere was found to actually increase by approximately 3.0%. With the synthetic jet at  $76^\circ$ , the drag was found to decrease by a very small amount of approximately 0.7% and a negligibly small decrease at  $100^\circ$ . At other time-steps the values differed so that it becomes difficult to gauge the effect of the synthetic jet using this measure.

## 6.5 Conclusion

The unsteady flow over a side-supported sphere was computationally simulated using a commercial CFD package. Active flow control was used to modify the aerodynamic performance of fluid structure interaction. The zero net mass flow technology of synthetic jet provided the active flow control through the injection of momentum of its counter-rotating train of vortices producing a turbulent shear flow. The synthetic jet oscillatory motion was numerically modelled based on the harmonic sinusoidal function that was derived from experimental work conducted by Findanis and Ahmed (2008). An open type boundary condition was used that allows flow to pass in both directions at this solid boundary generating an overall mass flow rate of zero and a velocity profile similar to the experimental synthetic jet. The synthetic jet cavity was also based on the physical experimental model. The cavity was constructed as a cylindrical hole of 1 mm diameter. The fluid volume of the side-supported sphere with synthetic jet orifice mounted in the wind tunnel was then formed in a commercial CAD package. The computational simulation was performed at a Reynolds number of  $5 \times 10^4$  producing a subsonic cross flow velocity of 10 m/s over the side-supported sphere. The asymmetrical localised synthetic jet

was placed at three separate locations at an angle of incidence of  $6.5^\circ$ ,  $76^\circ$  and  $100^\circ$ .

To develop an accurate numerical simulation of the side-supported sphere with the separated three-dimensional flow as well as the turbulent shear flow generated by the synthetic jet, two different turbulence models were trialled. It was found that the Shear Stress Transport (SST) model of Menter (1993) was a closer approximation to the experimental data.

The surface pressure distributions along the streamwise centreline of sphere showed that pre-separation of the synthetic jet at  $6.5^\circ$  produced the largest gain, accelerating the flow more so towards potential flow. Post separation of the synthetic jet at an angle of incidence of  $76^\circ$  and  $100^\circ$  was able to produce a slightly higher increase in performance as well as inclining the surface pressure distribution towards potential flow before separation had occurred.

The wake analysis showed that the localised synthetic jet is capable of decreasing the size of the wake and streamlining the flow of side supported sphere. Interestingly from the measures used to gauge the aerodynamic performance of the synthetic jet at  $6.5^\circ$ , it provided the largest increase in the streamwise velocity  $U$  and decrease the size of the wake in a certain plane. Upon closer examination, the localised synthetic jet at  $6.5^\circ$  also increased the crosswise velocity component  $V$  to a significant amount. The increase of the crosswise velocity components, whether or not there is large increase in the streamwise velocity, will generate an increase in the vorticity in the wake region. This was the case with the synthetic jet at  $6.5^\circ$ . Thus, when we examine the drag on the side-supported sphere we do not find the reduction that is expected and in fact at certain time-steps the drag increased at this angle of incidence of synthetic jet. Further insight can be gained by comparison of active flow control using acoustic excitation of the crossflow over base-supported sphere (Kim and Durbin 1988). The acoustic forcing frequency was excited at the

dominant shear layer instability frequency of the wake. This had the effect of moving the separated shear layer closer to base of the sphere reducing the size of wake but also increased base pressure and the drag. The mechanism differs with the localised synthetic at  $6.5^\circ$  but likewise instead of reducing drag it could increase by increasing the strength of the vortices.

With the synthetic jet at  $76^\circ$  and  $100^\circ$  it was found that the localised synthetic jet had similar effects in modifying the three-dimensional unsteady flow in wake region of the side-supported sphere. The crosswise velocity component was decreased which was able to decrease the vorticity relative to the baseline case. This was also seen when the junction of the support-sphere was analysed. The drag was thus also decreased slightly.

The present computational work suggests that the asymmetrical localised synthetic jet is able to modify the unsteady three-dimensional flow field on a side-supported sphere producing beneficial and adverse effects depending on the angle of incidence, location and configuration of the synthetic jet orifice. The synthetic jet at all angles of incidence produced an increase in the  $C_p$  distribution towards potential flow before separation although with the synthetic jet closer to the fore stagnation point generated increased vorticity in the wake region. With the synthetic jet at  $76^\circ$  and  $100^\circ$  the wake region was reduced, thus streamlining the flow field and reducing the interference at the support-sphere junction.

---

## Chapter 7

### Results and Discussion: Streamlined Bodies

---

## 7. Results and discussion: Streamlined bodies

Bluff bodies provide an aerodynamic basis with which to compare other more advanced streamlined designs or to compare aerodynamic characteristics in general as described in chapter 2.

We are concerned with applying synthetic jet technology not only to bluff bodies (Findanis and Ahmed 2008) as in Chapter 4 and 5 but also to streamlined bodies such as an airfoil (Duvigneau, Hay and Visonneau 2006) and wings (Margaris and Gursul 2006). When applying any flow control technology, including the synthetic jet, the desire is to improve the flow dynamics. Due consideration must be given to understand how the flow field might benefit from applying flow control technologies (Gad-el-Hak 2000). Chapter 3 describes the careful consideration given to the experimental design and the process undertaken to better understand the effects of localised synthetic jets on wings.

Chapter 7 describes the results obtained in applying an asymmetrical localised synthetic jet to symmetrical and asymmetrical streamlined bodies in three-dimensional flow fields. Firstly, the synthetic jet angular configuration is examined on a rectangular symmetrical wing with a four digit profile, the NACA-0012, with a cut-off wing tip. Secondly, we make use of a forward swept wing that is designed with a five-digit profile, the NACA-23012 airfoil shape. The forward swept wing enables us to apply the localised synthetic jet to an asymmetrical camber wing profile. The unique advantage of this forward swept wing (FSW) is the change in geometry that provides a juncture to study interference drag. Another unique advantage of the FSW, is the fact that the crossflow in the spanwise direction originates from the wing tip and flows towards the wing root which is in the opposite direction to a conventional swept wing. This is useful in determining the effectiveness of the synthetic jet at the juncture with a possibly greater interference

drag imposed by the forward sweep. Wing tip and near wing tip localised synthetic jets will be applied to decrease the induced drag and vorticity.

### **7.1 Optimal angle of a localised synthetic jet on a NACA-0012 wing**

The synthetic jet was initially placed at an angle normal to the surface of the NACA-0012 wing and at two different locations along the chord length. The localised synthetic jet was tested at 15% and 50% of the chord length so as to compare with published results at similar locations characteristic of the developing flow field and the desired flow modification (Kim and Kim 2006; Hassan and Janakim, 1997; Duvigneau, Hay, and Visonneau 2006). The pressure tapping locations are details in Chapter 3.

To ensure the integrity of the wing profile the pressure distribution was measured at  $0^\circ$  AOA. The experiment was conducted at a freestream velocity of 15 m/s. This corresponds to a flow Reynolds number of  $3.42 \times 10^5$ . The pressure distribution is shown in Figure 7.1.

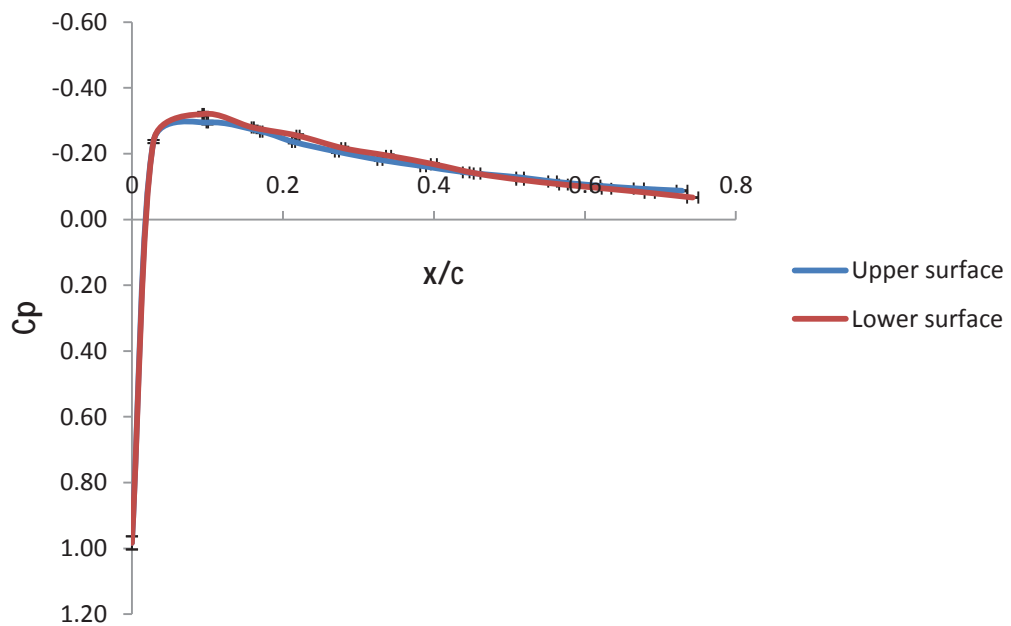


Figure 7.1.  $C_p$  distribution on the NACA-0012 wing at  $0^\circ$  AOA.

The measured  $C_p$  distribution produced a symmetrical match between the lower and upper surface of the wing. This ensured good symmetry of the profile. Additionally, the flow separation angle or stall was experimentally determined to ensure that the profile was in agreement with published results (Abbott and Von Doenhoff 1959). A 36-multitube vertical manometer was used to visually determine the angle. It was found that the wing was stalled at  $16^\circ$  AOA. The results are shown in Figure 7.2. Note that since the pressure tapings were not installed completely around the section the profile is disjointed but sufficient for the intended purpose of showing the effect of the synthetic jet along the majority of the chord length.

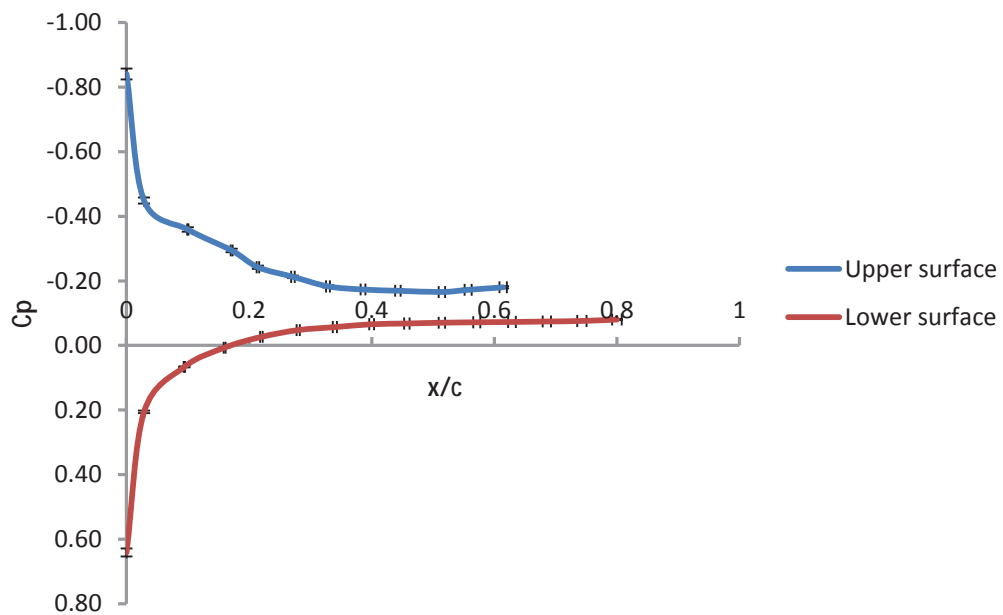


Figure 7.2.  $C_p$  distribution on the NACA-0012 wing at  $16^\circ$  AOA.

The localised synthetic jet was placed only on the suction side of the wing, thus producing an asymmetrical effect on the modified flow as intended. The separation takes place on the suction side and accordingly becomes the critical side to increase the wing performance.

The first case is with the wing placed at  $0^\circ$  AOA and the asymmetrical localised synthetic jet normal to the surface. This becomes the baseline case for comparison with the synthetic jet at the two different locations on the chord. Figure 7.3 shows the performance of the localized synthetic at both chord locations. There is no significant difference in performance relative to the baseline case. The lower surface of the wing showed a similar trend matching the baseline performance.

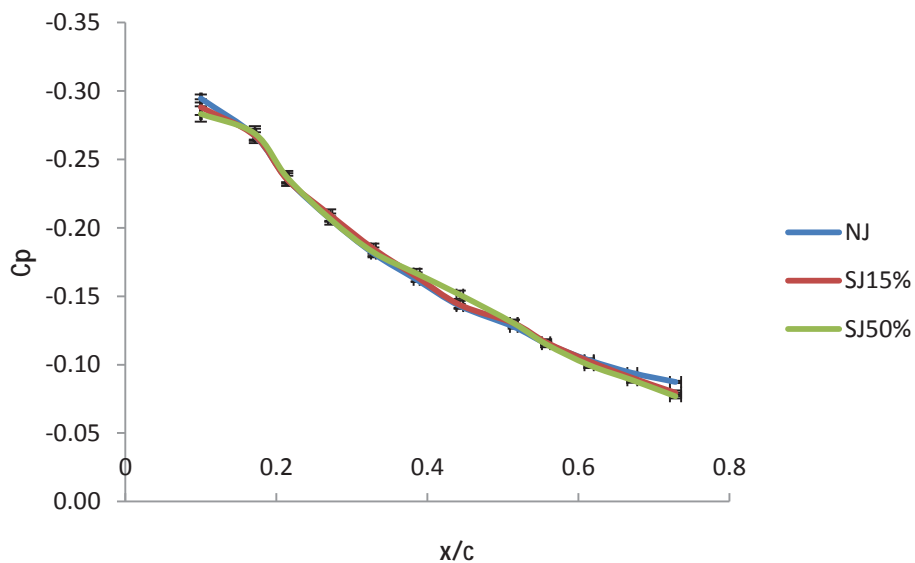


Figure 7.3.  $C_p$  distribution on the NACA-0012 wing at  $0^\circ$  AOA and SJ at  $90^\circ$ . Upper surface with localised synthetic jet. (NJ - no synthetic jet, SJ15% - synthetic jet at 15% chord, SJ50% - synthetic jet at 50% chord)

The wing was then turned to a  $16^\circ$  AOA, the stall angle, and the surface pressure distribution was recorded. The results at this high AOA were again unchanged relative to the base case for both surfaces.

The synthetic jet angle relative to the surface was then changed to  $45^\circ$  at both locations. The localized synthetic jet showed no significant changes in the pressure distribution at the measured location for both  $0^\circ$  and  $16^\circ$  AOA. The AOA was increased to  $20^\circ$ , ensuring that the wing had stalled and that the flow fully separated. The lower surface showed no change in performance due to the synthetic jet at either the 15% or 50% chord length. The upper surface  $C_p$  distribution is shown in Figure 7.4.

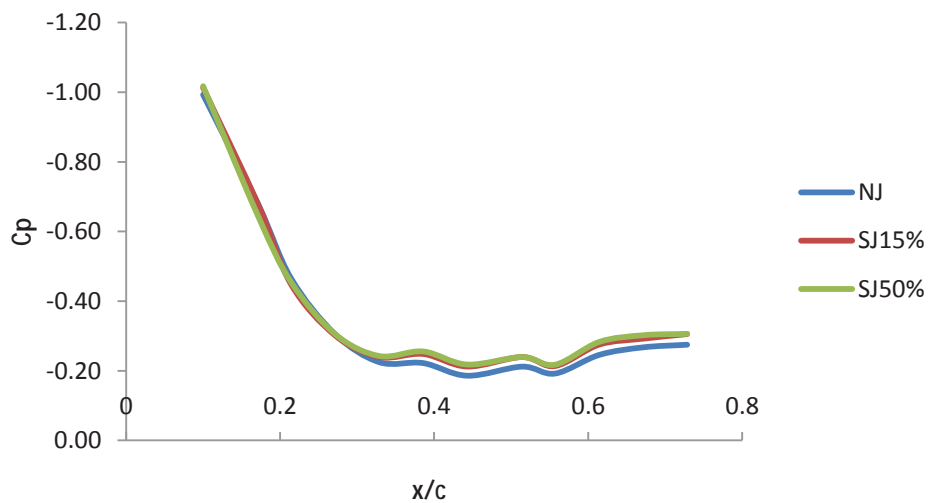


Figure 7.4.  $C_p$  distribution on the NACA-0012 wing at  $20^\circ$  AOA and SJ at  $45^\circ$ . Upper surface with localised synthetic jet. (NJ - no synthetic jet, SJ15% - synthetic jet at 15% chord, SJ50% - synthetic jet at 50% chord)

A slight change is seen in the negative direction of  $C_p$  values indicating a possible improvement in performance. Interestingly, both locations produce almost identical changes in the performance. At such a large angle of attack with the flow fully separated both locations are in the highly reversing wake region and thus could be the reason for producing a similar trend in the results.

The localised synthetic jet was also tested at  $23^\circ$  and  $10^\circ$  to optimise the angle for the most effective flow correction. It was found that at  $0^\circ$  AOA of the NACA-0012 wing there was no significant change in performance. At the stall angle of  $16^\circ$ , the slightly greater change was observed at a synthetic jet angle of  $23^\circ$ .

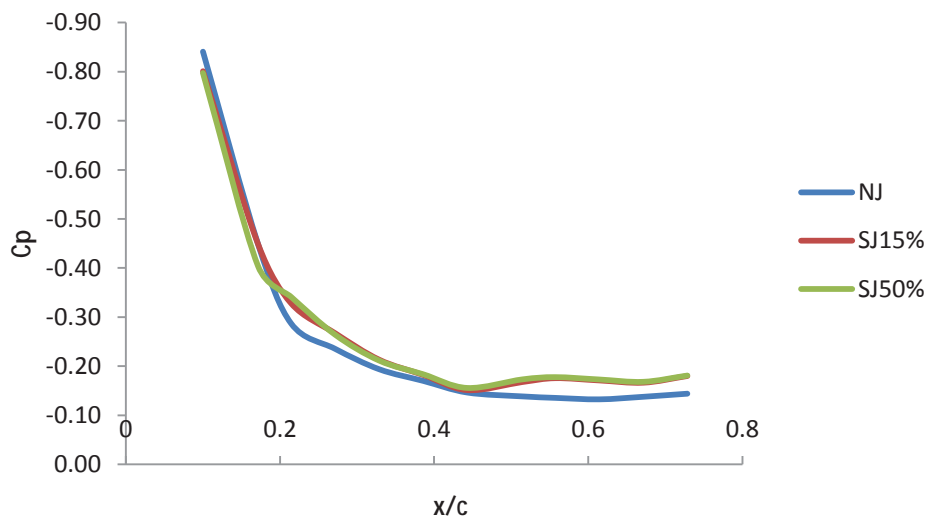


Figure 7.5.  $C_p$  distribution on the NACA-0012 wing at  $16^\circ$  AOA and SJ at  $23^\circ$ . Upper surface with localised synthetic jet. (NJ - no synthetic jet, SJ15% - synthetic jet at 15% chord, SJ50% - synthetic jet at 50% chord)

The higher performance is seen near the trailing edge of wing. The performance increase is only slight, although this is still greater than at other angles which showed no increase at all at  $16^\circ$  AOA. The location of the measurement plane is close to the wing tip as such possible vorticity from the flat cut-off wing tip could influence the measurements making it difficult to gauge the performance of the localised synthetic jet.

## 7.2 Surface pressure measurements on a forward swept wing

The FSW was tested at  $0^\circ$  AOA and the pressure distribution was indicative of NACA23012 performance. The freestream velocity was 10 m/s. The stall point of the wing was found to be  $16^\circ$ . The following pressure distributions were taken close to stall at  $15^\circ$ . The localised synthetic jet was placed at two different positions at each measurement station along the span of the FSW. Aside from the wing tip synthetic jets, the positions were approximately  $1/3$  and  $2/3$  along the chord. Since the results of the pressure distributions produced similar performance at both locations the  $1/3$  chord position only is examined. The results for both the fore ( $1/3$ ) and aft ( $2/3$ ) location of the synthetic jets is shown in Appendix D.

The localised synthetic jet was placed on the wing tip at two different positions of 19% and 54% of the wing tip chord. The localised synthetic jet showed similar performance for each position. The measurements were taken close to the wing tip at station 1. Figure 7.6 and Figure 7.7 show an improvement in the  $C_p$  distribution for mainly the upper surface although the lower surface also benefits from the seemingly reduction in vorticity from the wing tip mounted synthetic jet.

The synthetic jet was next tested at 32% of the chord length at station 1 with the measurements also taken at station 1. Figure 7.8 and Figure 7.9 show the  $C_p$  distribution. The upper surface shows a similar increase in performance at the wing tip location. Although the synthetic jet is asymmetrically placed on the upper surface it seems that the lower surface improves towards the trailing edge.

Figure 7.10 and Figure 7.11 show the synthetic jet located at Station 4 which is the juncture of the FSW. Profile measurements were also taken at Station 4. Interestingly, the  $C_p$  distribution indicates that the performance increases significantly for the first  $1/3$  of the chord and then decreases on the remainder.

Overall, the upper surface indicates a possible improvement in this disturbed junction region.

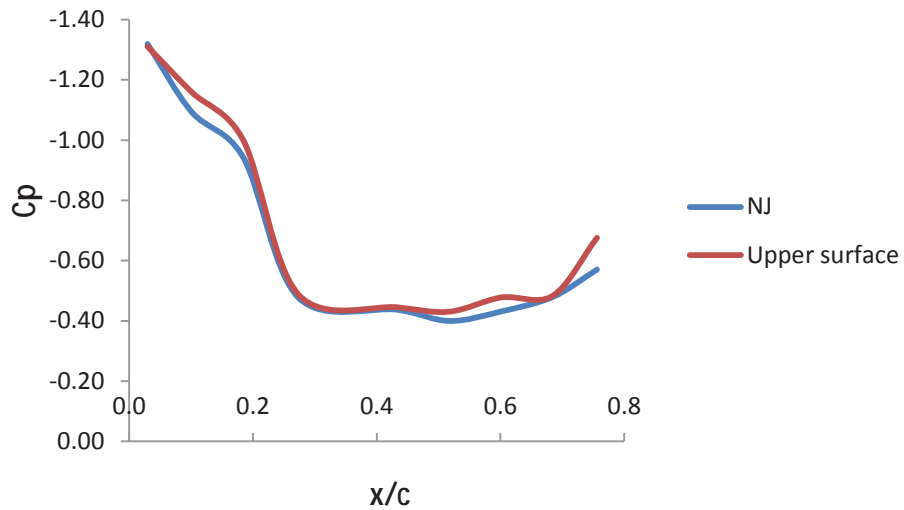


Figure 7.6.  $C_p$  distribution on the Upper surface of FSW at station 1,  $15^\circ$  AOA and SJ at  $23^\circ$ . Upper surface with localised synthetic jet. (NJ - no synthetic jet, Upper surface - synthetic jet at 19% chord of wing tip)

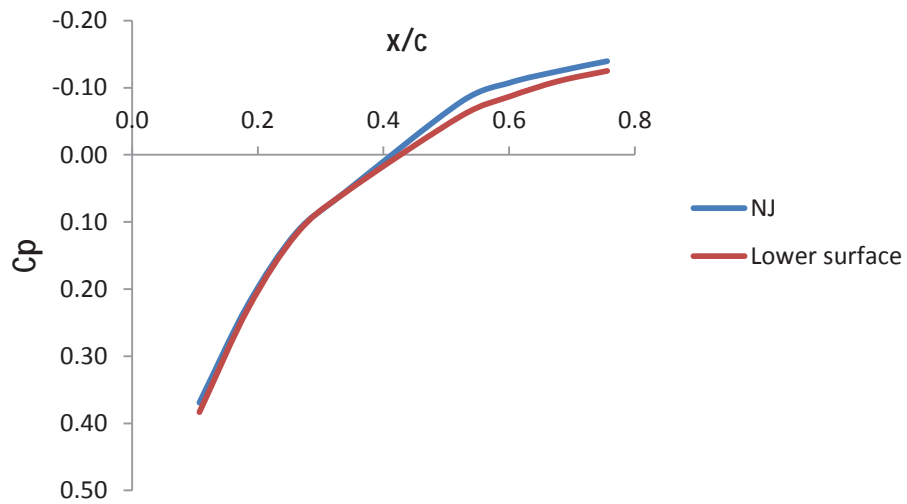


Figure 7.7.  $C_p$  distribution on the Lower surface of FSW at station 1,  $15^\circ$  AOA and SJ at  $23^\circ$ . Upper surface with localised synthetic jet. (NJ - no synthetic jet, Upper surface - synthetic jet at 19% chord of wing tip)

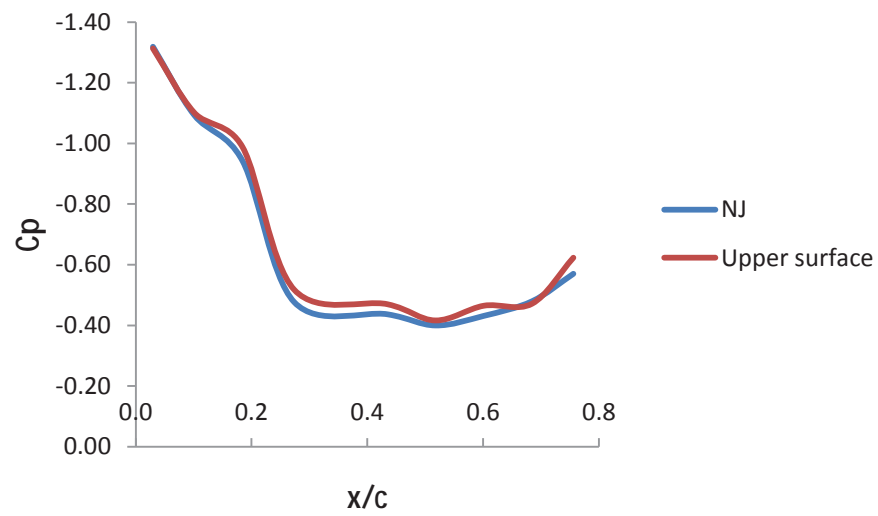


Figure 7.8.  $C_p$  distribution on the Upper surface of FSW at station 1,  $15^\circ$  AOA and SJ at  $23^\circ$ . Upper surface with localised synthetic jet. (NJ - no synthetic jet, Upper surface - synthetic jet at 32% chord of station 1)

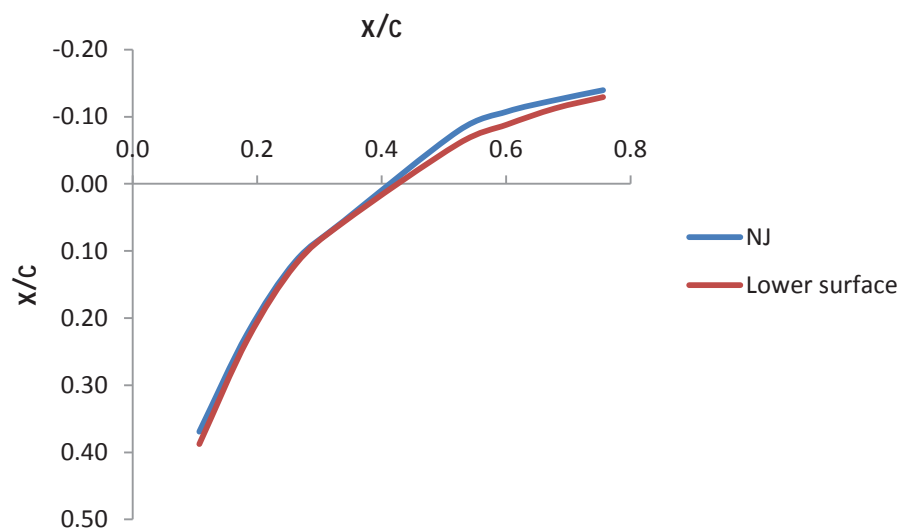


Figure 7.9.  $C_p$  distribution on the Lower surface of FSW at station 1,  $15^\circ$  AOA and SJ at  $23^\circ$ . Upper surface with localised synthetic jet. (NJ - no synthetic jet, Upper surface - synthetic jet at 32% chord of station 1)

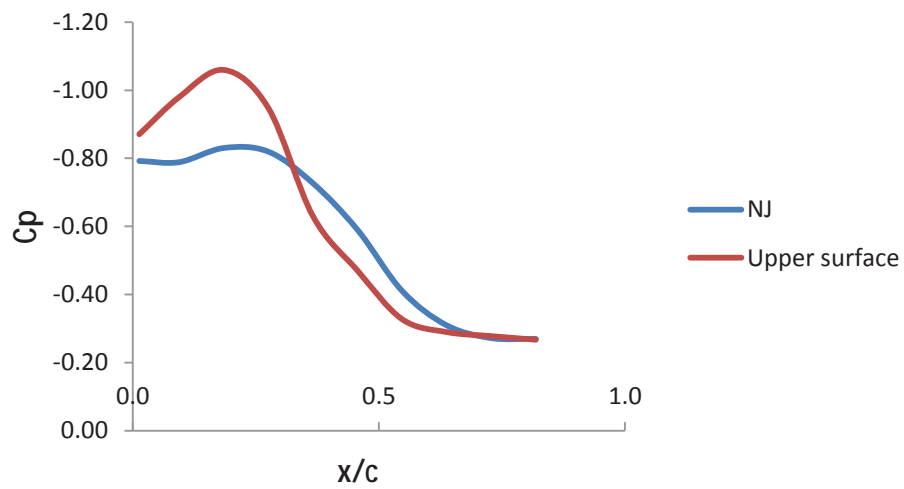


Figure 7.10.  $C_p$  distribution on the Upper surface of FSW at station 4,  $15^\circ$  AOA and SJ at  $23^\circ$ . Upper surface with localised synthetic jet. (NJ - no synthetic jet, Upper surface - synthetic jet at 37% chord of station 4)

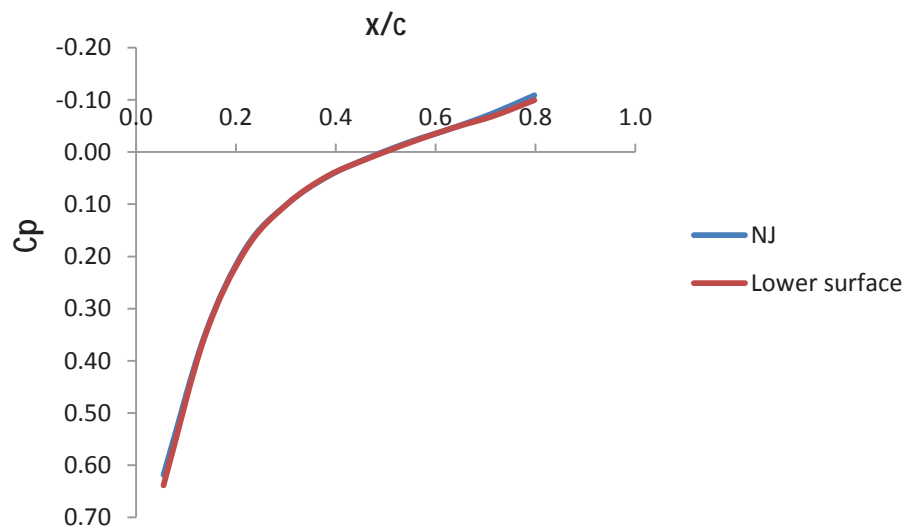


Figure 7.11.  $C_p$  distribution on the Lower surface of FSW at station 4,  $15^\circ$  AOA and SJ at  $23^\circ$ . Upper surface with localised synthetic jet. (NJ - no synthetic jet, Upper surface - synthetic jet at 37% chord of station 4)

### 7.3 CFD simulation of FSW with asymmetrical localised synthetic jet

The performance of the localised synthetic jet was compared to the baseline case at three different locations (WTP-F, SJ1-F, SJ4-F). As mentioned in the previous section, since the experimental surface pressure distribution showed similar results for the synthetic jet placed in the forward and aft location for each measurement station, the results for the forward were shown. As such, the CFD simulation was only performed on the fore location for each measurement station. The designation of these synthetic jet locations is given in section 3.4.

Table 7.1. shows that a significant drag decrease is achieved at all locations of synthetic jet. There is an indication that the synthetic jet is reducing flow separation and consequently reduces pressure drag. There are also possible reductions in induced drag and interference.

Case	Drag force (N)	% $\Delta$
NJ	1.385	-
WTP-F	1.046	24.48
SJ1-F	1.039	24.98
SJ4-F	1.046	24.47

Table 7.1. FSW drag at 15° AOA

Figure 7.12 is a velocity contour comparison of the wing at 15° AOA and at measuring station 4. The NJ case shows flow separating from the wing producing large pressure drag. When the localised synthetic jet is actuated, the reversed flow region is reduced indicating that the flow separation is reduced. The pressure drag would then also be reduced and possible interference. This is indicated by the vorticity plot of Figure 7.13.

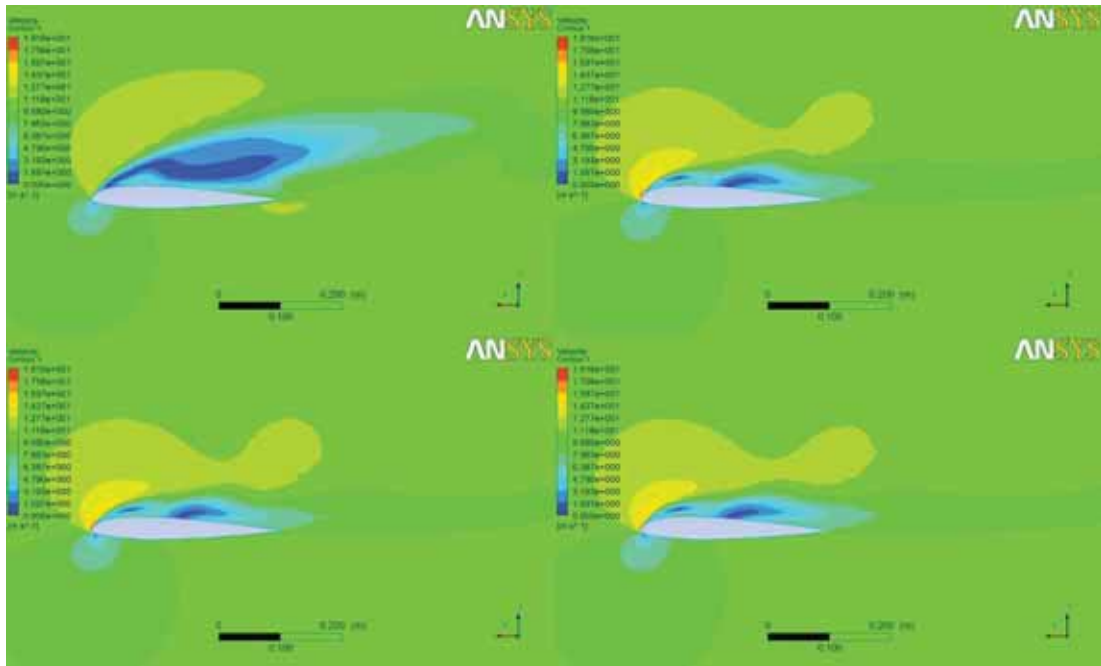


Figure 7.12. Velocity contour comparison 15° AOA. Clockwise from top left, NJ, WTP-F, SJ1-F, SJ4-F.

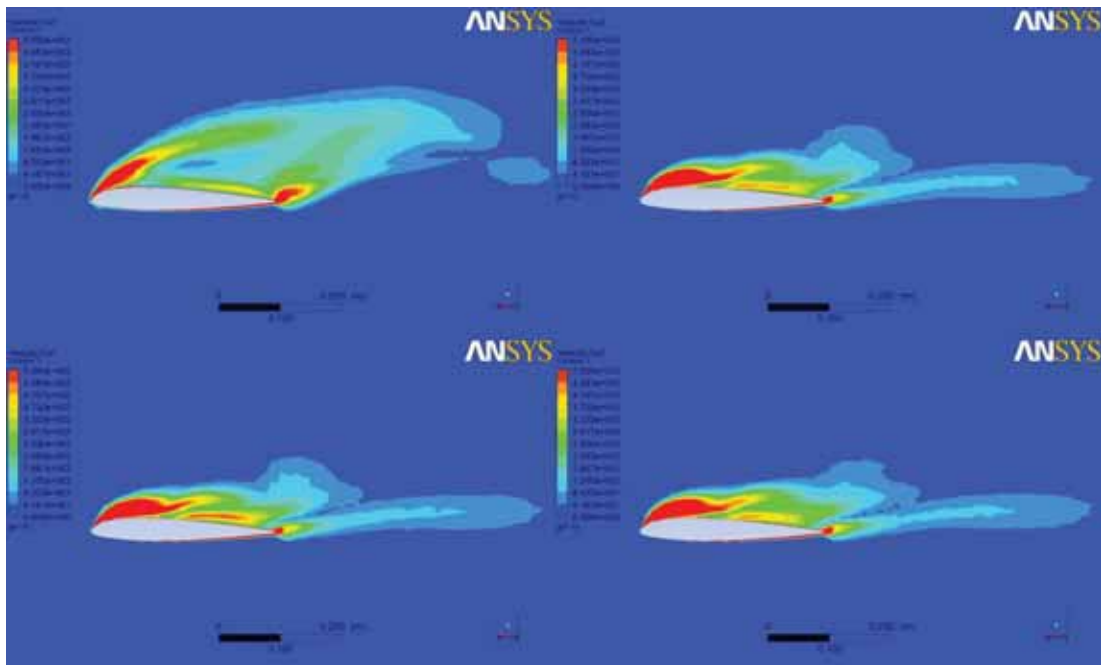


Figure 7.13. Total vorticity contour comparison 15° AOA. Clockwise from top left, NJ, WTP-F, SJ1-F, SJ4-F.

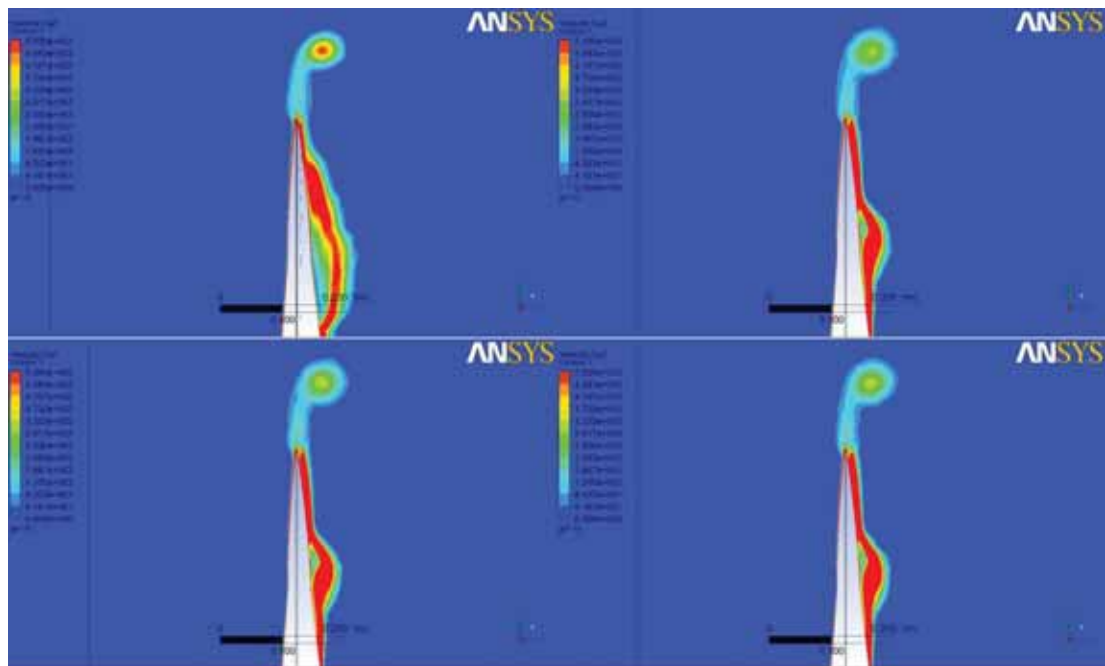


Figure 7.14. Total vorticity contour comparison  $15^\circ$  AOA on a plane perpendicular to streamwise direction, 150mm aft of the origin . Clockwise from top left, NJ, WTP-F, SJ1-F, SJ4-F.

Figure 7.14 shows that the total vorticity is substantially reduced around the wing tip region and all along the wing body in the spanwise direction for all localised synthetic jet locations. Further, Figure 7.15 shows the vorticity at measurement station 1. There is a discernible shortening of the wake, shown as a decrease in the vorticity for the cases with synthetic jet applied in the aft of the wing. The longer band of high vorticity is indicated by the red band over 50% longer in baseline case. The boundary layer has been energised indicated by the higher vorticity close to the surface and further attachment along the wing at this section. It is noteworthy that the localised synthetic jet is able to decrease the vorticity at all positions. Placement at the wing tip would be expected to aid the flow field even at measurement Station 1 with SJ1-F. It is not expected to provide much benefit at SJ4-F or measurement station 4. Evidently, it does provide flow correction significantly by

decreasing total vorticity and increasing the streamwise velocity. This is reflected as a decrease in drag. This indicates that a disruption to the spanwise flow whether it be around the wing tip near the wing tip or even much further away than the wing tip it will be reduced and inhibited significantly providing an increase in aerodynamic performance.

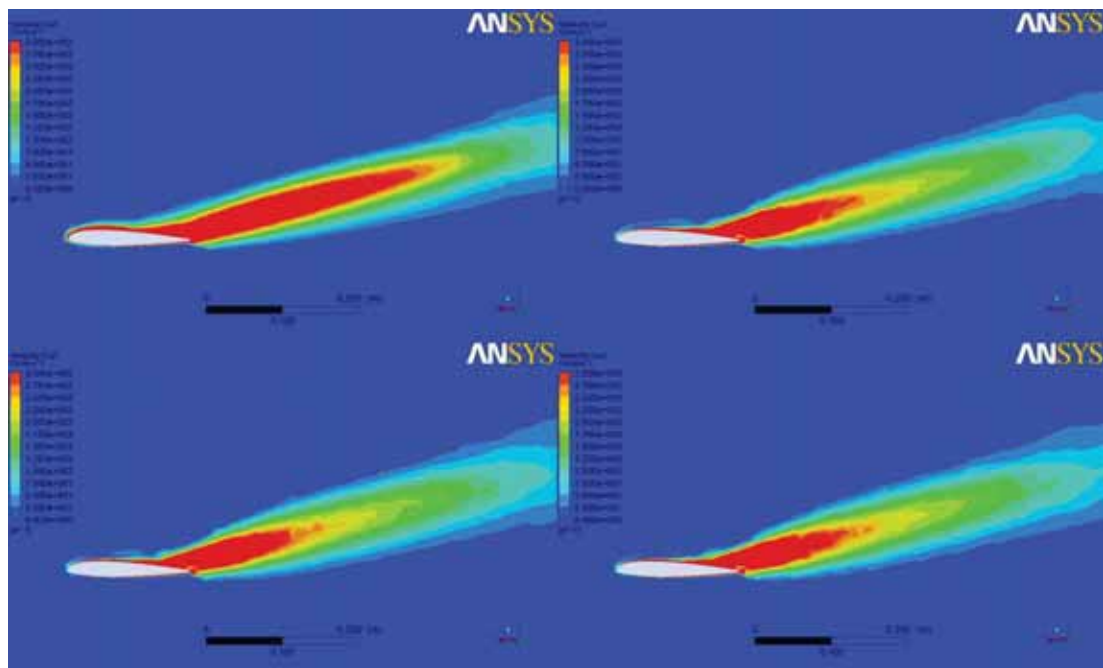


Figure 7.15. Total vorticity comparison  $15^\circ$  AOA at measurement station 1 cross-section through FSW wing. Clockwise from top left, NJ, WTP-F, SJ1-F, SJ4-F.

#### 7.4 Concluding remarks

It has been shown that the asymmetrical localised synthetic jet improved the aerodynamic performance on a symmetrical wing, namely the NACA-0012 airfoil and found that the synthetic jet angle of  $23^\circ$  was the optimal angle to reduce flow separation at  $15^\circ$  AOA.

The asymmetrical localised synthetic jet on the forward swept wing with a NACA-23012 profile was effective in all locations showing a significant reduction in pressure drag due to inhibiting flow separation. The localised synthetic jet mounted to the wing tip towards the leading edge position produced the greatest reduction in wing tip vorticity which would also imply a reduction in induced drag. Interference drag as a consequence would also have been reduced by the decrease in the cross flow velocity due to the localised synthetic jet at all locations. With the synthetic jet at measuring station 4 the localised synthetic jet was able to reduce the large pressure drag formed at this converging geometrical wing section.

---

## Chapter 8

### Conclusions and Recommendations

---

## 8. Conclusions and recommendations

The final chapter serves to bring together the main conclusions of the research and summarise the findings so as to make clear the contributions of the work for the application of asymmetrical localised synthetic jets to fluid dynamic flow control. To highlight the importance of being able to control flow separation in both bluff bodies that inherently do not have built-in aerodynamic shaping and to increase the performance of streamlined bodies at high angles of attack such as the all-important wings of an aircraft. This chapter concludes the thesis work with recommendations for future research in this particular progressive area of fluids.

### 8.1 Conclusions

The work conducted in this thesis has shown some notable effects on the aerodynamic performance of an asymmetrical localised synthetic jet on both bluff bodies and streamlined bodies.

The flow over the side-supported sphere showed that below the critical angle of  $27^\circ$  the flow modifications are ineffective. The aerodynamic improvement owing to the asymmetric localisation of the synthetic jet was manifested in the delay of separation of flow that was found to range the angles of  $83^\circ$  to  $120^\circ$  at a Reynolds number of  $5 \times 10^4$ . Additionally, the synthetic jet generated significant reductions to the total drag on the sphere with an overall reduction of over 12%.

The downstream effects of the sting support were observed from the flow visualization study, which showed the flow from the sphere wake combining with the wake from the sting support forming an asymmetrical interference type of flow. The actuation of the synthetic jet lessened the asymmetric effect of the sting and improved the flow.

The highly three-dimensional flow in the wake region produces flow reversal. Thus, in order to determine when the flow vector was outside the calibrated region of the instrument, a number of reversal of flow criteria were developed to be used for this purpose. The wake surveys conducted with the five-hole pressure probe were validated using hot-wire anemometry and also were effectively tested using a NACA23012 airfoil profile which confirmed the criteria to be applicable to other separated flows.

The three-dimensional velocity field was constructed for all cases with synthetic jet ( $6.5^\circ$ ,  $76^\circ$ ,  $100^\circ$ ) and the standard sphere which was used as the basis to compare the effects of the application of synthetic jet.

The wake region was further investigated by applying Bernoulli's principle in the wake and incorporating the concepts of wake displacement and momentum thickness we were able to successfully show that it is possible to predict the actual values that are obtained when the wake has sufficiently recovered to freestream conditions. The shape factor was also used to clearly characterise the difference between the measured and actual values showing that the synthetic jet improves these characteristics of the wake region.

The unsteady flow over a side-supported sphere was computationally simulated using a commercial CFD package. The CFD simulations were validated with the experimental work performed on the side-supported sphere. Interestingly, the synthetic jet at  $6.5^\circ$  provided the largest increase in the streamwise velocity  $U$  and decrease of the size of the wake in a certain plane. Upon closer examination, the localised synthetic jet at  $6.5^\circ$  also increased the crosswise velocity component  $V$  to significant amount. The increase of the crosswise velocity components, whether or not there is large increase in the streamwise velocity, will generate an increase in the vorticity in the wake region. This was the case with the synthetic jet at  $6.5^\circ$ .

Thus, when we examine the drag on the side-supported sphere we do not find the reduction that is expected and in fact at certain time-steps the drag increased at this angle of incidence of synthetic jet. Further insight can be gained by comparison of active flow control using acoustic excitation of the crossflow over base-supported sphere (Kim and Durbin 1988). The acoustic forcing frequency was excited at the dominant shear layer instability frequency of the wake. This had the effect of moving the separated shear layer closer to base of the sphere reducing the size of wake but also increased base pressure and the drag. The mechanism differs with the localised synthetic jet at  $6.5^\circ$  but likewise, instead of reducing drag, it could increase by increasing the strength of the vortices.

With the synthetic jet at  $76^\circ$  and  $100^\circ$ , it was found that the localised synthetic jet had similar effects in modifying the three-dimensional unsteady flow in the wake region of the side-supported sphere. The crosswise velocity component was decreased which was able to decrease the vorticity relative to the baseline case. This was also seen when the junction of the support-sphere was analysed. The drag was thus also decreased slightly.

The present computational work suggests that the asymmetrical localised synthetic jet is able to modify the unsteady three-dimensional flow field on a side-supported sphere producing beneficial and adverse effects depending on the angle of incidence, location and configuration of the synthetic jet orifice. The synthetic jet at all angles of incidence produced an increase in the  $C_p$  distribution towards potential flow before separation although with the synthetic jet closer to the fore stagnation point increased vorticity in the wake region was generated. With the synthetic jet at  $76^\circ$  and  $100^\circ$ , the wake region was reduced streamlining the flow field and reducing the interference at the support-sphere junction.

The above findings will have significance beyond those envisioned in this study. Apart from localised synthetic jet used as an effective tool for aero-shaping true

three-dimensional bluff and lifting bodies, the use of a localised synthetic jet will also have significance of practical importance in various fluid mechanical devices and in industries where control of three-dimensional flow separation and re-attachment and streamlining of flows is required.

This indicated that synthetic jets were capable of not only improving the flow on two-dimensional bodies but also streamlining the flow on three-dimensional bluff bodies with the added complexity of flow disturbances from interference effects.

The asymmetrical localised synthetic jet can be used as a localised point source to effect changes to the wake region. It can be strategically placed at different areas on a bluff or streamlined body to produce significant changes in the characteristics of the wake by reducing reversal of flow through delaying separation or directly injecting momentum in the separated flow region reducing the vorticity and streamlining the flow.

The asymmetrical localised synthetic jet on the forward swept wing with a NACA-23012 profile was effective in all locations, showing a significant reduction in pressure drag due to inhibiting flow separation. The localised synthetic jet mounted to the wing tip fore position produced the greatest reduction in wing tip vorticity which would imply a reduction of induced drag. Interference drag is also reduced by the reduction of the cross flow velocity, due to the localised synthetic jet at the juncture.

## 8.2 Recommendations

The design of machinery and transport vehicles that may consider, desire or indeed depend on, sophisticated aerodynamics must require an evaluation of the benefits versus cost and the overall gains in performance and efficiency. The future prospects of synthetic jet are evaluated against these and other measures.

It is preferable to use localised synthetic jets rather than using a large distribution of synthetic jets or large synthetic jet actuator to obtain similar aerodynamic improvements. Localised synthetic jets have the potential to be used in a strategic manner placing them in various locations over solid bodies at different angles to aeroshape bluff or streamlined bodies. In applications where a single localised synthetic jet might be inadequate, localised clusters of synthetic jet can be configured to increase the momentum of the turbulent shear flow can be used.

Micro-Electro-Mechanical-Systems (MEMS) are becoming more advanced and of lower cost. This research could influence the development of synthetic jet actuators that would be miniature in size and suitable for use in a localised manner and yet provide the momentum coefficient to effect significant flow modifications. This would be a future application in areas such as heat transfer in cooling computer components.

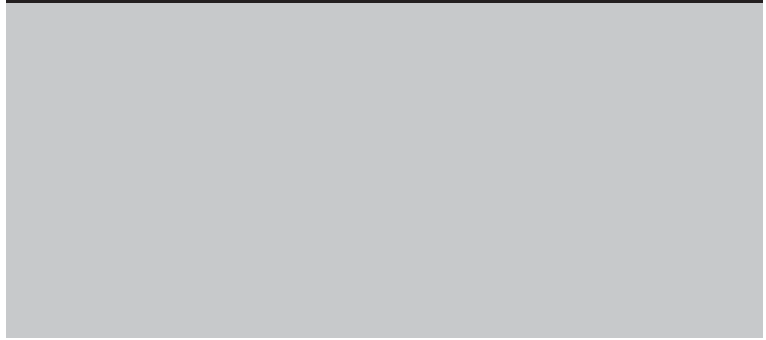
An important area, as mentioned at the outset, is the aerospace industry. Potential reduction in drag by inhibiting flow separation and decreased wing-tip vorticity is a real potential for localised synthetic jets.

Future research in synthetic jets needs to be directed towards three-dimensional applications with an emphasis on a reduction of synthetic jet power consumption increasing the efficiency of synthetic jet flow control. The localised synthetic jet can be used by investigating strategic and problematic flow regions where it can be

implemented most effectively to give global benefits without unnecessarily using distributed synthetic jet if not required. The asymmetrical nature of synthetic jet has been shown to improve the aerodynamic performance of both bluff and streamlined bodies and thus further research to make use of this lifting bodies would be advantageous.

---

## References



## References

- U.S. Energy Information Administration.* (2007). Retrieved from U.S. Energy Information Administration.
- U.S. Energy Information Administration.* (2010).
- Abbott, I. H., and Von Doenhoff, A. E. (1959). *Theory of Wing Sections* (Corrected ed.). New York: Dover Publications.
- Abergel, F., and Temam, R. (1990). On some control problems in fluid mechanics. *Theoretical Computational Fluid Dynamics, 1*, 303-325.
- Achenbach, E. (1972). Experiments on the flow past spheres at very high Reynolds numbers. *Journal of Fluid Mechanics, 54*, 565-575.
- Achenbach, E. (1974). The effects of surface roughness and tunnel blockage on the flow past spheres. *Journal of Fluid Mechanics, 65*, 113-125.
- Achenbach, E. (1974). Vortex shedding from spheres. *Journal of fluid mechanics, 62*, 209-221.
- Ahmed, N. A., and Archer, R. D. (2001). Post-stall behaviour of a wing under externally imposed sound. *Journal of Aircraft, 38*(5), 961-963.
- Ahmed, N. A., and Wagner, D. J. (2003). Vortex shedding and transition frequencies associated with flow around a circular cylinder. *AIAA Journal, 41*(3), 542-548.
- Amadolese, X., Hemon, P., and REGARDIN, C. (2004). An experimental study of the acoustic oscillations by flows over cavities. *Transactions of ASME, 126*, 190-195.
- Amitay, M., and Glezer, A. (2006). Aerodynamic flow control using synthetic jet actuators. *Active Flow Control*. Berlin: Springer.
- Amitay, M., Honohan, A., Trautman, M., and Glezer, A. (1997). Modification of aerodynamic characteristics of bluff bodies using fluidic actuators. *28th AIAA Fluid Dynamics Conference*, (pp. AIAA 97-2004).

- Amitay, M., Kibens, V., Parekh, D. E., and Glezer, A. (1999). Flow reattachment dynamics over a thick airfoil controlled with synthetic jet actuators. *37th AIAA Aerospace Sciences Meeting*, AIAA 99-1001.
- Amitay, M., Smith, D. R., Kibens, V., Parekh, D. E., and Glezer, A. (2001). Aerodynamic flow control over an unconventional airfoil using synthetic jet actuators. *AIAA Journal*, *39*(3), 361-70.
- Anderson, J.D. (2001). *Fundamentals of Aerodynamics*. New York: McGraw-Hill.
- Anderson, E., and Szewczyk, A. (1997). Effects of splitter plate on the near wake of a circular cylinder in 2 and 3-dimensional flow configurations. *Experiments in Fluids*, *23*, 161-174.
- Anderson, J. D. (2000). *Introduction to flight*. Boston: McGraw-Hill Book Company.
- Bardina, J. E., Huang, P. G., and Coakley, T. J. (1997). *Turbulence modelling, validation, testing and development*. NASA TM-110446.
- Barlow, B. J., Rae Jr, W. H., and Pope, A. (1999). *Low-speed wind tunnel testing* (3rd ed.). New York: John Wiley and Sons.
- Batchelor, G. K. (2000). *An introduction to fluid dynamics*. Cambridge: Cambridge University Press.
- Bearman, P. W., and Harvey, J. K. (1976). Golf ball aerodynamics. *Aeronautical Quarterly*, *22*, 112-122.
- Bradshaw, P. (1970). *Experimental Fluid Mechanics* (2nd ed.). Pergamon Press.
- Bridges, A., and Smith, D. R. (2003). Influence of orifice orientation on a synthetic jet-boundary-layer interaction. *AIAA Journal*, *41*(12), 2394-2402.
- Buresti, G. (2000). Bluff-body aerodynamics. *Wind-Excited and Aeroelastic Vibrations of Structures*. Genoa.
- Camhi, E. (2009, December). Editorial: Greener skies ahead. *Aerospace America*, p.3.
- Cengel, Y. A., and Cimbala, J. M. (2006). *Fluid Mechanics (Fundamentals and Applications)*. New York: McGraw-Hill.
- Chang, P. K. (1970). *Separation of flow* (1st ed.). New York: Pergamon Press.
- Chang, P. K. (1976). *Control of flow separation*. McGraw-Hill.

- Chang, Y. K., and Vakili, A. D. (1995). Dynamics of vortex rings. *Physics of Fluids*, 7(7), 1583-1597.
- Choi, H., Jeon, W.-P., and Kim, J. (2008). Control of flow over a bluff body. *Annual Review of Fluid Mechanics*, 40, 113-139.
- Chomaz, J.-M. (2005). Global instabilities in spatially developing flows: non-normality and nonlinearity. *Annual Review of Fluid Mechanics*, 357-392.
- Clift, R., Grace, J. R., and Weber, M. E. (1978). *Bubbles, drops and particles*. New York: Academic Press.
- Coles, D. (1956). The law of the wake in the turbulent boundary layer. *Journal of Fluid Mechanics*, 1(2), 191-226.
- Cometta, C. (1957). An investigation of the unsteady flow pattern in the wake of cylinders and spheres using hot-wire probe. *Thesis*, WT-21.
- Committee on assessment of aircraft winglets for large aircraft fuel efficiency and National Research Council. (2007). *Assessment of wingtip modifications to increase the fuel efficiency of air force aircraft*. National Academies Press.
- Coustols, E., Stumpf, E., Jaquin, L., Moens, F., Vollmers, H., and Gerz, T. (2003). Minimised Wake: A collaborative research programme on aircraft wake vortices. *41st Aerospace Sciences Meeting and Exhibit*, (pp. AIAA 2003-0938). Reno.
- Crocker, M. J. (1978). *Encyclopedia of Acoustics*. John Wiley and Sons Inc.
- Curry, M. (2009). *NASA Dryden Fact Sheet X-29*. Retrieved May 2006, from NASA: [www.nasa.gov/centers/dryden/news/FactSheets/FS-008-DFRC.html](http://www.nasa.gov/centers/dryden/news/FactSheets/FS-008-DFRC.html)
- Devore, J. L. (1995). *Probability and statistics for engineering and the sciences* (4th ed.). Belmont: Duxbury Press.
- Duvigneau, R., Hay, A., and Visonneau, M. (2006). Study on the optimal location of a synthetic jet for stall control. *3rd AIAA Flow Control Conference*, (pp. AIAA 2006-3679). San Francisco.
- Findanis, N., and Ahmed, N. A. (2006). Wake study of flow over a sphere with synthetic jet. *AIAA 24th Applied Aerodynamics Conference*, (pp. AIAA 2006-3855). San Francisco.

- Findanis, N., and Ahmed, N. A. (2007). A flow study over a sphere with localised synthetic jet. *The 12th Australian International Aerospace Congress*. Melbourne.
- Findanis, N., and Ahmed, N. A. (2008). The interaction of an asymmetrical localised synthetic jet on a side supported sphere. *Journal of Fluids and Structures*, 24(7), 1006-1020.
- Findanis, N., and Ahmed, N. A. (2009). Active Flow Control Over a Bluff Body Utilising Localised Synthetic Jet Technology. *The 13th Australian International Aerospace Congress*.
- Findanis, N., and Ahmed, N. A. (2011, January). Three-dimensional flow reversal and wake characterisation of a sphere modified with active flow control using synthetic jet. *Advances and Applications in Fluid Mechanics*, 9(1), 17-76.
- Gad-el-Hak, M. (2000). *Flow Control: Passive, Active and Reactive Flow Management*. Cambridge: Cambridge university Press.
- Gilarranz, J. L., and Rediniotis, O. K. (2001). Compact, high-power synthetic jet actuators for flow separation control. *39th Aerospace Science Meeting and Exhibit*, (pp. AIAA 2001-0737). Reno.
- Glezer, A., and Amitay, M. (2002). Synthetic jets. *Annual Review of Fluid Mechanics*, 34, 503-529.
- Gogineni, S. P., Joslin, R. D., and Gaitonde, D. V. (2003, December). Aerospace Sciences, Fluid Dynamics. *Aerospace America*.
- Goldstein, M. E. (1976). *Aeroacoustics*.
- Gorder, P. F. (2004, October). Vortex drive. *New Scientist*, 30-34.
- Griffin, O. M., and Hall, M. S. (1991). Review: vortex shedding lock-on and flow control in bluff body wakes. *Transactions ASME Journal of fluids Engineering*(113), 526-537.
- Guo, D., Gary, A. W., and Agarwal, R. K. (2003). Numerical simulation of vectoring of a primary jet with a synthtic jet. *AIAA Journal*, 41(12), 2364-2370.

- Hassan, A. A., and Janakim, R. D. (1997). Effects of zero-mass "synthetic" jets on the aerodynamics of the NACA-0012 airfoil. *15th AIAA Applied Aerodynamics Conference: AIAA 97-2326*, (pp. 867-877).
- Henning, L., Pastoor, M., King, R., Noack, B. R., and Tadmor, G. (2006). Feedback control applied to bluff body wake. *Active flow control*. Berlin.
- Hoerner, S. F. (1965). *Fluid-Dynamic Drag*. Hoerner Fluid Dynamics.
- Howe, M. S. (1998). *Aoustics of Fluid-Structure Interactions*.
- Hsiao, F. B., Liang, P. F., and Huang, C. Y. (1998). High incidence airfoil aerodynamics improvement by leading-edge oscillating flap. *Journal of Aircraft*, 35(3), 508-510.
- Hwang, D. P., and Biesiadny, T. J. (1998). Experimental Evaluation of Penalty Associated With Micro-Blowing for Reducing Skin Friction., (pp. AIAA 98-0677).
- Jeon, S., Choi, J., Jeon, W.-P., Choi, H., and Park, J. (2004). Active flow control over a sphere for drag reduction at a subcritical Reynolds number. *Journal of Fluid Mechanics*, 517, 113-129.
- Jones, R. T. (1953). *Theory of wing-body drag at supersonic speeds*. NACA.
- Karim, M. M., Rahman, M. M., and Alim, M. A. (2009). Computation of axisymmetric turbulent viscous flow around sphere. *Journal of Scientiifc Research*, 1, 209-219.
- Kim, H. J., and Durbin, P. A. (1988). Observations of the frequencies in a sphere wake and of drag increase by acoustic excitation. *Physics of Fluids*, 31, 3260-3265.
- Kim, S. H., and Kim, C. (2006). Separation control on NACA23012 using synthetic jet. *3rd AIAA Flow Control Conference*, (pp. AIAA 2006-2853).
- Klebanoff, P. S. (1954). Characteristics of turbulence in aboundary layer with zero pressure gradient. *NACA Technical Report*, TC-1247.
- Klebanoff, P. S., and Diehl, Z. W. (1951). Some features of artificially thickned fully developed turbulent boundary layers with zero pressure gradient. *NACA Technical Report*, TC-1110.

- Kral, L. D., Donovan, J. F., Cain, A. B., and Cary, A. W. (1997). Numerical simulation of synthetic jet actuators. *4th AIAA Shear Flow Control Conference*, (pp. AIAA 97-1824).
- Krause, E. (2005). *Fluid Mechanics (with problems solutions and an aerodynamics laboratory)*. Berlin: Springer.
- Kroo, I. (2001). Drag due to lift: concepts for prediction and reduction. *Annual Review of Fluid Mechanics*, 33, 587-617.
- Kwak, D., Rogers, S. E., Kaul, U. K., and Chang, J. L. (1986). A numerical study of incompressible juncture flows. *NASA TM 88319*.
- Lebedeva, I. V. (1980). Experimental study of acoustic streaming in the vicinity of orifices. *Soviet Physics - Acoustics*, 26(4), 331-333.
- Lee, C. S., Tavella, D., Wood, N. J., and Roberts, L. (1989). Flow structure and scaling laws in lateral wing-tip blowing. *AIAA Journal*, 27(8), 1002-1007.
- Lee, C. Y., and Goldstein, D. B. (2000). Two-dimensional synthetic jet simulation. *AIAA Fluids Meeting*, (pp. AIAA 2000-0406).
- Lighthill, M. J. (1958). On displacement thickness. *Journal of Fluid Mechanics*, 4(4), 383-392.
- Lighthill, M. J. (1978). *Waves in Fluids*. Cambridge: Cambridge University Press.
- Lin, J. C. (2002). Review of research on low-profile vortex generators to control boundary-layer separation. *Progress in Aerospace Sciences*, 38, 389-420.
- Lord, W. T. (1962). *On the design of wing-body combinations of low zero-lift drag rise at transonic speeds*. Aeronautical Research Council.
- Madsen, C., Hassan, A. A., and Schwimley, S. (2006). Alteration of the flowfield in a transonic flow environment using synthetic jets. *AIAA 24th Applied Aerodynamics Conference*, (pp. AIAA 2006-3159). San Francisco.
- Margaris, P., and Gursul, I. (2006). Wing tip vortex control using synthetic jet. *The Aeronautical Journal*, 673-681.
- Massey, B. S. (1996). *Mechanics of Fluids* (6th ed.). London: Chapman and Hall.
- Mednikov, E. P., and Novitskii, B. G. (1975). Experimental study of intense acoustic streaming. *Soviet Physics-Acoustics*, 21(2), 152-154.

- Menter, F. R. (1993). Zonal two equation k-w turbulence models for aerodynamic flows. *24th AIAA Fluid Dynamics Conference*, (pp. AIAA 93-2906).
- Miranda, S., Telionis, D., and Zeiger, M. (2001). Flow control of a sharp-edged airfoil. AIAA Paper No. 2001-0119.
- Mittal, R., and Rampungoon, P. (2002). On the virtual aeroshaping effect of synthetic jets. *Physics of Fluids*, 14(4), 1533-1536.
- Moore, F. K. (1953). *Displacement effect of a three-dimensional boundary layer*. Research Memoranda of the National Advisory Committee for Aeronautics Washington.
- Nakanishi, Y., and Kamemoto, K. (1993). Numerical simulation of flow around a sphere with vortex blobs. *Journal of Wind Engineering and Industrial Aerodynamics*, 46-47, 363-369.
- Nakano, M., and Rockwell, D. (1993). The wake from a cylinder subjected to amplitude-modulated excitation. *Journal of Fluid Mechanics*, 247, 79-110.
- Norberg, C. (2002). Fluctuating lift on a circular cylinder: review and new measurements. *Journal of Fluids and Structures*, 17, 57-96.
- Oertel Jr, J. (1990). Wakes behind bluff bodies. *Annual Review of Fluid Mechanics*, 22, 539-564.
- Ogata, K. (1997). *Modern control theory* (3rd ed.). New Jersey: Prentice-Hall.
- Pao, H., and Kao, T. W. (1977). Vortex structure in the wake of a sphere. *Physics of Fluids*, 20, 187-191.
- Peterson, D. M., Subbareddy, P. K., and Candler, G. V. (2006). Simulation of injection into a supersonic crossflow using DES with synthetic inflow. *AIAA 24th Applied Aerodynamics Conference*, (pp. AIAA 2006-3326). San Francisco.
- Pierce, A. D. (1981). *Acoustics: An introduction to its physical principles and applications* (1st ed.). New York: McGraw Hill.
- Pisasale, A. J., and Ahmed, N. A. (2002). A novel method for extending the calibration range of five-hole probe for highly three-dimensional flows. *Flow Measurement and Instrumentation*, 13, 23-30.

- Pisasale, A. J., and Ahmed, N. A. (2002). Theoretical calibration for highly three-dimensional low-speed flows of a five-hole probe. *Measurement Science and Technology*, 13, 1100-1107.
- Pisasale, A. J., and Ahmed, N. A. (2003). Examining the effect of flow reversal on seven-hole probe measurements. *AIAA Journal*, 41(12), 2460-2467.
- Pisasale, A. J., and Ahmed, N. A. (2004). Development of a functional relationship between port pressures and flow properties for the calibration and application of mulithole probes to highly three-dimensional flows. *Experiments in Fluids*, 36(3), 422-436.
- Plesniak, M. W. (2010, December). Fluid Dynamics. *Aerspace America*, p. 15.
- Randall, R. H. (1951). *An introduction to acoustics*. New York: Addison-Wesley.
- Reshotko, E. (1976). Boundary-layer stability and transition. *Annual Review of Fluid Mechanics*, 8, 311-349.
- Saffman, P. G. (1995). *Vortex Dynamics*. New York: Cambridge University Press.
- Sakamoto, H., and Haniu, H. (1990). A study on vortex shedding from spheres in a uniform flow. *Journal of Fluids Engineering*, 112, 386-392.
- Schlichting, H., and Gersten, K. (2003). *Boundary-Layer Theory* (8th revised and enlarged ed.). Berlin: Springer-Verlag.
- Schwartzberg, M. A. (1959). Blown flaps for STOL operation: An examination of the lift increment due to the deflexion of propeller slipstream by large span blown flaps. *Aircraft engineering and aerospace technology*, 31(10), 308-311.
- Shih, W. C., Wang, C., Coles, D., and Roshko, A. (1993). Experiments on flow past rough circular cylinders at large Reynolds numbers. *Journal of Wind Engineering and Industrial Aerodynamics*, 49, 351-368.
- Simpson, R. G., Ahmed, N. A., and Archer, R. D. (2002). Near field study of vortex attenuation using wing-tip blowing. *The Aeronautical Journal*, 106(1057), 117-120.

- Slooff, J. W., De Wolf, W. B., Van Der Wal, H. M., and Maseland, J. E. (2002). Aerodynamic and aero-acoustic effects of flap tip fences. *40th Aerospace Sciences Meeting and Exhibit*, (pp. AIAA 2002-0848). Reno.
- Smith, B. L., and Glezer, A. (1997). Vectoring and small-scale motions effected in free shear flows using synthetic jet actuators. *97-0213*. 35th Aerospace Sciences Meeting.
- Smith, B. L., and Glezer, A. (1998). The formation and evolution of synthetic jet. *Physics of Fluids*, *10*(9), 2281-2297.
- Smith, B. L., and Swift, G. W. (2003). A comparison between synthetic and jets continuous jets. *Experiments in Fluids*, *34*, 467-472.
- Taneda, S. (1978). Visual observations of the flow past a sphere at Reynolds numbers between  $10^4$  and  $10^6$ . *Journal of Fluid Mechanics*, *85*, 187-192.
- Tetrault, P.-A. (2000). *Numerical prediction of the interference drag of a streamlined strut intersecting a surface in transonic flow*. Virginia Polytechnic Institute and State University: PhD.
- Thomas, A. S. (1985). Aircraft viscous drag reduction technology. *Lockheed Horizons*(19), pp. 22-32.
- Treaster, A. L., and Yocum, A. M. (1978). The calibration and application of five-hole probes. *ISA Transactions*, *18*(3), 23-34.
- Wu, J. M., Vakill, A., and Chen, Z. L. (1983). Investigation on the effects of discrete wingtip jets. *AIAA 21st Aerospace Sciences Meeting*, (pp. AIAA -83-0546). Reno.
- Wu, J. Z., Lu, X. Y., Denny, A. G., Fan, M., and Wu, J. M. (371). Post-stall flow control on an airfoil by local unsteady forcing. *Journal of Fluid Mechanics*, 21-58.
- Yun, G., Choi, H., and Kim, D. (2003). Turbulent flow past a sphere at  $Re=3700$  and  $10^4$ . *Physics of Fluids*, *15*, S6.
- Zdravkovich, M. M. (1981). Review and classification of various aerodynamic and hydrodynamic means for suppressing vortex shedding. *Journal of Wind Engineering and Industrial Aerodynamics*, *7*, 145-189.

---

## Appendix A

### Model Details

---

## Appendix A - Model Details

### A.1 Side-supported sphere drawings and photos

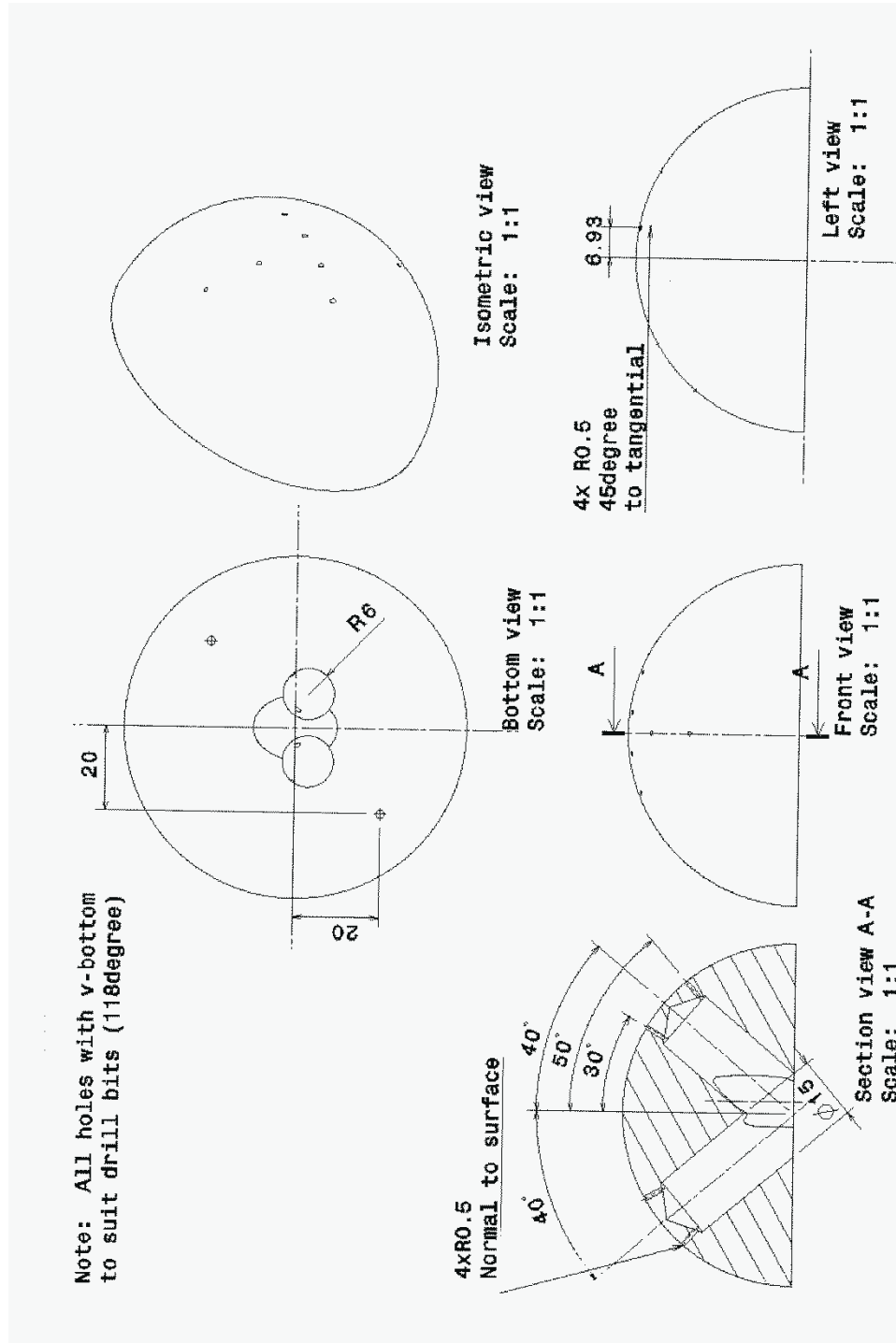


Figure A.1. Side-supported sphere engineering drawing 1.





Figure A.3. Side-supported sphere mounted in the 457 mm x 457 mm wind tunnel.

## A.2 Forward swept wing drawings and photos

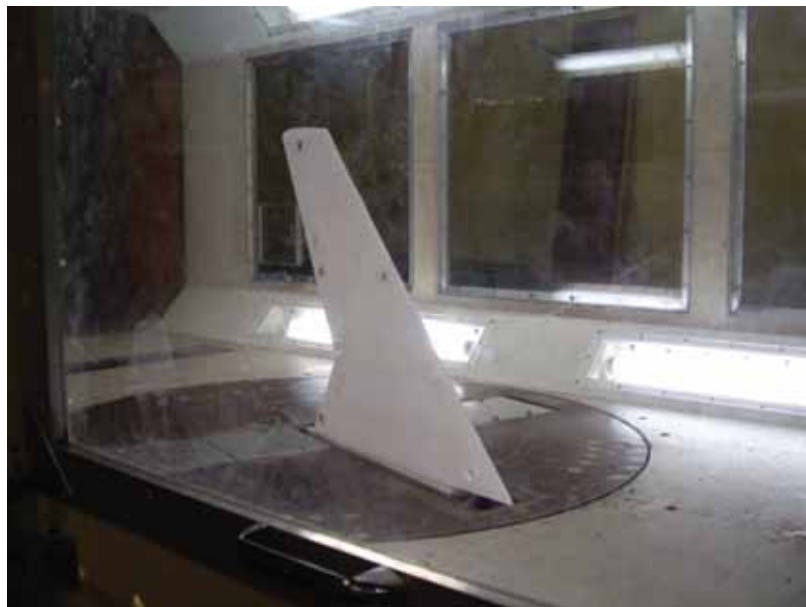


Figure A.4.FSW in 1219 mm x 914 mm wind tunnel.

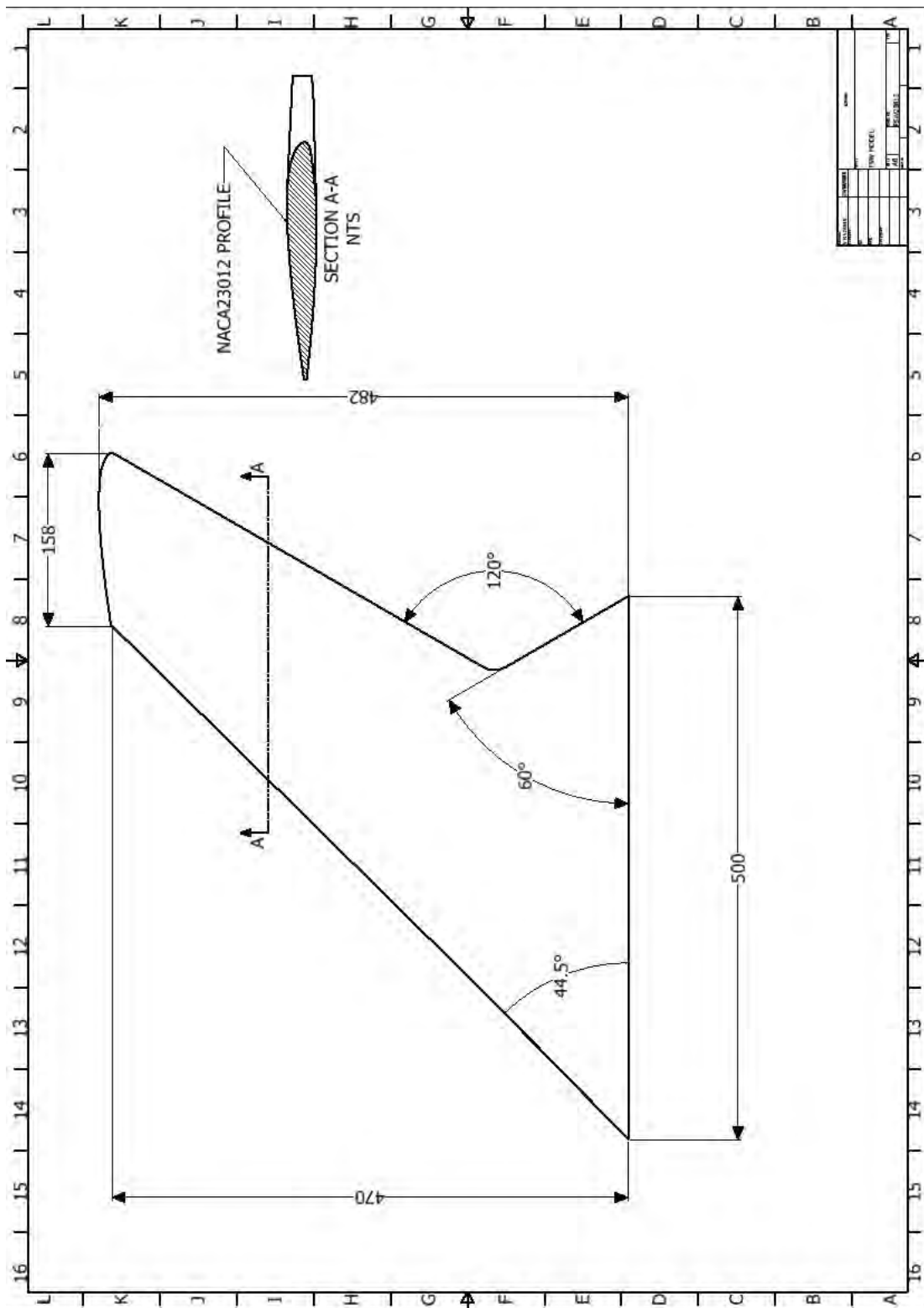


Figure A.5. FSW overall dimensions.

### A.3 Synthetic jet generator

The synthetic jet for the experiments was constructed using a novel method. As mentioned in Chapter 3 section 3.2 a compressor powered by a 12VDC power supply was modified to create the zero net mass flow oscillatory flow. The compressor is shown below in Figure A.6.



Figure A.6. 12VDC Compressor

The compressor is of a single piston type. The compressor piston is driven by a motor powered off the 12 VDC power supply which can be varied to adjust the flow rate. The compressor inlet path has attached a one-way valve that opens on the piston suction stroke to draw air into the cylinder. The compressor needed to draw air in from the outlet and eject the air back through the outlet. Thus the one-way inlet valve was sealed forcing the air to be drawn in from the outlet. This oscillatory suction and blowing from the outlet results in zero net mass flow, a requirement and unique property of synthetic jets. Figure A.7 shows the compressor head removed revealing the piston and one-way valve that was sealed shut.



Figure A.7. Compressor one-way valve.

The speed of the compressor was measured by removing the crank casing and placing a reflective strip on the crank counter balance. The piston rotational speed was then measured using an infrared tachometer. The relation between the voltage and rotational speed was found to be:

$$\omega = 300v \quad (A-1)$$

Where

v – voltage (V)

$\omega$  – rotational speed (r.p.m.)

The corresponding frequency range was between 10 Hz at the base voltage and 75Hz at the maximum voltage used in the experimental work.

---

## Appendix B

### Wind Tunnel Blockage

---

## Appendix B – Wind Tunnel Blockage

### B.1 Wind tunnel blockage

When performing wind tunnel experiments it is important to determine if any boundary corrections need to be applied to the result to the proximity of the tunnel walls. A standard text that is used to ascertain the wall corrections is Barlow, Rae Jr, and Pope (1999).

Surface pressure measurements taken on a bluff or streamlined body in a wind tunnel are then usually used to calculate the  $C_p$  distribution. The reference freestream velocity measured upstream in the wind tunnel using a Pitot-static tube will be different from the local freestream velocity at the solid body. By what amount depends on the effect of the boundaries on the model. For a total blockage correction factor of  $\varepsilon$  the expression for the corrected freestream velocity becomes:

$$V_{\infty c} = (1 + \varepsilon)V_{\infty} \quad (\text{B-1})$$

An approximation that is suggested by Barlow, Rae Jr, & Pope, 1999 is based on cross sectional geometries of the model and the wind tunnel test section to calculate the total correction factor,  $\varepsilon_t$ .

$$\varepsilon_t = \frac{1}{4} \frac{\text{model frontal area}}{\text{test section frontal area}} \quad (\text{B-2})$$

Using this approach the maximum total correction for the forward swept wing at  $20^\circ$  AOA  $\varepsilon_t = 0.013$ . The ratio of areas is at this AOA is 5.14% which below the maximum recommended by Barlow, Rae Jr, & Pope, 1999 The frontal area calculation for the wing is shown in Table B.1. For the side-supported sphere the

area ratio is 3.75%. With the blockage calculated 2.8% using a method for the bluff body.

Frontal Area for <b>Wing</b>		
Spanwise	470.0000	mm
Degree	<b>Area</b>	
20	<b>58052.5</b>	<b>mm<sup>2</sup></b>
25	<b>66343.17316</b>	mm <sup>2</sup>
30	<b>74128.93729</b>	mm <sup>2</sup>
45	<b>93886.10287</b>	mm <sup>2</sup>

Table B.1

The experiments were conducted with the purpose of comparing the aerodynamic performance of the baseline case with the cases of localised synthetic jet as such wall correction factors were not applied to the experimental results.

---

## Appendix C

### Five-Hole Probe Calibration

---

## Appendix C – Five-Hole Probe Calibration

### C.1 Five-hole probe calibration

The five-hole pressure probe was used in the wake surveys to obtain basic physical variables that were then used to determine the wake characteristics and patterns in the flow in the wake region. A calibration process was used to ensure that these measurements obtained were accurate.

The five-hole probe was connected to five pressure transducers for each the five pressure ports on the tip of the probe. The transducer box set was calibrated through an air speed range from 0 to 28 m/s to obtain the relationship between voltage and pressure for each of the five transducers and the freestream reference pressure was measured using a Pitot-static tube connected to an electronic Micromanometer.

The next step was to calibrate the five-hole pressure probe. The purpose of the calibration is to create a set of calibration constants that allows us to interpret three parameters when the five hole probe is placed in flow:

- Local static pressure
- Local total pressure
- Local flow vector (pitch angle,  $\alpha$  and yaw angle  $\beta$ )

With the determination of these physical variables from the calibrated measurements the local velocity components ( $u$ ,  $v$ ,  $w$ ) can be calculated at each survey point.

To calibrate the probe we need to acquire the pressure of each port on the probe tip through a range of predetermined angles. A jig was designed to support the probe and allow for the rotation of the probe in two different planes. The rotation

about the horizontal axis, the pitch plane (Figure C.1) and the rotation about the vertical axis, yaw plane (Figure C.2).

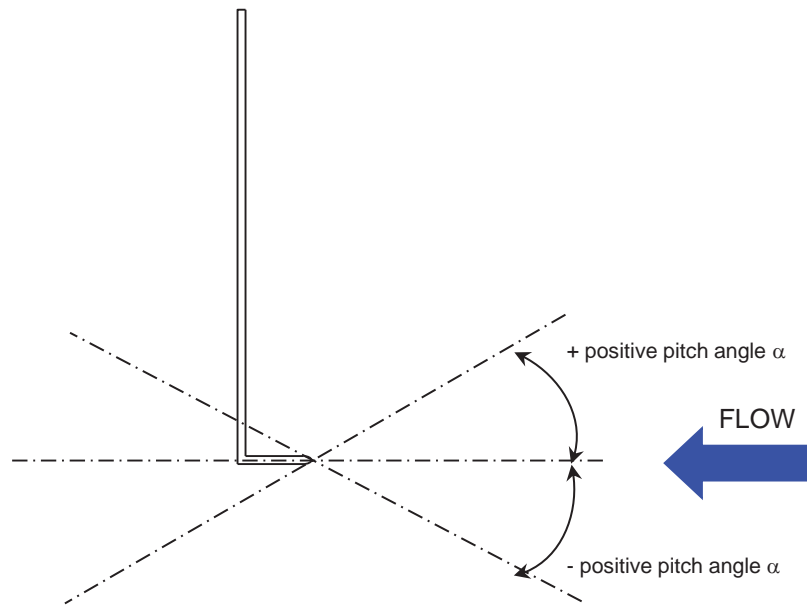


Figure C.1. Five-hole calibration, pitch plane.

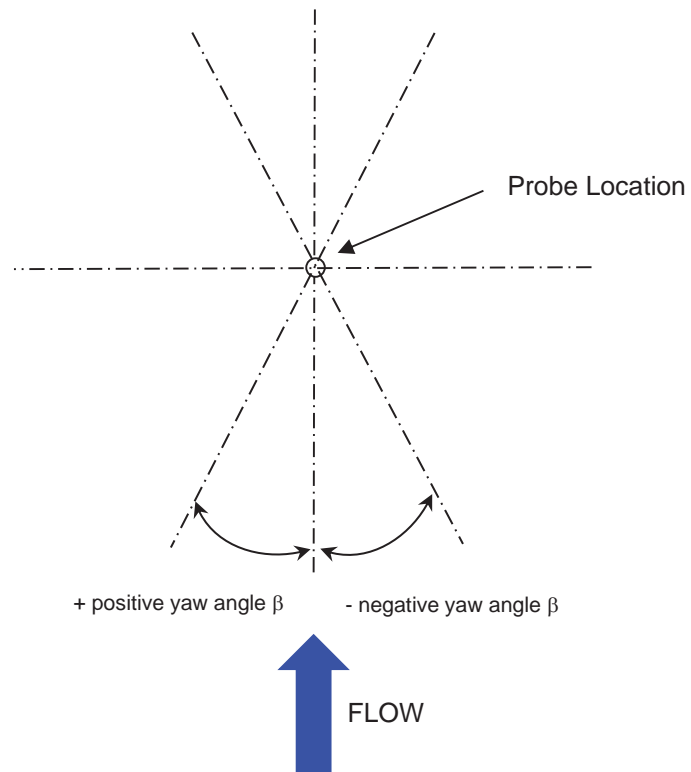


Figure C.2. Five-hole calibration, yaw plane.

The pressure and corresponding angular position for each data point allows us to calculate the following calibration coefficients.

$$C_{P_{yaw}} = \frac{(P_2 - P_3)}{(P_1 - \bar{P})} \quad (C-1)$$

$$C_{P_{pitch}} = \frac{(P_4 - P_5)}{(P_1 - \bar{P})} \quad (C-2)$$

$$C_{P_{total}} = \frac{(P_1 - P_{total})}{(P_1 - \bar{P})} \quad (C-3)$$

$$C_{P_{static}} = \frac{(\bar{P} - P_{static})}{(P_1 - \bar{P})} \quad (C-4)$$

$$\bar{P} = (P_2 + P_3 + P_4 + P_5) / 4 \quad (C-5)$$

The calibration map can be constructed by plotting  $C_{P_{yaw}}$  vs  $C_{P_{pitch}}$ . This is shown in Figure C.3. As a result of the calibration map the five-hole probe can be used in any flow to determine the total and static pressure and flow vector within its calibration range. This is achieved by using the Matlab program to carry out a double interpolation of the required variables from the calibration map. The two independent variables of  $C'_{P_{yaw}}$  and  $C'_{P_{pitch}}$  are calculated using equations (C-1) and (C-2) and represent the measured data. The short Matlab program is shown below.

*Appendix C: Five-Hole Probe Calibration*

---

```
load cpy.txt %(calibration data)
load cpp.txt %(calibration data)
load cppitch.txt %(measured data)
load cpyaw.txt %(measured data)
load pangle.txt %(pitch angle calibration)
load yangle.txt %(yaw angle calibration)
pitchangle = griddata(cpp,cpy,pangle,cppitch,cpyaw);
yawangle = griddata(cpp,cpy,yangle,cppitch,cpyaw);
load cpt.txt %(calibration data)
load cps.txt %(calibration data)
cpttotal = griddata(pangle,yangle,cpt,pitchangle,yawangle);
cpstatic = griddata(pangle,yangle,cps,pitchangle,yawangle);
```

Appendix C: Five-Hole Probe Calibration

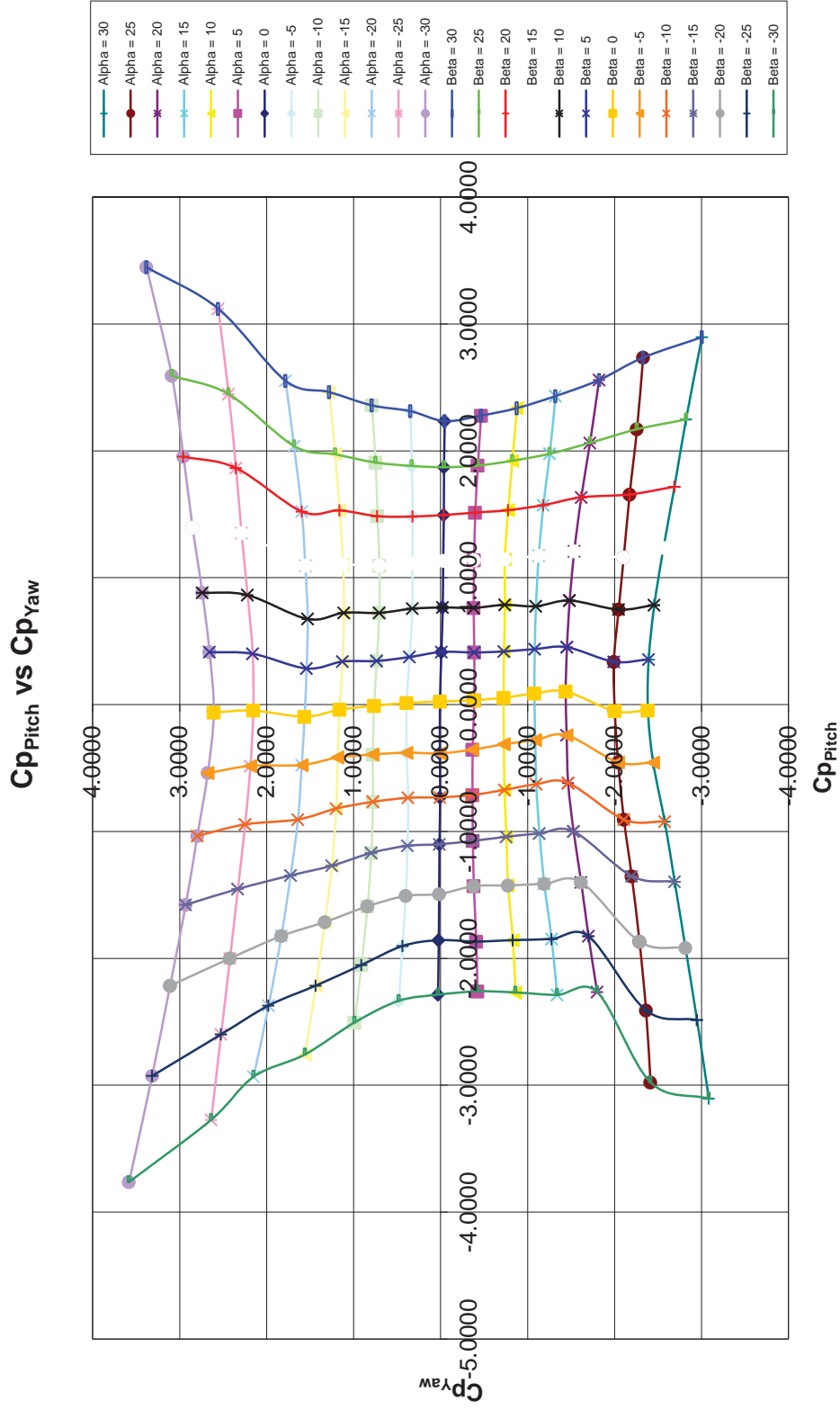


Figure C.3. Five-Hole probe calibration map.

The Matlab program calculates firstly the experimental values of  $\alpha'$  and  $\beta'$ . Secondly the values of  $C'_{P_{Total}}$  and  $C'_{P_{Static}}$  are also interpolated from the calibration curves. With the experimental coefficients calculated and the pitch and yaw angle of the flow vector determined we can then calculate the total and static pressure at the survey point using the following equations (C-6) and (C-7) respectively.

$$P_{Total} = P_{ref} + \Delta P - C'_{P_{Static}} (\Delta P_1 - \overline{\Delta P}) \quad (C-6)$$

$$P_{Static} = P_{ref} + \overline{\Delta P} - C'_{P_{Static}} (\Delta P_1 - \overline{\Delta P}) \quad (C-7)$$

$P_{ref}$  is the reference pressure used in the differential pressure transducer. This research work used the freestream static pressure obtained from the Pitot-static tube. Although the absolute external atmospheric/barometric pressure may be used. This value is measured using a calibrated Barometer.

Then by extension using Bernoulli's equation the local total velocity vector may be calculated using equation (C-8).

$$\bar{V} = \sqrt{\frac{2}{\rho} (P_{Total} - P_{Static})} \quad (C-8)$$

And since we know the pitch and yaw angles at the survey point we can calculate the velocity components (u, v ,w) given in equations (C-9), (C-10) and (C-11) respectively.

$$u = \bar{V} \cos \alpha \cos \beta \quad (C-9)$$

$$v = \bar{V} \sin \alpha \quad (C-10)$$

$$w = \bar{V} \cos \alpha \sin \beta \quad (C-11)$$

The following calibration work is based on that conducted by Treaster & Yocum (1978).

---

## Appendix D

### Surface Pressure Data

---

## Appendix D – Surface Pressure Data

### D.1 FSW Surface Pressure

This section of the Appendix presents the surface pressure data for the forward swept wing based on the NACA-23012 profile. The measurements taken along the chord length  $x/c$ , were of upper and lower surfaces of the wing at different spanwise locations. These have been defined in Chapter 3 section 3.4. The number of pressure tappings are shown in Figure 3.12 although the location is not shown. The specifics of the pressure tapping are shown in the following tables.

Measurement station 1 is shown in Table D.1 (a) and (b).

Measurement station 2 is shown in Table D.2 (a) and (b).

Measurement station 3 is shown in Table D.3 (a) and (b).

Measurement station 4 is shown in Table D.4 (a) and (b).

Measurement station 5 is shown in Table D.5 (a) and (b).

Dist. LE - Distance to Leading Edge

Appendix D: Surface Pressure Data

Tapping	Row 1 Lower	Row 1 Lower
	Dist LE (mm)	x/c
1	18	0.1071
2	31	0.1845
3	44	0.2619
4	57	0.3393
5	88	0.5238
6	101	0.6012
7	114	0.6786
8	127	0.7560

(a)

Tapping	Row 1 Upper	Row 1 Upper
	Dist LE (mm)	x/c
1	5	0.0298
2	17	0.1012
3	31	0.1845
4	46	0.2738
5	73	0.4345
6	87	0.5179
7	101	0.6012
8	115	0.6845
9	127	0.7560

(b)

Table D.1. Measurement station 1. (a) 9 tappings, upper surface. (b) 8 tappings, lower surface.

Tapping	Row 2 Lower	Row 2 Lower
	Dist LE (mm)	x/c
9	18	0.0857
10	34	0.1619
11	50	0.2381
12	66	0.3143
13	82	0.3905
14	98	0.4667
15	114	0.5429
16	130	0.6190
17	146	0.6952
18	162	0.7714

(a)

Tapping	Row 2 Upper	Row 2 Upper
	Dist LE (mm)	x/c
10	4	0.0190
11	21	0.1000
12	38	0.1810
13	56	0.2667
14	74	0.3524
15	92	0.4381
16	110	0.5238
17	128	0.6095
18	146	0.6952
19	164	0.7810

(b)

Table D.2. Measurement station 2. (a) 10 tappings, upper surface. (b) 10 tappings, lower surface.

Appendix D: Surface Pressure Data

Tapping	Row 3 Lower	Row 3 Lower
	Dist LE (mm)	x/c
19	16	0.0627
20	37	0.1451
21	58	0.2275
22	79	0.3098
23	100	0.3922
24	121	0.4745
25	142	0.5569
26	163	0.6392
27	184	0.7216
28	205	0.8039

(a)

Tapping	Row 3 Upper	Row 3 Upper
	Dist LE (mm)	x/c
20	3	0.0118
21	27	0.1059
22	50	0.1961
23	73	0.2863
24	96	0.3765
25	119	0.4667
26	142	0.5569
27	165	0.6471
28	188	0.7373
29	211	0.8275

(b)

Table D.3. Measurement station 3. (a) 10 tapplings, upper surface. (b) 10 tapplings, lower surface.

Tapping	Row 4 Lower	Row 4 Lower
	Dist LE (mm)	x/c
29	17	0.0550
30	42.5	0.1375
31	68	0.2201
32	93.5	0.3026
33	119	0.3851
34	144.5	0.4676
35	170	0.5502
36	195.5	0.6327
37	221	0.7152
38	246.5	0.7977

(a)

Tapping	Row 4 Upper	Row 4 Upper
	Dist LE (mm)	x/c
30	4	0.0129
31	29	0.0939
32	57	0.1845
33	85	0.2751
34	113	0.3657
35	141	0.4563
36	169	0.5469
37	197	0.6375
38	225	0.7282
39	253	0.8188

(b)

Table D.4. Measurement station 4. (a) 10 tapplings, upper surface. (b) 10 tapplings, lower surface.

Appendix D: Surface Pressure Data

Tapping	Row 5 Lower	Row 5 Lower
	Dist LE (mm)	x/c
39	18	0.0444
40	53.5	0.1321
41	89	0.2198
42	124.5	0.3074
43	160	0.3951
44	195.5	0.4827
45	231	0.5704
46	266.5	0.6580
47	302	0.7457
48	337.5	0.8333

(a)

Tapping	Row 5 Upper	Row 5 Upper
	Dist LE (mm)	x/c
40	5	0.0123
41	41	0.1012
42	78.5	0.1938
43	116	0.2864
44	153.5	0.3790
45	191	0.4716
46	228.5	0.5642
47	266	0.6568
48	303.5	0.7494
49	341	0.8420

(b)

Table D.5. Measurement station 5. (a) 10 tappings, upper surface. (b) 10 tappings, lower surface.

*Appendix D: Surface Pressure Data*

The surface pressure distribution for the FSW at AOA 15° is plotted for the baseline case with no synthetic jet applied.

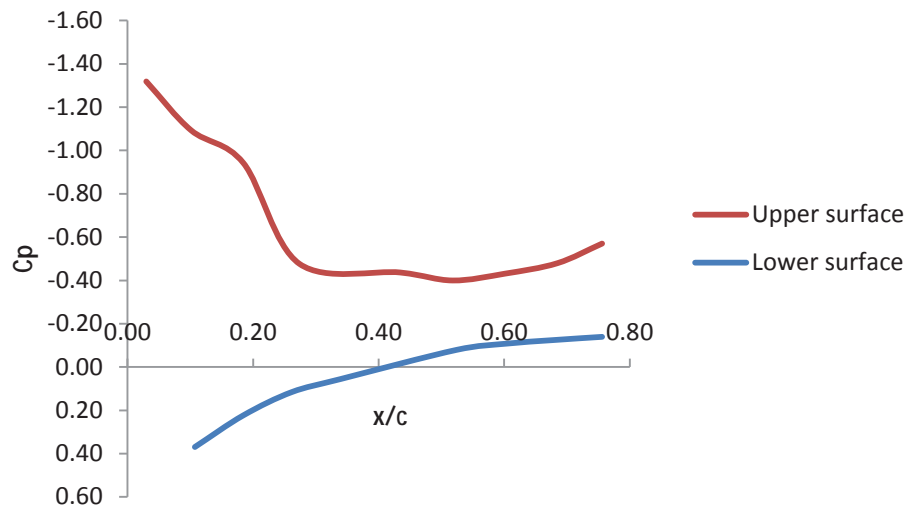


Figure D.1. FSW,  $C_p$  distribution at AOA 15°, Measuring station 1.

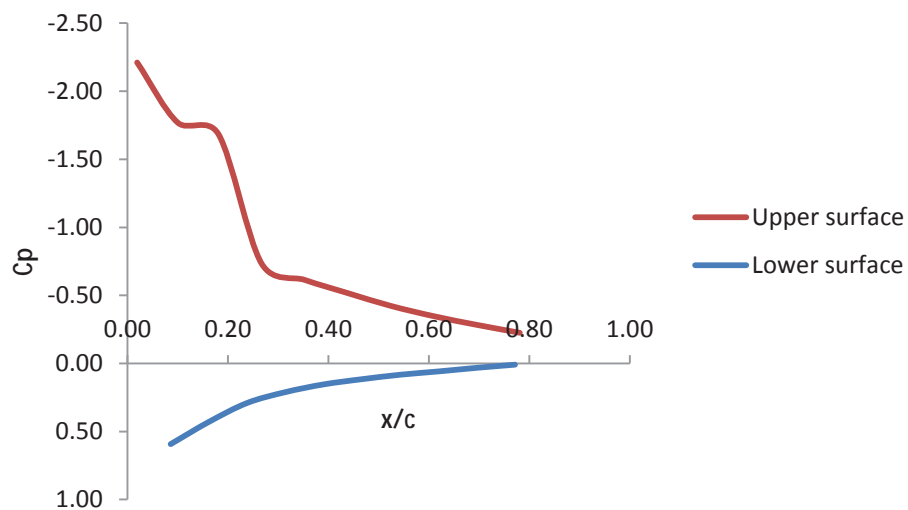


Figure D.2. FSW,  $C_p$  distribution at AOA 15°, Measuring station 2.

Appendix D: Surface Pressure Data

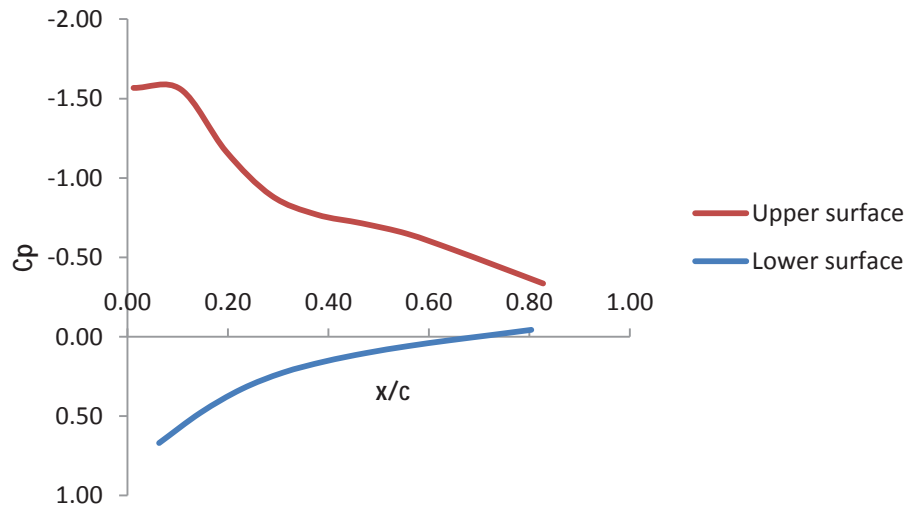


Figure D.3. FSW,  $C_p$  distribution at AOA  $15^\circ$ , Measuring station 3.

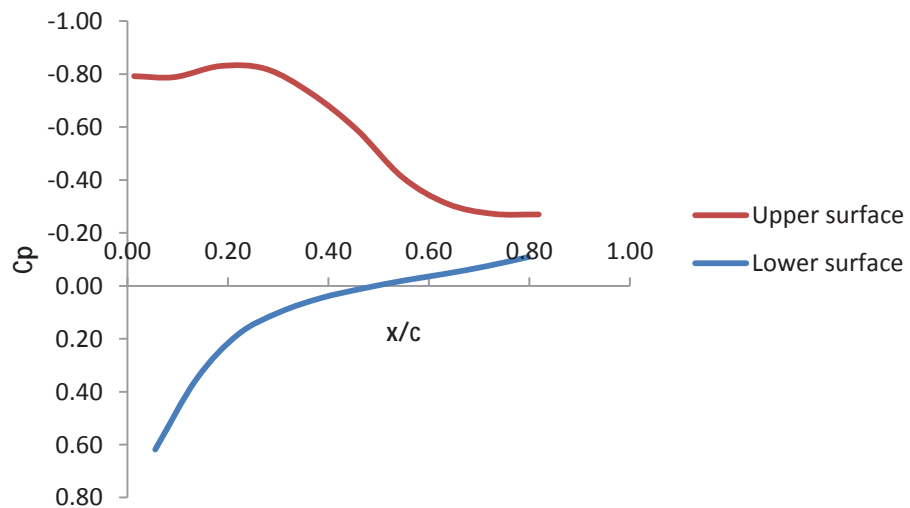


Figure D.4. FSW,  $C_p$  distribution at AOA  $15^\circ$ , Measuring station 4.

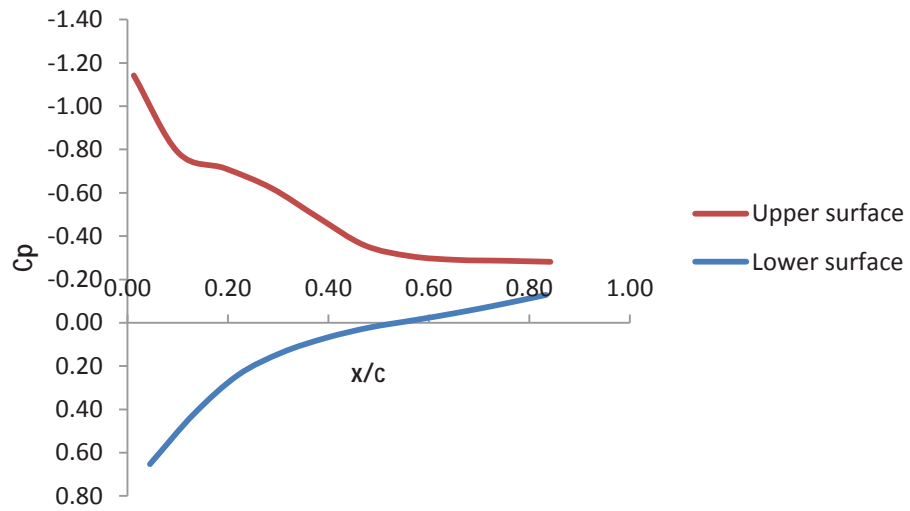


Figure D.5. FSW,  $C_p$  distribution at AOA  $15^\circ$ , Measuring station 5.

The surface pressure distribution for the FSW at AOA  $15^\circ$  is plotted for the case with synthetic jet applied at  $90^\circ$  to the surface normal (SJ at  $90^\circ$ ) at each synthetic jet point as defined in section 3.4 (WTP-F, WTP-A, SJ1-F, SJ1-A, SJ4-F, SJ4-A).

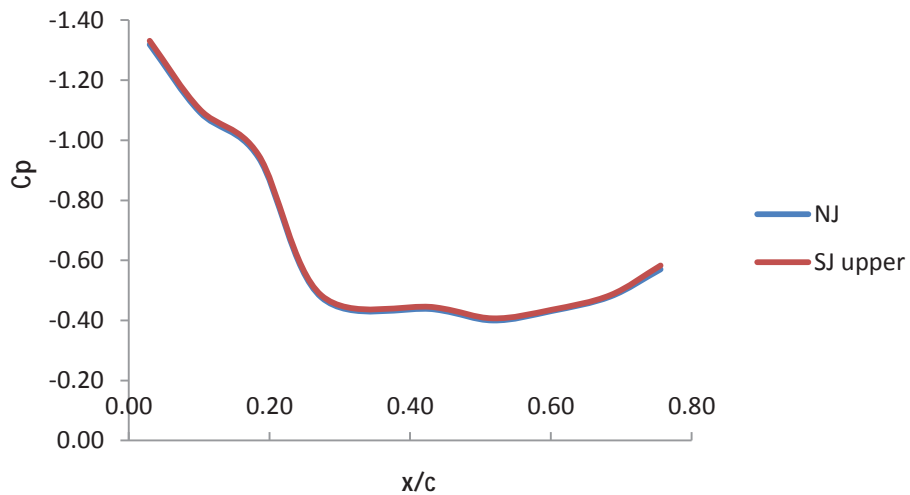


Figure D.6. Comparison of FSW NJ and with WTP-F at  $90^\circ$ ,  $C_p$  distribution at AOA  $15^\circ$ , Measuring station 1. Upper surface.

Appendix D: Surface Pressure Data

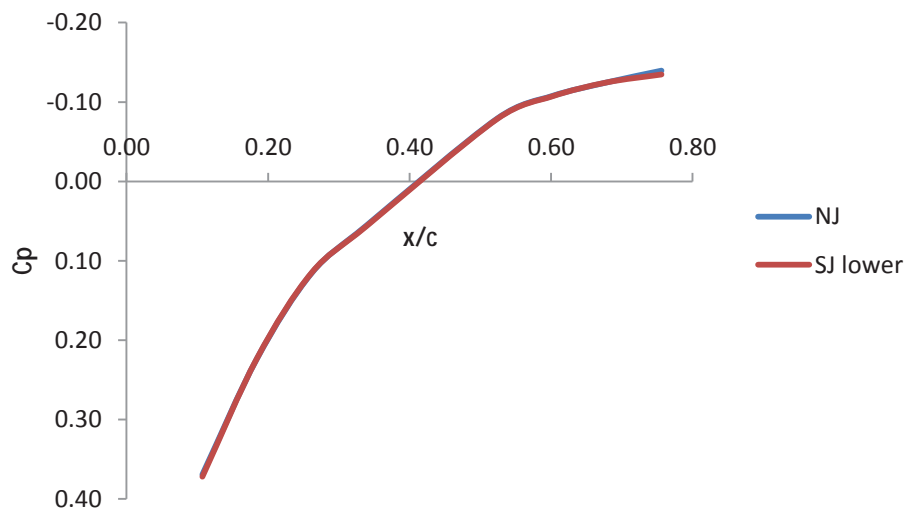


Figure D.7. Comparison of FSW NJ and with WTP-F at 90°,  $C_p$  distribution at AOA 15°, Measuring station 1. Lower surface.

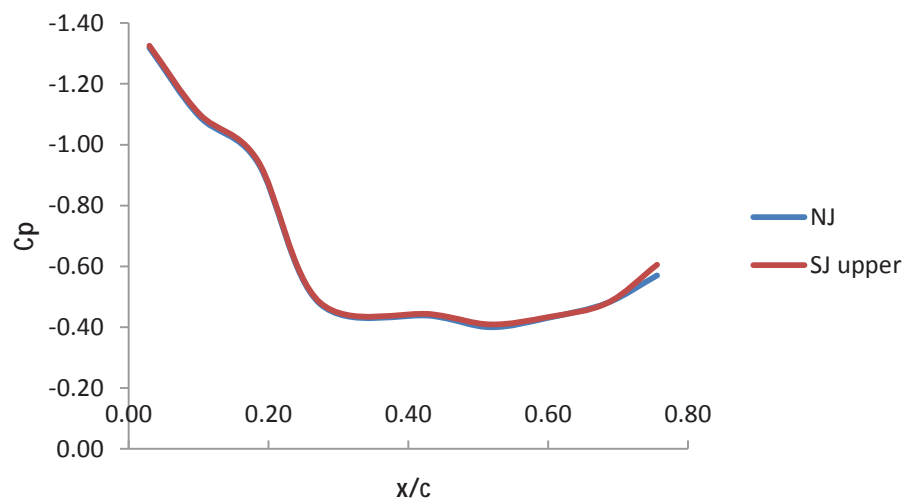


Figure D.8. Comparison of FSW NJ and with WTP-A at 90°,  $C_p$  distribution at AOA 15°, Measuring station 1. Upper surface.

Appendix D: Surface Pressure Data

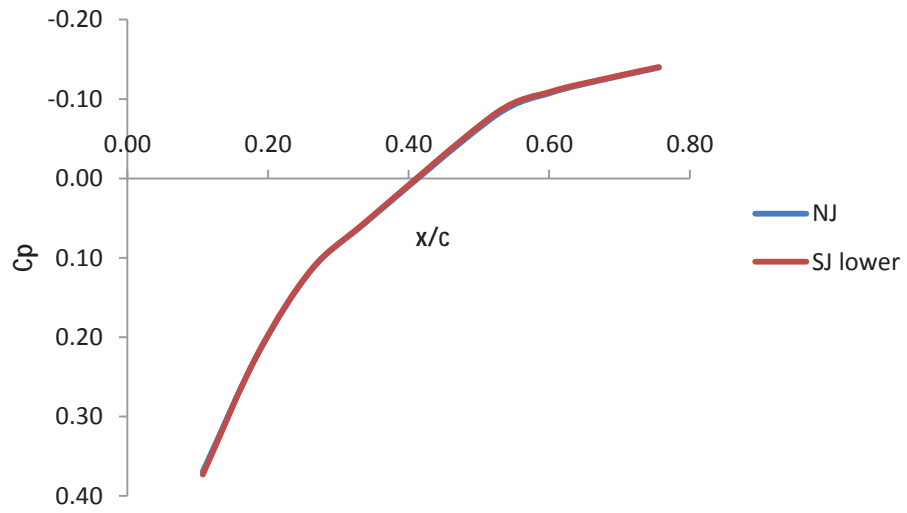


Figure D.9. Comparison of FSW NJ and with WTP-A at 90°, Cp distribution at AOA 15°, Measuring station 1. Lower surface.

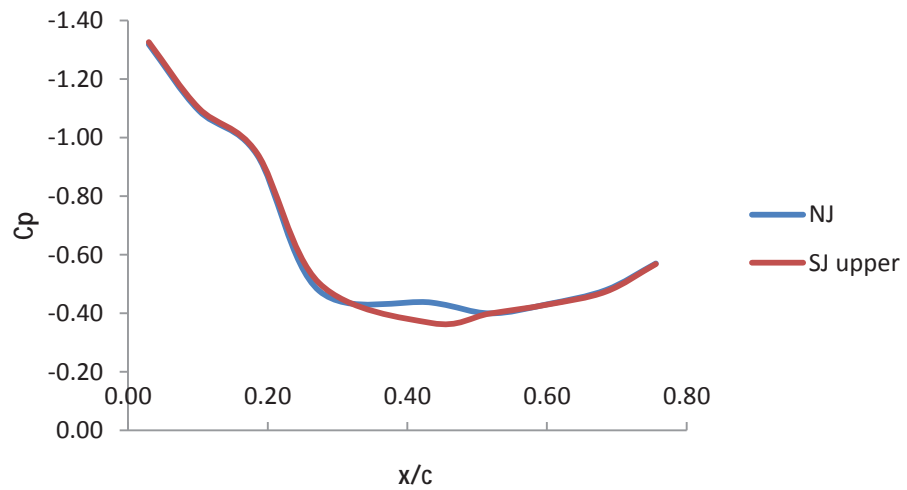


Figure D.10. Comparison of FSW NJ and with SJ1-F at 90°, Cp distribution at AOA 15°, Measuring station 1. Upper surface.

Appendix D: Surface Pressure Data

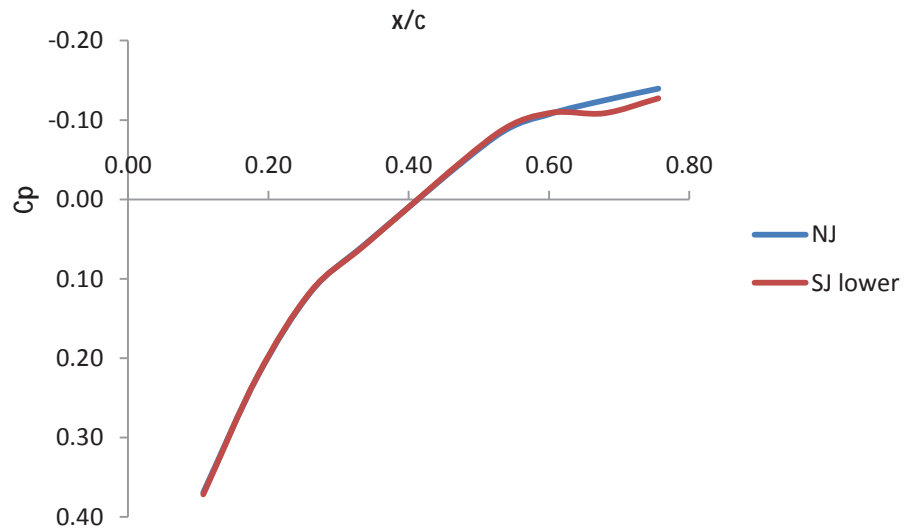


Figure D.11. Comparison of FSW NJ and with SJ1-F at  $90^\circ$ ,  $C_p$  distribution at AOA  $15^\circ$ , Measuring station 1. Lower surface.

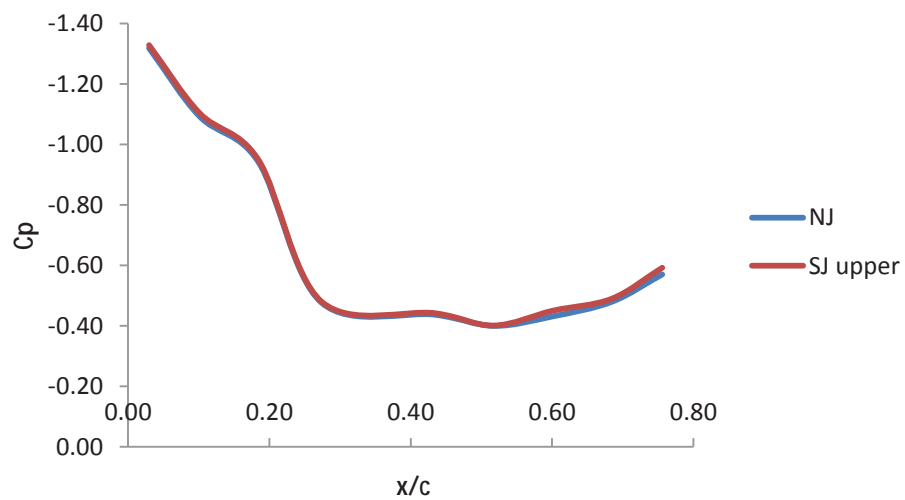


Figure D.12. Comparison of FSW NJ and with SJ1-A at  $90^\circ$ ,  $C_p$  distribution at AOA  $15^\circ$ , Measuring station 1. Upper surface.

Appendix D: Surface Pressure Data

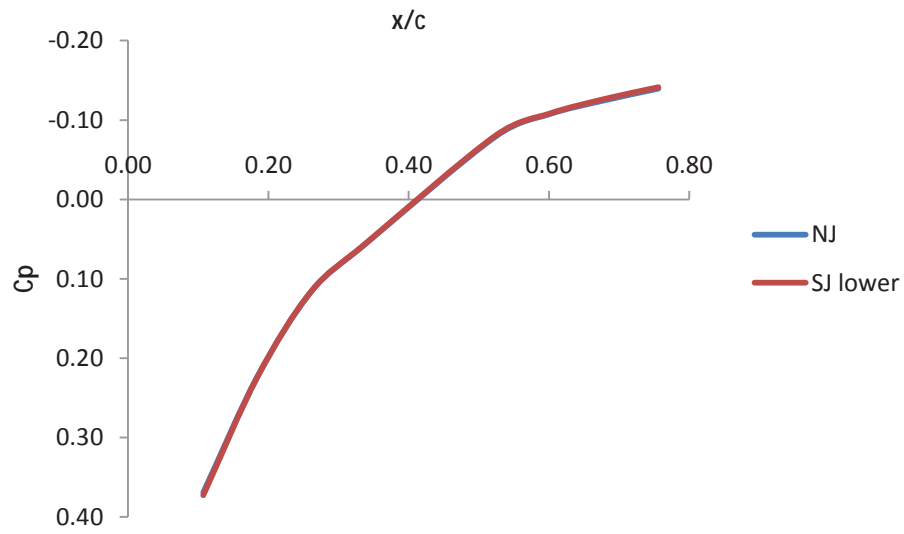


Figure D.13. Comparison of FSW NJ and with SJ1-A at 90°, Cp distribution at AOA 15°, Measuring station 1. Lower surface.

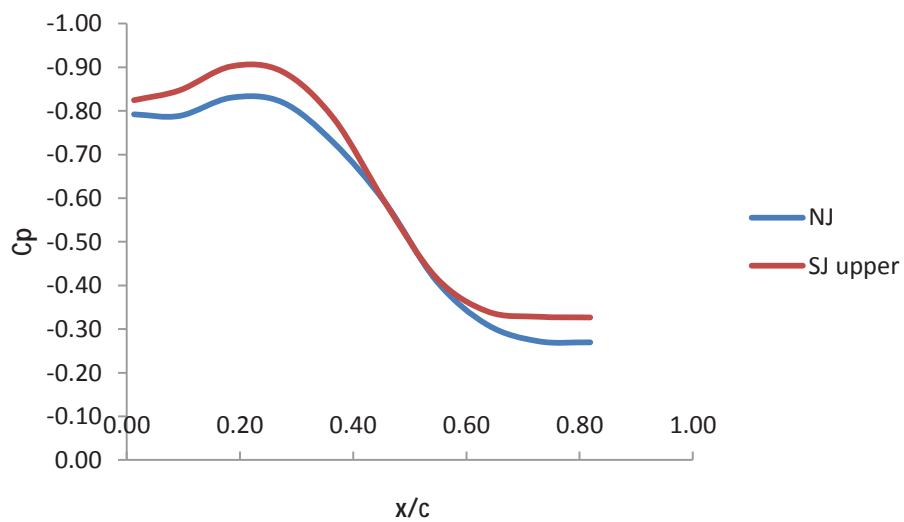


Figure D.14. Comparison of FSW NJ and with SJ4-F at 90°, Cp distribution at AOA 15°, Measuring station 4. Upper surface.

Appendix D: Surface Pressure Data

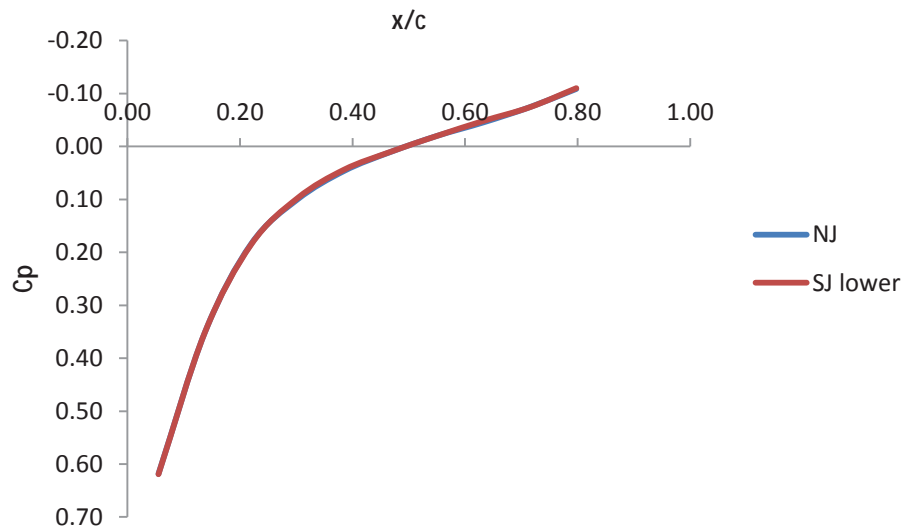


Figure D.15. Comparison of FSW NJ and with SJ4-F at 90°,  $C_p$  distribution at AOA 15°, Measuring station 4. Lower surface.

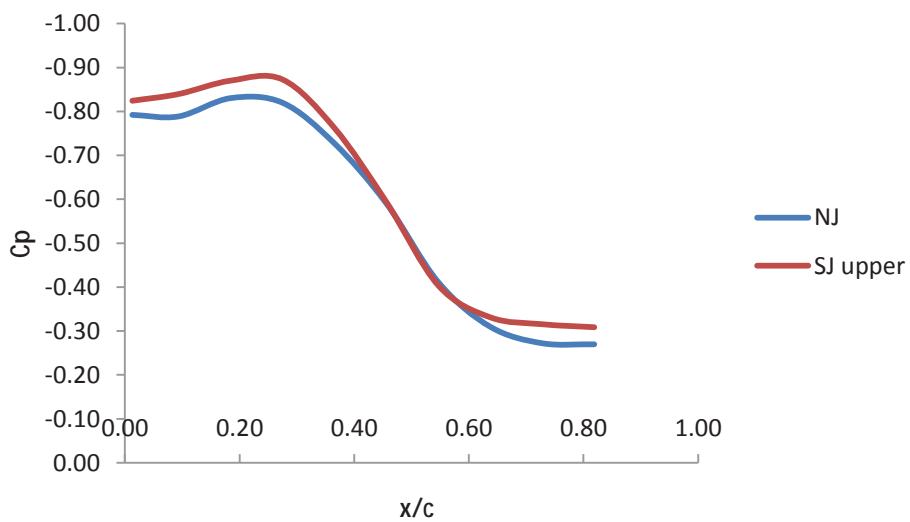


Figure D.16. Comparison of FSW NJ and with SJ4-A at 90°,  $C_p$  distribution at AOA 15°, Measuring station 4. Upper surface.

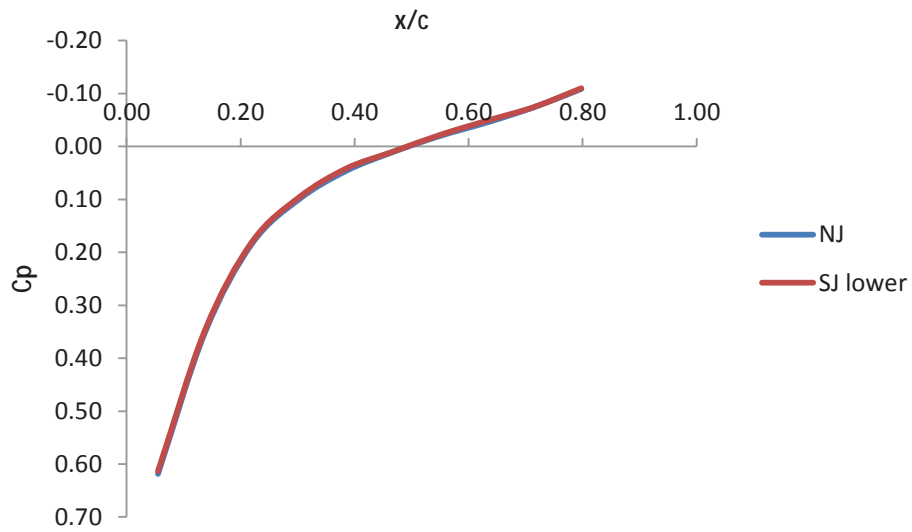


Figure D.17. Comparison of FSW NJ and with SJ4-A at 90°, Cp distribution at AOA 15°, Measuring station 4. Lower surface.

The surface pressure distribution for the FSW at AOA 15° is plotted for the case with synthetic jet applied at 23° to the surface normal (SJ at 23°) at each synthetic jet point as defined in section 3.4 (WTP-F, WTP-A, SJ1-F, SJ1-A, SJ4-F, SJ4-A).

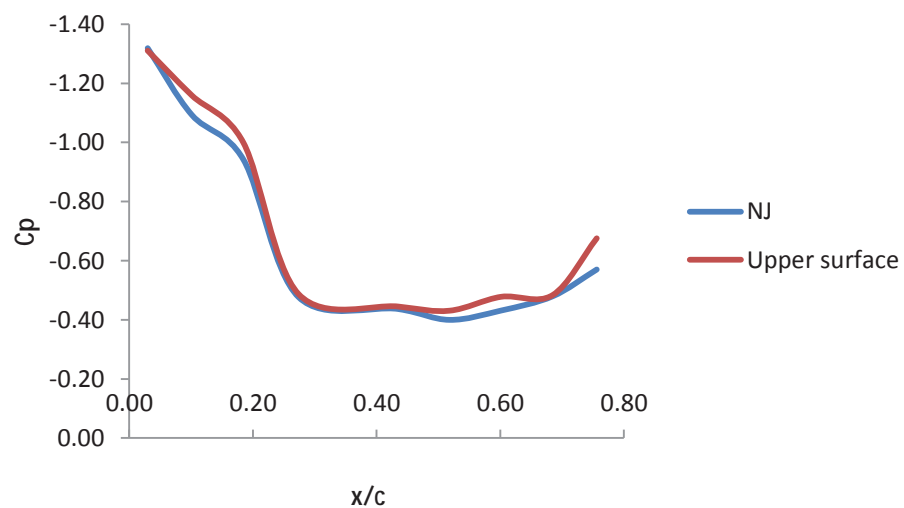


Figure D.18. Comparison of FSW NJ and with WTP-F at 23°, Cp distribution at AOA 15°, Measuring station 1. Upper surface.

Appendix D: Surface Pressure Data

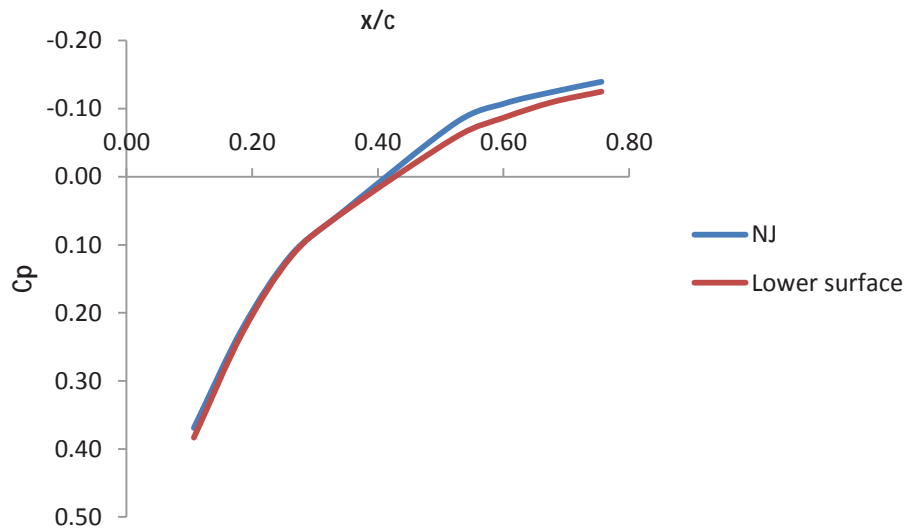


Figure D.19. Comparison of FSW NJ and with WTP-F at 23°,  $C_p$  distribution at AOA 15°, Measuring station 1. Lower surface.

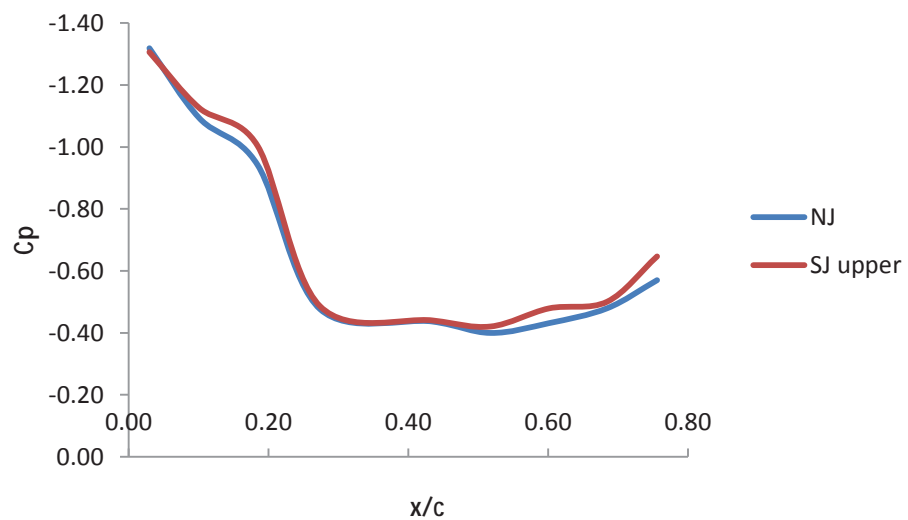


Figure D.20. Comparison of FSW NJ and with WTP-A at 23°,  $C_p$  distribution at AOA 15°, Measuring station 1. Upper surface.

Appendix D: Surface Pressure Data

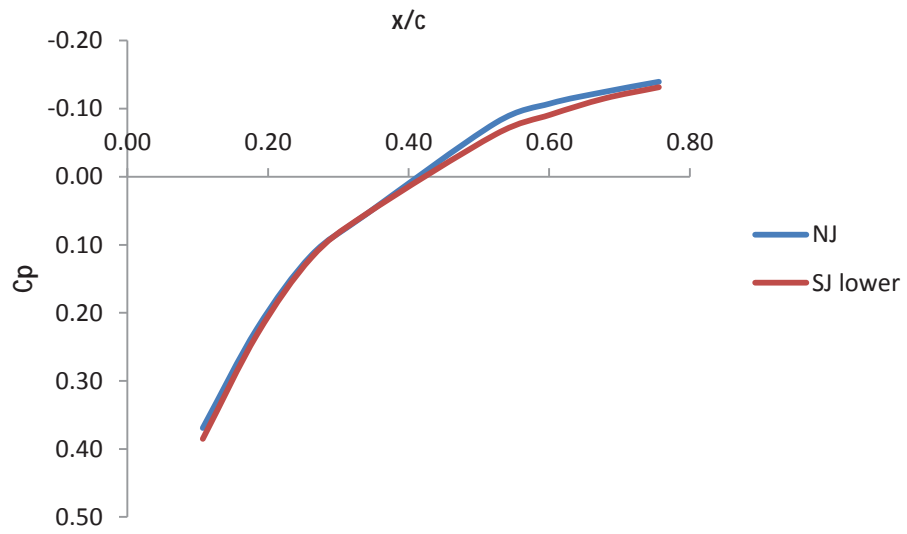


Figure D.21. Comparison of FSW NJ and with WTP-A at 23°, Cp distribution at AOA 15°, Measuring station 1. Lower surface.

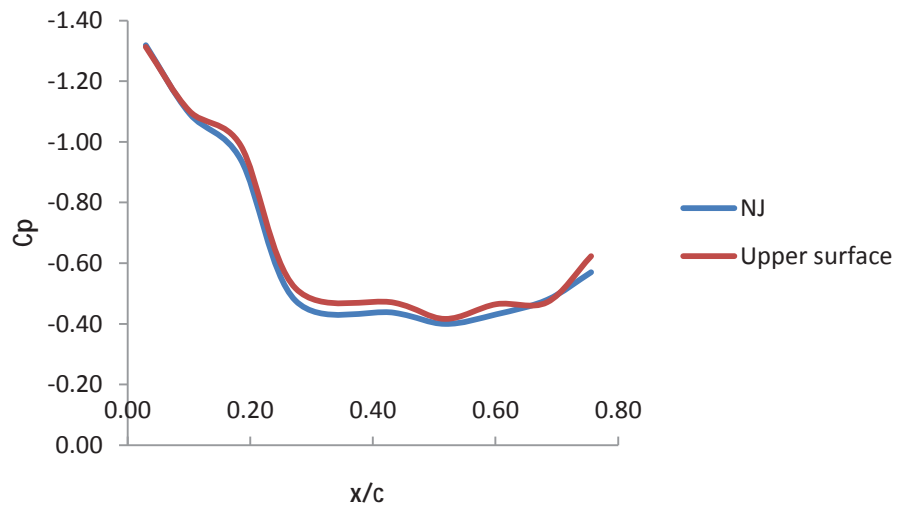


Figure D.22. Comparison of FSW NJ and with SJ1-F at 23°, Cp distribution at AOA 15°, Measuring station 1. Upper surface.

Appendix D: Surface Pressure Data

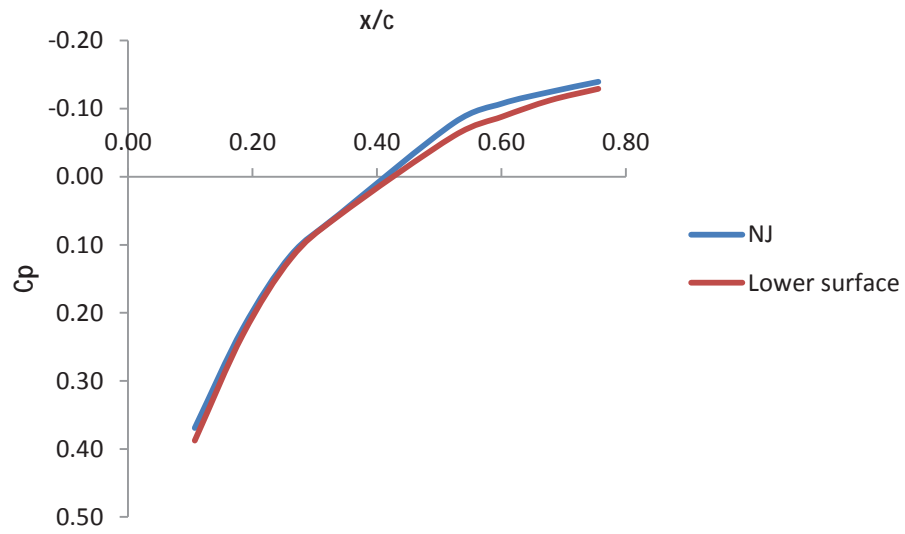


Figure D.23. Comparison of FSW NJ and with SJ1-F at  $23^\circ$ ,  $C_p$  distribution at AOA  $15^\circ$ , Measuring station 1. Lower surface.

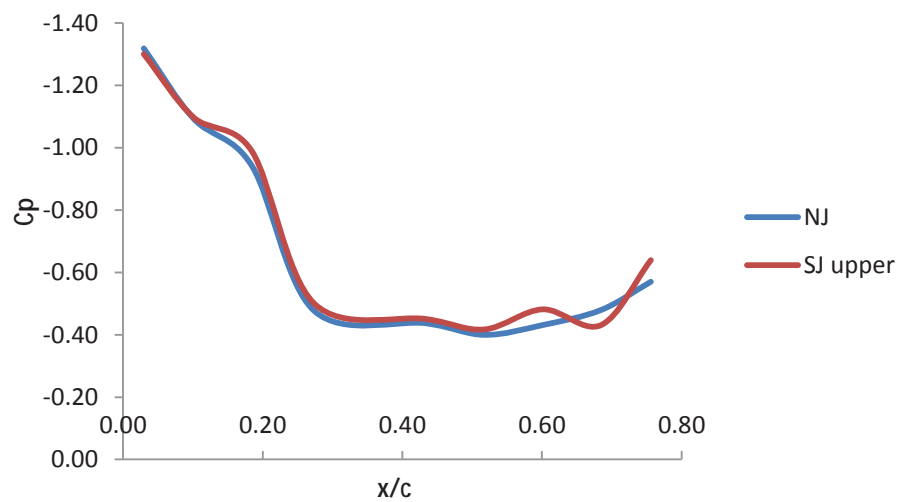


Figure D.24. Comparison of FSW NJ and with SJ1-A at  $23^\circ$ ,  $C_p$  distribution at AOA  $15^\circ$ , Measuring station 1. Upper surface.

Appendix D: Surface Pressure Data

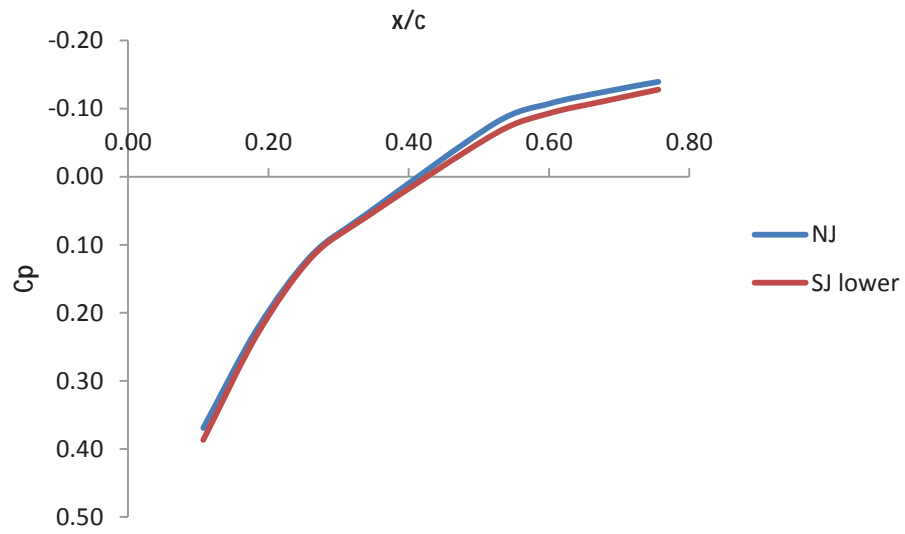


Figure D.25. Comparison of FSW NJ and with SJ1-A at 23°, Cp distribution at AOA 15°, Measuring station 1. Lower surface.

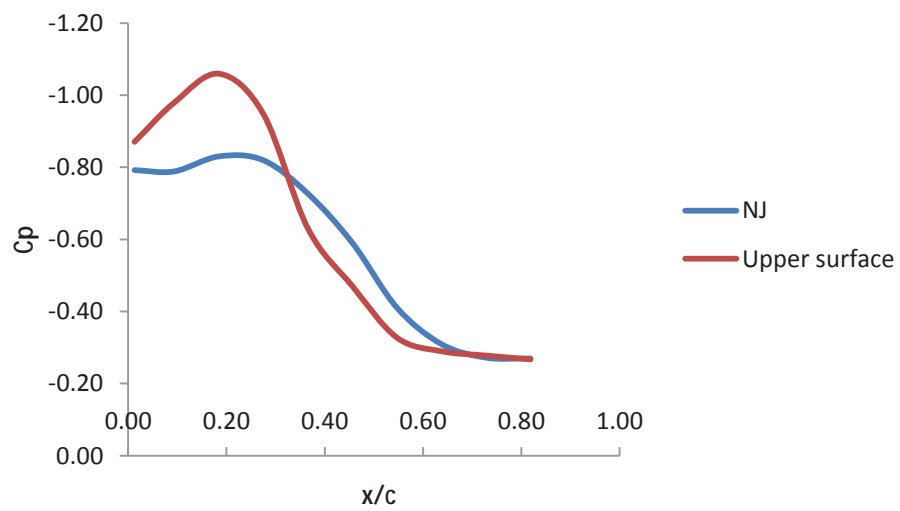


Figure D.26. Comparison of FSW NJ and with SJ4-F at 23°, Cp distribution at AOA 15°, Measuring station 4. Upper surface.

Appendix D: Surface Pressure Data

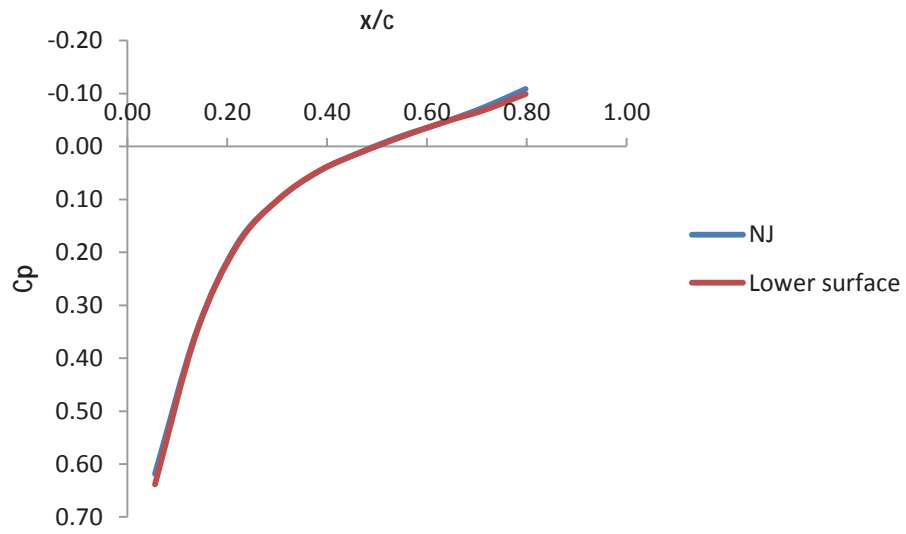


Figure D.27. Comparison of FSW NJ and with SJ4-F at 23°,  $C_p$  distribution at AOA 15°, Measuring station 4. Lower surface.

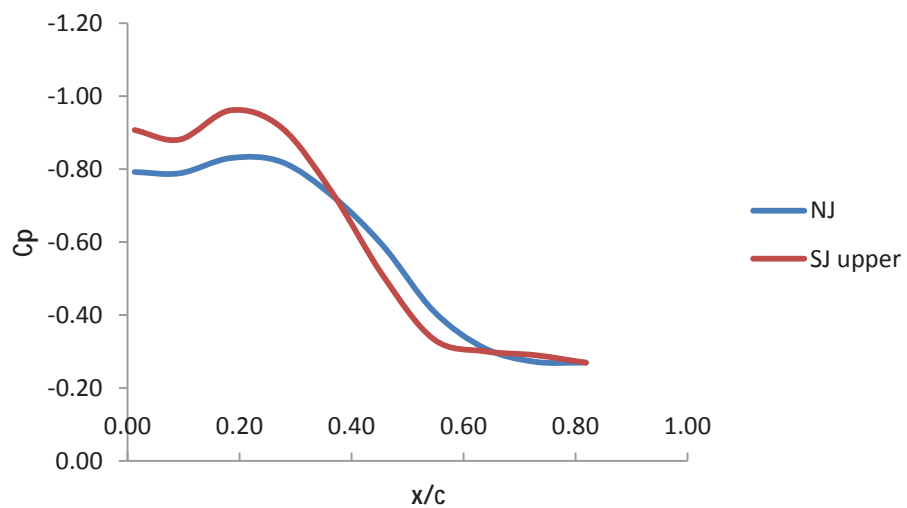


Figure D.28. Comparison of FSW NJ and with SJ4-A at 23°,  $C_p$  distribution at AOA 15°, Measuring station 4. Upper surface.

Appendix D: Surface Pressure Data

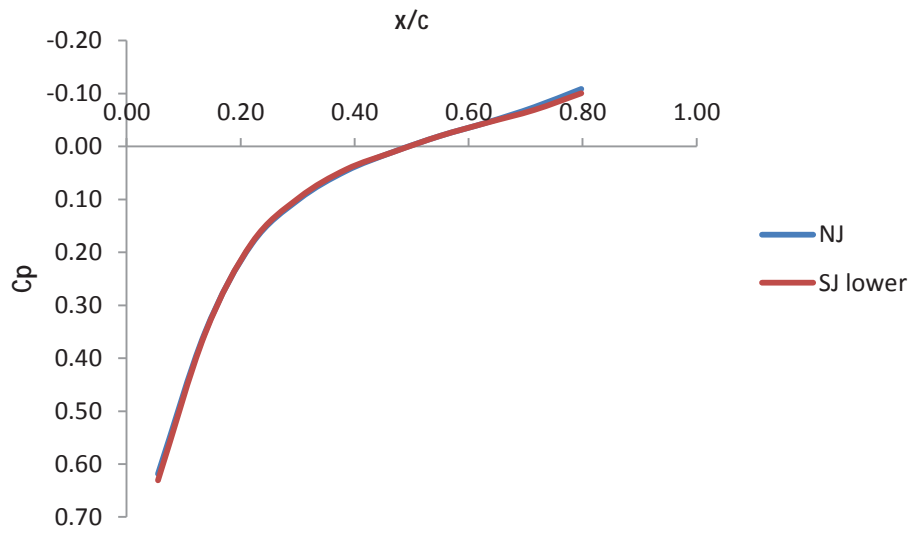


Figure D.29. Comparison of FSW NJ and with SJ4-A at  $23^\circ$ ,  $C_p$  distribution at AOA  $15^\circ$ , Measuring station 4. Lower surface.